University of Cambridge

Department of Chemistry

Carbon nitride for solar H$_2$ production coupled to organic chemical transformations

A dissertation submitted for the degree of Doctor of Philosophy

September 2018

Hatice Kasap

St Edmund's College

Declaration

The work presented in this thesis titled as 'Carbon nitride for solar H_2 production coupled to organic chemical transformations' is the result of my own work carried out between October 2014 and September 2018 in University of Cambridge and is not the outcome of any collaborations except as declared in Acknowledgements and specified in the text.

The reported results in this thesis have already been published in peer-reviewed articles, as specified in the List of publications and stated at the beginning of each chapter. I further state that no substantial part of my dissertation has already been submitted, or, is being concurrently submitted for any such degree, diploma or other qualification at the University of Cambridge or any other University of similar institution except as declared in the Acknowledgements and specified in the text. The thesis does not exceed the 60,000 word limit.

Hatice Kasap

September 2018

Acknowledgements

This thesis is dedicated to my parents, brothers and partner for their endless support, encouragement and love.

List of publications

The peer-reviewed articles discussed in this thesis are listed below:

1. <u>Kasap, H.</u>; Caputo, C. A.; Martindale, B. C. M.; Godin, R.; Lau, V. W.; Lotsch, B. V.; Durrant, J. R.; Reisner, E., 'Solar-driven reduction of aqueous protons coupled to selective alcohol oxidation with a carbon nitride-molecular Ni catalyst system', *J. Am. Chem. Soc.*, **2016**, *138*, 9183–9192.

2. *Lau, V. W.-h.; *Klose, D.; *<u>Kasap, H.</u>; Podjaski, F.; Pigne, M.-C.; Reisner, E.; Jeschke, G.; Lotsch, B. V., 'Dark photocatalysis: storage of solar energy in carbon nitride for time-delayed hydrogen production', *Angew. Chem. Int. Ed.*, **2017**, *56*, 510–514.

3. <u>Kasap, H.</u>; Godin, R.; Jeay-Bizot, C.; Achilleos, D. S.; Fang, X.; Durrant, J. R.; Reisner, E., 'Interfacial engineering of a carbon nitride-graphene oxide-molecular Ni catalyst hybrid for enhanced photocatalytic activity', *ACS Catal.*, **2018**, *8*, 6914–6926.

4. *<u>Kasap, H.</u>; *Achilleos, D. S.; Huang, A.; Reisner, E., 'Photoreforming of lignocellulose into H_2 using nano-engineered carbon nitride under benign conditions', *J. Am. Chem. Soc.,* **2018***, 140*, 11604–11607.

*equal contributions

The articles which are not included in this thesis are listed below:

1. Achilleos, D. S.; <u>Kasap, H.</u>; Reisner, E., 'Carbon dots from biomass waste for sustainable solar H_2 Generation', *submitted*.

2. Yang, W.; Godin, R.; <u>Kasap, H.</u>; Moss, B.; Dong, Y.; Hillman, S. Y.; Ludmilla Steier, L.; Reiner, E.; Durrant, J. R., ' Electron accumulation induces efficiency bottleneck for hydrogen production in carbon nitride photocatalysts', *in preparation*.

Patent

A patent application on waste reformation using carbon based light harvesters under benign conditions has been filed (UK patent application number GB1808905.2), which lists Hatice Kasap, Demetra S. Achilleos and Erwin Reisner as inventors.

Abstract

Artificial photosynthesis utilises solar-light for clean fuel H_2 production and is emerging as a potential solution for renewable energy generation. Photocatalytic systems that combine a light harvester and catalysts in one-pot reactor are promising strategies towards this direction. Yet, most of the reported systems function by consuming excess amount of expensive sacrificial reagents, preventing commercial development.

In this thesis, carbon nitrides (CN_x) have been selected as non-toxic, stable and low-cost photocatalysts. CN_x are first introduced as efficient light harvesters, to couple alcohol oxidation with proton reduction, in the presence of a Ni-based molecular catalyst. This system operated in a single compartment while the oxidation and reduction products were collected in the solution and gaseous phases, respectively, demonstrating a closed redox system. In the presence of an organic substrate and absence of a proton reduction catalyst, photoexcited CN_x was found to accumulate long-lived "trapped-electrons", which enables decoupling oxidation and reduction reactions temporarily and spatially. This allows solar H_2 generation in the dark, following light exposure, replication light and dark cycle of natural photosynthesis in an artificial set-up. The stability of the designed system was found to be limited by the Ni-based molecular catalyst, and the spectroscopic studies revealed electron transfer from CN_x to catalyst as the kinetic bottleneck. Graphene based conductive scaffolds were introduced to the CN_x-Ni system, to accelerate the rate of electron transfer from CN_x to the Ni catalyst. Time-resolved spectroscopic techniques revealed that introducing these conductive binders enabled better electronic communication between CN_x and Ni, resulting in significantly enhanced photocatalytic activity.

To improve the solar-light utilisation and the photocatalytic performance of bulk CN_x, a straightforward ultra-sonication approach was introduced. This pre-treatment was found to break aggregates of bulk CN_x, and the resulting activated CN_x had significantly improved activity. The activated CN_x showed record activities per gram of the material used, for H_2 evolution with a molecular Ni catalyst. The use of abundant waste sources instead of organic substrates was investigated in the presence of activated CN_x. The system demonstrated to photoreform purified and raw lignocellulose samples into H_2 in the presence of various H_2 evolution catalysts over a wide range of pH.

Table of contents

Abbreviations

AA	ascorbic acid
AM 1.5G	air mass 1.5 global
ATR	attenuated total reflectance
BET	Brunauer-Emmett-Teller
bpy	2,2'-bipyridine
CB	conduction band
CDs	carbon dots
CN_x	carbon nitride
$^{H_2N}CN_x$	amine-terminated carbon nitride
$^{NCN}CN_x$	cyanamide-functionalised carbon nitride
Cys	cysteine
DHA	dehydroascorbic acid
EA	electron acceptor
ED	electron donor
EDTA	ethylenediaminetetraacetic acid
EQE	external quantum efficiency
EPR	electron paramagnetic resonance
FNR	ferredoxin-$NADP^+$ reductase
FT	fourier transform
GC	gas chromatography
GO	graphene oxide
HOMO	highest occupied molecular orbital
H_2ase	hydrogenase
IR	infrared
KIE	kinetic isotope effect
LUMO	lowest unoccupied molecular orbital
MS	mass spectrometry

NaDC	sodium deoxycholate
NADP	nicotinamide adenine dinucleotide phosphate
NADPH	reduced nicotinamide adenine dinucleotide phosphate
NHE	normal hydrogen electrode
NMR	nuclear magnetic resonance
OEC	oxygen evolving complex
PIAS	photoinduced absorption spectroscopy
PS	photosensitiser
PSI	photosystem I
PSII	photosystem II
QDs	quantum dots
RGO	reduced graphene oxide
RHE	reversible hydrogen electrode
SEM	scanning electron microscopy
TAS	transient absorption spectroscopy
TCSPC	time-correlated single photon counting
TEA	triethylamine
TEM	transmission electron microscopy
TEOA	triethanolamine
TOF	turnover frequency
TON	turnover number
tr-PL	time-resolved photoluminescence
UV–vis	UV–visible
VB	valence band
WRC	water reduction catalyst
WOC	water oxidation catalyst
XPS	X-ray photoelectron spectroscopy
XRD	X-ray diffraction
4-MBA	4-methyl benzyl alcohol
4-MBAd	4-methyl benzaldehyde

Chapter 1

Introduction

1.1 Overview

The threatening shortage in global energy supply, increasing environmental concerns as well as economic factors greatly emphasise the need to find alternative clean, cheap and renewable energy sources, that could either replace or minimise the demand for fossil fuels.[1,2] Today, more than 80% of total energy is produced from fossil fuel sources and it is predicted that at the current consumption rate, these sources will diminish in the next 50–100 years.[1,2] The use of fossil fuel feedstocks has resulted in increased greenhouse gas emission, especially CO_2, which has been identified as the main driving force of global warming and climate change.[3] It is also predicted that global energy consumption will double by 2050, therefore there is a great need to develop low-cost technologies with large-scale applications to tackle this problem.[1,4]

1.2 Hydrogen

H_2 has been identified as the most promising energy carrier candidate and potential transportation fuel to replace currently used non-renewable fossil derived fuels. H_2 is a clean energy source that possesses a very high combustion enthalpy (-286 kJ mol^{-1}) and can be used directly in fuel cells, producing H_2O as the only oxidation product.[5] With the rapid development of fuel cell technologies, H_2 fuelled cars are now commercially available and they may play a crucial role in reducing CO_2 emission in the future.[6] Globally, more than 50 million tonnes of H_2 are produced and used by

industry every year.[7] The main use of H_2 is for NH_3 production, the key raw material used for fertilisers, while it is also being used as a common reactant in the chemical industry and in oil refining process to produce light carbon-based fuels.[8]

Although hydrogen is the most abundant element in the universe, the stocks in Earth are limited and thus needs to be produced in massive scales.[7] Currently large scale H_2 production is carried out using the steam-gas reforming process, in which CH_4 obtained from fossil fuels is converted into H_2 (Equation 1.1).[7] To obtain purified H_2 from *syngas* (CO and H_2 mixture), CO is subsequently converted into CO_2 and H_2 by water-gas shift reactions (Equation 1.2). This process produces large amounts of CO_2 as the side product, reaching on average 7 kg of CO_2 per kg of H_2 generated.[9]

$$CH_4 + H_2O \xrightleftharpoons{Ni_{Cat},\Delta} CO + 3H_2 \qquad (1.1)$$

$$CO + H_2O \xrightleftharpoons{Cu_{cat},\Delta} CO_2 + H_2 \qquad (1.2)$$
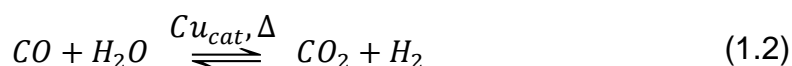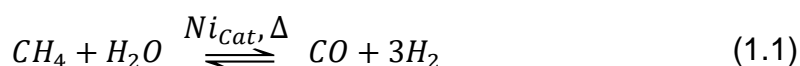
In order to meet the growing energy demands of the global society, a sustainable strategy needs to be developed to produce H_2 as energy carrier from renewable sources at low cost, while eliminating the formation of any undesired side products. The most promising way forward is to utilise water as the feedstock for clean H_2 generation. For this purpose, water splitting into its components H_2 and O_2 has attracted significant research focus.

1.3 Water electrolysis

Water splitting is a promising approach for sustainable H_2 generation from highly abundant water, yet it is a thermodynamically uphill reaction with an energy input demand of 237.2 kJ mol^{-1}.[10–12] In electrochemical terms, this corresponds to a minimum cell potential of 1.23 V, but in reality much higher cell voltages are required to overcome additional energy loses during water electrolysis.[13] Electrolysis include water oxidation and proton reduction half-reactions occurring at the anode and cathode, respectively (Equations 1.3–1.5).

$$2H^+ + 2e^- \longrightarrow H_2 \qquad \text{(E° = 0 V } vs. \text{ RHE)} \qquad (1.3)$$

$$2H_2O \longrightarrow O_2 + 4H^+ + 4e^- \qquad \text{(E° = 1.23 V } vs. \text{ RHE)} \qquad (1.4)$$

$$\overline{2H_2O \longrightarrow 2H_2 + O_2} \qquad \text{(E° = −1.23 V } vs. \text{ RHE)} \qquad (1.5)$$
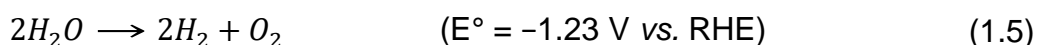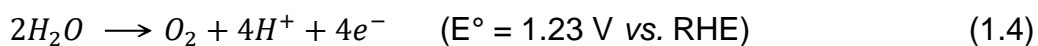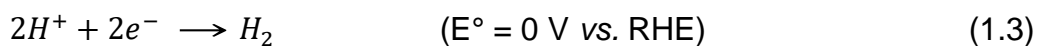
The intricate nature of the water oxidation reaction involves multiple electron and proton transfers that are believed to be the main obstacles in achieving efficient water splitting systems.[14] In addition, to lower the cost of H_2 evolution via water splitting, the ultimate goal is to replace the external electrical energy input with a sustainable energy source. Amongst all the renewable energy sources, solar energy is the most feasible and attractive to replace the electrical input. This is because the sun delivers enough energy to Earth in an hour to cover the anthropogenic global energy consumption annually.[4] Efficient utilisation of small portion of solar energy is the most promising strategy towards satisfying the energy needed by water splitting. Therefore, solar-light driven water splitting is one of the strategies towards sustainable solar-fuel H_2 production from water.

1.4 Photocatalytic water splitting

1.4.1   Natural photosynthesis

In nature, plants are perfectly functioning 'power stations' that are efficiently converting solar energy into chemical energy. Plants have evolved a complex architecture to utilise solar light to convert naturally abundant CO_2 and H_2O into carbohydrates and O_2 respectively, through a series of light and dark reactions cycles; via nature's major energy generation process, which is known as "natural photosynthesis".[15] Natural photosynthesis is accomplished by a series of enzymes, which are energetically and kinetically orchestrated to harvest light, produce charge carriers and subsequently carry out physiological redox reactions.

In the photosynthetic Z-Scheme, solar light is absorbed by photosystem I and II (PSI and PSII), which contain multiple chlorophyll pigments to harvest light efficiently. Solar light irradiation of the reaction centre P680 found in PSII, leads to generation of photoexcited electrons and holes (Figure 1.1).[16] The holes are used up to oxidise H_2O to O_2 at Mn_4Ca cluster, which is the oxygen evolving complex (OEC). The photoexcited electrons are delivered to PSI through several electron mediators,

3
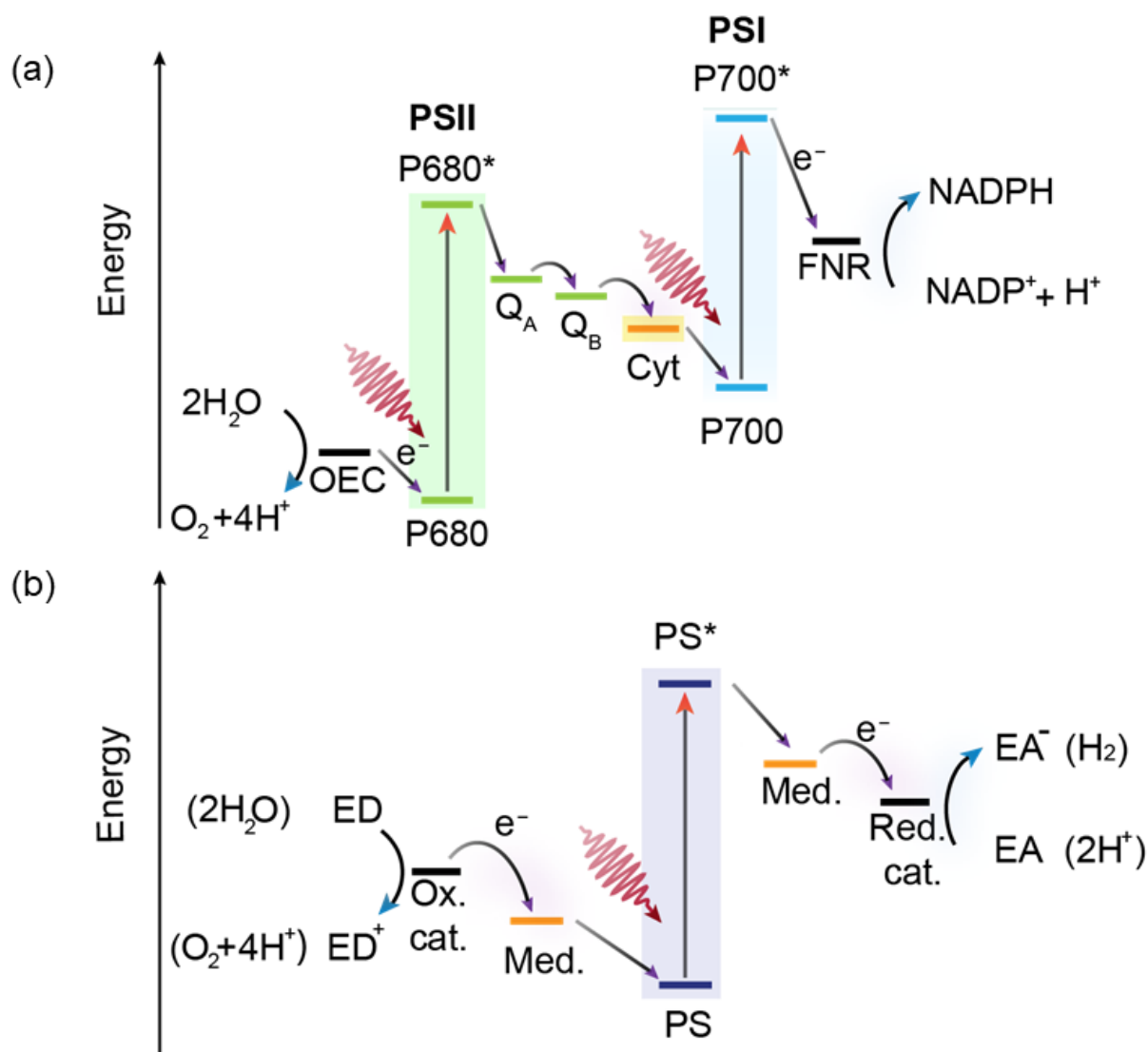
Figure 1.1. Schematic representation of (a) natural and (b) artificial photosyhthesis. Arrows represent the direction of electron flow. Abbreviations: OEC, oxygen evolving complex; PSII, photosystem II; Q_A, plastoquinone A; Q_B, plastoquinone B; Cyt, cytochrome b_6f; PSI, photosystem I; FNR, ferredoxin-NADP$^+$ reductase (FNR); NADP, nicotinamide adenine dinucleotide phosphate; ED, electron donor; Ox. cat., oxidation catalyst; Med., mediator; PS, photosensitiser, Red. cat., reduction catalyst, EA, electron acceptor.

plastoquinone A (Q_A), plastoquinone B (Q_B) and cytochrome b_6f (Cyt). In PSI, the second photoexcitation takes place at the reaction centre P700, in which the photogenerated electrons are used to reduce nicotinamide adenine dinucleotide phosphate, $NADP^+$, to NADPH (biological hydrogen) by ferredoxin-$NADP^+$ reductase (FNR). NADPH is then used as both proton and electron source in "dark" (light-independent) Calvin cycle to convert CO_2 into carbohydrates.[15]

Inspired by the efficiency of fundamental steps in natural photosynthesis, which are light harvesting, charge generation and delivery of the photogenerated charge carriers to catalytically active sites, great research efforts have been invested in developing artificial photosynthetic schemes for water splitting.[17]

1.4.2 Artificial photosynthesis

Artificial photosynthesis mimics the key functions of natural photosynthesis with the aim to develop inexpensive systems that can efficiently produce solar fuels using synthetic light harvesters and catalysts, while tackling the bottleneck solar-to-fuel efficiencies of natural photosynthesis (< 2%).[17] The scope of artificial photosynthesis is not limited to H_2 production from water splitting, but many other reactions are also studied including solar-light-driven organic transformations,[18] CO_2 reduction to CO and N_2 conversion to NH_3.[19–21]

In order to replicate the multi-component array of natural photosynthesis at the synthetic level, three main components are essential; a photosensitiser (PS), a water oxidation catalyst (WOC) and a water reduction catalyst (WRC), (Figure 1.1). The efficient capture of solar-light by the PS is a crucial step in providing the required energy of minimum 1.23 eV to overcome the uphill nature of the water splitting reaction. Upon excitation with light, an electron in the LUMO or valence band (VB) of PS is excited to the HOMO or conduction band (CB) of the PS, forming an excited state (PS*) and the photogenerated holes on PS are quenched by a water oxidation catalyst (WOC) to form O_2, while the photogenerated electrons are transferred to WRC to generate H_2.[10–12] It is an essential requirement for the charge transfer from the PS to the WOC and WRC to occur in faster timescales than the charge recombination in PS, while the charge transfer can directly happen *via* collusion of components or can be assisted with redox mediators.[13,22,23]

There are a number of strategies in designing artificial photosynthesis schemes, which include photovoltaic electrolysis, photoelectrochemical cells and photocatalytic systems.[24] For the purpose of this thesis, photocatalytic systems will be studied in which the photosensitiser(s) and catalyst(s) are mixed in a single pot, eliminating the need for expensive wiring or conductive substrates.[11,24,25] This approaches use all components dissolved in the medium used (homogeneous) or some insoluble parts may form a suspension (semi-heterogeneous). Hybrid systems are also common containing some soluble (homogenous) and some insoluble components (heterogeneous).

The first example of water splitting reaction was reported in 1972 using TiO_2 as the light harvester (see Section 1.5.2).[26] Water splitting is a promising approach to produce H_2 sustainably from the unlimited source of H_2O, while H_2O oxidation to O_2 is recognised as the kinetically demanding half-reaction, which involves four electron and proton transfers.[27] This process leads to production of explosive gas mixtures of O_2 and H_2, therefore multi compartment design is essential to separate these gasses. There is also the possibility of O_2 and H_2 back reaction to generate H_2O.[27] In addition, many WRCs are O_2 sensitive and O_2 has limited commercial applications.[28–30]

To overcome the complex nature of water splitting reaction, it has often been studied as two half-reactions, oxidation or reduction half reaction in isolation, in the presence of sacrificial reagents.[27,31] In these systems, sacrificial scavengers are used to minimise electron-hole recombination, where they act as charge traps by irreversibly reacting with the charge carriers, which are electrons and holes for oxidation and reduction half reactions, respectively. Despite the great interest in oxidative artificial photosynthetic schemes, this thesis focuses on reductive ones and exclusively on photocatalytic solar-fuel H_2 production.

1.4.3   Sacrificial reagents for solar-fuel H_2 evolution

It is difficult to couple catalysts and conditions required for a closed redox system, in which simultaneous oxidation and reduction reactions are carried out to selectively produce a single oxidation and a single reduction product with stoichiometric amounts in a single pot.[25] For that reason, sacrificial reagents have been extensively used to isolate and study H_2 evolution half-reaction in photocatalytic systems. Under these conditions, a sacrificial electron donor reagent is consumed constantly to produce H_2,

while the H_2 and O_2 back reaction to H_2O is suppressed, due to use of a sacrificial reagent. The unselective oxidation of donor reagents under sacrificial conditions produce destructive radicals and a cocktail of non-innocent oxidation products, which are usually not monitored or characterised, demonstrating an uncontrolled and unsustainable approach.[11]

Various organic compounds including alcohols, amines and acids are being used as ED to produce H_2 photocatalytically under sacrificial conditions.[32] Methanol (MeOH) is one of the most commonly used EDs, yet the consumption of MeOH for H_2 generation will only be sustainable if it is obtained from waste sources.[27] MeOH undergoes single electron oxidation reaction as it quenches the photogenerated hole on the PS forming a $^{\bullet}CH_2OH$ radical. This highly reactive radical can then undergo further oxidation to form HCHO through e^- injection to the CB of the PS, through a process known as current doubling effect, generating two CB electrons per hole.[33,34] In the presence of a WRC, these e^- will be used for H_2 production, increasing overall the yield of H_2 formation. This mechanism is likely to occur in sacrificial H_2 production systems employing commonly used alcohol donors with hydrogen atoms at α-position with respect to OH group (ethanol, butanol).[27]

It is challenging to find single-electron donors that do not produce destructive radical species after one-electron oxidation, while commonly used tertiary amine donors, triethylamine (TEA), triethanolamine (TEOA) and ethylenediaminetetraacetic acid (EDTA), also suffer from this.[31] Upon single electron oxidation of these reagents, nitrogen centred cationic radicals are formed.[35,36] Deprotonation of these radicals with another molecule of the ED generate strongly reducing carbon-based radicals, which will rapidly undergo second electron transfer to the PS. Therefore, it is not the starting material acting as the ED but the radical species generated, which contribute to the overall photocatalytic H_2 production.[36] These reactive radicals are also destructive for other components of the system, typically towards catalysts.[37]

Ascorbic acid (AA) is another attractive ED as it is water soluble and it functions at slightly acidic and neutral pH in comparison to TEA and TEOA that work best under basic conditions.[31] The oxidation product of AA, dehydroascorbic acid (DHA), is an EA and therefore AA/DHA couple represents a reversible EA/ED cycle. However, as the concentration of DHA increases in the reaction solution during solar-driven H_2

production, DHA starts to compete with the WRC to collect photoexcited electrons from the PS, terminating the proton reduction reaction.[38]

Introduction of sacrificial reagents to study H_2 production half reaction brings along the problems of increased cost, formation of reactive intermediates and possible "short-cut" reactions that interfere with the fuel forming reaction. Therefore, the need remains to move away from non-innocent sacrificial reagents and to design alternative water splitting systems.

In order to overcome the limitations of sacrificial donors, an alternative approach is to design closed redox systems and couple proton reduction with selective organic oxidation reactions (useful organic transformations). The other possible approach is to use abundant, cheap and sustainable donors (waste) to drive solar-fuel H_2 production. This eliminates the need for any commercially available products to drive the oxidation half of the scheme (see Section 1.7).

The work in this thesis focuses on designing hybrid systems for these two alternative water splitting approaches in the presence of carbon-based light harvester and a variety of proton reduction catalysts. In the following sections, state-of-the-art photocatalytic systems with commonly used light harvesters, proton reduction catalysts and alternative approaches for sustainable H_2 evolution will be established.

1.5 Photosensitisers

Nature uses pigments to absorb a wide spectrum of light during natural photosynthesis while in artificial photosynthetic schemes, pigments are replaced with synthetic light harvesters. Fundamentally, a photosensitiser should absorb solar light efficiently, preferably visible-light ($\lambda > 400$ nm), and provide fast charge transfer to catalytic active sites, while suppressing competitive charge-hole recombination. The band gap and band positions of artificial light harvesters (molecular dyes and semiconductors) are critical in providing enough driving force for solar-light-driven reactions.[32,39] Furthermore, photostability, low cost and low-toxicity are other desirable features of a photosensitiser.
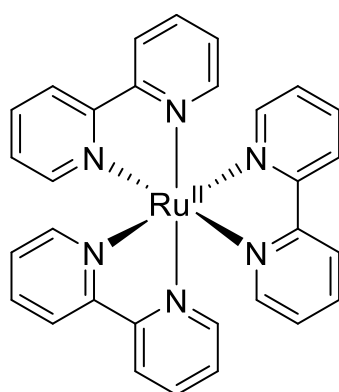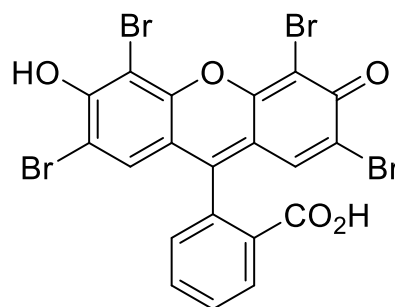
Figure 1.2. Structures of ruthenium tris-2,2'-bipryidine $[Ru(bpy)_3]^{2+}$ and Eosin Y molecular dyes.

1.5.1 Molecular dyes

Molecular dyes are commonly used photosensitisers of photocatalytic systems and they are designed by mimicking naturally occurring light absorbing centres, such as chlorophylls. Most of the studied inorganic molecular dyes consist of precious metal centres (iridium, ruthenium and rhenium) and aromatic ligands.[40]

Dyes such as $[Ru(bpy)_3]^{2+}$ are amongst the most studied metal-based photosensitisers, especially for dye-sensitised solar cells[41] with long-lived excited states, due to their metal to ligand charge transfer (MLCT) states (Figure 1.2).[42,43] The bipyridine (bpy) backbone can be modified with different functional groups, allowing solubility in a wide range of solvents, as well as enabling covalent linkage or anchoring with different surfaces or catalysts.[22,44,45] Despite the well-defined absorption band and high efficiencies as photosensitisers, these precious-metal-based dyes suffer from high cost and low molar absorption coefficient, limiting their large-scale application.[46,47] In addition these dyes can generate highly reducing or oxidising intermediate species, reducing the stability of the system.[46,47]

Metal-free organic dyes have also been used in the field of photocatalysis for H_2 evolution in conjunction with a variety of catalysts.[48–51] Molecular dyes provide flexibility to engineer side chains and anchoring groups, allowing fine-tuning of their solubility, electrochemical properties and absorption profiles.[22,52,53] In comparison to metal-based dyes, organic dyes such as xanthene-based Eosin Y, have high molar absorption coefficients and long-lived triplet excited states due to the heavy-atom

9

effect (Figure 1.2).[52,54] Organic dyes are free of precious metals, making them alternatives to traditionally used expensive metal-based dyes, but they typically have low photostabilities.[49,50,55]

1.5.2 Semiconductors

Semiconductors have the same principles of light absorption and charge separation as natural photosynthesis.[56] Unlike molecular dyes, semiconductors have broad absorption spectra and better photostability with a capacity to accumulate multiple charges.[10,57] Since the ground-breaking water splitting report of Honda and Fujishima in 1972 using TiO_2, the potential of semiconductors to drive photocatalytic reactions took a great amount of research interest.[26] TiO_2 is a widely studied inexpensive and stable semiconductor with a band gap of 3.0–3.2 eV, absorbing light mainly in the UV-region of the solar spectrum (λ < 400 nm).[58,59] Although the CB of TiO_2 (−0.29 V *vs.* NHE, pH 0) lies above the potential of proton reduction, the driving force it can provide is small.[60,61] The VB of TiO_2 lies at a very positive potential, therefore the photogenerated holes are highly oxidising, producing reactive oxygen species ($O_2^{\bullet-}$, $HO^{\bullet}$), that can be destructive towards the components of the system.[62,63]

Dye-sensitisation of TiO_2 with visible light absorbing dyes is a popular approach to increase visible light utilisation of TiO_2 nanoparticles as well as to extend the lifetime of the charge separated states.[22,64] Visible-light irradiation excites the dye and the photogenerated electron of the dye is subsequently injected into TiO_2 CB, which acts as a reservoir for long-lived electrons (Figure 1.3).[13,23,65] These electrons can then be transferred to a catalyst to carry out a reduction reaction, replicating the electron relay in natural photosynthesis.[22] A commonly used dye for this purpose is phosphonated $[Ru(bpy)_3]^{2+}$, **RuP**, that can immobilise to TiO_2 surface through the anchoring groups.[23,66]

The **RuP** dye-sensitised TiO_2 has been used for solar-light-driven proton reduction in the presence of Co-based catalysts (Figure 1.3).[65,67] More recently, precious metal-free light harvesters, including carbon nitride,[68] carbon dots,[69] and organic molecular dyes,[51] have also been used as sensitisers for TiO_2 to drive photocatalytic H_2 evolution.

10
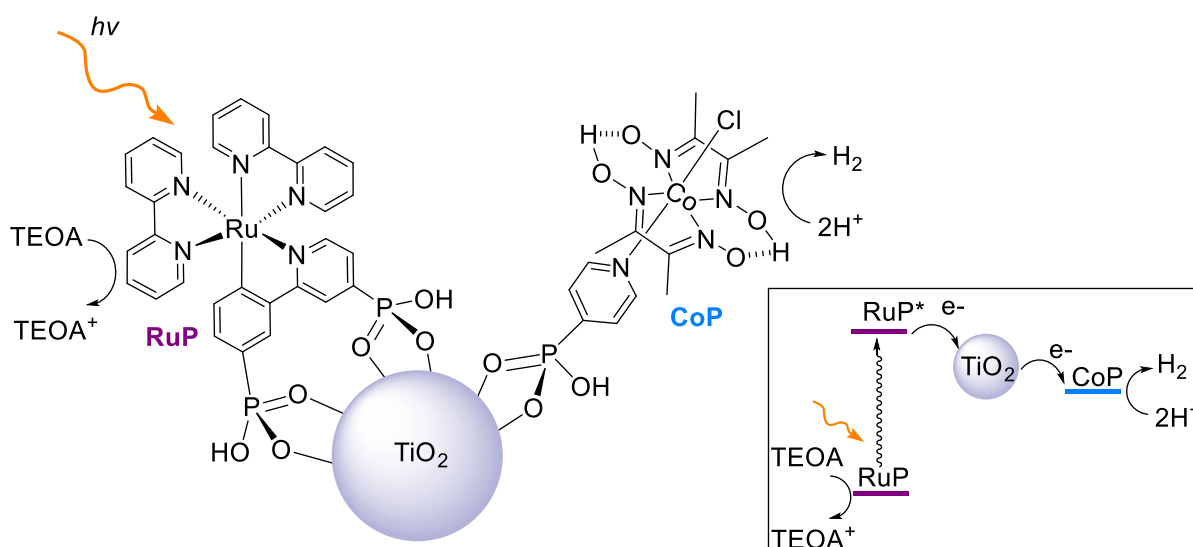
Figure 1.3. Schematic representation of a **RuP** sensitised TiO_2 hybrid system for sacrificial H_2 production in the presence of a Co catalyst.

Many other semiconductor materials have been utilised for photocatalytic applications (Figure 1.4).[56,70] Band edges of CdS, CdSe and ZnS are well positioned for water splitting, while there is only enough driving force for reduction or oxidation half-reactions for the majority of other semiconductors. CdS is an example of visible light absorbing quantum dots (QDs), with tuneable size and band positions.[71,72] CdS have been utilised in proton reduction as well as for CO_2 reduction systems due to its highly-reducing photogenerated electrons.[73–76] The photogenerated electrons in ZnS are also highly reducing (−1.85 V *vs.* NHE, pH 7), while due to its wide band gap, it does not show visible light absorption.[77]

Yet, these metal chalcogenides lack the photostability of TiO_2 nanoparticles due to sulphide auto-oxidation by the photogenerated holes in the semiconductor.[11,78] The photo-oxidation consequently decomposes these metal chalcogenides, while introducing sulphite electron donors often supress this unwanted oxidation pathway.[79,80] CdSe has a narrower band gap than CdS, therefore, it utilises visible light better, while still suffers from auto-oxidation.[74,79] However, the fundamental drawback of CdS, CdSe and ZnSe QDs is their toxicity, which limits their use and large-scale application.[81]

$BiVO_4$ is a narrow band gap semiconductor (2.4 eV) with strong visible light absorption ($\lambda < 540$ nm) and photostability.[82] It is commonly used in oxidation reactions including O_2 evolution and organic transformation due to highly oxidising VB holes.[83,84]

11
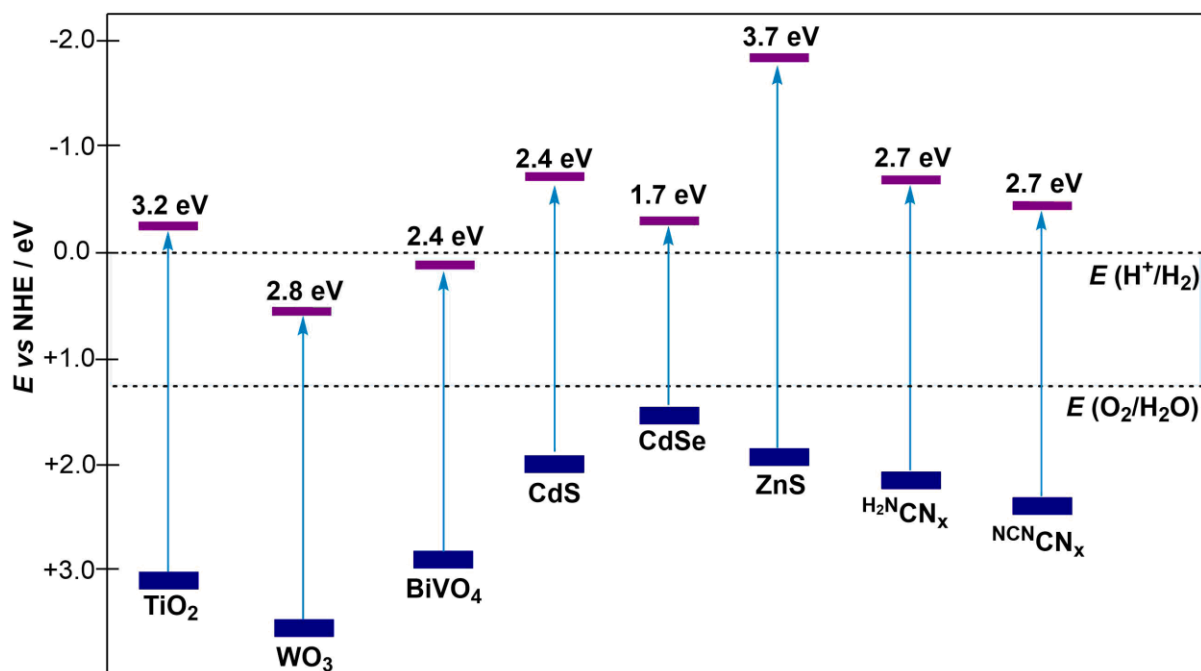
Figure 1.4. Band energy diagram for selected semiconductors showing VB (blue) and CB (purple) energies.[56,70] Dashed lines indicate the potentials for proton reduction and water oxidation versus normal hydrogen electrode (NHE) at pH 0.

WO_3 is also a semiconductor frequently used for solar-light-driven oxidation reactions although it suffers from photocorrosion.[85] Both $BiVO_4$ and WO_3 are inactive towards H_2 evolution due to mismatch between their CB positions and proton reduction potential.[11]

Carbonaceous materials, carbon dots (CDs) and carbon nitrides (CN_x), are emerging as the new-generation, low-cost, non-toxic and easy-to-synthesise light harvesters. In comparison to traditional semiconductors, these materials are metal-free and are very attractive for large-scale application.

CDs are 2–10 nm in size and contain a carbon-based core with a diverse degree of graphitisation, while the surface of the CDs is capped with oxidised groups (alcohols and carboxylic acids) making them soluble in aqueous media.[86–88] CDs are highly fluorescent particles with strong light absorption in the UV region which tail into the near-visible region and have been heavily used for *in vivo* biological applications.[89,90] CDs can be synthesised in multi-gram scale either by "bottom-up" or "top-down" approaches, through thermal decomposition of organic precursors (citric acid),[91] or exfoliation of pre-ordered graphitic structures (graphene oxide), respectively.[92] CDs have been shown to work for CO_2 reduction,[93] and H_2 evolution

12

under sacrificial conditions in the presence of enzymatic or molecular catalysts reaching up to specific activity of 7,950 μmol H_2 (g CD)$^{-1}$ h^{-1}.[94–97] While CDs benefit from high solubility and easy surface functionalisation, the recycling of dots after photocatalysis is difficult from a single pot containing all the components, which usually makes them single-use semiconductors. Furthermore, in depth characterisation of this new class of material is lacking and structural optimisation at molecular level is challenging.[88] For photocatalytic applications, graphitic CN_x is an attractive material with well-understood structural details and reusability (recyclability) due to its hydrophobic nature.

Carbon Nitride

Graphitic CN_x has been known for almost 200 years. It was first obtained as yellow residue by Berzelius in 1835 and named as "melon" by Liebig.[98,99] CN_x can be easily synthesised by thermal condensation of low-cost nitrogen-rich commercially available precursors including cyanamide, dicyanamide, urea and melamine at high temperature (> 500 °C) at very low costs (< 0.1 $ g^{-1}).[100–102] CN_x possesses a 2D stacked structure with a nitrogen heteroatom-substituted graphite layer, formed from C and N sp^2 hybridisation. Two different building blocks have been suggested as the repeating unit in a single layer of CN_x, which are condensed *s*-triazine (C_3N_3) and tri-*s*-triazine (C_6N_7, heptazine).[103] Theoretical calculations and experimental evidence demonstrated that C_6N_7 is energetically more stable and widely accepted as the building block in a single chain of CN_x structure.[104–106] Individual polymeric chains of CN_x orient themselves in a way that every second chain is inverted, fitting like a lock and key to each other, resulting in strong π-π interactions between chains as well as strong hydrogen bonding between NH_2 groups and NH edge groups.[101]

Polymeric CN_x is non-toxic and metal-free.[107] CN_x shows thermal stability (> 600 °C) and is insoluble in many conventionally used solvents (water, alcohol, THF, DMF), establishing chemical stability and application as a heterogeneous photocatalyst.[106,108] Polymeric CN_x shows visible light response due to a moderate band gap separation of 2.7 eV (λ < 460 nm), while the band edge positions (Figure 1.4), CB (−1.3 V *vs.* NHE, pH 7) and VB (+1.4 V *vs.* NHE, pH 7), make its application feasible in both oxidative and reduction photocatalytic reactions.[109–111]

As a semiconductor, CN_x provides enough driving force for the water splitting reaction. In 2009, for the first time, Antonietti and his co-workers demonstrated photocatalytic H_2 and O_2 evolution under sacrificial conditions in the presence of CN_x.[112] This re-visit to the historical semiconductor CN_x, has attracted great research interest in order to utilise this sustainable material with huge potential in different photocatalytic applications.[113]

More recently, a solar-driven closed water splitting system has been demonstrated using CN_x by photodeposition of multiple co-catalysts on the surface-active sites of the material. Simultaneous H_2 and O_2 evolution was achieved in 2:1 ratio while the need for sacrificial reagents was eliminated.[114] The quantum efficiency of the system was determined as 0.3% ($\lambda = 405$ nm) and there was a need for precious metal catalysts for the system to function. A photocatalytic system consisting of CN_x and CDs has also been reported for water splitting *via* stepwise two electron transfer reactions.[115] First, CN_x absorbs visible light and converts H_2O to H_2O_2 and H_2, then the CDs disproportionate H_2O_2 into O_2 and H_2O. The CN_x-CD hybrid showed better visible light absorption than bare CN_x and a quantum efficiency of 16% ($\lambda = 420$ nm) was achieved.[115]

Photocatalytic reduction of CO_2 into hydrocarbon fuels over CN_x has also been reported under sacrificial conditions, by depositing CN_x with noble metal co-catalyst (Pt). Mixture of reduction products including CH_4, CH_3OH and HCHO were detected with low yields.[116] Co-based molecular catalysts were also used in conjunction with CN_x for CO_2 reduction to CO, but the system was limited by the further application of CO. More recently, a hybrid system consisting of CN_x and a binuclear Ru(II) complex, demonstrated conversion of CO_2 into formate through a Z-scheme electron-transfer mechanism.[117] The system showed around 98% selectivity towards formate formation, a common intermediate molecule for chemical industry.[117,118]

Many examples of solar-light driven proton reduction under sacrificial conditions have also been reported with CN_x as the light harvester.[119–121] In the presence of CN_x and an electron donor, EDTA, with a Ni-based molecular catalyst, **NiP** (Figure 1.5), a specific activity of 437.1 ± 43.7 µmol H_2 (g CN_x)$^{-1}$ h^{-1} was reached.[122] Under only visible light irradiation ($\lambda > 420$ nm), 36% of this initial activity towards photocatalytic H_2-evolution was maintained. This is due to limited visible light absorption ability of CN_x, leaving room for further improvements.[122]

14
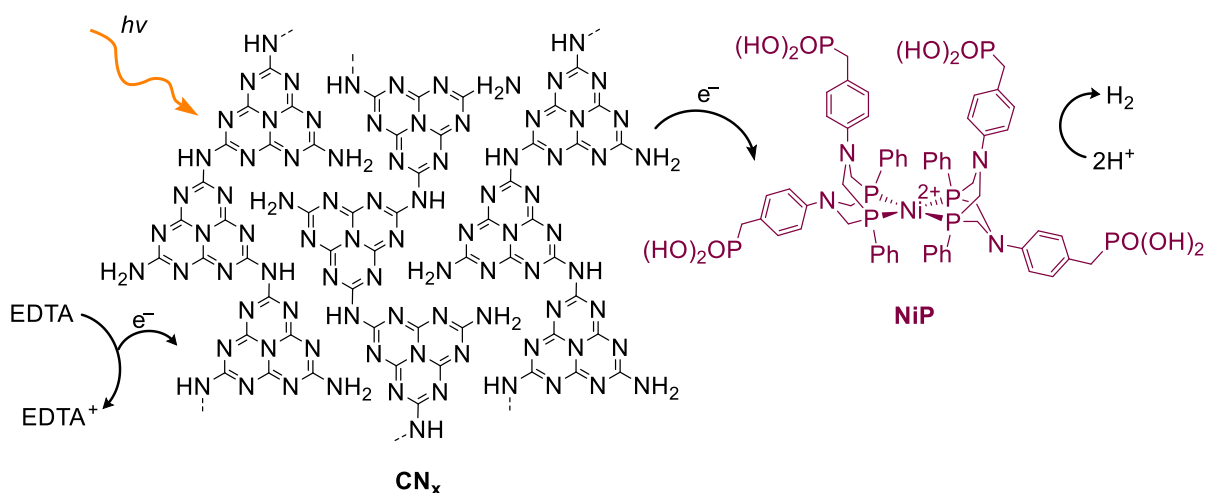
Figure 1.5. Schematic representation of photocatalytic H_2 production in the presence of CN_x, **NiP** and EDTA as the sacrificial electron donor.

The organic nature of CN_x material offers a variety of structural modification directions. Huge advances have been made in the CN_x field and materials reaching specific activities of 20,000 µmol H_2 (g CN_x)$^{-1}$ h^{-1} and 37,680 µmol H_2 (g CN_x)$^{-1}$ h^{-1} have been reported for H_2-evolution under sacrificial conditions with Pt as the co-catalyst.[100,123]

As a semiconductor, CN_x have already been used for pollutant degradation[111,124,125] and organic transformations.[126–128] The examples given represent a wide spectrum for photocatalytic applications of the polymeric CN_x. Yet, the performance of CN_x is mainly limited by the fast charge recombination, insufficient utilisation of visible light ($\lambda > 460$ nm) and small active surface area available for interfacial reactions in semi-heterogeneous systems.[112,122,129] In order to overcome these limitations, different strategies have been developed, aiming to improve the photocatalytic activity of CN_x by tuning its structure, composition and properties. Some of the possible approaches are to use different precursors as the building blocks,[130–132] engineer structures with different morpohologies,[133–136] construct heterojunctioning,[137–141] and to introduce metal or non-metal doping.[142–144]

An alternative strategy is to modify surface termination groups and defect sites in CN_x structure that have been identified as vital reaction centres for photocatalysis.[108] Lotsch and co-workers designed a range of heptazine-based structures by altering the amine (–NH$_2$) end-groups found in the benchmark CN_x structure (from this point onwards, amine-terminated CN_x will be referred to as $^{H_2N}CN_x$). Amongst all tested, the

15
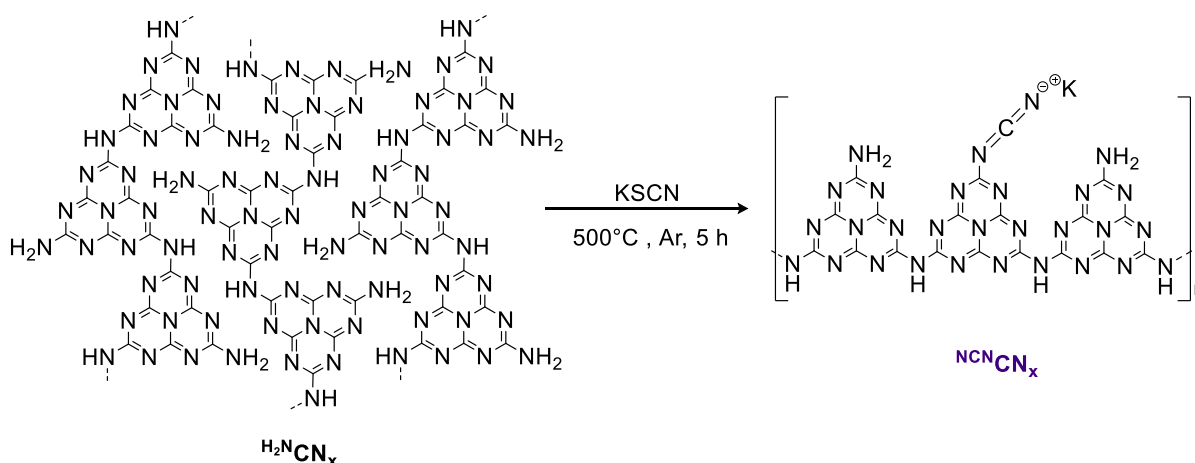
Figure 1.6. Thermal condensation of $^{H_2N}CN_x$ to $^{NCN}CN_x$ in the presence of KSCN.

cyanamide surface-functionalised CN_x, $^{NCN}CN_x$, showed the best photocatalytic activity, which was prepared by thermal treatment of $^{H_2N}CN_x$ and KSCN (Figure 1.6).[145] Polymeric nature of the material was preserved after the KSCN treatment, while the surface terminating –NH_2 groups were replaced with –NCN moieties.[145]

The H_2 production activity of $^{NCN}CN_x$ was tested in methanol solution with Pt as the co-catalyst. The system maintained its activity over 70 h and a H_2 production rate of 24.7 µmol h^{-1} was reached, showing 12 times better activity than the benchmark $^{H_2N}CN_x$.[145] The enhanced activity was attributed to longer-lived charge separated states due to built-in potential differences across chains, as well as the improved charge transfer from more exposed active sites of $^{NCN}CN_x$ to the co-catalyst.[145]

Following the initiation of this project, $^{NCN}CN_x$ was only used for H_2-evolution under sacrificial conditions. In addition, carbon-based semiconductors were never used in the literature for alternative water splitting systems defined earlier: (1) simultaneous selective organic oxidation and proton reduction, (2) solar-driven waste conversion into H_2.

1.6 H_2 evolution catalysts

In order to generate a molecule of H_2, two protons and two photoexcited electrons are required. Light harvesters can only provide small driving force for this conversion and in the absence of a catalyst, the kinetics of this reaction will be very slow.

Inspired from natural photosynthesis, many WRCs have been designed and used in the artificial schemes to catalyse H_2-evolution reaction. WRCs are

16

fundamentally required to be photostable, inexpensive, selective towards proton reduction and function under mild conditions preferably in aqueous media. Roughly, these catalysts can be divided into three categories; heterogeneous catalysts, enzymes and molecular catalysts.

1.6.1   Heterogeneous catalysts

For the H_2-evolution reaction, platinum is the benchmark WRC, due to its optimum hydrogen adsorption energy allowing rapid proton reduction and H_2 desorption.[146,147] It is usually deposited in the metal nanoparticle form on the surface of the light harvesters, including TiO_2 and **H_2NCN_x**,[112,148] *via in situ* photoreduction of a Pt precursor, typically H_2PtCl_6. As a noble metal, Pt shows stability over a wide range of reaction conditions while suffering from high cost and low abundance.[149] Selectivity is another significant drawback of Pt, as under aerobic conditions, there will be competition between oxygen and proton reduction.[150] Therefore, a need remains to find precious metal-free catalysts that are inexpensive when designing sustainable systems for large-scale application.

As an alternative to Pt, first row transition metal salts (Ni, Fe and Co) can also undergo *in situ* photoreduction to form catalytically-active metal sites. In conjunction with CN_x, photodeposited Ni co-catalyst from $NiCl_2$ salt has been demonstrated to function as active site for H_2 evolution.[151] CdS QDs have also been shown to work efficiently for proton reduction in the presence of Co co-catalysts using $CoCl_2$ and $Co(NO_3)_2$ as the catalytic precursors.[73] Yet, identification of heterogeneous nanoparticles that form upon degradation of metal salts is still challenging, as these species are not stable.[152]

Recently metal dichalcogenide materials, such as MoS_2 have attracted great research interest as WRC.[153] Computational and experimental studies indicate that the exposed sulphur edge groups are catalytically active towards proton reduction while the basal phase is inactive.[154,155] MoS_2 has been shown to work efficiently as a catalyst under homogenous and semi-heterogeneous conditions in the presence of a wide range of light harvesters, including Ru dyes,[156] **H_2NCN_x**,[157] TiO_2,[158] and CdS.[159,160]

Therefore, metal salts can be utilised as precursors for WRCs in photocatalytic systems, providing an inexpensive and easy-to-assemble approach. Yet, the photo-

induced reduction of these precursors generally introduce a delay, induction period, prior to catalysis, while it remains difficult to define the catalytically active species.[161]

1.6.2   Enzymes

In nature, hydrogenase (H$_2$ase) enzymes reversibly catalyse the reduction of protons to H$_2$ with very high activities, reaching turn over frequencies (TOFs) up to 9,000 s^{-1}.[162] These enzymes contain only earth-abundant metals iron and nickel in their active sites and function with minimum overpotential.[56,163,164] Different types of H$_2$ases have been used in hybrid systems including **RuP** sensitised TiO$_2$,[66] CdS,[165,166] **H$_2$NCN$_x$**,[122] and **H$_2$NCN$_x$** sensitised TiO$_2$.[68] These semi-biological systems showed variety of activities, while in the presence of CdS QDs a TOF of 900 s^{-1} was reached.[166]

Despite the model systems reported using H$_2$ases as WRC in photocatalytic schemes, efficient utilisation of this biocatalyst is challenging. It is an expensive process to extract and purify H$_2$ases.[167] Most of these enzymes are highly oxygen-sensitive, requiring extreme care under anaerobic conditions when handling.[168] Despite the small size of catalytically-active sites, enzymes are very bulky in comparison to metal nanoparticles or small molecular catalysts.[168] In addition, H$_2$ases have a fragile framework and only function under certain reaction conditions and pH.[167] Therefore, utilisation of enzymes as WRC for real-life applications is challenging, but the structural information serves as a guide when designing synthetic catalysts.

H$_2$ases are categorised according to the metal centres found in their active sites.[167] [FeFe]-H$_2$ases and [NiFe]-H$_2$ases are the only ones active towards H$_2$-evolution (Figure 1.7).[169] As their characteristic features, there are sulphur bridges between bimetallic centres and CO and CN$^-$ ligands.[170–172] Active sites of H$_2$ases are bound to protein matrix that facilitates electron transfer to and from metal centres.[167] [NiFe]-H$_2$ases generally have better O$_2$-tolerance than [FeFe]-H$_2$ases but they are more biased towards H$_2$ oxidation than H$^+$ reduction.[173] The arginine residue in the outer coordination sphere of [NiFe]-H$_2$ases is positioned above the Ni and Fe metal centres and the amine group facilitates proton transfer to active site.[174] [FeFe]-H$_2$ases with the bridgehead amine group, show the highest H$_2$ evolution rate.[175] The flexible pendant amine shuttles protons to the Fe centre and this unique feature is crucial for the high activity of the [FeFe]-H$_2$ases. All the structural information obtained from enzymes can be synthetically implemented in designing catalysts inspired from nature.
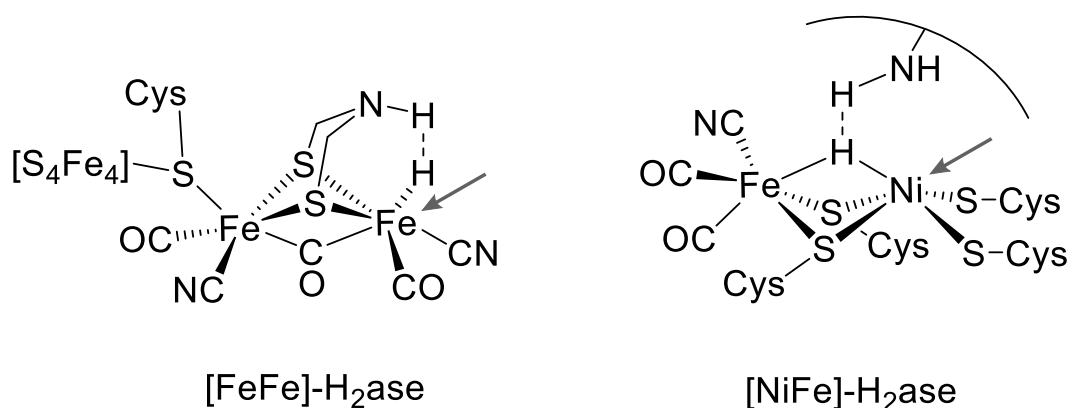
Figure 1.7. Structures of the active sites of [FeFe]-H$_2$ase and [NiFe]-H$_2$ase. The grey arrows indicate the metal coordinates sites for H$_2$. The outer coordination sphere with arginine residue is represented with an arc and an amine group, respectively, for [NiFe]-H$_2$ase. Abbreviations: [Fe$_4$S$_4$], iron-sulphur cluster; Cys, cysteine.

1.6.3   Molecular catalysts

Since the structures of H$_2$ases have been resolved, replicating active sites of this "hydrogen-processing" enzymes attracted great attention. Numerous iron complexes have been synthesised for proton reduction as molecular mimics of the [FeFe]-H$_2$ase active site.[175] Photocatalytic systems which incorporated these complexes (Figure 1.8) required large overpotentials (> 500 mV) and showed very low TOFs.[176,177] On the other hand, due to the fragile framework of [NiFe]-H$_2$ase mimics, the activity observed usually arises form heterogeneous metal precursors deposited on the semiconductor formed upon degradation of the molecular catalysts.[178,179] In addition, this bimetallic-nature-inspired complexes require organic-aqueous reaction mixtures to function, while being highly O$_2$ intolerant.[176] These findings indicate that, simply replicating the catalytically active site from a macromolecule does not necessarily mean that all of the desired features are preserved. Therefore, significant research effort has been shifted towards designing simple molecules in which the key functional features of H$_2$ases are implemented for efficient proton transfer and reduction mechanism.

Bio-inspired cobalt complexes with diglyoxime ligand framework, known as cobaloximes, are amongst the most studied catalysts for H$_2$-evolution (Figure 1.8). These complexes, as molecular mimics of vitamin B$_{12}$, are easy to synthesise, functionalise and show high initial rates at low overpotentials.[180,181] Cobaloxime complexes with phosphonated anchoring group demonstrated to work under aqueous

| [FeFe]-H$_2$ase mimic | Cobaloxime | [Ni(P$_2$N$_2$)$_2$]$^{2+}$ |
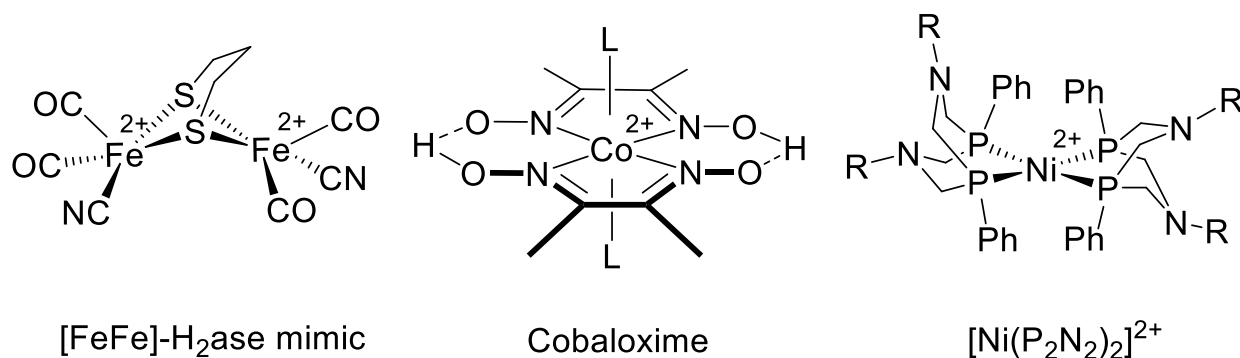
Figure 1.8. Schematic representations of the nature-inspired molecular catalysts. Abbreviations: L, ligand; R, alkyl or aryl groups.

conditions in the presence **RuP**-sensitised TiO$_2$ nanoparticles, reaching a TOF of 19 h^{-1} (Figure 1.3).[67] Cobaloxime complexes are amongst the few synthetic catalysts that have been reported to sustain H$_2$ production in the presence of O$_2$, an essential requirement for full water splitting.[48,182] As a general drawback, these complexes have poor stability, due to equatorial ligands being prone to degradation and the axial ligands becoming labile during catalysis, therefore detaching from the metal core.[183,184]

Different strategies have been considered to improve the stability of these complexes, such as equatorial ligand engineering and coordination to polymeric scaffolds, at the expense of rate or high overpotential requirements.[185–187]

Another first-row transition metal which attracted great scientific interest in designing bio-inspired complexes is nickel. Dubois and co-workers developed a series of mononuclear Ni-bisdiphosphine based molecular catalysts with a general formula of [Ni(P$_2$N$_2$)$_2$]$^{2+}$ (Figure 1.8).[188,189] Same as in nature, these catalysts are capable of reducing protons and oxidising H$_2$ (Figure 1.9), while functioning at low overpotentials (200 mV).[188,189] Initially these complexes were used for electrocatalytic H$_2$ production, reaching up to TOF of 100,000 s^{-1}, competing with the activities of H$_2$ases.[190,191] The H$_2$ production is initiated by reduction of the Ni-centre followed by protonation of an amine. The superior activity of this class of catalyst arises from the strategically positioned flexible amines, which deliver protons to reduced Ni centre, replicating the proton relay found in the active site of H$_2$ases.[191,192] The Ni-centre then undergoes second reduction forming a nickel-hydride intermediate (Figure 1.9), followed by protonation. Consequently, H–H bond is formed, releasing H$_2$ and recovering catalyst.
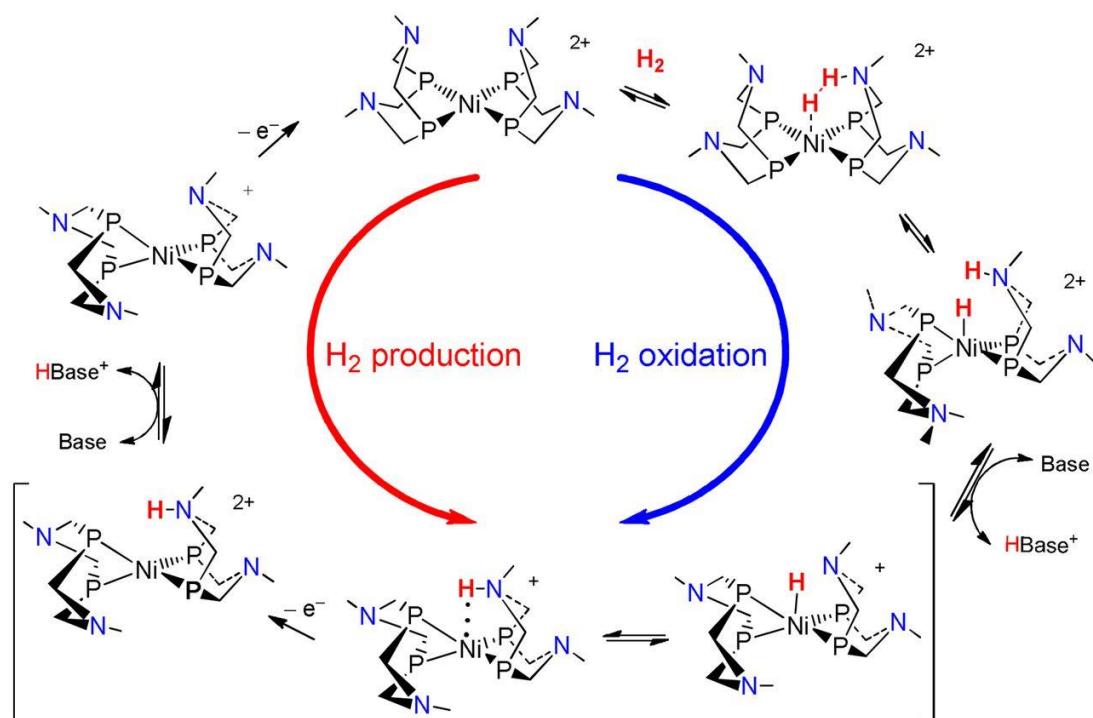
Figure 1.9. Mechanism for H$^+$ reduction and H$_2$ oxidation by Dubois type molecular catalysts with a general formula of [Ni(P$_2$N$_2$)$_2$]$^{2+}$. Reprinted with permission from *J. Phy. Chem. C,* **2012**, *116*, 3171–3180. Copyright (2012) American Chemical Society.

Even though the initially designed complexes were active for H$_2$ production under electrocatalytic conditions, organic solvents and the addition of strong acids were essential.[193,194]

Photocatalytic H$_2$ production under sacrificial conditions was first reported using the [Ni(P$_2$N$_2$)$_2$]$^{2+}$ catalyst in the presence of [Ru(bpy)$_3$]$^{2+}$ or Eosin Y.[194] The system functioned in the presence of H$_2$O/MeCN (1:1) solvent mixture and AA as the electron donor reaching a TOF up to 20 h^{-1} with a turn over number (TON) of 450 after 24 h of irradiation.[194]

More recently, [Ni(P$_2$N$_2$)$_2$]$^{2+}$ type catalysts which function under fully aqueous conditions have been synthesised by incorporating phosphonic acid groups on the ligand framework, **NiP**, (Figure 1.5).[45] Under homogenous conditions with **RuP**, **NiP** and AA as the sacrificial donor, a TOF of 406 h^{-1} and TON of 700 after 2 h of irradiation were reached.[45] **NiP** has also been utilised in semi-heterogeneous photocatalytic systems as a proton reduction catalyst in the presence of ^{H_2N}CN$_x$ (Figure 1.5),[122] and dye-sensitised TiO$_2$.[45,51] Homogenous systems using **NiP** as WRC in the presence of CDs have also been reported.[94,95] In addition, the phosphonic acid moieties on **NiP**

act as anchors enabling immobilisation on metal oxide surfaces, expanding the use of **NiP** into photoelectrochemical cells for H_2-evolution.[85,195,196]

The stability of the systems utilising **NiP** is usually limited due to photodegradation (UV irradiation) and decomposition of the catalyst with the radicals generated upon oxidation of sacrificial electron donors. These problems have been recently addressed by using CDs in the presence of clean donor system, which eliminates the formation of destructive radicals.[37,197] **NiP** showed record-high activity, reaching a TON of 1,094 after 24 h of irradiation, while maintaining its activity over 5 days under visible light irradiation.[37]

It is important to maintain an inert atmosphere for systems involving **NiP**, as it is intolerant towards O_2, the phosphine groups undergo irreversible oxidation, terminating its activity.[182,198] Still, Dubois-type catalysts are the state-of-the-art molecular complexes for photocatalytic H_2-evolution systems.

1.7 Strategies for sustainable H_2 production

Despite the great research effort put forward for solar-fuel H_2 generation, the systems reported to date heavily rely on sacrificial reagents. Under these conditions, excess amounts of electron donors are constantly consumed for H_2 production. Additionally, the role of oxidation products formed upon consumption of these reagents is often unclear and underestimated. In order to design sustainable H_2 production systems, there is a need to move away from uncontrolled oxidation of sacrificial donors.

One methodology would be to replace electron donor oxidation half-reactions with industrially important organic transformations, aiming to form oxidation products with higher value than the starting substrates and to couple this with H_2 production.[199–201] Photocatalytic systems for organic substrate oxidation under sacrificial conditions have been previously reported. In the presence of Ru-based oxidation catalyst, $[Ru(bpy)_3]^{2+}$ or $BiVO_4$ as the light harvester and sacrificial electron acceptor $[Co(NH_3)_5Cl]^{2+}$, oxidation of benzylic alcohols was achieved, with the highest conversion yield of 44%.[83,202]

Organic substrate oxidation (substituted benzyl alcohol) in the presence of TiO_2 has also been reported using O_2 as the sacrificial electron acceptor.[203–208] In the presence of dye-sensitised TiO_2 with an oxidant TEMPO, (2,2,6,6-tetramethyl-1-

piperidinyloxy), up to 100% conversion yield was achieved for 4-methoxy benzylalcohol after 15 h of irradiation.[204] Despite the high conversion yields with TiO_2, these systems operated under high pressure of O_2 and organic solvents were used to enhance the solubility of O_2.[203,204,207]

Without the need for an additional oxidation catalyst, **$^{H_2N}CN_x$** has also been demonstrated to function as a photocatalyst for the oxidation of amines, alcohols, alkanes and hydrocarbons in the presence of O_2.[108,127,209] After 2 h of irradiation full 4-methoxy benzylalcohol conversion to aldehyde was achieved, but same as TiO_2, the system functioned under high pressure of O_2 and in organic solvents.[209]

Nevertheless, a need remains to replace the sacrificial electron acceptors with a WRC as the final electron acceptor for H_2 production. This closed redox system would enable simultaneous solar-chemical and solar-fuel formation with stoichiometric amount of oxidation and reduction products. In addition, the products will be separated *in situ* as the oxidation product will stay in solution while H_2 will be collected in the headspace.

Subsequent to the start of this project, there was only one example of a photocatalytic system which coupled organic transformation and proton reduction in a single reactor. This homogeneous multicomponent system used Ru and Ir-based light harvesters, a Ru and Fe-based oxidation and reduction catalysts, repectively.[210] Although simultaneous styrene oxidation to benzaldehyde and H_2 production was detected, the yield of styrene conversion was less than 6%, and the mechanism behind this complex catalytic cycle was not clear.[210] These results indicate the importance of designing a simple system, preferably with minimum number of inexpensive components.

The second possible approach for sustainable solar-fuel H_2 production, is to use abundant, cheap and sustainable donors (waste).[211] The ultimate goal is to replace all of the commercially available chemicals, when designing a system with large-scale application with waste materials. It is estimated that the United States has the capacity to produce one billion tons of dry biomass per year, enough to replace 30% of the country's current gasoline consumption annually.[212] Utilisation of lignocellulose, the most abundant form of biomass, as the ED has the potential to produce clean and renewable H_2. Lignocellulose has a multi-component structure,

composed of cellulose, hemicellulose and lignin, which has evolved to prevent its degradation.[213,214] Due to the complex nature of lignocellulose, it is kinetically challenging to oxidise at ambient conditions.

Photocatalytic reforming of biomass implements the basics of water splitting but instead of water oxidation, biomass oxidation quenches the photogenerated holes, while the electrons are used for H_2 evolution. Despite the uphill nature of water splitting, biomass reforming is almost an energy-neutral reaction.[211] Only a handful of examples are available for direct photoreforming of unprocessed biomass, as the research heavily relied on processed biomass derivatives including glucose,[215] glycerol,[216] and 5-hydroxymethylfurfural.[217] This is due to the high insolubility of raw substrates, as well as the strong light scattering and absorbing nature of the biomass components.

The first examples of unprocessed biomass photoreforming used TiO_2 in the presence of Pt as the co-catalyst.[218,219] The biomass substrates including turf, cherry wood, laver and algae were all successfully reformed under alkaline conditions (5 M KOH). The activities reported were low, 4–18 µmol H_2 (g TiO_2)$^{-1}$ h^{-1}, while introducing oxidation catalyst (RuO_2) almost tripled the activity.[218,219] Photoreforming under elevated temperature also showed to increase the rate of H_2 production with TiO_2.[220,221]

More recently, raw biomass photoreforming at 25 °C with visible light absorbing CdS has been reported.[222] The system operated under strongly alkaline conditions (10 M KOH) to enhance the solubility of raw biomass samples and to improve the stability of the CdS QDs. In the presence of sawdust and wooden branch as the electron donors, activities of 750 µmol H_2 (g CdS)$^{-1}$ h^{-1} and 5,100 µmol H_2 (g CdS)$^{-1}$ h^{-1} were reached, respectively.[222]

High H_2 evolution rates were reached with a Co/CdS/CoO$_x$ photocatalytic system without the need for any precious metals. Yet, the system operated under strongly basic conditions (pH~15) in the presence of a toxic Cd-based light harvester. Therefore, there is a great interest in developing photoreforming systems that function under aqueous conditions while eliminating expensive or toxic components.

1.8 Project outline

As detailed in the introduction, artificial photosynthesis represents a sustainable route for storing solar energy in chemical bonds to be used on demand. For photocatalytic applications, inexpensive, easy-to-synthesise, scalable and non-toxic materials are crucial as solar light harvesters. CN_x present a great number of advantages over other traditionally used light harvesters and their potential as photocatalysts for a wide spectrum of reactions had already been explored under sacrificial conditions. Prior to the start of this project, carbon nitride had not been used as a photocatalyst for closed redox systems carrying out two useful chemical transformations in a single reactor, simultaneous organic oxidation and proton reduction, eliminating the need for sacrificial reagents. In addition, there were not any raw biomass photoreforming studies using carbon-based light harvesters.

The aim of this work was to use carbon nitride as the light harvester for these two sustainable H_2-evolution strategies. In Chapter 2, the general procedures for preparing the materials and photocatalytic experiments are detailed. The experimental set-ups and physical characterisation techniques used throughout this work are explained. In addition, the methods to quantify and characterise the oxidation and reduction products are discussed. Spectroscopic methods to follow the charge transfer kinetics in the hybrid systems designed are also discussed.

The first goal objective was to design a photocatalytic system for simultaneous substrate oxidation and proton reduction in the presence of $^{NCN}CN_x$ and **NiP** under N_2 atmosphere (Chapter 3). This photocatalytic system demonstrates solar-fuel and solar-chemical synthesis under simulated solar light irradiation in a single pot. The product formation over time was monitored and the limiting factors behind this redox system were identified.

It was found that $^{NCN}CN_x$ was able to oxidise organic substrates even in the absence of **NiP**, by storing electrons in the heptazine framework. This unusual behaviour was further studied to develop a better understanding on these trapped electrons (Chapter 4). This ability enabled decoupling oxidation and reduction reactions in the light and dark cycles, overcoming the diurnal availability of sunlight. Therefore, replicating natural photosynthesis in a single pot artificial set-up. The mechanism behind the full redox system was investigated and transient absorption

spectroscopy was used to understand the photophysics behind this system. The kinetics of each charge transfer reactions were studied and the extraction of photoexcited electrons from $^{NCN}CN_x$ was found to be the slowest, rate limiting, step.

In Chapter 5, graphene oxide and reduced graphene oxide were introduced as conductive scaffolds to enhance the rate of electron extraction from $^{NCN}CN_x$ in a full closed redox system. Significant enhancement in photoactivity, up to 3-times, were observed in the presence of graphene oxide and reduced graphene oxide in comparison to bare $^{NCN}CN_x$. For the first time, a wide range of optical spectroscopic techniques, namely time-resolved photoluminescence, transient absorption spectroscopy and photoinduced absorption spectroscopy, were used to understand the interaction in these heterojunctions while the kinetics behind the improved photocatalytic activities were investigated.

In Chapter 6, the activity of bulk $^{NCN}CN_x$ was enhanced by ultra-sonication, which enabled breaking aggregates of bulk $^{NCN}CN_x$. The activated $^{NCN}CN_x$ showed the highest H_2 production rate in the field of carbon nitrides, reaching up to 39 mmol H_2 $(^{NCN}CN_x)^{-1}$ h^{-1}. This activated material was subsequently used for photoreforming purified lignocellulosic component and raw biomass samples over a wide range of pH (2–15) and in the presence of molecular and heterogenous H_2-evolution catalysts. This is the first report on utilising carbon-based light harvester for abundant waste biomass photoreforming.

Finally in Chapter 7, the work presented in this thesis is summarised and possible future directions are envisaged. In particular, the possibility of expanding the photoreforming into plastics and other types of waste is described. The use of waste metals as H_2-evolution catalysts and abundant waste sources as precursors for synthesis of photocatalysts are among the targets towards sustainable H_2 production. The main goal is to design a system that functions in large-scale without the need for any commercially purchased components.

1.9 References

(1)   Matzenberger, J.; Kranzl, L.; Tromborg, E.; Junginger, M.; Daioglou, V.; Sheng Goh, C.; Keramidas, K. *Renew. Sustain. Energy Rev.* **2015**, *43*, 926–941.

(2)   Guo, M.; Song, W.; Buhain, J. *Renew. Sustain. Energy Rev.* **2015**, *42*, 712–725.

(3)   Dhillon, R. S.; von Wuehlisch, G. *Biomass and Bioenergy* **2013**, *48*, 75–89.

(4)   U.S. Energy Information Administration. *International Energy Outlook* **2015**, 1–154.

(5)   Bennoua, S.; Le Duigou, A.; Quéméré, M. M.; Dautremont, S. *Int. J. Hydrogen Energy* **2015**, *40*, 7231–7245.

(6)   Wilberforce, T.; Alaswad, A.; Palumbo, A.; Dassisti, M.; Olabi, A. G. *Int. J. Hydrogen Energy* **2016**, *41*, 16509–16522.

(7)   Lubitz, W.; Tumas, W. *Chem. Rev.* **2007**, *107*, 3900–3903.

(8)   Winter, C.-J. *Int. J. Hydrogen Energy* **2009**, *34*, S1–S52.

(9)   Cheng, X.; Shi, Z.; Glass, N.; Zhang, L.; Zhang, J.; Song, D.; Liu, Z.-S.; Wang, H.; Shen, J. *J. Power Sources* **2007**, *165*, 739–756.

(10)   Wen, F.; Li, C. A. N. *Acc. Chem. Res.* **2013**, *46*, 2355–2364.

(11)   Kudo, A.; Miseki, Y. *Chem. Soc. Rev.* **2009**, *38*, 253–278.

(12)   Han, Z.; Eisenberg, R. *Acc. Chem. Res.* **2014**, *47*, 2537–2544.

(13)   Cowan, A. J.; Durrant, J. R. *Chem. Soc. Rev.* **2013**, *42*, 2281–2293.

(14)   Joya, K. S.; Joya, Y. F.; Ocakoglu, K.; van de Krol, R. *Angew. Chem. Int. Ed.* **2013**, *52*, 10426–10437.

(15)   Nelson, N.; Ben-Shem, A. *Nat. Rev. Mol. Cell Biol.* **2004**, *5*, 971–982.

(16)   Caffarri, S.; Tibiletti, T.; Jennings, R.; Santabarbara, S. *Curr. Protein Pept. Sci.* **2014**, *15*, 296–331.

(17)   Barber, J. *Chem. Soc. Rev.* **2009**, *38*, 185–196.

(18)   Maciá-Agulló, J. A.; Corma, A.; Garcia, H. *Chem. Eur. J.* **2015**, *21*, 10940–10959.

(19)   Kumar, B.; Llorente, M.; Froehlich, J.; Dang, T.; Sathrum, A.; Kubiak, C. P. *Annu. Rev. Phys. Chem.* **2012**, *63*, 541–569.

(20)   Brown, K. A.; Harris, D. F.; Wilker, M. B.; Rasmussen, A.; Khadka, N.; Hamby, H.; Keable, S.; Dukovic, G.; Peters, J. W.; Seefeldt, L. C.; King, P. W. *Science* **2016**, *352*, 448–450.

(21) Roth, L. E.; Nguyen, J. C.; Tezcan, F. A. *J. Am. Chem. Soc.* **2010**, *132*, 13672–13674.

(22) Willkomm, J.; Orchard, K. L.; Reynal, A.; Pastor, E.; Durrant, J. R.; Reisner, E. *Chem. Soc. Rev.* **2016**, *45*, 9–23.

(23) Reynal, A.; Lakadamyali, F.; Gross, M. A.; Reisner, E.; Durrant, J. R. *Energy Environ. Sci.* **2013**, *6*, 3291–3300.

(24) Maeda, K.; Domen, K. *J. Phys. Chem. Lett.* **2010**, *1*, 2655–2661.

(25) Teets, T. S.; Nocera, D. G. *Chem. Commun.* **2011**, *47*, 9268–9274.

(26) Fujishima, A.; Honda, K. *Nature* **1972**, *238*, 37–38.

(27) Schneider, J.; Bahnemann, D. W. *J. Phys. Chem. Lett.* **2013**, *4*, 3479–3483.

(28) Eckenhoff, W. T.; Eisenberg, R. *Dalt. Trans.* **2012**, *41*, 13004–13021.

(29) Wakerley, D. W.; Reisner, E. *Energy Environ. Sci.* **2015**, *8*, 2283–2295.

(30) Liu, J.; Zhang, Y.; Lu, L.; Wu, G.; Chen, W. *Chem. Commun.* **2012**, *48*, 8826–8828.

(31) Pellegrin, Y.; Odobel, F. *Comptes Rendus Chim.* **2017**, *20*, 283–295.

(32) Chen, X.; Shen, S.; Guo, L.; Mao, S. S. *Chem. Rev.* **2010**, *110*, 6503–6570.

(33) Hykaway, N.; Sears, W. M.; Morisaki, H.; Morrison, S. R. *J. Phys. Chem.* **1986**, *90*, 6663–6667.

(34) Ahmed, A. Y.; Kandiel, T. A.; Ivanova, I.; Bahnemann, D. *Appl. Surf. Sci.* **2014**, *319*, 44–49.

(35) Chan, S. F.; Chou, M.; Creutz, C.; Matsubara, T.; Sutin, N. *J. Am. Chem. Soc.* **1981**, *103*, 369–379.

(36) Probst, B.; Rodenberg, A.; Guttentag, M.; Hamm, P.; Alberto, R. *Inorg. Chem.* **2010**, *49*, 6453–6460.

(37) Martindale, B. C. M.; Joliat, E.; Bachmann, C.; Alberto, R.; Reisner, E. *Angew. Chem. Int. Ed.* **2016**, *55*, 9402–9406.

(38) Guttentag, M.; Rodenberg, A.; Kopelent, R.; Probst, B.; Buchwalder, C.; Brandstätter, M.; Hamm, P.; Alberto, R. *Eur. J. Inorg. Chem.* **2012**, *2012*, 59–64.

(39)   Yang, J.; Wang, D.; Han, H.; Li, C. *Acc. Chem. Res.* **2013**, *46*, 1900–1909.

(40)   Argazzi, R.; Murakami Iha, N. Y.; Zabri, H.; Odobel, F.; Bignozzi, C. A. *Coord. Chem. Rev.* **2004**, *248*, 1299–1316.

(41)   Hagfeldt, A.; Boschloo, G.; Sun, L.; Kloo, L.; Pettersson, H. *Chem. Rev.* **2010**, *110*, 6595–6663.

(42)   Kalyanasundaram, K. *Coord. Chem. Rev.* **1982**, *46*, 159–244.

(43)   Caspar, J. V.; Meyer, T. J. *J. Am. Chem. Soc.* **1983**, *105*, 5583–5590.

(44)   Fihri, A.; Artero, V.; Razavet, M.; Baffert, C.; Leibl, W.; Fontecave, M. *Angew. Chem. Int. Ed.* **2008**, *47*, 564–567.

(45)   Gross, M. A.; Reynal, A.; Durrant, J. R.; Reisner, E. *J. Am. Chem. Soc.* **2014**, *136*, 356–366.

(46)   Du, P.; Knowles, K.; Eisenberg, R. *J. Am. Chem. Soc* **2008**, *130*, 12576–12577.

(47)   Chen, L.; Chen, G.; Leung, C. F.; Yiu, S. M.; Ko, C. C.; Anxolabéhère-Mallart, E.; Robert, M.; Lau, T. C. *ACS Catal.* **2015**, *5*, 356–364.

(48)   Lakadamyali, F.; Kato, M.; Muresan, N. M.; Reisner, E. *Angew. Chem. Int. Ed.* **2012**, *51*, 9381–9384.

(49)   Yin, M.; Ma, S.; Wu, C.; Fan, Y. *RSC Adv.* **2015**, *5*, 1852–1858.

(50)   Han, Z.; McNamara, W. R.; Eum, M. S.; Holland, P. L.; Eisenberg, R. *Angew. Chem. Int. Ed.* **2012**, *51*, 1667–1670.

(51)   Warnan, J.; Willkomm, J.; Ng, J. N.; Godin, R.; Prantl, S.; Durrant, J. R.; Reisner, E. *Chem. Sci.* **2017**, *8*, 3070–3079.

(52)   Sabatini, R. P.; Eckenhoff, W. T.; Orchard, A.; Liwosz, K. R.; Detty, M. R.; Watson, D. F.; McCamant, D. W.; Eisenberg, R. *J. Am. Chem. Soc.* **2014**, *136*, 7740–7750.

(53)   Ooyama, Y.; Yamaguchi, N.; Imae, I.; Komaguchi, K.; Ohshita, J.; Harima, Y. *Chem. Commun.* **2013**, *49*, 2548–2550.

(54)   Lazarides, T.; McCormick, T.; Du, P.; Luo, G.; Lindley, B.; Eisenberg, R. *J. Am. Chem. Soc.* **2009**, *131*, 9192–9194.

(55)   McCormick, T. M.; Calitree, B. D.; Orchard, A.; Kraut, N. D.; Bright, F. V.; Detty,

M. R.; Eisenberg, R. *J. Am. Chem. Soc.* **2010**, *132*, 15480–15483.

(56) Tran, P. D.; Wong, L. H.; Barber, J.; Loo, J. S. C. *Energy Environ. Sci.* **2012**, *5*, 5902–5918.

(57) Boschloo, G.; Fitzmaurice, D. *J. Phys. Chem. B* **1999**, *103*, 7860–7868.

(58) Kavan, L.; Grätzel, M.; Gilbert, S. E.; Klemenz, C.; Scheel, H. J. *J. Am. Chem. Soc.* **1996**, *118*, 6716–6723.

(59) Soc, C.; Berardi, S.; Drouet, S.; Franca, L.; Gimbert-surin, C.; Guttentag, M.; Richmond, C.; Stoll, T.; Llobet, A. *Chem. Soc. Rev.* **2014**, *43*, 7501–7519.

(60) Kosmulski, M. *Adv. Colloid Interface Sci.* **2009**, *152*, 14–25.

(61) Xu, Y.; Schoonen, M. A. A. *Am. Mineral.* **2000**, *85*, 543–556.

(62) Xiao-e, L.; Green, A. N. M.; Haque, S. A.; Mills, A.; Durrant, J. R. *J. Photochem. Photobiol. A* **2004**, *162*, 253–259.

(63) Tachikawa, T.; Majima, T. *Langmuir* **2009**, *25*, 7791–7802.

(64) O'Regan, B.; Gratzel, M. *Nature* **1991**, *353*, 737–740.

(65) Lakadamyali, F.; Reynal, A.; Kato, M.; Durrant, J. R.; Reisner, E. *Chem. Eur. J.* **2012**, *18*, 15464–15475.

(66) Reisner, E.; Powell, D. J.; Cavazza, C.; Fontecilla-Camps, J. C.; Armstrong, F. A. *J. Am. Chem. Soc.* **2009**, *131*, 18457–18466.

(67) Lakadamyali, F.; Reisner, E. *Chem. Commun.* **2011**, *47*, 1695–1697.

(68) Caputo, C. A.; Wang, L.; Beranek, R.; Reisner, E. *Chem. Sci.* **2015**, *6*, 5690–5694.

(69) Yu, H.; Zhao, Y.; Zhou, C.; Shang, L.; Peng, Y.; Cao, Y.; Wu, L.-Z.; Tung, C.-H.; Zhang, T. *J. Mater. Chem. A* **2014**, *2*, 3344.

(70) Wang, M.; Han, K.; Zhang, S.; Sun, L. *Coord. Chem. Rev.* **2015**, *287*, 1–14.

(71) Peng, Z. A.; Peng, X. *J. Am. Chem. Soc.* **2001**, *123*, 183–184.

(72) Harris, R. D.; Bettis Homan, S.; Kodaimati, M.; He, C.; Nepomnyashchii, A. B.; Swenson, N. K.; Lian, S.; Calzada, R.; Weiss, E. A. *Chem. Rev.* **2016**, *116*, 12865–12919.

(73) Chang, C. M.; Orchard, K. L.; Martindale, B. C. M.; Reisner, E. *J. Mater. Chem. A* **2016**, *4*, 2856–2862.

(74) Holmes, M. A.; Townsend, T. K.; Osterloh, F. E. *Chem. Commun.* **2012**, *48*, 371–373.

(75) Kuehnel, M. F.; Orchard, K. L.; Dalle, K. E.; Reisner, E. *J. Am. Chem. Soc.* **2017**, *139*, 7217–7223.

(76) Zeng, P.; Zhang, Q.; Peng, T.; Zhang, X. *Phys. Chem. Chem. Phys.* **2011**, *13*, 21496–21502.

(77) Kudo, A.; Sekizawa, M. *Chem. Commun.* **2000**, 1371–1372.

(78) Weide, P.; Schulz, K.; Kaluza, S.; Rohe, M.; Beranek, R.; Muhler, M. *Langmuir* **2016**, *32*, 12641–12649.

(79) Chakrapani, V.; Baker, D.; Kamat, P. V. *J. Am. Chem. Soc.* **2011**, *133*, 9607–9615.

(80) Bang, J. H.; Kamat, P. V. *ACS Nano* **2009**, *3*, 1467–1476.

(81) Rani, A.; Kumar, A.; Lal, A.; Pant, M. *Int. J. Environ. Health Res.* **2014**, *24*, 378–399.

(82) Tokunaga, S.; Kato, H.; Kudo, A. *Chem. Mater.* **2001**, *13*, 4624–4628.

(83) Zhou, X.; Li, F.; Li, X.; Li, H.; Wang, Y.; Sun, L. *Dalt. Trans.* **2015**, *44*, 475–479.

(84) Zhang, B.; Li, J.; Zhang, B.; Chong, R.; Li, R.; Yuan, B.; Lu, S.-M.; Li, C. *J. Catal.* **2015**, *332*, 95–100.

(85) Rosser, T.; Gross, M. A.; Lai, Y.-H.; Reisner, E. *Chem. Sci.* **2016**, *18*, 15464–15475.

(86) Baker, S. N.; Baker, G. A. *Angew. Chem. Int. Ed.* **2010**, *49*, 6726–6744.

(87) Cayuela, A.; Soriano, M. L.; Carrillo-Carrión, C.; Valcárcel, M. *Chem. Commun.* **2016**, *52*, 1311–1326.

(88) Hutton, G. A. M.; Martindale, B. C. M.; Reisner, E. *Chem. Soc. Rev.* **2017**, *46*, 6111–6123.

(89) Yang, Shengtao; Cao, Li; Luo, Pengju G; Lu, Fushen; Wang, xin; Wang, Haifeng; Meziani, Mohammed J.; Liu, Yuanfang, Qi, Gang; Sun, Y. *J. Am.*

Chem. Soc. **2009**, *131*, 11308–11309.

(90) Cao, L.; Wang, X.; Meziani, M. J.; Lu, F.; Wang, H.; Luo, P. G.; Lin, Y.; Harruff, B. A.; Veca, L. M.; Murray, D.; Xie, S. Y.; Sun, Y. P. *J. Am. Chem. Soc.* **2007**, *129*, 11318–11319.

(91) Guo, C. X.; Zhao, D.; Zhao, Q.; Wang, P.; Lu, X. *Chem. Commun.* **2014**, *50*, 7318.

(92) Yeh, T.-F.; Teng, C.-Y.; Chen, S.-J.; Teng, H. *Adv. Mater.* **2014**, *26*, 3297–3303.

(93) Cao, L.; Sahu, S.; Anilkumar, P.; Bunker, C. E.; Xu, J.; Fernando, K. A. S.; Wang, P.; Guliants, E. A.; Tackett, K. N.; Sun, Y. P. *J. Am. Chem. Soc.* **2011**, *133*, 4754–4757.

(94) Martindale, B. C. M.; Hutton, G. A. M.; Caputo, C. A.; Reisner, E. *J. Am. Chem. Soc.* **2015**, *137*, 6018–6025.

(95) Martindale, B. C. M.; Hutton, G. A. M.; Caputo, C. A.; Prantl, S.; Godin, R.; Durrant, J. R.; Reisner, E. *Angew. Chem. Int. Ed.* **2017**, *56*, 6459–6463.

(96) Yang, P.; Zhao, J.; Wang, J.; Cui, H.; Li, L.; Zhu, Z. *ChemPhysChem* **2015**, *16*, 3058–3063.

(97) Hutton, G. A. M.; Reuillard, B.; Martindale, B. C. M.; Caputo, C. A.; Lockwood, C. W. J.; Butt, J. N.; Reisner, E. *J. Am. Chem. Soc.* **2016**, *138*, 16722–16730.

(98) Gmelin, L. *Ann. Pharm.* **1835**, *15*, 252–264.

(99) Liebig, J. *Ann. Chem. Pharm.* **1844**, *50*, 337–363.

(100) Martin, D. J.; Qiu, K.; Shevlin, S. A.; Handoko, A. D.; Chen, X.; Guo, Z.; Tang, J. *Angew. Chem. Int. Ed.* **2014**, *53*, 9240–9245.

(101) Thomas, A.; Fischer, A.; Goettmann, F.; Antonietti, M.; Müller, J.-O.; Schlögl, R.; Carlsson, J. M. *J. Mater. Chem.* **2008**, *18*, 4893–4908.

(102) Dai, Y.; Li, C.; Shen, Y.; Lim, T.; Xu, J.; Li, Y.; Niemantsverdriet, H.; Besenbacher, F.; Lock, N.; Su, R. *Nat. Commun.* **2018**, *9*, 1–7.

(103) Jürgens, B.; Irran, E.; Senker, J.; Kroll, P.; Müller, H.; Schnick, W. *J. Am. Chem. Soc.* **2003**, *125*, 10288–10300.

(104) Kroke, E.; Schwarz, M.; Horath-Bordon, E.; Kroll, P.; Noll, B.; Norman, A. D.

New J. Chem. **2002**, *26*, 508–512.

(105) Sehnert, J.; Baerwinkel, K.; Senker, J. *J. Phys. Chem. B* **2007**, *111*, 10671–10680.

(106) Lotsch, B. V; Döblinger, M.; Sehnert, J.; Seyfarth, L.; Senker, J.; Oeckler, O.; Schnick, W. *Chem. Eur. J.* **2007**, *13*, 4969–4980.

(107) Zhang, X.; Xie, X.; Wang, H.; Zhang, J.; Pan, B.; Xie, Y. *J. Am. Chem. Soc.* **2013**, *135*, 18–21.

(108) Wang, Y.; Wang, X.; Antonietti, M. *Angew. Chem Int. Ed.* **2012**, *51*, 68–89.

(109) Zhang, G.; Zhang, M.; Ye, X.; Qiu, X.; Lin, S.; Wang, X. *Adv. Mater.* **2014**, *26*, 805–809.

(110) Yu, J. and S. C. *J. Phys. Chem. Lett* **2014**, *5*, 2101–2107.

(111) Cui, Y.; Ding, Z.; Liu, P.; Antonietti, M.; Fu, X.; Wang, X. *Phys. Chem. Chem. Phys.* **2012**, *14*, 1455–1462.

(112) Wang, X.; Maeda, K.; Thomas, A.; Takanabe, K.; Xin, G.; Carlsson, J. M.; Domen, K.; Antonietti, M. *Nat. Mater.* **2009**, *8*, 76–80.

(113) Li, X. H.; Antonietti, M. *Chem. Soc. Rev.* **2013**, *42*, 6593–6604.

(114) Zhang, G.; Lan, Z.-A.; Lin, L.; Lin, S.; Wang, X. *Chem. Sci.* **2016**, *7*, 3062–3066.

(115) Liu, J.; Liu, Y.; Liu, N.; Han, Y.; Zhang, X.; Huang, H.; Lifshitz, Y.; Lee, S.-T.; Zhong, J.; Kang, Z. *Science* **2015**, *347*, 970–974.

(116) Yu, J.; Wang, K.; Xiao, W.; Cheng, B. *Phys. Chem. Chem. Phys.* **2014**, *16*, 11492–11501.

(117) Kuriki, R.; Yamamoto, M.; Higuchi, K.; Yamamoto, Y.; Akatsuka, M.; Lu, D.; Yagi, S.; Yoshida, T.; Ishitani, O.; Maeda, K. *Angew. Chem. Int. Ed.* **2017**, *56*, 4867–4871.

(118) Enthaler, S.; Von Langermann, J.; Schmidt, T. *Energy Environ. Sci.* **2010**, *3*, 1207–1217.

(119) Gong, Y.; Li, M.; Wang, Y. *ChemSusChem* **2015**, *8*, 931–946.

(120) Zhang, G.; Lan, Z.-A.; Wang, X. *Chem. Sci.* **2017**, *8*, 5261–5274.

(121) Li, X.; Masters, A. F.; Maschmeyer, T. *Chem. Commun.* **2017**, *53*, 7438–7446.

(122) Caputo, C. A.; Gross, M. A.; Lau, V. W.-h; Cavazza, C.; Lotsch, B. V.; Reisner, E. *Angew. Chem. Int. Ed.* **2014**, *53*, 11538–11542.

(123) Han, Q.; Cheng, Z.; Wang, B.; Zhang, H.; Qu, L. *ACS Nano* **2018**, *12*, 5221–5227.

(124) Ai, B.; Duan, X.; Sun, H.; Qiu, X.; Wang, S. *Catal. Today* **2015**, *258*, 668–675.

(125) Cheng, N.; Tian, J.; Liu, Q.; Ge, C.; Qusti, A. H.; Asiri, A. M.; Al-Youbi, A. O.; Sun, X. *ACS Appl. Mater. Interfaces* **2013**, *5*, 6815–6819.

(126) Zhao, Y.; Shalom, M.; Antonietti, M. *Appl. Catal. B Environ.* **2017**, *207*, 311–315.

(127) Su, F.; Mathew, S. C.; Möhlmann, L.; Antonietti, M.; Wang, X.; Blechert, S. *Angew. Chem. Int. Ed.* **2011**, *50*, 657–660.

(128) Li, X.; Chen, J.; Wang, X.; Sun, J.; Antonietti, M. *J. Am. Chem. Soc.* **2011**, *133*, 8074–8077.

(129) Wen, J.; Xie, J.; Chen, X.; Li, X. *Appl. Surf. Sci.* **2017**, *391*, 72–123.

(130) Ishida, Y.; Chabanne, L.; Antonietti, M.; Shalom, M. *Langmuir* **2014**, *30*, 447–451.

(131) Zhang, J.; Chen, X.; Takanabe, K.; Maeda, K.; Domen, K.; Epping, J. D.; Fu, X.; Antonietti, M.; Wang, X. *Angew. Chem. Int. Ed.* **2010**, *49*, 441–444.

(132) Zhang, M.; Wang, X. *Energy Environ. Sci.* **2014**, *7*, 1902–1906.

(133) Zhang, N.; Yang, M.-Q.; Tang, Z.-R.; Xu, Y.-J. *J. Catal.* **2013**, *303*, 60–69.

(134) Lu, X.; Xu, K.; Chen, P.; Jia, K.; Liu, S.; Wu, C. *J. Mater. Chem. A* **2014**, *2*, 18924–18928.

(135) Yang, Z.; Zhang, Y.; Schnepp, Z. *J. Mater. Chem. A* **2015**, *3*, 14081–14092.

(136) Zhang, J.; Zhang, M.; Yang, C.; Wang, X. *Adv. Mater.* **2014**, *26*, 4121–4126.

(137) Hou, Y.; Laursen, A. B.; Zhang, J.; Zhang, G.; Zhu, Y.; Wang, X.; Dahl, S.; Chorkendorff, I. *Angew. Chem. Int. Ed.* **2013**, *52*, 3621–3625.

(138) Xiang, Q.; Yu, J.; Jaroniec, M. *J. Phys. Chem. C* **2011**, *115*, 7355–7363.

(139) Han, C.; Ge, L.; Chen, C.; Li, Y.; Xiao, X.; Zhang, Y.; Guo, L. *Appl. Catal. B Environ.* **2014**, *147*, 546–553.

(140) Iwashina, K.; Iwase, A.; Ng, Y. H.; Amal, R.; Kudo, A. *J. Am. Chem. Soc.* **2015**, *137*, 604–607.

(141) Dong, F.; Zhao, Z.; Xiong, T.; Ni, Z.; Zhang, W.; Sun, Y.; Ho, W. K. *ACS Appl. Mater. Interfaces* **2013**, *5*, 11392–11401.

(142) Gao, L.-F.; Wen, T.; Xu, J.-Y.; Zhai, X.-P.; Zhao, M.; Hu, G.-W.; Chen, P.; Wang, Q.; Zhang, H.-L. *ACS Appl. Mater. Interfaces* **2016**, *8*, 617–624.

(143) Zhang, Y.; Mori, T.; Ye, J.; Antonietti, M. *J. Am. Chem. Soc.* **2010**, *132*, 6294–6295.

(144) Wang, H.; Wang, B.; Bian, Y.; Dai, L. *ACS Appl. Mater. Interfaces* **2017**, *9*, 21730–21737.

(145) Lau, V. W.-h; Moudrakovski, I.; Botari, T.; Weinberger, S.; Mesch, M. B.; Duppel, V.; Senker, J.; Blum, V.; Lotsch, B. V. *Nat. Commun.* **2016**, *7*, 12165.

(146) Greeley, J.; Jaramillo, T. F.; Bonde, J.; Chorkendorff, I.; Nørskov, J. K. *Nat. Mater.* **2006**, *5*, 909–913.

(147) Conway, B. E.; Jerkiewicz, G. *Electrochim. Acta* **2000**, *45*, 4075–4083.

(148) Xiang, Q.; Yu, J.; Jaroniec, M. *Nanoscale* **2011**, *3*, 3670–3678.

(149) McCrory, C. C. L.; Jung, S.; Ferrer, I. M.; Chatman, S. M.; Peters, J. C.; Jaramillo, T. F. *J. Am. Chem. Soc.* **2015**, *137*, 4347–4357.

(150) Marković, N. M.; Schmidt, T. J.; Stamenković, V.; Ross, P. N. *Fuel Cells* **2001**, *1*, 105–116.

(151) Indra, A.; Menezes, P. W.; Kailasam, K.; Hollmann, D.; Schröder, M.; Thomas, A.; Brückner, A.; Driess, M. *Chem. Commun.* **2016**, *52*, 104–107.

(152) Kaeffer, N.; Morozan, A.; Fize, J.; Martinez, E.; Guetaz, L.; Artero, V. *ACS Catal.* **2016**, *6*, 3727–3737.

(153) Li, Y.; Wang, H.; Xie, L.; Liang, Y.; Hong, G.; Dai, H. *J. Am. Chem. Soc.* **2011**, *133*, 7296–7299.

(154) Hinnemann, B.; Moses, P. G.; Bonde, J.; Jørgensen, K. P.; Nielsen, J. H.; Horch, S.; Chorkendorff, I.; Nørskov, J. K. *J. Am. Chem. Soc.* **2005**, *127*, 5308–5309.

(155) Jaramillo, T. F.; Jorgensen, K. P.; Bonde, J.; Nielsen, J. H.; Horch, S.;

Chorkendorff, I. *Science* **2007**, *317*, 100–102.

(156) Zong, X.; Na, Y.; Wen, F.; Ma, G.; Yang, J.; Wang, D.; Ma, Y.; Wang, M.; Sun, L.; Li, C. *Chem. Commun.* **2009**, 30, 4536–4538.

(157) Gu, Q.; Sun, H.; Xie, Z.; Gao, Z.; Xue, C. *Appl. Surf. Sci.* **2017**, *396*, 1808–1815.

(158) Xiang, Q.; Yu, J.; Jaroniec, M. *J. Am. Chem. Soc.* **2012**, *134*, 6575–6578.

(159) Zong, X.; Wu, G.; Yan, H.; Ma, G.; Shi, J.; Wen, F.; Wang, L.; Li, C. *J. Phys. Chem. C* **2010**, *114*, 1963–1968.

(160) Zong, X.; Yan, H.; Wu, G.; Ma, G.; Wen, F.; Wang, L.; Li, C. *J. Am. Chem. Soc.* **2008**, *130*, 7176–7177.

(161) Artero, V.; Fontecave, M. *Chem. Soc. Rev.* **2013**, *42*, 2338–2356.

(162) Cammack, R. *Nature* **1999**, *397*, 214–215.

(163) Na, Y.; Wang, M.; Pan, J.; Zhang, P.; Åkermark, B.; Sun, L. *Inorg. Chem.* **2008**, *47*, 2805–2810.

(164) Wang, F.; Wang, W.-G.; Wang, X.-J.; Wang, H.-Y.; Tung, C.-H.; Wu, L.-Z. *Angew. Chem. Int. Ed.* **2011**, *50*, 3193–3197.

(165) Wilker, M. B.; Utterback, J. K.; Greene, S.; Brown, K. A.; Mulder, D. W.; King, P. W.; Dukovic, G. *J. Phys. Chem. C* **2018**, *122*, 741–750.

(166) Brown, K. A.; Wilker, M. B.; Boehm, M.; Dukovic, G.; King, P. W. *J. Am. Chem. Soc.* **2012**, *134*, 5627–5636.

(167) Lubitz, W.; Ogata, H.; Rüdiger, O.; Reijerse, E. *Chem. Rev.* **2014**, *114*, 4081–4148.

(168) Thoi, V. S.; Sun, Y.; Long, J. R.; Chang, C. J. *Chem. Soc. Rev.* **2013**, *42*, 2388–2400.

(169) Fontecilla-Camps, J. C.; Amara, P.; Cavazza, C.; Nicolet, Y.; Volbeda, A. *Nature* **2009**, *460*, 814–822.

(170) Happe, R. P.; Roseboom, W.; Pierik, A. J.; Albracht, S. P. J.; Bagley, K. A. *Nature* **1997**, *385*, 126–126.

(171) Peters, J. W. *Science* **1998**, *282*, 1853–1858.

(172) Nicolet, Y.; Piras, C.; Legrand, P.; Hatchikian, C. E.; Fontecilla-Camps, J. C.

Structure **1999**, *7*, 13–23.

(173) Shafaat, H. S.; Rüdiger, O.; Ogata, H.; Lubitz, W. *Biochim. Biophys. Acta, Bioenerg.* **2013**, *1827*, 986–1002.

(174) Evans, R. M.; Brooke, E. J.; Wehlin, S. A. M.; Nomerotskaia, E.; Sargent, F.; Carr, S. B.; Phillips, S. E. V.; Armstrong, F. A. *Nat. Chem. Biol.* **2016**, *12*, 46–50.

(175) Berggren, G.; Adamska, A.; Lambertz, C.; Simmons, T. R.; Esselborn, J.; Atta, M.; Gambarelli, S.; Mouesca, J. M.; Reijerse, E.; Lubitz, W.; Happe, T.; Artero, V.; Fontecave, M. *Nature* **2013**, *499*, 66–69.

(176) Gloaguen, F.; Rauchfuss, T. B. *Chem. Soc. Rev.* **2009**, *38*, 100–108.

(177) Wang, H. Y.; Wang, W. G.; Si, G.; Wang, F.; Tung, C. H.; Wu, L. Z. *Langmuir* **2010**, *26*, 9766–9771.

(178) Wombwell, C.; Reisner, E. *Dalt. Trans.* **2014**, *43*, 4483–4493.

(179) Wombwell, C.; Reisner, E. *Chem. Eur. J.* **2015**, *21*, 8096–8104.

(180) Du, P.; Eisenberg, R. *Energy Environ. Sci.* **2012**, *5*, 6012–6021.

(181) Dempsey, J. L.; Brunschwig, B. S.; Winkler, J. A. Y. R.; Gray, H. B. *Acc. Chem. Res.* **2009**, *42*, 1995–2004.

(182) Wakerley, D. W.; Gross, M. A.; Reisner, E. *Chem. Commun.* **2014**, *50*, 15995–15998.

(183) McCormick, T. M.; Han, Z.; Weinberg, D. J.; Brennessel, W. W.; Holland, P. L.; Eisenberg, R. *Inorg. Chem.* **2011**, *50*, 10660–10666.

(184) Jacques, P.; Artero, V.; Pécaut, J. *Proc. Natl. Acad. Sci. U.S.A.* **2009**, *106*, 20627–20632.

(185) Willkomm, J.; Muresan, N. M.; Reisner, E. *Chem. Sci.* **2015**, *6*, 2727–2736.

(186) Joliat, E.; Schnidrig, S.; Probst, B.; Bachmann, C.; Spingler, B.; Baldridge, K. K.; Von Rohr, F.; Schilling, A.; Alberto, R. *Dalt. Trans.* **2016**, *45*, 1737–1745.

(187) Reuillard, B.; Warnan, J.; Leung, J. J.; Wakerley, D. W.; Reisner, E. *Angew. Chem. Int. Ed.* **2016**, *55*, 3952–3957.

(188) Wilson, A. D.; Newell, R. H.; Mcnevin, M. J.; Muckerman, J. T.; Dubois, M. R.;

Dubois, D. L. *J. Am. Chem. Soc.* **2006**, *128*, 358–366.

(189) Wiese, S.; Kilgore, U. J.; Dubois, D. L.; Bullock, R. M. *ACS Catal.* **2012**, *2*, 720–727.

(190) Le Goff, A.; Artero, V.; Jousselme, B.; Tran, P. D.; Guillet, N.; Metaye, R.; Fihri, A.; Palacin, S.; Fontecave, M. *Science* **2009**, *326*, 1384–1387.

(191) Helm, M. L.; Stewart, M. P.; Bullock, R. M.; DuBois, M. R.; DuBois, D. L. *Science* **2011**, *333*, 863–866.

(192) Wang, M.; Chen, L.; Sun, L. *Energy Environ. Sci.* **2012**, *5*, 6763–6778.

(193) Rakowski DuBois, M.; DuBois, D. L. *Chem. Soc. Rev.* **2009**, *38*, 62–72.

(194) McLaughlin, M. P.; McCormick, T. M.; Eisenberg, R.; Holland, P. L. *Chem. Commun.* **2011**, *47*, 7989–7991.

(195) Leung, J. J.; Warnan, J.; Nam, D. H.; Zhang, J. Z.; Willkomm, J.; Reisner, E. *Chem. Sci.* **2017**, *8*, 5172–5180.

(196) Creissen, C. E.; Warnan, J.; Reisner, E. *Chem. Sci.* **2018**, *9*, 1439–1447.

(197) Bachmann, C.; Probst, B.; Guttentag, M.; Alberto, R. *Chem. Commun.* **2014**, *50*, 6737.

(198) Yang, J. Y.; Bullock, R. M.; Dougherty, W. G.; Kassel, W. S.; Twamley, B.; DuBois, D. L.; Rakowski DuBois, M. *Dalt. Trans.* **2010**, *39*, 3001.

(199) Kasap, H.; Caputo, C. A.; Martindale, B. C. M.; Godin, R.; Lau, V. W.-h; Lotsch, B. V.; Durrant, J. R.; Reisner, E. *J. Am. Chem. Soc.* **2016**, *138*, 9183–9192.

(200) Maeda, K.; Higashi, M.; Lu, D.; Abe, R.; Domen, K. *J. Am. Chem. Soc.* **2010**, *132*, 5858–5868.

(201) Sakimoto, K. K.; Zhang, S. J.; Yang, P. *Nano Lett.* **2016**, *16*, 5883–5887.

(202) Kalita, D.; Radaram, B.; Brooks, B.; Kannam, P. P.; Zhao, X. *ChemCatChem* **2011**, *3*, 571–573.

(203) Pan, X.; Zhang, N.; Fu, X.; Xu, Y.-J. *Appl. Catal. A Gen.* **2013**, *453*, 181–187.

(204) Zhang, M.; Chen, C.; Ma, W.; Zhao, J. *Angew. Chem. Int. Ed.* **2008**, *47*, 9730–9733.

(205) Palmisano, G.; García-López, E.; Marcì, G.; Loddo, V.; Yurdakal, S.; Augugliaro,

V.; Palmisano, L. *Chem. Commun.* **2010**, *46*, 7074–7089.

(206) Palmisano, G.; Yurdakal, S.; Augugliaro, V.; Loddo, V.; Palmisano, L. *Adv. Synth. Catal.* **2007**, *349*, 964–970.

(207) Higashimoto, S.; Suetsugu, N.; Azuma, M.; Ohue, H.; Sakata, Y. *J. Catal.* **2010**, *274*, 76–83.

(208) Yurdakal, S.; Palmisano, G.; Loddo, V.; Alagöz, O.; Augugliaro, V.; Palmisano, L.; Alagoz, O.; Augugliaro, V.; Palmisano, L. *Green Chem.* **2009**, *11*, 510–516.

(209) Su, F.; Mathew, S. C.; Lipner, G.; Fu, X.; Antonietti, M.; Blechert, S.; Wang, X. *J. Am. Chem. Soc.* **2010**, *132*, 16299–16301.

(210) Singh, W. M.; Pegram, D.; Duan, H.; Kalita, D.; Simone, P.; Emmert, G. L.; Zhao, X. *Angew. Chem. Int. Ed.* **2012**, *51*, 1653–1656.

(211) Kuehnel, M. F.; Reisner, E. *Angew. Chem. Int. Ed.* **2018**, *57*, 3290–3296.

(212) Stokes, R. D.; Perlack, B. J. *U.S. Dep. Energy* **2011**.

(213) Hendriks, A. T. W. M.; Zeeman, G. *Bioresour. Technol.* **2009**, *100*, 10–18.

(214) Isikgor, F. H.; Becer, C. R. *Polym. Chem.* **2015**, *6*, 4497–4559.

(215) John, M. R. S.; Furgala, A. J.; Sammells, A. F. *J. Phys. Chem.* **1983**, *87*, 801–805.

(216) Daskalaki, V. M.; Kondarides, D. I. *Catal. Today* **2009**, *144*, 75–80.

(217) Cha, H. G.; Choi, K. S. *Nat. Chem.* **2015**, *7*, 328–333.

(218) Kawai, T.; Sakata, T. *Chem. Lett.* **1981**, *10*, 81–84.

(219) Sakata, T.; Kawai, T. *Nouv. J. Chim.* **1981**, *5*, 279–281.

(220) Speltini, A.; Sturini, M.; Dondi, D.; Annovazzi, E.; Maraschi, F.; Caratto, V.; Profumo, A.; Buttafava, A. *Photochem. Photobiol. Sci.* **2014**, *13*, 1410–1419.

(221) Caravaca, A.; Jones, W.; Hardacre, C.; Bowker, M. *Proc. R. Soc. A* **2016**, *472*, 20160054.

(222) Wakerley, D. W.; Kuehnel, M. F.; Orchard, K. L.; Ly, K. H.; Rosser, T. E.; Reisner, E. *Nat. Energy* **2017**, *2*, 17021.

Chapter 2

Experimental section

The author of this thesis carried out all of the work described in this section unless specified otherwise. Xin Fang synthesised graphene oxide and reduced graphene oxide. XPS measurements were recorded by Dr. Mitsuharu Konuma at Kratos Analytical, Manchester. BET measurements were performed by Ailun Huang at University of Cambridge. TEM and SEM images were recorded by Dr. Heather F. Greer at University of Cambridge. Time-resolved spectroscopic techniques were performed and analysed by Dr. Robert Godin and Chiara Jeay-Bizot at Imperial College London.

2.1 Materials

All of the reagents were purchased from commercial suppliers and used without further purification. The buffer solutions were prepared using analytical grade reagents and titrated to the desired pH with a pH meter (Mettler Toledo; SevenEasy).

Synthesis of NiP and CN$_x$. ^{H_2N}CN$_x$ was prepared by heating melamine at 550 °C for 12 h under Ar atmosphere following a published procedure.[1] The yellow solid obtained was then thoroughly ground using a pestle and mortar prior to further analysis and applications. ^{NCN}CN$_x$ was prepared from ground ^{H_2N}CN$_x$ and KSCN (weight ratio of 1:2; dried overnight at 140 °C under vacuum) and heated at 400 °C for 1 h and then at 500 °C for 30 min under Ar as previously reported.[2] After cooling to room temperature the

residual KSCN was removed by washing with water and the product was dried under vacuum at 60 °C.[2]

Preparation of GO and RGO. A modified Hummer's method was used to synthesise graphene oxide (GO).[3] In the preoxidation step, H_2SO_4 (20 mL) was slowly heated up to 80 °C followed by the addition of $K_2S_2O_8$ (4.2 g) and P_2O_5 (4.2 g) with vigorous stirring. Graphite powder (5 g, Alfa Aesar, 325 mesh) was then added to the solution and the temperature was kept at 80 °C for 4.5 h followed by cooling down to room temperature. The mixture was diluted with water and left overnight. The mixture was repeatedly washed with deionised water (1 L) and centrifuged at 10,000 rpm followed by drying under air overnight to obtain a pre-oxidised product graphite oxide.

For the second oxidation step, H_2SO_4 (58 mL) was kept at 0 °C followed by the slow addition of graphite oxide (2.5 g) with vigorous stirring. Then, KNO_3 (1.25 g) and $KMnO_4$ (8 g) were slowly added while the temperature was kept below 10 °C. The mixture was then heated up to 35 °C and stirred for 2 h. After that, the mixture was diluted with water (58 mL) and stirred for 2 h, followed by addition of water (350 mL) to obtain a dark solution. H_2O_2 (25 mL, 30%) was added dropwise to the solution and kept overnight for stratification. The supernatant was decanted, and the gel sediment was washed with water and centrifuged with HCl for 5 times to remove the metal oxides. Then, the product was washed multiple times with water to remove any water soluble impurities. Finally, the product was sonicated for 30 min and the resulting dark brown GO was dried at 50 °C for 24 h. The reduction of GO to reduced graphene oxide (RGO) was carried out by adding 5 mg GO powder into a *L*-ascorbic acid solution (50 mL, 1 mg mL^{-1}) and stirred vigorously for 48 h, following a published procedure.[4]

2.2 Physical characterisation techniques

UV–vis absorption spectroscopy was performed on a Varian Cary 50 UV–vis spectrophotometer using 1 cm pathway quartz cuvettes. Photoluminescence emission spectra of $^{NCN}CN_x$ samples were recorded on a FS5 spectrofluorometer (Edinburgh Instruments) equipped with an integrating sphere. The spectra were generated using a Fluoracle software supplied with the instrument. Samples of $^{NCN}CN_x$ were pressed onto an indium foil for X-ray photoelectron spectroscopy (XPS) and the spectra were collected on an Axis Ultra (Kratos Analytical, Manchester) XPS instrument with charge neutralisation. The spectra were processed using the software CasaXPS 2.3.16 and

referenced with the adventitious carbon 1s peak at 284.8 eV. Binding energies were compared with the NIST Standard Reference Database 30 unless otherwise specified.

Brunauer-Emmett-Teller (BET) measurements were performed on a 3Flex Surface Characterisation Analyser (Micromeritics) at −196 °C. Prior to measurements, the samples were degassed under vacuum for 6 h at 150 °C. The specific surface areas were calculated by fitting the data to the BET isotherm. The X-ray diffraction (XRD) patterns were recorded with a BV X'Pert PRO diffractor (PANalytical). Scanning electron microscopy (SEM) images were collected on a MIRA3 FEG-SEM (TESCAN), at an accelerating voltage of 5 kV. Transmission electron microscopy (TEM) images were acquired on a Tecnai G2 transmission electron microscope (FEI Company) performed at an accelerating voltage of 200 kV. Attenuated total reflectance-Fourier transform infrared (ATR-FT-IR) spectra were recorded on a Nicolet iS50 FTIR spectrometer (ThermoScientific) and analysed using the Omnic software.

2.3 Photocatalytic experiments

Photocatalytic experiments were carried out using borosilicate glass photoreactors (total volume 7.74 mL) in a water-jacketed reservoir kept at 25 °C. The suspensions were prepared by mixing $^{NCN}CN_x$ and **NiP** in aqueous potassium phosphate solution (KP$_i$) containing 4-methylbenzyl alcohol (4-MBA) in a reactor equipped with a stirrer bar (total solvent volume 3 mL). The container was then tightly sealed with a rubber septum and purged with N_2 containing 2% CH_4 as the internal gas chromatography (GC) standard. The vials were irradiated using a solar light simulator with a Xe lamp (100 mW cm^{-2}, 1 sun, Newport Oriel) whilst stirring. The solar light simulator was equipped with an air mass 1.5 global filter (AM 1.5G). Infrared irradiation was removed from all experiments using a water filter while additional UV cut-off filters and neutral density filters (UQG optics) were used when specified.

For the biomass photoreforming experiments, the photoreactors were prepared as described above, but 4-MBA was replaced by lignocellulosic substrates (100 mg) unless specified otherwise. In several experiments, **NiP** was substituted by Pt (precursor: H_2PtCl_6) or MoS_2 (precursor: $H_8N_2MoS_4$).

2.3.1 Quantification and characterisation of products

The amount of accumulated H_2 was quantified *via* periodic headspace gas injections (20 µL) into a GC (Agilent 7890A) equipped with a 5 Å molecular sieve column. The temperature of the GC oven was maintained at 45 °C and N_2 was used as the carrier gas. The source of protons for H_2 production was identified by mass spectrometry (MS), through examining the composition of the headspace gases with mass/charge ratios between 1 and 5 amu after 24 h irradiation, by using KPi buffer prepared in H_2O and D_2O or by using labelled alcohol substrates, unless specified otherwise. MS was recorded using Hidden Analytical HPR-20 benchtop gas analysis system to a HAL 101 RC electron impact quadrupole mass spectrometer with a Faraday detector.

In order to analyse the oxidation products, 4-MBA and 4-methylbenzaldehyde (4-MBAd) were extracted following photocatalysis with CH_2Cl_2 and quantified by ^1H nuclear magnetic resonance (NMR) spectroscopy on a Bruker DPX 400 spectrometer at 25 °C. The work-up procedure was confirmed to leave the ratio of starting material to product unaffected. Three vials containing different 4-MBA:4-MBAd (1:2, 1:1 and 2:1) ratios were prepared following the described procedure for the photocatalytic experiments (except the irradiation step). The initial 4-MBA to 4-MBAd ratios were preserved in the ^1H NMR after working up the solutions as described above.

2.3.2 External photon to H_2 quantum efficiency

The external quantum efficiency (EQE) was determined using simulated solar light simulator (LOT LSN 254) equipped with a monochromator (LOT MSH 300) to irradiate the samples at a single wavelength of $\lambda = 360 \pm 10$ nm and at a light intensity (I) of $I = 4.05$ mW cm^{-2}. EQE was calculated using the following equation:

$$\text{EQE (\%)} = \frac{2 \cdot n_{H_2} \cdot N_A \cdot h \cdot c}{t_{irr} \cdot \lambda \cdot I \cdot A} \cdot 100$$

where n_{H_2} is the moles of photogenerated H_2, N_A is Avogadro's constant, h is Planck's constant, c is the speed of light, t_{irr} is the time of irradiation, and A is the cross-sectional area of irradiation.

2.3.3   Treatment of analytical data

All measurements were performed as triplicates and the data is reported as mean value ± standard deviation (σ). A minimum σ of 5% was assumed in all cases for photocatalytic experiments.[5]

2.4 Time-resolved spectroscopic techniques

For the time-resolved spectroscopic techniques the data was acquired either by using suspensions of carbon nitride or by preparing hydrogels of these powders to overcome the settling problems (see Chapter 5 for details).

Hydrogel Preparation. Sodium deoxycholate (NaDC) powder was diluted in water at 13.8 mg mL^{-1} concentration.[6] This stock solution was then used to disperse $^{NCN}CN_x$ or $^{H_2N}CN_x$ powders and KP$_i$ buffer (1 M, pH 4.5) was added to prepare a final concentration of 0.1 M KP$_i$ solution with a 1.67 mg mL^{-1} of carbon nitride concentration. When 4-MBA was used in the experiments, it was previously added to the NaDC stock solution. The NaDC mixtures with carbon nitrides ($^{NCN}CN_x$ or $^{H_2N}CN_x$) were heated up to ~60 °C for 15 min, then KP$_i$ was added to the hot solution followed by an additional 15 min heating. Afterwards, the mixture was left undisturbed and cooled down at room temperature to form the hydrogel.

Steady-state-spectroscopy. Steady-state spectra were acquired for $^{NCN}CN_x$ and $^{H_2N}CN_x$ suspensions in KP$_i$ under Ar, in 1 mm path length cuvettes. A Shimadzu UV-2600 spectrometer equipped with an integrating sphere was used for recording UV–vis diffuse reflectance spectra. Fluorescence spectra were recorded using a Jobin Yvon FluoroLog fluorometer.

Time-correlated single photon counting (TCSPC). Both $^{NCN}CN_x$ and $^{H_2N}CN_x$ powders were dispersed in KP$_i$ at (1.67 mg mL^{-1}) and purged with Ar before acquisition. The decay of emissive states was monitored by TCSPC (DeltaFlex, Horiba). Data was acquired on two timescales (up to 100 ns and up to 6.5 µs) to follow the decay over several orders of magnitude. Pulsed excitation of $\lambda = 404$ nm (10 kHz repetition rate) was generated by a laser diode and fluorescence was detected at $\lambda = 490$ nm (SPC-650 detector, Horiba). Excitation fluence was estimated to be ~20 pJ cm^{-2}.

Transient Absorption Spectroscopy (TAS). Microsecond to second transient absorption decays of $^{NCN}CN_x$ and $^{H_2N}CN_x$ were acquired in a diffuse reflectance mode.[7] As an excitation source, an Nd:YAG laser (OPOTEK Opolette 355 II, 7 ns pulse width) was used. 355 nm light was generated and transmitted to the sample through a light guide to photoexcite the $^{NCN}CN_x$. Typical excitation power densities of 300 μJ cm^{-2} or 460 μJ cm^{-2} were used. As the changes of reflectance observed were low (< 1%), the transient signal was taken to be directly proportional to the concentration of excited state species.[8]

The probe light source was a 100 W Bentham IL1 quartz halogen lamp. Long pass filters (Comar Instruments) and an IR filter (H_2O, 5 cm path length) were placed between the lamp and sample to minimise the short wavelength irradiation and heating of the sample. Diffuse reflectance from the sample was collected by a focal length lens and relayed to a monochromator (Oriel Cornerstone 130) to select the probe wavelength. An additional high pass filter was positioned in front of the monochromator to reduce laser scatter.

Time-resolved intensity data was collected with a Si photodiode (Hamamatsu S3071). Data at times faster than 1 ms was recorded by an oscilloscope (Tektronics DPO3012) after passing through an amplifier box (Costronics) while data slower than 1 ms was simultaneously recorded on a National Instrument DAQ card (NI USB-6251). Kinetic traces were typically obtained from the average of 32–64 laser pulses.

Samples were prepared by dispersing $^{NCN}CN_x$ or $^{H_2N}CN_x$ in KP$_i$ at the concentrations of 1–5 mg mL^{-1}. NaDC hydrogel samples were also tested with or without GO or RGO as conductive scaffolds (Chapter 5). The dispersions were transferred to 2 mm path length cuvettes. The samples were stirred prior to the start of each kinetic acquisition and were measured under Ar. Data was collected and processed using a home-built software written in the LabVIEW environment.

Photoinduced absorption spectroscopy (PIAS). The photoinduced absorption spectra of $^{NCN}CN_x$ and $^{H_2N}CN_x$ hydrogel samples were recorded in second to minute timescale. The monitoring wavelength was chosen as λ = 610 and 800 nm for $^{NCN}CN_x$ and $^{H_2N}CN_x$ respectively in a diffuse reflectance mode. The samples prepared were irradiated with an LED at λ = 365 nm (0.5 mW cm^{-2}) for 2 s followed by 58 s off for

NCNCN$_x$ and 5 s off for **H$_2$NCN$_x$**, and a single acquisition per wavelength per sample was performed.

2.5 References

(1)   Caputo, C. A.; Gross, M. A.; Lau, V. W.-h; Cavazza, C.; Lotsch, B. V.; Reisner, E. *Angew. Chem. Int. Ed.* **2014**, *53*, 11538–11542.

(2)   Lau, V. W.-h; Moudrakovski, I.; Botari, T.; Weinberger, S.; Mesch, M. B.; Duppel, V.; Senker, J.; Blum, V.; Lotsch, B. V. *Nat. Commun.* **2016**, *7*, 12165.

(3)   Sun, H.; You, X.; Deng, J.; Chen, X.; Yang, Z.; Ren, J.; Peng, H. *Adv. Mater.* **2014**, *26*, 2868–2873.

(4)   Zhang, J.; Yang, H.; Shen, G.; Cheng, P.; Zhang, J.; Guo, S. *Chem. Commun.* **2010**, *46*, 1112–1114.

(5)   Gross, M. A.; Reynal, A.; Durrant, J. R.; Reisner, E. *J. Am. Chem. Soc.* **2014**, *136*, 356–366.

(6)   Liang, W.; Guman-Sepulveda, J. R.; He, S.; Dogariu, A.; Fang, J. Y. *J. Mater. Sci. Chem. Eng.* **2015**, *3*, 6–15.

(7)   Wilkinson, F. *J. Chem. Soc. Faraday Trans. 2* **1986**, *82*, 2073–2081.

(8)   Kessler, R. W.; Krabichler, G.; Uhl, S.; Oelkrug, D.; Hagan, W. P.; Hyslop, J.; Wilkinson, F. *Opt. Acta Int. J. Opt.* **1983**, *30*, 1099–1111.

Chapter 3

Simultaneous proton reduction and alcohol oxidation with carbon nitride and a molecular Ni catalyst

The data presented in this chapter was published in a peer-reviewed article: J. Am. Chem. Soc., 2016, 138, 9183–9192. The author of this thesis carried all of the work unless specified otherwise. Dr. Benjamin C. M. Martindale and Prof. Christine A. Caputo are acknowledged for synthesising the NiP catalyst. Prof. Vincent Wing-hei Lau is greatly acknowledged for providing and characterising the carbon nitrides.

3.1 Introduction

Despite the large research efforts that have been put in designing water splitting systems, commercial application of such technology does not exist. Replacing the water oxidation half-reaction with valuable substrate oxidation reaction would bypass O_2 production and enable the synthesis of a high-value organic chemical, a so-called solar chemical, in addition to the solar fuel H_2 in a closed redox cycle.[1]

A fundamental organic transformation is the selective oxidation of benzyl alcohols to carbonyl compounds both in the laboratory and at an industrial scale. Carbonyl derivatives such as aldehydes and ketones are widely used as precursors in the pharmaceutical and fragrance industries and for complex syntheses.[2–4] Since many classical oxidation reactions are currently being carried out in organic solvents

47

at high pressure and temperature, while employing hazardous stoichiometric oxidants, such as MnO_4^- or CrO_3, there is a clear need for green synthetic routes.[5]

Simultaneous photo-reduction of aqueous protons and organic substrate photo-oxidation in a single compartment requires coupling between the light harvester and the catalysts, catalysing two redox reactions, and the accumulation of products without their interference in the opposite half-reaction. To simplify this demanding task, the two halves of the system are typically studied separately with a sacrificial reagent closing the catalytic cycle.

Solar-light driven H_2 production from water has been reported in the presence of sacrificial electron donors under homogenous and semi-heterogeneous colloidal systems with molecular, enzymatic and metallic catalysts.[6–12] Photocatalytic oxidation of organic substrates containing alkene,[13,14] amine,[15] alcohol,[16,17] and sulfide[17,18] groups have also been reported in the presence of electron scavengers in fully homogeneous and hybrid systems (see Chapter 1 for details).

Only rare examples are available which couple substrate oxidation and H_2 production in a single reactor. Fully-homogenous systems and photoelectrochemical cells have been previously reported to carry out these two processes simultaneously.[1,19,20] However, most of these reported systems were operated in organic solvents, employed multiple expensive and fragile noble-metal based dyes and catalysts, leading to complicated schemes with low efficiencies, and thereby limited practical applications.

Therefore, a need remained to find inexpensive and robust photosensitisers, which can couple proton reduction and substrate oxidation, while eliminating the need to consume non-innocent and unsustainable sacrificial reagents.[21,22] Polymeric carbon nitrides are introduced as attractive light harvesters for photocatalytic applications (Chapter 1), and have been shown to work efficiently as photocatalysts for H_2 evolution,[11,23–25] and oxidation of benzylic alcohols under sacrificial conditions.[26,27]

Here for the first time, a closed redox system that photocatalysis the production of H_2 coupled to the selective oxidation of benzyl alcohols to aldehyde is reported in the presence of $^{NCN}CN_x$ and **NiP**. This hybrid system functions in a single pot under a purely aqueous solution, at room temperature and ambient pressure, in the absence of organic co-solvents and sacrificial reagents (Figure 3.1).
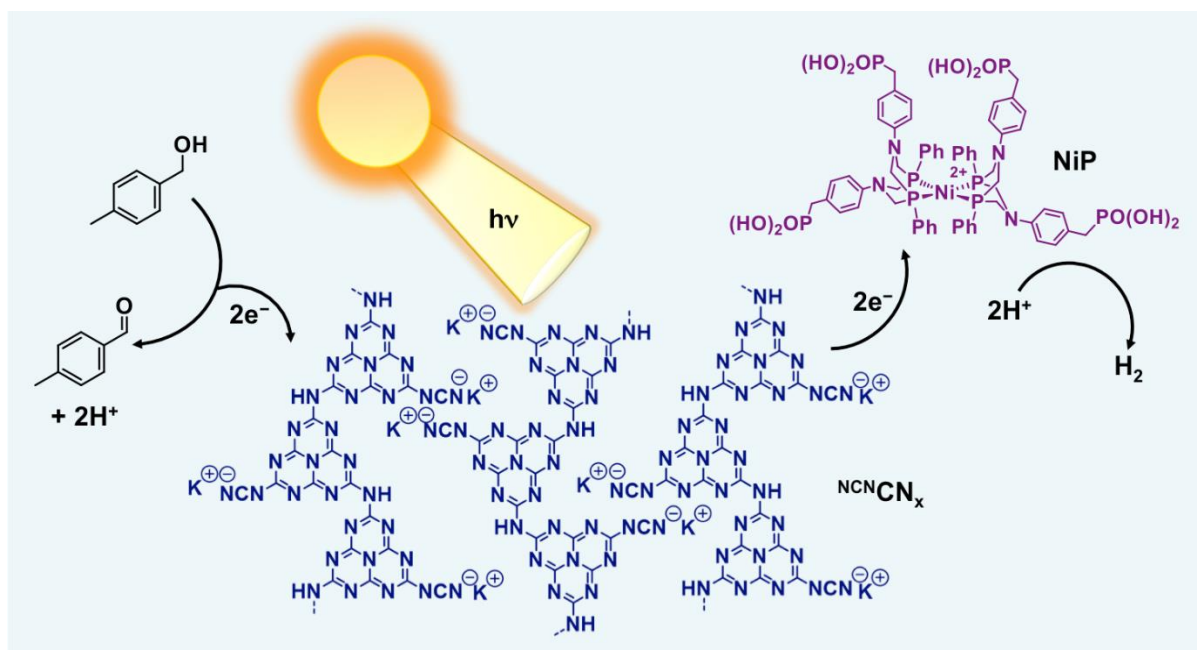
Figure 3.1. Schematic representation of a closed redox system for proton reduction and alcohol oxidation. Irradiation of **NCNCN$_x$**, results in the formation of a photoexcited state in which the holes are quenched by alcohol for aldehyde formation and the photoexcited electrons are transferred from **NCNCN$_x$** to the molecular catalyst **NiP** (bromide counterions omitted for clarity) resulting in H$_2$ formation.

3.2 Results and discussion

3.2.1 Synthesis and characterisation of carbon nitride

Carbon-based, non-toxic and inexpensive carbon nitrides with long-term activity and stability were chosen as the photocatalysts for this full redox system.[23] **H$_2$NCN$_x$** was prepared by one-step thermal polymerisation of melamine.[11] **NCNCN$_x$** was synthesised in multi-gram scale by surface functionalisation of benchmark **H$_2$NCN$_x$** with KSCN at high temperature as described previously (See Experimental Section, Chapter 2, for details).[28,29]

  NCNCN$_x$ and **H$_2$NCN$_x$** were characterised to understand the differences in their structure and composition by attenuated total reflectance-Fourier transform infrared (ATR-FT-IR), diffuse reflectance UV–vis absorption spectroscopy, X-ray diffraction (XRD) and zeta potential measurements (Figure 3.2). IR spectra of both samples showed a characteristic heptazine core vibration at 804 cm^{-1} and bridging secondary amine bending vibrations at 1311 and 1221 cm^{-1}, indicating polymeric nature of these

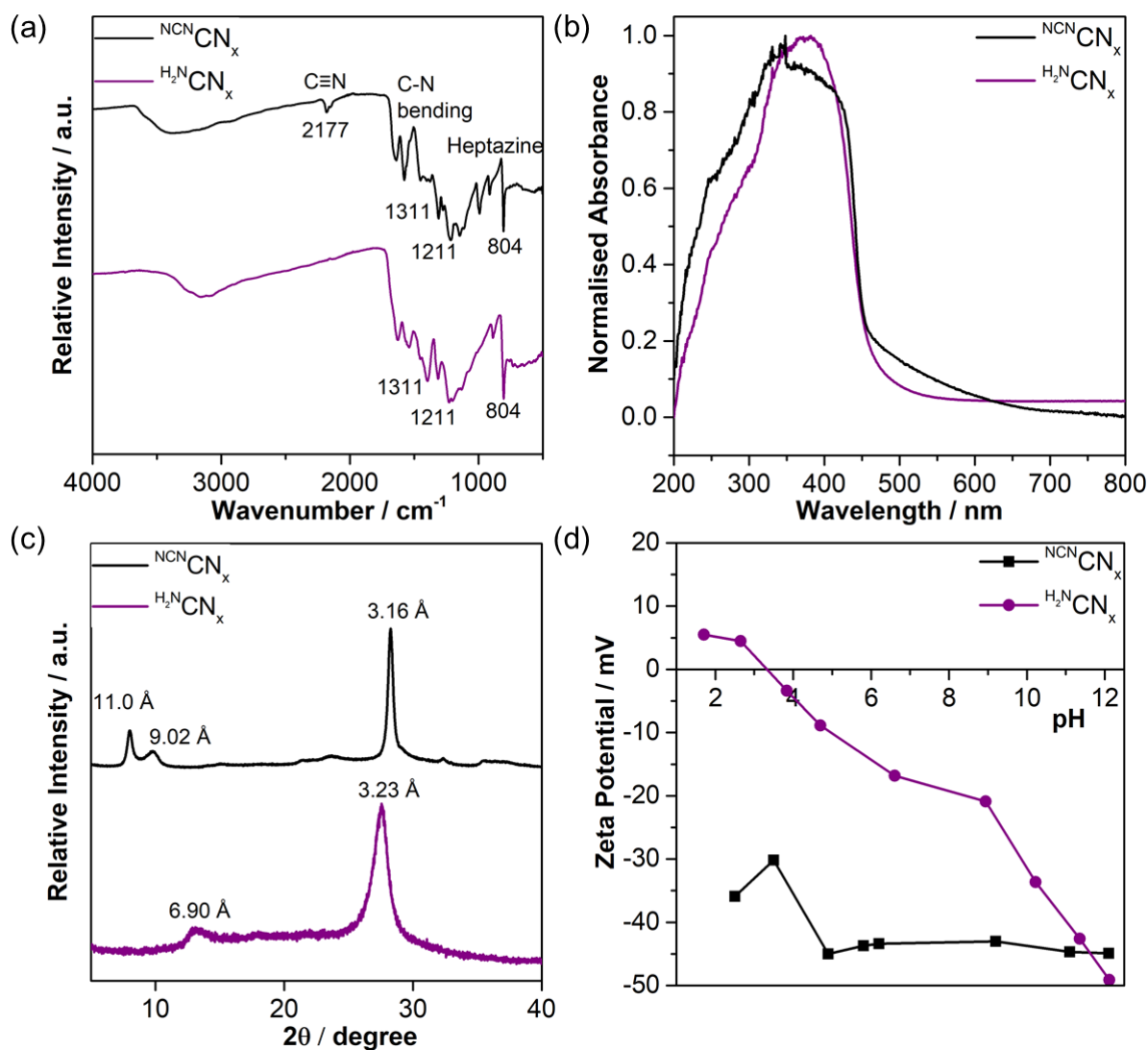Figure 3.2. (a) ATR-FT-IR spectra of $^{NCN}CN_x$ and $^{H_2N}CN_x$. The most significant stretches are indicated. (b) Normalised UV–vis absorption spectra of $^{NCN}CN_x$ and $^{H_2N}CN_x$ recorded in KP$_i$ solution. (c) Powder X-ray diffraction patterns of $^{NCN}CN_x$ and $^{H_2N}CN_x$. Inter and intra-layer spacing are specified. (d) Zeta potential measurements of $^{NCN}CN_x$ and $^{H_2N}CN_x$.

materials. X-ray photoelectron spectra (XPS) of ^{NCN}CN$_x$ further supported the presence of the heptazine core by the appearance of sp^2 carbon (N-C-N), 288.4 eV, and nitrogen (C-N-C), 398.8 eV, signals (Figure A.1).[30] In addition, the polymeric structure was confirmed by the XPS signal at 401.1 eV, corresponding to the bridging secondary amine groups. IR spectra showed the cyanamide (C≡N) stretch at 2177 cm^{-1} only for ^{NCN}CN$_x$, consisting with the appearance of this group on the material after the surface functionalisation by KSCN.[31] Both samples showed strong UV absorptions which tailed into the near-visible region. XRD of ^{NCN}CN$_x$ showed denser packing than ^{H_2N}CN$_x$ with an inter-layer spacing of 3.16 Å (28.26⁰ 2θ) and intra-layer periodicities of 9.02 Å (9.82⁰ 2θ) and 11.0 Å (8.03⁰ 2θ).[32,33]

Zeta potential of ^{NCN}CN$_x$ was determined as −44 eV across all pH where the material is stable (pH > 4), which was attributed to the anionic cyanamide group on the surface.[29] At pH values below 4, the material lost its yellow colour and turned white, indicating hydrolysis of surface cyanamide groups. On the other hand, ^{H_2N}CN$_x$ showed pH dependent zeta potential.

3.2.2   Photocatalytic assembly and performance

The closed redox system for simultaneous alcohol oxidation and proton reduction in the presence of inexpensive and non-toxic light harvester ^{NCN}CN$_x$ and Ni-based proton reduction catalyst is already shown (Figure 3.1). As the proton reduction catalyst, noble-metal free and hydrogenase-inspired molecular catalysts **NiP**, with a Ni-bis(diphosphine) catalytic core was selected for this sysem,[34,35] and synthesised by following a published procedure.[6] It was previously reported that under sacrificial conditions, ^{H_2N}CN$_x$ and **NiP** efficiently produce H$_2$.[11] For the purpose of this work, recently reported surface functionalised ^{NCN}CN$_x$ was selected, with an order of magnitude better H$_2$ production activity than the benchmark ^{H_2N}CN$_x$ in the presence of Pt co-catalyst.[29]

Photocatalytic systems were assembled by dispersing ^{NCN}CN$_x$, **NiP** and 4-methylbenzyl alcohol (4-MBA) in an aqueous potassium phosphate solution (KP$_i$, 3 mL), in a photoreactor with a total volume of 7.74 mL. The photoreactor was sealed with a rubber septum, purged with N$_2$ (containing 2% CH$_4$) and subsequently irradiated using a solar light simulator equipped with an air mass 1.5 global (AM 1.5G) filter at 1
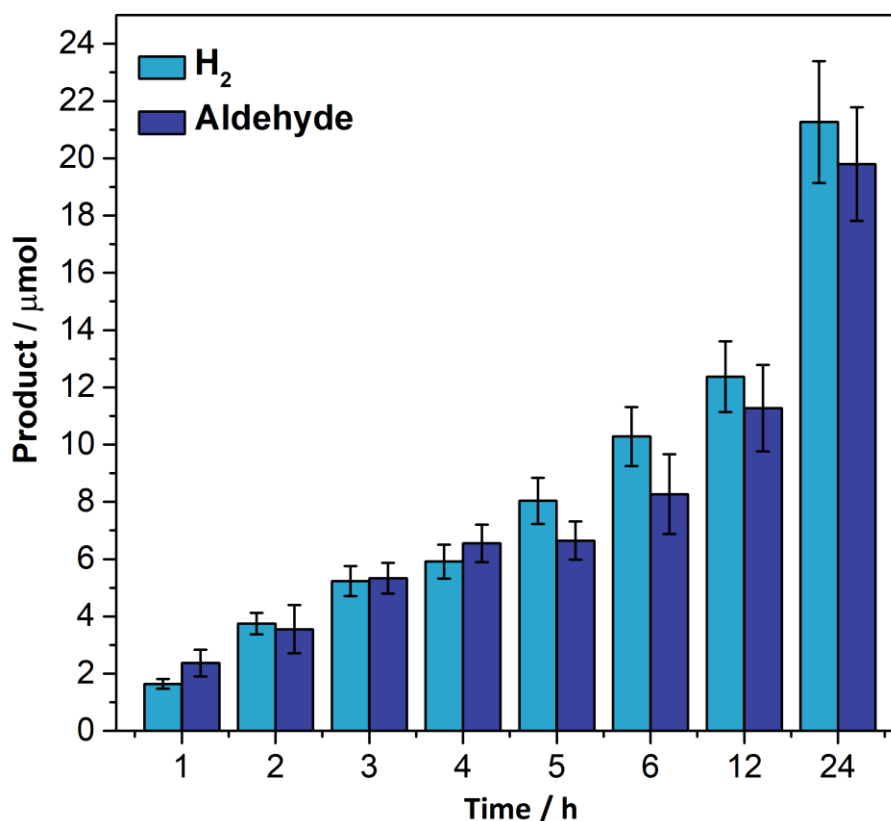
Figure 3.3. Time-dependent photocatalytic H_2 and aldehyde production with $^{NCN}CN_x$ (5 mg), **NiP** (50 nmol) and 4-MBA (30 µmol) in KP$_i$ (0.02 M, pH 4.5, 3 mL) under 1 sun irradiation (AM 1.5G) at 25 °C.

sun intensity (100 mW cm^{-2}) and 25 °C. The headspace H_2 gas was quantified in regular intervals by gas chromatography (GC), while 4-MBA and other possible oxidation products were analysed by ^{1}H NMR spectroscopy (see Experimental Section, Chapter 2, for details). The conversion yield was determined based on the percentage conversion of benzyl alcohol to oxidation products (Figure A.2).

The reaction conditions were optimised systematically for H_2 production activity per catalyst, expressed as **NiP**-based turnover frequency (TOF$_{NiP}$; mol H_2 (mol **NiP**)$^{-1}$ h^{-1} determined after 1 h irradiation) and turnover number (TON$_{NiP}$; mol H_2 (mol **NiP**)$^{-1}$ determined after 24 h irradiation, unless specified otherwise), as well as the conversion yield and selectivity of alcohol oxidation to oxidation products after 24 h. The activity of **NiP** (TOF and TON) is limited by the availability of 4-MBA at high conversion yields, as there is not enough alcohol to quench the photoexcited holes on $^{NCN}CN_x$, thus limiting electron delivery to **NiP**. The parameters of optimisation were the amount of **NiP**, the amount of 4-MBA and the pH of the solution (Table A.1).
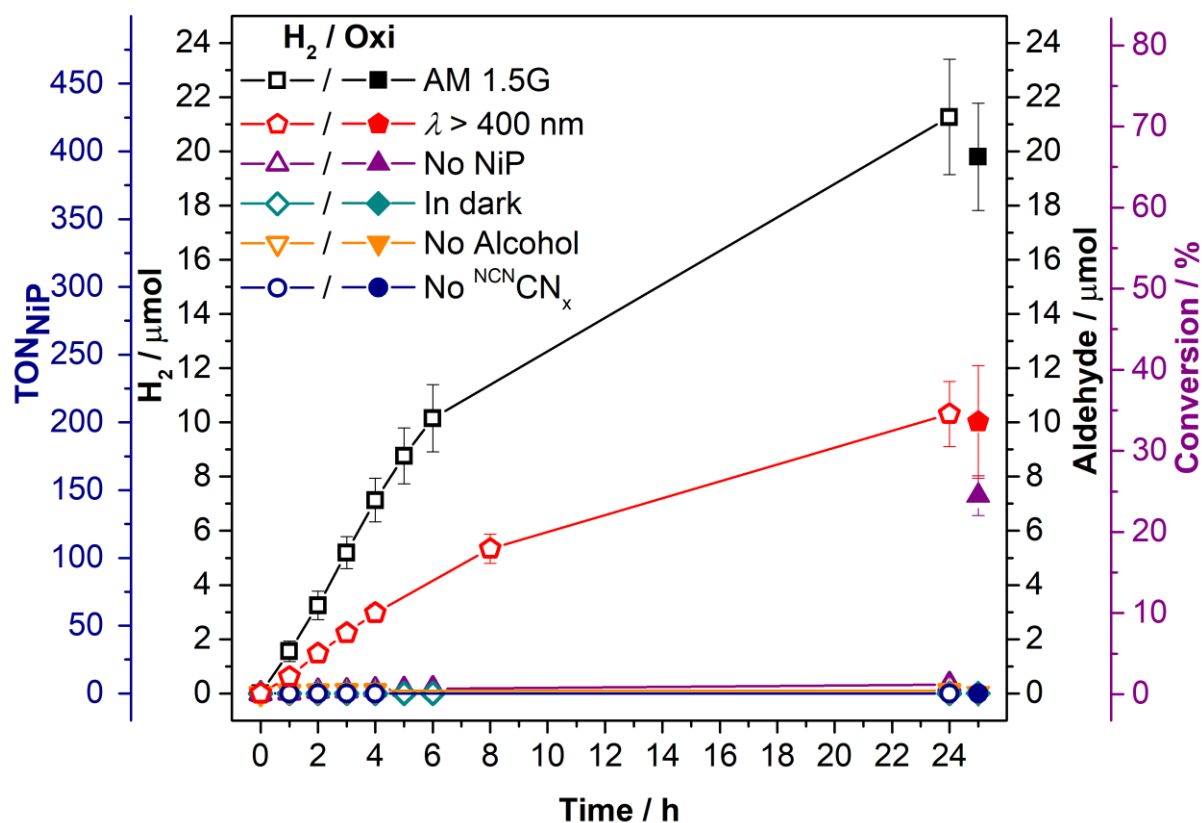
Figure 3.4. Photocatalytic H_2 and aldehyde production with $^{NCN}CN_x$ (5 mg), **NiP** (50 nmol), 4-MBA (30 µmol) in KP_i (0.02 M, pH 4.5, 3 mL) under 1 sun irradiation (AM 1.5G) at 25 °C. The pair of hollow and filled symbols of the same shape and colour corresponds to H_2 and aldehyde formation under specified conditions. Control experiments in the presence of a UV-filter (λ > 400 nm) and in the absence of **NiP**, 4-MBA, $^{NCN}CN_x$ and in dark are also shown.

The optimised conditions for the $^{NCN}CN_x$-**NiP** system consist of 5 mg of $^{NCN}CN_x$ suspended in 3 mL KP_i (0.02 M, pH 4.5) with 50 nmol of **NiP** and 30 µmol of 4-MBA under simulated solar light irradiation (Figure 3.3). There was a linear increase in both H_2 and aldehyde production for the first six hours of irradiation (Figure 3.3, Table A.2), whereupon the rate started to decrease over time due to stability of the molecular catalyst (see below for details, Figure 3.8). A TOF_{NiP} of 31.1 ± 3.1 h^{-1} and an activity of 311 µmol (g $^{NCN}CN_x)^{-1}$ h^{-1} towards H_2 and aldehyde production were reached. After 24 h of full solar spectrum irradiation, TON_{NiP} of 425.4 ± 42.5 was achieved, while oxidation of 4-MBA afforded 4-methylbenzaldehyde (4-MBAd) selectively in 66.0 ± 6.6% yield without further oxidation to form the carboxylic acid. Thus, H_2 and 4-MBAd were photo-generated cleanly and in a 1:1 stoichiometry over time and reached 21.3 ± 2.1 µmol and 19.8 ± 2.0 µmol after 24 h, respectively (Figure 3.4).

Control experiments in the dark or in the absence of $^{NCN}CN_x$ did not yield H_2 or aldehyde (Figure 3.4, Table A.3). In the absence of **NiP**, only negligible amounts of H_2 were detected during irradiation, but selective 4-MBA oxidation to 4-MBAd was observed with a 24.3 ± 2.4% conversion, suggesting that 4-MBA oxidation may be the first step in the catalytic redox cycle (see Chapter 4 for details). In the absence of 4-MBA only a minimal amount of H_2 was detected.

The $^{NCN}CN_x$−**NiP** photosystem was also studied under visible only irradiation (λ > 400 nm). A TOF_{NiP} of 12.3 ± 1.2 h^{-1} and a TON_{NiP} of 206.3 ± 24.1 were observed, with 33.7 ± 6.5% 4-MBA conversion, corresponding to approximately 50% of the activity observed under full spectrum irradiation (Figure 3.4). The visible light response of the $^{NCN}CN_x$−**NiP** system showed an improvement when compared to the previously reported sacrificial $^{H2N}CN_x$−**NiP** photosystem, where only 16% of the activity observed under full spectrum irradiation was preserved under visible-light irradiation.[11]

The activity of **NiP** in this closed redox cycle compares well with previously reported sacrificial H_2 production hybrid systems using colloidal light absorbers. $^{H2N}CN_x$−**NiP** in EDTA sacrificial electron donor solution at pH 4.5 resulted in a TOF_{NiP} of 109.3 ± 10.9 h^{-1} and TON of 155. Sacrificial photo-H_2 generation was also reported with **NiP** and **RuP** dye-sensitised TiO_2 and showed TOF_{NiP} of 72 ± 5 h^{-1} and TON of 278 ± 19.[6] More recently, carbon dots were used as a photosensitiser in the presence of EDTA as the sacrificial donor with **NiP**, and a TOF_{NiP} of 41 h^{-1} and TON of 64 mol H_2 (mol NiP)$^{-1}$ were reported.[12]

The activity of $^{NCN}CN_x$ for benzyl alcohol oxidation is also comparable with systems reported for substrate oxidation with a sacrificial electron acceptor. Photocatalytic 4-MBA oxidation in the presence of carbon nitride, under high pressure of O_2 resulted in 77% 4-MBAd formation with 99% selectivity, but the oxidation was carried out in a fluorinated organic solvent to promote O_2 solubility and at 100 °C.[26] Another system with carbon nitride and O_2 as the sacrificial acceptor reported 59% 4-MBA oxidation with 66% selectivity for 4-MBAd in water,[27] but required 100 °C and strongly acidic conditions (pH 0).[27] $^{NCN}CN_x$ provides a platform for selective benzyl alcohol oxidation whereas substrate oxidation reactions on metal oxides (TiO_2) are limited by low selectivity due to formation of highly reactive radicals in water.[36–39] The $^{NCN}CN_x$−**NiP** colloidal suspension system reported in here combines selective substrate oxidation and H_2 production in a single compartment, thereby eliminating the

need for a sacrificial reagent, remaining functional under fully aqueous solution, at room temperature and ambient pressure for up to 24 h.

3.2.3 Analysis of individual components

A series of benzyl alcohols with different para-substituents were studied to probe the effect of substrate structure on photocatalytic performance (Table A.3). Conversion yields observed did not show a direct correlation with respect to the electron-donating or withdrawing nature of the substituents. Only with the strongest electron-withdrawing substituent tested, $-CF_3$, a significant reduction in conversion yield to 6.1 ± 2.0% was observed. All of the benzyl alcohol derivatives underwent selective conversion to the aldehyde, except for the strongest electron donating group, ^tBu, in which 64% selectivity for aldehyde formation was observed and further oxidation to 4-^tBu benzoic acid also occurred. When 4-MBA (30 μmol) was replaced with methanol (30 μmol) under otherwise identical conditions ($^{NCN}CN_x$ and **NiP** in KP$_i$), no oxidation products or H$_2$ were observed, in contrast to systems using excess amount of aliphatic alcohols as a sacrificial reagent for photocatalytic proton reduction.

Replacing the KP$_i$ with acetate buffer (pH 4.5, 0.1 M) did not alter the photocatalytic rate of H$_2$ and aldehyde generation during the first few hours, indicating that the activity of the $^{NCN}CN_x$−**NiP** system is not significantly buffer-dependent, although the photoactivity decayed faster in the acetate buffered system (Table A.4). Increasing the phosphate buffer concentration from 0.02 M to 0.1 M and 0.5 M led to an enhancement in initial activity from TOF$_{NiP}$ = 31.1 ± 3.1 to 76.3 ± 7.6 and 111.4 ± 11.1 h^{-1} and 311 to 763 and 1,114 μmol products (g $^{NCN}CN_x$)$^{-1}$ h^{-1}, respectively. However, after 24 h, the system performances equalised with a TON$_{NiP}$ of approximately 400 mol H$_2$ (mol NiP)$^{-1}$ and a 4-MBA-to-4-MBAd conversion yields between 60 to 83% for all the systems (Tables A.1 and A.4). Further experiments in 20 mM KP$_i$ solution with 80 mM KCl or 80 mM K$_2$SO$_4$ showed a slight increase in the photocatalytic rate of H$_2$ production with TOF$_{NiP}$ of 53.9 ± 5.9 and TOF$_{NiP}$ of 49.20 ± 4.9, respectively (Table A.4). These results suggest that the enhanced photocatalytic activity is partially due to the ionic strength of the buffer used but also the significant increase in phosphate ion (a weak acid) concentration that acts potentially as a proton relay, improving the rate of proton transfer to the molecular catalyst.[40,41]
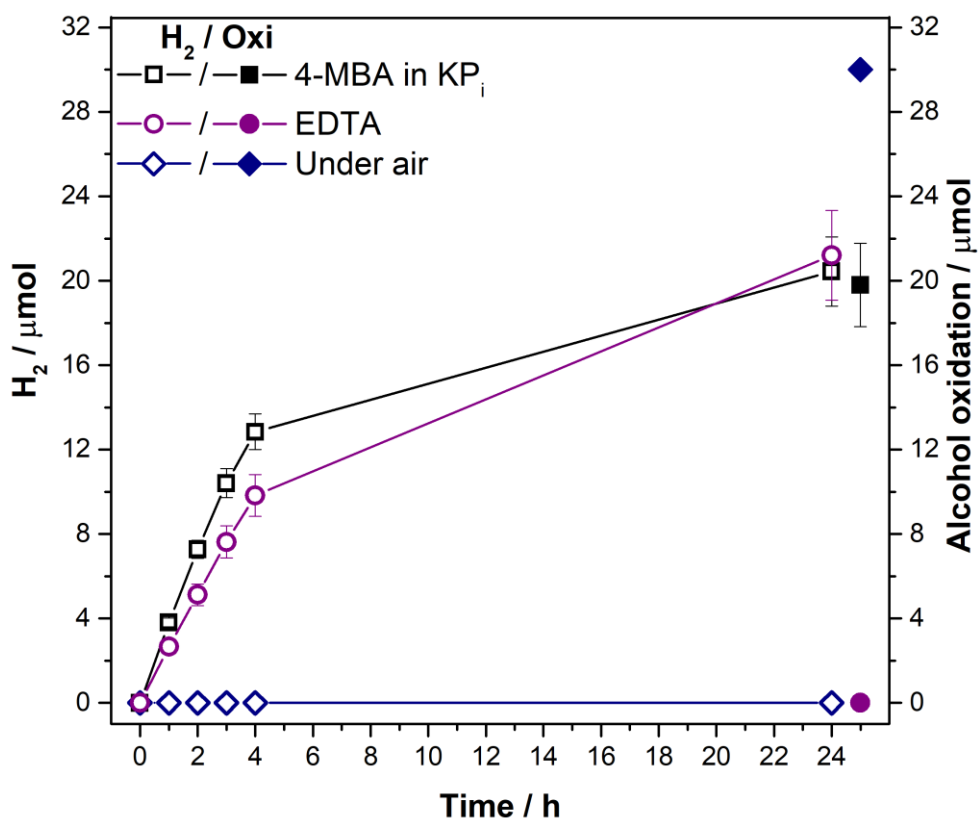
Figure 3.5. Photocatalytic H_2 and aldehyde production in the presence of $^{NCN}CN_x$ (5 mg), 4-MBA (30 µmol) and **NiP** (50 nmol) in an aqueous KP_i solution (0.1 M, pH 4.5, 3 mL) under 1 sun irradiation (100 mW cm^{-2}, AM 1.5G, 25°C). Sacrificial H_2 production with $^{NCN}CN_x$ (5 mg) and **NiP** (50 nmol) in EDTA (0.1 M, pH 4.5, 3 mL) without 4-MBA. Sacrificial alcohol oxidation with $^{NCN}CN_x$ (5 mg) and 4-MBA (30 µmol) in an aqueous KP_i solution (0.02 M, pH 4.5, 3 mL) under air, as the sacrificial electron acceptor, in the absence of **NiP**. The pair of hollow and filled symbols of the same shape and colour corresponds to H_2 and oxidation product formation under specified conditions.

The efficiencies of the individual half-reactions of the photocatalytic system were also examined separately in sacrificial schemes (Figure 3.5). Solar-light-driven H_2 production was tested with $^{NCN}CN_x$ (5 mg) and **NiP** (50 nmol) in EDTA as the electron donor solution at pH 4.5, in the absence of 4-MBA. A TOF_{NiP} of 53.2 ± 5.3 h^{-1} and a TON_{NiP} of 424.18 ± 42.4 were reached in EDTA solution, similar to the 4-MBA system, suggesting that the $^{NCN}CN_x$−**NiP** hybrid system is not limited by the electron donation ability of 4-MBA (Table A.4).

The ability of the system to carry out alcohol oxidation was investigated by replacing the molecular catalyst **NiP** with air (O_2) as an electron acceptor. Solar-light

driven alcohol oxidation with $^{NCN}CN_x$ (5 mg) and 4-MBA (30 µmol), resulted in quantitative alcohol oxidation with 70% selectivity towards benzoic acid formation after 24 h, with respect to the products detected by ^1H NMR. This implies that the degree of oxidation of alcohols with this material can be tuned by varying the nature of the electron acceptor and demonstrates an advantage of using **NiP** over the sacrificial acceptor O_2. The ability of O_2 to act as an electron acceptor in this system also highlights a key advantage of substrate oxidation over full water splitting in one-pot systems, where the O_2 formed would compete with and inhibit proton reduction.

The photocatalytic activity of $^{NCN}CN_x$−**NiP** was compared with conventional unfunctionalised carbon nitride, $^{H2N}CN_x$ (Table A.5). The H_2 and aldehyde production activity of $^{NCN}CN_x$−**NiP** was determined to be an order of magnitude greater than $^{H2N}CN_x$−**NiP** under the same experimental conditions. After 24 h of irradiation $^{H2N}CN_x$−**NiP** system produced only 2.49 ± 0.71 µmol H_2 and 1.44 ± 0.71 µmol 4-MBAd, indicating that surface functionalisation of the carbon nitride is vital for the enhanced photocatalytic activity.

The *in situ* photodeposition of H_2PtCl_6 to platinise $^{NCN}CN_x$ or $^{H2N}CN_x$ was carried out following an optimised Pt loading procedure,[29] resulting in the formation of $^{NCN}CN_x$−**Pt** and $^{H2N}CN_x$−**Pt** systems for photo-H_2 generation.[23] These systems were then studied for simultaneous alcohol oxidation and proton reduction (Figure 3.6) in the absence of **NiP** under otherwise identical conditions. $^{NCN}CN_x$−**Pt** showed one third of the photocatalytic activity observed using $^{NCN}CN_x$−**NiP** towards H_2 production during the initial 4 h of irradiation, whereas $^{H2N}CN_x$−**Pt** was not active for H_2 production at all. Both $^{NCN}CN_x$−**Pt** and $^{H2N}CN_x$−**Pt** showed only approximately 5% 4-MBA oxidation to aldehyde after 4 h of irradiation. The initially low photocatalytic activity of Pt could be attributed to an induction period associated with the photodeposition of the active catalyst.[23] Even after 24 h irradiation, the overall photocatalytic activity of $^{NCN}CN_x$−**NiP** (H_2:4-MBAd = 21:20 µmol) was still better than with $^{NCN}CN_x$−**Pt** (14:12 µmol), representing a clear advantage of the molecular Ni catalyst over noble-metal based nanoparticles in this system. A similar trend was previously reported with a sacrificial system containing carbon dots and **NiP**.[12]

A control experiment was carried out to confirm that Pt is only catalytically involved in proton reduction and does not interfere with the 4-MBAd formed as a result
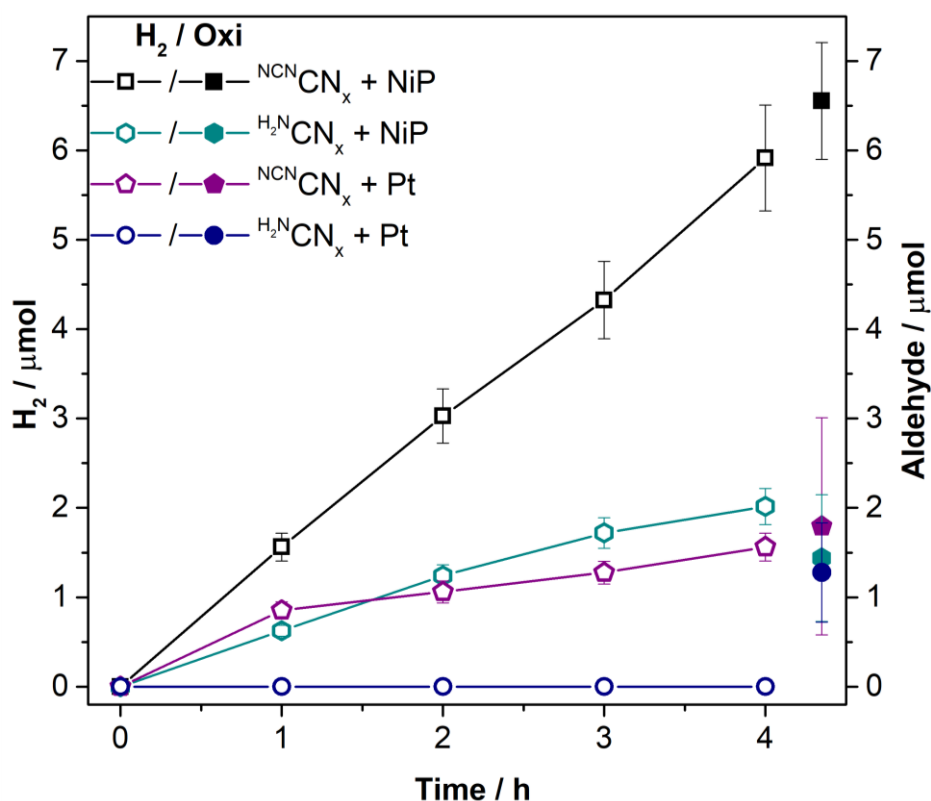
Figure 3.6. Photocatalytic H_2 and aldehyde production with $^{NCN}CN_x$ or $^{H_2N}CN_x$ (5 mg), in the presence of 4-MBA (30 μmol) with **NiP** (50 nmol) or H_2PtCl_6 (10 μL, 8 wt%) in KP_i (0.02 M, pH 4.5, 3 mL) under 1 sun irradiation (AM 1.5G, 25 °C). The pair of hollow and filled symbols of the same shape and colour corresponds to H_2 and aldehyde formation under specified conditions.

of 4-MBA oxidation. In sacrificial EDTA solution, $^{NCN}CN_x$−**Pt** and 4-MBAd (30 μmol) were combined in the absence of **NiP** (Table A.5). After 24 hours of irradiation, 18% of the 4-MBAd was oxidised to carboxylic acid, whereas 4-MBA was not detected by ^1H NMR spectroscopy, indicating that Pt is not able to reduce 4-MBAd and is only catalytically active for the proton reduction half reaction.

This significant enhancement in the photocatalytic activity of $^{NCN}CN_x$ in comparison to benchmark $^{H_2N}CN_x$ has been previously attributed to the improved interaction and charge transfer *via* the cyanamide moieties of the $^{NCN}CN_x$ in the presence of Pt catalyst.[29] We demonstrate here that this enhanced activity with $^{NCN}CN_x$ is also the case when the Pt is replaced with the molecular **NiP** catalyst. In the later investigations it was discovered that the VB position of $^{NCN}CN_x$ is at 300 mV more positive potential than $^{H_2N}CN_x$ (2.2 and 1.9 V *vs.* NHE at pH 6), therefore the photogenerated holes are more oxidising towards the organic substrates.[42]
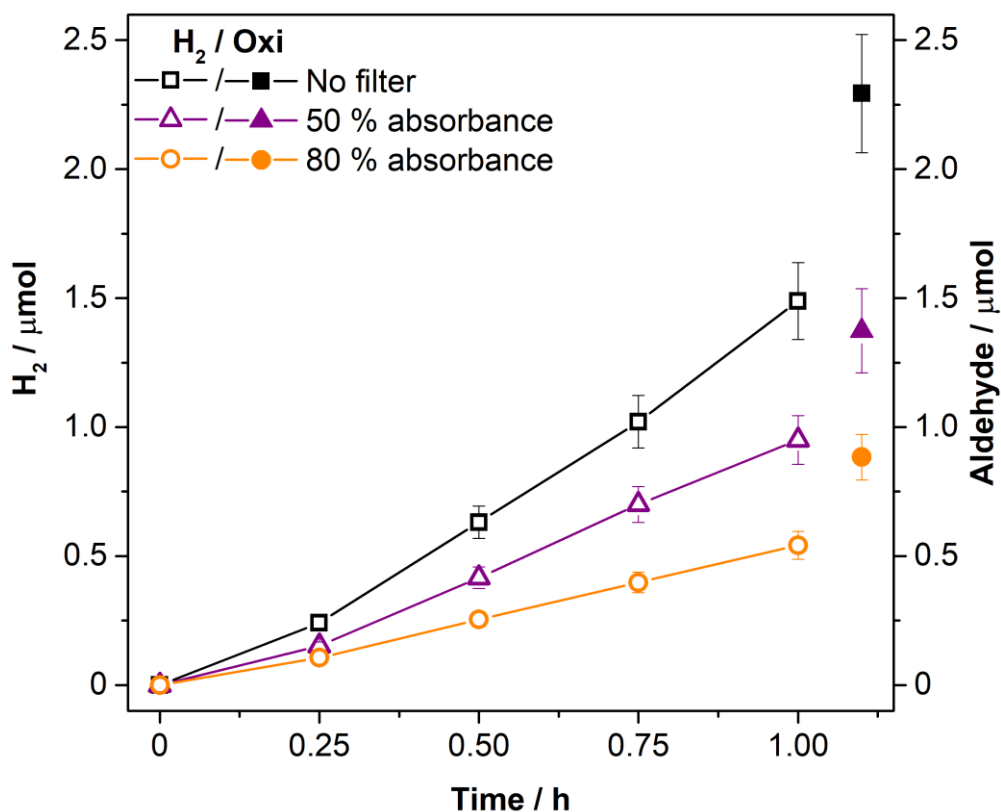
Figure 3.7. Photocatalytic H_2 and aldehyde production with $^{NCN}CN_x$ (5 mg), **NiP** (50 nmol), 4-MBA (30 μmol) in KP_i (0.02 M, pH 4.5, 3 mL) under 1 sun irradiation (AM 1.5G) at 25 °C, followed by the addition of neutral density filters that absorb 50% and 80% of the incident light. The pair of hollow and filled symbols of the same shape and colour corresponds to H_2 and aldehyde formation under specified conditions.

3.2.4 Photoactivity and stability limiting components

To gain better insights into the rate-limiting factors of the $^{NCN}CN_x$−**NiP** hybrid system, the amounts of **NiP**, 4-MBA, and light intensity were varied. Doubling the amount of **NiP** from 50 to 100 nmol per 5 mg of $^{NCN}CN_x$ or the amount of 4-MBA from 30 to 60 μmol did not result in a significant change in photoactivity (Table A.1). However, reducing the light intensity by 50% and 80% with neutral density filters resulted respectively in 40% and 85% reductions in photocatalytic activity for H_2 and 4-MBAd production after 1 h of irradiation (Figure 3.7, Table A.6). The activity was therefore proportional and dependent on the light intensity, which is also consistent with the reduced photoactivity of $^{NCN}CN_x$−**NiP** when filtering the UV light off the solar spectrum (see above).
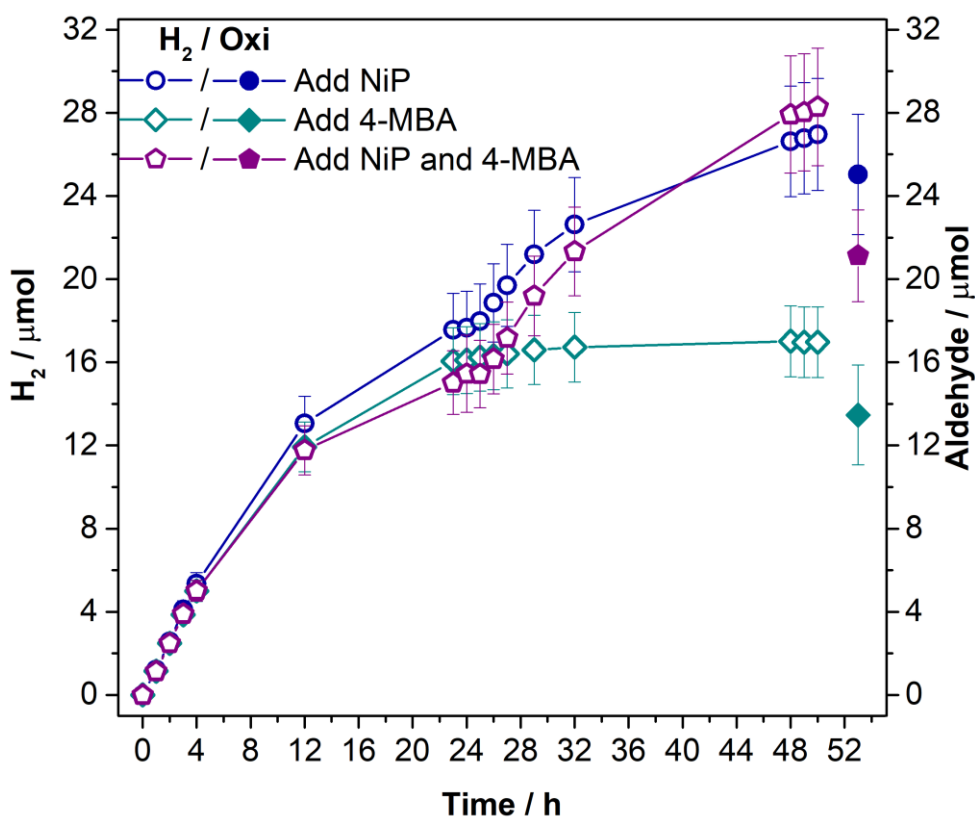
59

Figure 3.8. Long term photocatalytic H_2 and aldehyde production with $^{NCN}CN_x$ (5 mg), **NiP** (50 nmol), 4-MBA (30 µmol) in KP_i (0.02 M, pH 4.5, 3 mL) under 1 sun irradiation (AM 1.5G) at 25 °C. After 25 h of irradiation, **NiP** (50 nmol), 4-MBA (30 µmol), and both **NiP** (50 nmol) and 4-MBA (30 µmol) were added to photoreactors to test the system re-activation over the next 25 h of irradiation.

It was important to investigate the photostability of the $^{NCN}CN_x$ and **NiP** to understand if they are limiting the long-term activity of the system. The stability-limiting component of the system was identified by re-activation experiments by injecting **NiP**, 4-MBA and both to a suspension of $^{NCN}CN_x-$**NiP** after 25 h of irradiation (Figure 3.8, Table A.7).

Re-addition of 4-MBA (30 µmol) did not reactivate the system, whereas addition of fresh **NiP** (50 nmol) restored solar-H_2 production and enhanced the conversion yield for selective 4-MBA oxidation to 83.5 ± 9.7%. Addition of both 4-MBA and **NiP** also recovered the activity while the selectivity towards aldehyde formation is preserved despite the longer irradiation period (50 h). This indicates that the lifetime of the system is limited by the degradation of **NiP** while $^{NCN}CN_x$ maintained its activity for at least 50 h (Figure 3.8).[6,11,12]

60

XPS and FTIR characterisation of the $^{NCN}CN_x$ before and after irradiation for 24 h in the presence and absence of **NiP** showed negligible differences (Figures A.3–A.5). Thus, $^{NCN}CN_x$ showed long term activity and stability for simultaneous alcohol oxidation and H_2 production. The XPS spectra also confirmed that **NiP** was not physically adsorbed on the $^{NCN}CN_x$ surface during the period of irradiation and acted as a homogenous catalyst in the solution.

The external quantum efficiency (EQE) of the system was determined using a solar light simulator equipped with a monochromator ($\lambda = 360 \pm 10$ nm, $I = 4.43$ mW cm^{-2}). The highest EQE of $15.23 \pm 0.16\%$ was obtained with $^{NCN}CN_x$ (5 mg), 4-MBA (30 µmol) in 3 mL of KP$_i$ (0.1 M) buffer at pH 4.5 after an hour of irradiation. The EQE measured was significantly higher than the previously reported $^{H_2N}CN_x$−**NiP** hybrid system with an EQE of $0.37 \pm 0.02\%$,[11] as well as the homogenous **RuP−NiP** system with an EQE of $9.7 \pm 1.2\%$.[6] The EQE can be further improved by enhancing the charge extraction from the photocatalysts and by facilitating efficient utilisation of these charge carriers by the catalysts (see Chapter 6 for details).

3.3 Conclusions

A closed redox system for simultaneous photocatalytic alcohol oxidation and proton reduction is demonstrated utilising $^{NCN}CN_x$ and molecular Ni-based H_2-evolution catalyst. The hybrid system consists of earth abundant materials which functions in a purely aqueous solution and at room temperature in the absence of organic or sacrificial reagents. $^{NCN}CN_x$−**NiP** system showed an activity of 763 µmol (g $^{NCN}CN_x$)$^{-1}$ h^{-1} toward H_2 and aldehyde production with a remarkable EQE of 15% ($\lambda = 360 \pm 10$ nm). Under optimised conditions, a H_2 production rate (TOF$_{NiP}$) of 76.3 ± 7.6 h^{-1}, and a TON$_{NiP}$ of 408.8 ± 40.9 were achieved, with a 4-MBA conversion yield of $83.0 \pm 8.3\%$ with quantitative selectivity for 4-MBAd.

This colloidal $^{NCN}CN_x$−**NiP** system is straightforward to prepare and provides a novel platform to produce a valuable organic chemical and a H_2 fuel simultaneously, while the products are separated *in situ* in the solution and gaseous phase, respectively. The lifetime of the hybrid system was found to be limited by the stability of the molecular catalyst **NiP**, whereas $^{NCN}CN_x$ maintained its activity for at least 50 h of irradiation, providing a significant advantage over similar systems based on photodegrading molecular dyes.[6,16,19] These results demonstrate that identification

and design of photostable molecular catalysts could enhance the long-term photocatalytic activity of the hybrid system. The reported system also provides a platform for broad range of other useful organic transformations and reduction reactions by altering the molecular catalysts used. Fully understanding the rate limiting steps and the mechanism behind this full redox system would enable improving the activity of systems utilising carbon nitride and to expand its use for other applications.

3.4 References

(1)   Farràs, P.; Di Giovanni, C.; Clifford, J. N.; Palomares, E.; Llobet, A. *Coord. Chem. Rev.* **2015**, *304–305*, 202–208.

(2)   Brink, G. T.; Arends, I. W. C. E.; Sheldon, R. A. *Science* **2000**, *287*, 1636–1639.

(3)   Palmisano, G.; Augugliaro, V.; Pagliaro, M.; Palmisano, L. *Chem. Commun.* **2007**, 3425–3437.

(4)   Palmisano, G.; García-López, E.; Marcì, G.; Loddo, V.; Yurdakal, S.; Augugliaro, V.; Palmisano, L. *Chem. Commun.* **2010**, *46*, 7074–7089.

(5)   Fukuzumi, S.; Kishi, T.; Kotani, H.; Lee, Y.-M.; Nam, W. *Nat. Chem.* **2011**, *3*, 38–41.

(6)   Gross, M. A.; Reynal, A.; Durrant, J. R.; Reisner, E. *J. Am. Chem. Soc.* **2014**, *136*, 356–366.

(7)   Lakadamyali, F.; Reisner, E. *Chem. Commun.* **2011**, *47*, 1695–1697.

(8)   Han, Z.; Qiu, F.; Eisenberg, R.; Holland, P. L.; Krauss, T. D. *Science* **2012**, *338*, 1321–1324.

(9)   Wilker, M. B.; Shinopoulos, K. E.; Brown, K. A.; Mulder, D. W.; King, P. W.; Dukovic, G. *J. Am. Chem. Soc.* **2014**, *136*, 4316–4324.

(10)   Lakadamyali, F.; Kato, M.; Muresan, N. M.; Reisner, E. *Angew. Chem. Int. Ed.* **2012**, *51*, 9381–9384.

(11)   Caputo, C. A.; Gross, M. A.; Lau, V. W.-h; Cavazza, C.; Lotsch, B. V.; Reisner, E. *Angew. Chem. Int. Ed.* **2014**, *53*, 11538–11542.

(12)   Martindale, B. C. M.; Hutton, G. A. M.; Caputo, C. A.; Reisner, E. *J. Am. Chem. Soc.* **2015**, *137*, 6018–6025.

(13) Ding, Z.; Chen, X.; Antonietti, M.; Wang, X. *ChemSusChem* **2011**, *4*, 274–281.

(14) Fukuzumi, S.; Mizuno, T.; Ojiri, T. *Chem. Eur. J.* **2012**, *18*, 15794–15804.

(15) Su, F.; Mathew, S. C.; Möhlmann, L.; Antonietti, M.; Wang, X.; Blechert, S. *Angew. Chem. Int. Ed.* **2011**, *50*, 657–660.

(16) Kalita, D.; Radaram, B.; Brooks, B.; Kannam, P. P.; Zhao, X. *ChemCatChem* **2011**, *3*, 571–573.

(17) Zhou, X.; Li, F.; Li, X.; Li, H.; Wang, Y.; Sun, L. *Dalt. Trans.* **2015**, *44*, 475–479.

(18) Zhang, B.; Li, J.; Zhang, B.; Chong, R.; Li, R.; Yuan, B.; Lu, S.-M.; Li, C. *J. Catal.* **2015**, *332*, 95–100.

(19) Singh, W. M.; Pegram, D.; Duan, H.; Kalita, D.; Simone, P.; Emmert, G. L.; Zhao, X. *Angew. Chem. Int. Ed.* **2012**, *51*, 1653–1656.

(20) Song, W.; Vannucci, A. K.; Farnum, B. H.; Lapides, A. M.; Brennaman, M. K.; Kalanyan, B.; Alibabaei, L.; Concepcion, J. J.; Losego, M. D.; Parsons, G. N.; Meyer, T. J. *J. Am. Chem. Soc.* **2014**, *136*, 9773–9779.

(21) Harriman, A. *Eur. J. Inorg. Chem.* **2014**, 573–580.

(22) Schneider, J.; Bahnemann, D. W. *J. Phys. Chem. Lett.* **2013**, *4*, 3479–3483.

(23) Wang, X.; Maeda, K.; Thomas, A.; Takanabe, K.; Xin, G.; Carlsson, J. M.; Domen, K.; Antonietti, M. *Nat. Mater.* **2009**, *8*, 76–80.

(24) Cao, S.-W.; Liu, X.-F.; Yuan, Y.-P.; Zhang, Z.-Y.; Fang, J.; Loo, S. C. J.; Barber, J.; Sum, T. C.; Xue, C. *Phys. Chem. Chem. Phys.* **2013**, *15*, 18363–18366.

(25) Song, X.-W.; Wen, H.-M.; Ma, C.-B.; Cui, H.-H.; Chen, H.; Chen, C.-N. *RSC Adv.* **2014**, *4*, 18853–18861.

(26) Su, F.; Mathew, S. C.; Lipner, G.; Fu, X.; Antonietti, M.; Blechert, S.; Wang, X. *J. Am. Chem. Soc.* **2010**, *132*, 16299–16301.

(27) Long, B.; Ding, Z.; Wang, X. *ChemSusChem* **2013**, *6*, 2074–2078.

(28) Sattler, A.; Schnick, W. *Eur. J. Inorg. Chem.* **2009**, *7*, 4972–4981.

(29) Lau, V. W.-h; Moudrakovski, I.; Botari, T.; Weinberger, S.; Mesch, M. B.; Duppel, V.; Senker, J.; Blum, V.; Lotsch, B. V. *Nat. Commun.* **2016**, *7*, 12165.

(30) Thomas, A.; Fischer, A.; Goettmann, F.; Antonietti, M.; Müller, J.-O.; Schlögl, R.;

Carlsson, J. M. *J. Mater. Chem.* **2008**, *18*, 4893–4908.

(31) Irran, E.; Jürgens, B.; Schnick, W. *Solid State Sci.* **2002**, *4*, 1305–1311.

(32) Lotsch, B. V; Döblinger, M.; Sehnert, J.; Seyfarth, L.; Senker, J.; Oeckler, O.; Schnick, W. *Chem. Eur. J.* **2007**, *13*, 4969–4980.

(33) Fina, F.; Callear, S. K.; Carins, G. M.; Irvine, J. T. S. *Chem. Mater.* **2015**, *27*, 2612–2618.

(34) Helm, M. L.; Stewart, M. P.; Bullock, R. M.; DuBois, M. R.; DuBois, D. L. *Science* **2011**, *333*, 863–866.

(35) Kilgore, U. J.; Roberts, J. A. S.; Pool, D. H.; Appel, A. M.; Stewart, M. P.; DuBois, M. R.; Dougherty, W. G.; Kassel, W. S.; Bullock, R. M.; DuBois, D. L. *J. Am. Chem. Soc.* **2011**, *133*, 5861–5872.

(36) Palmisano, G.; Yurdakal, S.; Augugliaro, V.; Loddo, V.; Palmisano, L. *Adv. Synth. Catal.* **2007**, *349*, 964–970.

(37) Yurdakal, S.; Palmisano, G.; Loddo, V.; Augugliaro, V.; Palmisano, L. *J. Am. Chem. Soc.* **2008**, *130*, 1568–1569.

(38) Yurdakal, S.; Palmisano, G.; Loddo, V.; Alagöz, O.; Augugliaro, V.; Palmisano, L.; Alagoz, O.; Augugliaro, V.; Palmisano, L. *Green Chem.* **2009**, *11*, 510–516.

(39) Yurdakal, S.; Augugliaro, V. *RSC Adv.* **2012**, *2*, 8375–8380.

(40) Shinagawa, T.; Takanabe, K. *J. Phys. Chem. C* **2015**, *119*, 20453–20458.

(41) Liu, G.; Wang, T.; Zhang, H.; Meng, X.; Hao, D.; Chang, K.; Li, P.; Kako, T.; Ye, J. *Angew. Chem. Int. Ed.* **2015**, *54*, 13561–13565.

(42) Meyer, A. U.; Lau, V. W.-h; König, B.; Lotsch, B. V. *European J. Org. Chem.* **2017**, *2017*, 2179–2185.

Chapter 4

Dark photocatalysis with carbon nitride using trapped electrons for time-delayed solar fuel production

The data presented in this chapter was published in peer-reviewed articles: J. Am. Chem. Soc., 2016, 138, 9183–9192; Angew. Chem. Int. Ed. 2016, 55, 510–514; ACS Catal. 2018, 8, 6914–6926. The author of this thesis carried all of the work presented unless specified otherwise. Transient absorption spectroscopy measurements were performed and analysed by Dr. Robert Godin. Prof. Vincent Wing-hei Lau synthesised the carbon nitride.

4.1 Introduction

Natural photosynthesis serves as a model system for efficient utilisation of solar energy in chemical bonds. It demonstrates a full redox system, consisting of light-dependent and light-independent ("dark") half cycles, carrying out water oxidation and carbon dioxide reduction respectively.[1] The dark cycle functions independent of the primary light source and without a need for continuous energy supply.

Designing artificial systems with an aim to replicate the perfectly functioning complex mechanism behind natural photosynthesis is taking a great amount of research interest. Mimicking natural photosynthesis would imply generating long-lived and highly reducing "trapped" electrons in the photocatalyst during irradiation, to be

used subsequently on demand, and reproducing the ability to decouple light-dependent and light-independent reactions, enabling catalysis in the dark. Despite intensive research, artificial photosynthetic schemes designed up to date are not commercially viable to capture and store solar energy as chemical fuels. The storage and release of solar energy as well as the diurnal availability of sunlight are the main limitations behind these systems, leaving room for improvement.

Colloidal TiO_2 nanoparticles have been previously reported to trap electrons (forming Ti^{3+}) on the surface of the particles and in the conduction band after photoexcitation, in the presence of sacrificial electron donor without an electron acceptor.[2] These trapped electrons give rise to a broad absorption band (λ_{max} = 650 nm) and can be subsequently released, to drive various reactions, including reduction of commonly used oxidants such as O_2 and H_2O_2.[3,4] These long-lived electrons in TiO_2 have also been demonstrated to reduce toxic metal contaminants.[4] However, TiO_2 particles can only utilise the high energy UV portion of the solar spectrum in photocatalytic applications.

A number of photoelectrochemical cells have also been demonstrated to decouple O_2 and H_2 evolution reactions by using molecular redox mediators or electron-coupled-proton buffers.[5–8] These approaches overcome the main limitations of pressure increase and gas separation in conventional photoelectrochemical cells, by decoupling the time and space for O_2 and H_2 evolution. Nevertheless, the multicomponent set-up and the complicated cell design increase the manufacturing cost significantly.[9]

Herein we investigate the $^{NCN}CN_x$−NiP system, introduced in Chapter 3, for the ability to decouple the oxidation and reduction half reactions of a redox scheme in light and dark cycles through the utilisation of long-lived "trapped" electrons (Figure 4.1). This artificial scheme replicates natural photosynthesis, using carbon nitride that functions as the light harvester and electron relay, without the need for multiple component and complex assembly in nature.[1] This bio-inspired system is straightforward to assemble and only consists of earth-abundant components. The mechanism and the rate-limiting steps of the $^{NCN}CN_x$−NiP hybrid are also investigated using transient absorption spectroscopy (TAS), aiming to improve the understanding behind this system.
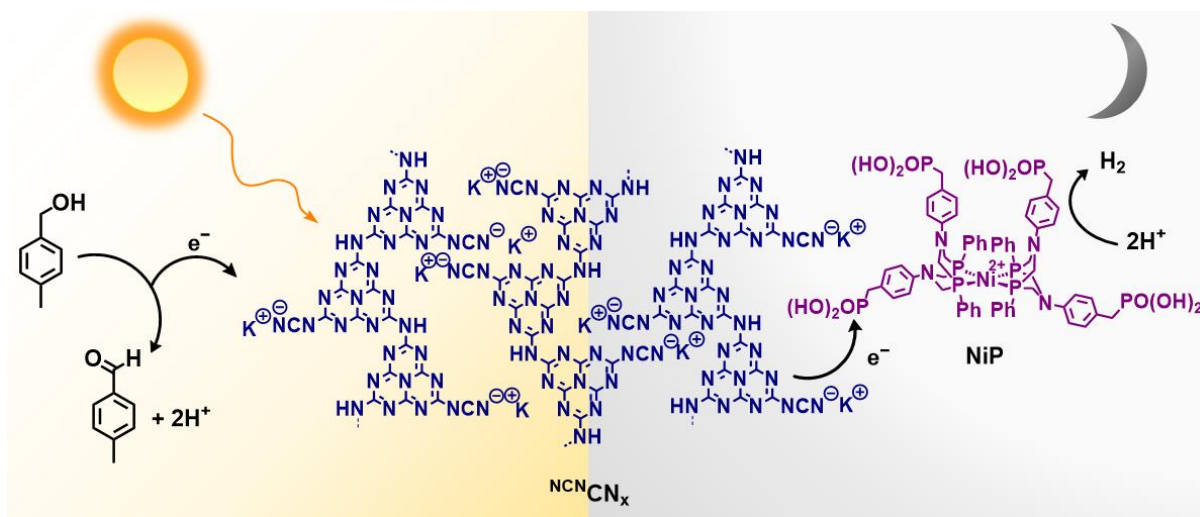
Figure 4.1. Schematic representation of a $^{NCN}CN_x$−**NiP** colloidal system for decoupled oxidation and reduction reactions in the light and dark phase respectively.

4.2 Results and discussion

4.2.1 Dark photocatalysis

The colloidal suspensions of $^{NCN}CN_x$ and **NiP** were prepared as described in Chapter 3. An unexpected behaviour was observed during the control experiments that $^{NCN}CN_x$ oxidised 4-MBA under N_2 without the need for an electron acceptor **NiP** (Figure 4.2a). This result implied that $^{NCN}CN_x$ can accumulate photoexcited charge carriers in its structure while carrying out catalysis.[10] The other important observation was the instantaneous colour change of colloidal suspension prepared with $^{NCN}CN_x$, **NiP** and 4-MBA upon irradiation. The colour of the solution changed immediately when exposed to a light source from pale yellow to intense blue and this colour persisted during 24 h of continuous irradiation (Figure 4.2b).

Initially this colour change was studied by replacing **NiP** with a sacrificial electron acceptor, ammonium persulfate or air (O_2), in which the colour of the suspension remained yellow during irradiation in the presence of 4-MBA. On the other hand, when 4-MBA was substituted with sacrificial electron donor EDTA in the absence of **NiP**, the colour of the solution remained blue under inert N_2 atmosphere. The observed colour change was therefore attributed to photogenerated electrons in the photosensitiser.

67

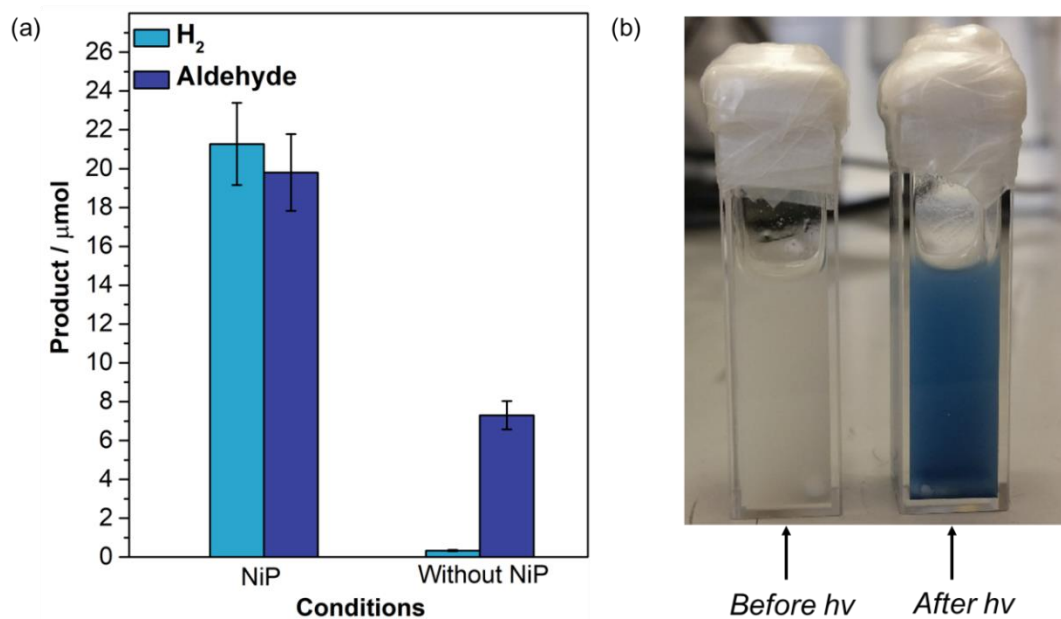Figure 4.2. (a) Bar chart representing photocatalytic H_2 and aldehyde formation in the presence of $^{NCN}CN_x$ (5 mg) and 4-MBA (30 μmol) with and without **NiP** in KP_i (0.02 M, pH 4.5, 3 mL) after 24 h of 1 sun irradiation (AM 1.5G) at 25 °C. (b) Suspension of $^{NCN}CN_x$ (5 mg) and 4-MBA (30 μmol) in an aqueous KP_i solution (0.02 M, pH 4.5) before irradiation (pale yellow) and after irradiation (blue).
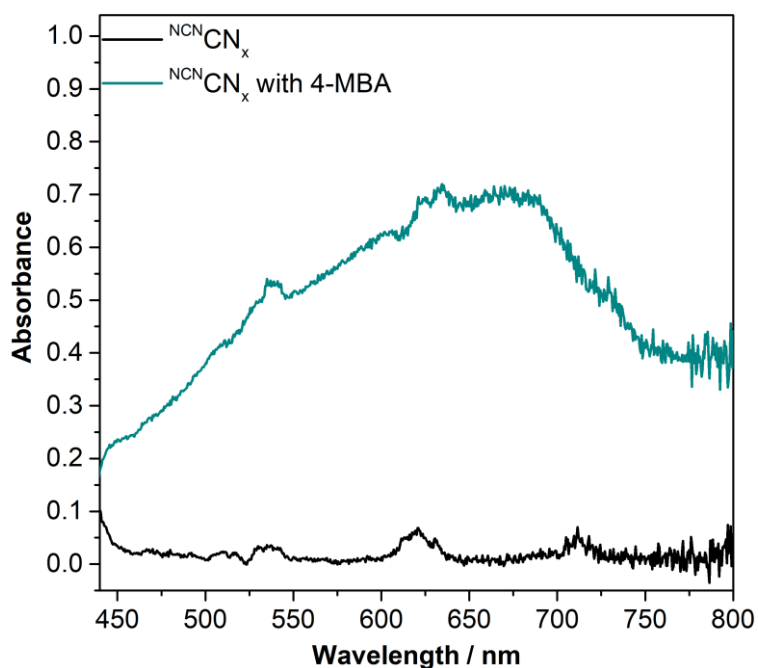

Figure 4.3. UV–vis absorption spectra of colloidal suspensions of $^{NCN}CN_x$ (5 mg) and 4-MBA (30 μmol) in KP_i (3 mL) were generated by comparing samples before and after irradiation under 1 sun for 30 min (AM 1.5G, 25 °C).

In order to characterise the colour change upon irradiation of the $^{NCN}CN_x$, UV–vis absorption spectra were recorded for $^{NCN}CN_x$ (5 mg) in KP_i (3 mL, 0.02 M, pH 4.5) with and without 4-MBA (30 µmol) after 30 min of simulated solar light irradiation (AM 1.5G). As the heterogeneous $^{NCN}CN_x$ particles scatter the incident light and settle during the period of measurement, spectrofluorometer (Edinburgh Instruments FS5) equipped with an integrating sphere was used for measuring UV–vis spectra. Synchronous scans ($\lambda_{ex} = \lambda_{em}$) were run for samples and the absorption spectra were generated by comparing samples before and after irradiation using the Fluoracle software supplied with the FS5 instrument.

The suspension prepared with 4-MBA turned intense blue immediately upon irradiation and consequently a broad absorption peak at λ = 650 nm was obtained (Figure 4.3), a direct spectroscopic observation of the trapped electrons in the $^{NCN}CN_x$. In the absence of 4-MBA no colour change was observed, indicating that 4-MBA reductively quenches the photoexcited state of the $^{NCN}CN_x$.

The next step was to test if the electrons stored in $^{NCN}CN_x$ can be extracted and monitored spectroscopically. **NiP** (50 nmol) was added to a blue suspension using an airtight syringe under N_2 and the peak at λ = 650 nm was monitored every 15 min for 1 h, while the suspension was stirred in the dark (Figure 4.4). A significant decay in the absorption peak was observed in the first 15 min ($\tau_{1/2}$ = 10 min), indicating the transfer of the trapped electrons from $^{NCN}CN_x$ to **NiP**. After 30 min, the broad peak at λ = 650 nm disappeared. The photoexcited electrons were thus collected by **NiP** and the colour of the suspension turned back to yellow again. In a control experiment, a **NiP**-free KP_i solution was added to another $^{NCN}CN_x$ suspension irradiated for 30 min and the solution remained blue with no significant change in the absorption spectra. Therefore, these ultra-long-lived "trapped electrons" can be stored in the dark for prolonged periods of time (> 30 min) in the heptazine framework of $^{NCN}CN_x$ and transferred to **NiP** when available.[11]

To demonstrate quantitative H_2 evolution in the dark phase, two photoreactors were prepared using $^{NCN}CN_x$ (5 mg) and 4-MBA (30 µmol) in KP_i in the absence **NiP** and were irradiated under simulated solar light (AM 1.5G) for 4 h (Figure 4.5). Then, both systems were moved to dark and **NiP** (50 nmol) was added to only one of the photoreactors and the H_2 production was monitored for both (Table B.1). The same effect was observed, the photoreactor kept in the dark without **NiP** did not show any
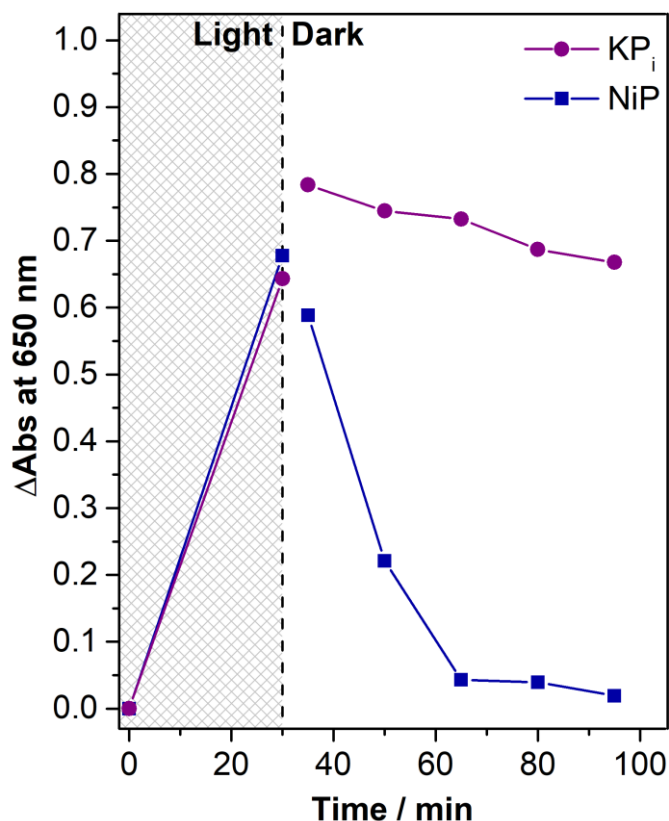
Figure 4.4. Spectrophotometry of the appearance (during irradiation) and disappearance (upon addition of **NiP**) of photoexcited electrons in $^{NCN}CN_x$ at λ = 650 nm. Two photoreactors were prepared with $^{NCN}CN_x$ (5 mg) and 4-MBA (30 μmol) in KP_i (0.02 M, pH 4.5, 3 mL) and irradiated (AM 1.5G) for 30 min, followed by the addition of **NiP** (50 nmol, 400 μL) or KP_i (400 μL) using an air tight syringe.

H_2 production in the 20 h dark phase, whereas the vial containing **NiP** showed a substantially increased H_2 production. The amount of aldehyde produced after 24 h was the same for both of the systems (independent of the **NiP**) indicating that alcohol oxidation ceased as soon as the vials were removed from light. These results agree with efficient alcohol oxidation by $^{NCN}CN_x$, using the photogenerated holes, even in the absence of an electron acceptor (Figure 4.2a).

Thus, $^{NCN}CN_x$ can be charged during the light phase by 4-MBA oxidation and the electrons can be released in the absence of light to carry out proton reduction to H_2, which enables the temporary decoupling of the oxidative and reductive half reactions.[5] This system directly replicates natural photosynthesis in a single reactor with light and dark cycles of reactions occurring at different times.
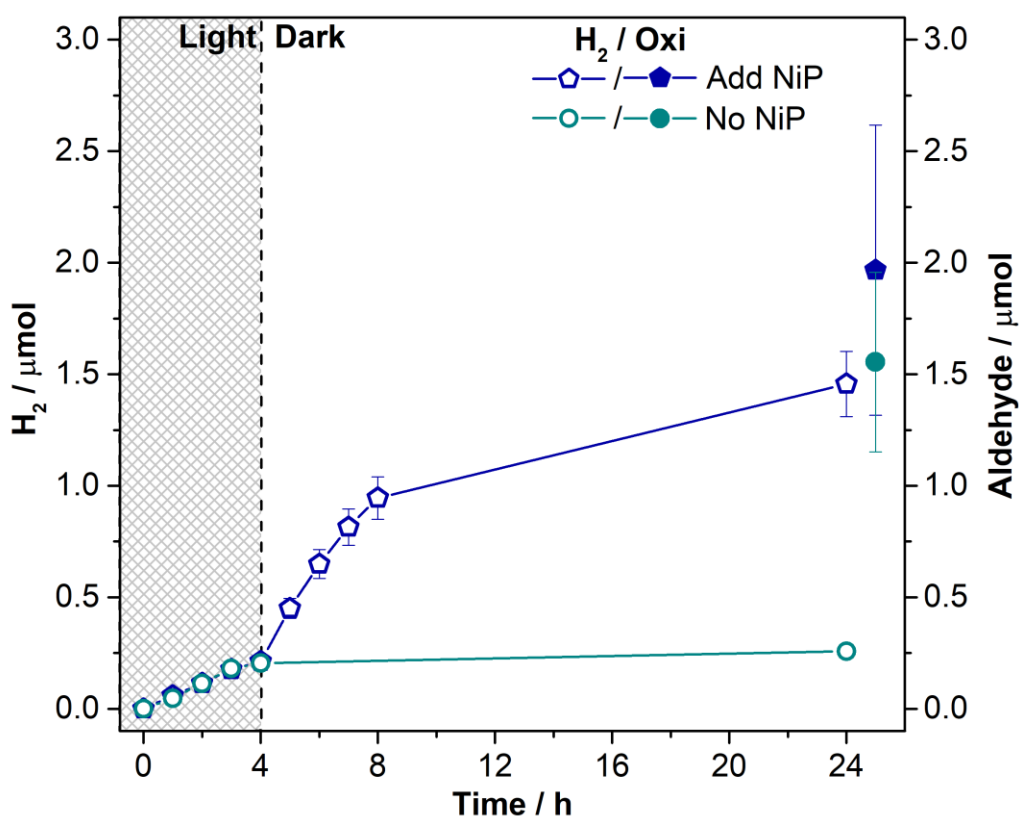
Figure 4.5. Photoreactors were prepared with $^{NCN}CN_x$ (5 mg) and 4-MBA (30 µmol) in the absence of **NiP** in an aqueous KP_i (0.02 M, pH 4.5, 3 mL) under 1 sun irradiation (AM 1.5G, 25 °C). Both of the photoreactors were taken into the dark after 4 h of irradiation, while **NiP** (50 nmol) was added to one of them using an air tight syringe. The pair of hollow and filled symbols of the same shape and colour corresponds to the specified reaction conditions.

Further studies were carried out on characterising the nature of these ultra-long-lived "trapped electrons" in $^{NCN}CN_x$ using electron paramagnetic resonance (EPR) spectroscopy and computational calculations.[12] The results revealed that electrons are stored as heptazine-based radicals with partially neutral and anionic cyanamide side groups. Under fully inert atmosphere the material was found to preserve this charged state for up to 6 months.

The amount of H_2 produced in the dark cycle provides an indirect measure on the total number of heptazine based radicals generated during the irradiation of the material.[12] After 4 h of irradiation, 1.5 ± 0.1 µmol of H_2 was generated from $^{NCN}CN_x$ in the dark. Assuming that trapped electrons are quantitatively converted into H_2, and this is the only reaction pathway for the radicals, it is estimated that 3.0 ± 0.2 µmol of

radicals are accumulated in $^{NCN}CN_x$. For the purpose of this experiment 5 mg of $^{NCN}CN_x$ was used which corresponds to 20 μmol of heptazine units with a molecular weight of 249 g mol^{-1}. Therefore, approximately a 1:10 ratio of radical to heptazine units were preserved in the charged state of $^{NCN}CN_x$.

4.2.2   Mechanism

Developing a better understanding on the mechanism behind this closed redox system for simultaneous alcohol oxidation and proton reduction is of great interest, as this would enable the determination of rate-limiting steps and the range of organic substrates that can be oxidised under the utilised conditions (Figure 4.1). It is well known that proton reduction by **NiP** occurs *via* successive multiple electron and proton transfers.[13–15] For the alcohol oxidation half of the scheme, many mechanistic studies have been reported on organic substrate oxidation with colloidal light harvesters such as CN_x,[16–18] TiO_2,[19–21] and $BiVO_4$ [22,23] under O_2 atmosphere. However, there are only few reports on high-yielding alcohol photo-oxidation under N_2, which precludes the formation and potential involvement of reactive oxygen species.[24–26]

To identify the source of protons for H_2 production, KP$_i$ buffer was prepared in H_2O and D_2O (Figure 4.6a, Table B.2). The headspace gas produced was monitored by GC and characterised by mass spectrometry (MS), through examining the composition of the gases with mass/charge ratios between 1 and 5 amu over the irradiation period (Figure 4.6a, inset). Over the course of 4 h, linear gas production at a comparable rate was observed regardless of using H_2O or D_2O as solvent. In the presence of D_2O, the peak corresponding for D_2 grew selectively over time with negligible amounts of H_2 and HD being detected. This indicated that aqueous protons were selectively delivered to **NiP** for H_2 formation. The rate of H_2 gas production was not affected by D_2O substitution, demonstrating that O−H/D bond breaking is not the rate-determining step for proton reduction.[27]

The kinetic isotope effect (KIE) of an isotopically labelled 4-MBA substrate was then studied by using α-D_2 benzyl alcohol (BA). The substitution with D_2-BA did not influence the rate of proton reduction, while MS analysis confirmed that the headspace gas was H_2 (Figure 4.6b), demonstrating that aliphatic protons from BA were not used for proton reduction. Independent of BA labelling, around 6 μmol of aldehyde was produced after 4 h of irradiation, showing that the rate of proton abstraction from BA
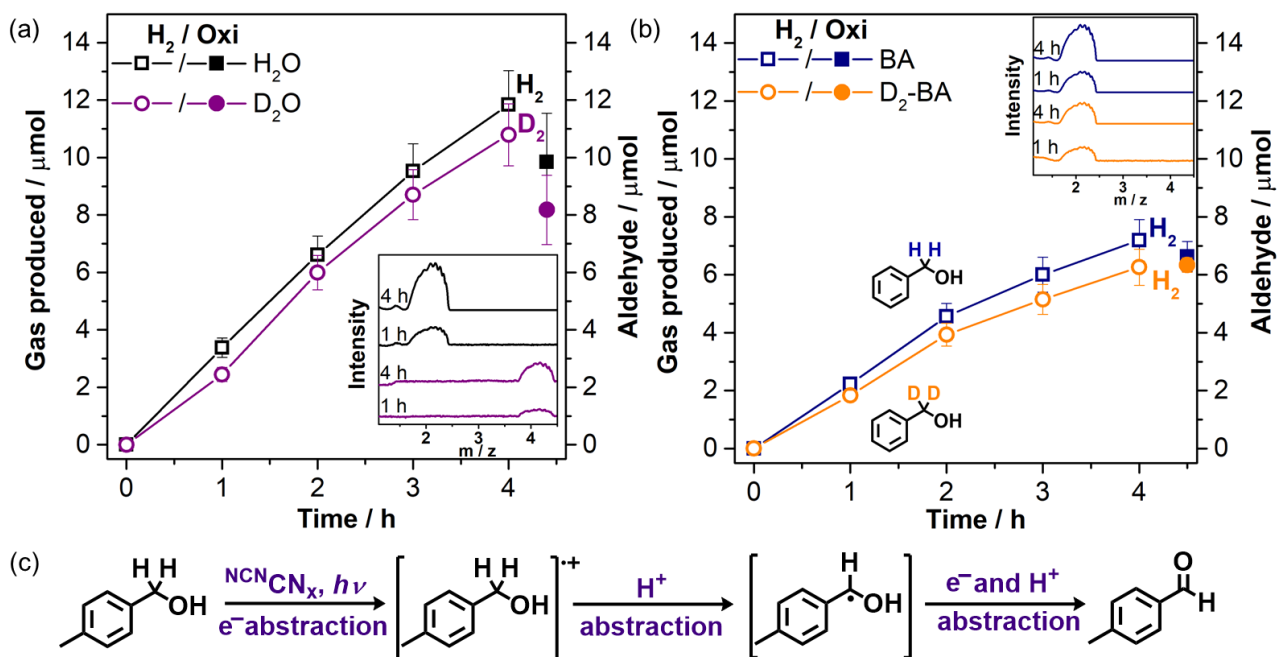
Figure 4.6. (a) Photocatalytic H_2 and aldehyde production with $^{NCN}CN_x$ (5 mg), **NiP** (50 nmol), 4-MBA (30 µmol) in KP_i (0.1 M, pH 4.5, 3 mL) prepared in H_2O or D_2O under 1 sun irradiation (100 mW cm^{-2}, AM 1.5G, 25 °C). Inset: MS monitoring the headspace gas produced overtime in suspension prepared with H_2O and D_2O. (b) Photocatalytic H_2 production with $^{NCN}CN_x$ (5 mg), **NiP** (50 nmol) and BA or D_2-BA (30 µmol) in KP_i (0.1 M, pH 4.5, 3 mL) under 1 sun irradiation (100 mW cm^{-2}, AM 1.5G, 25 °C) Inset: MS monitoring the headspace gas produced overtime in the presence of BA and D_2-BA. The pair of hollow and filled symbols of the same shape and colour corresponds to H_2 and aldehyde production, respectively. Amount of aldehyde formed is detected after 4 h of irradiation. (c) Proposed mechanism for alcohol oxidation with $^{NCN}CN_x$, **NiP** and 4-MBA in KP_i under inert (N_2) atmosphere.

was not limiting the oxidation process. The first step of oxidation is presumably the hole transfer from photoexcited $^{NCN}CN_x$ to the substrate (Figure 4.6c).[28,29]

Alcohol oxidation was further investigated under a N_2 or air atmosphere without **NiP** (Table B.2). After 4 h of irradiation, selective production of 2 and 14 µmol of 4-MBAd was detected under N_2 and air atmospheres, respectively (for comparison, 10 µmol 4-MBAd are detected in the presence of **NiP** and N_2). These results indicated that the presence of a strong electron acceptor such as O_2 assisted faster extraction of photogenerated electrons from $^{NCN}CN_x$, quickly regenerating the ground-state of the photocatalyst and increasing the turnover frequency for alcohol oxidation.[19,21]

The possibility of hydroxyl radical (HO$^{\bullet}$) formation was explored by using the hydroxyl radical scavenger benzene-1,4-dicarboxylic acid (terephthalic acid, THA).[30] Hydroxylation of THA by HO$^{\bullet}$ yields a highly fluorescent THA-OH, with an emission at 426 nm when excited with 315 nm light.[30] $^{NCN}CN_x$ suspensions irradiated in the presence of THA for one hour showed an insignificant amount (< 0.02 μmol) of THA-OH formation (Figure B.1), indicating that this is a minor reaction pathway for the oxidation reaction. This is supported by the mismatch between the valence band position of $^{NCN}CN_x$ (approximately 1.4 V *vs.* NHE at pH 7), and the redox potential of HO$^-$ to hydroxyl radicals (E°(HO$^{\bullet}$/HO$^-$) = 2.4 V *vs.* NHE at pH 7).[18,31] Photocatalytic substrate oxidation under O$_2$ atmosphere is believed to occur through superoxide radical formation, O$_2$$^{\bullet-}$, but this possibility can be excluded in the reported system as the experiments were carried out under N$_2$.[18]

Our mechanistic studies therefore support that presumably a direct hole transfer occurs first from photoexcited $^{NCN}CN_x$ to 4-MBA, followed by slow electron transfer from $^{NCN}CN_x$ to **NiP** to reduce aqueous protons to H$_2$ (Figure 4.6c).[32,33] Consumption of the photogenerated charge carriers is ultimately essential to promote the production of H$_2$ and aldehyde in 1:1 stoichiometry and close the photo-redox cycle, but the oxidative and reductive half-reactions can be temporarily, and in principle, spatially decoupled.[25]

4.2.3 Transient absorption spectroscopy

To gain a better understanding on the kinetics behind electron transfer in this closed redox system, TAS measurements were carried out. As detailed below, TAS investigations confirmed that electron transfer from photoexcited $^{NCN}CN_x$ to **NiP** is the rate-limiting step for the photocatalytic system (Figure 4.7). Titration experiments carried out by increasing the **NiP** concentration did not quench the excited state of the photosensitiser, $^{NCN}CN_x$*, eliminating the possibility for an oxidative quenching mechanism (Figures B.2 and B.3).

Photoexcitation of $^{NCN}CN_x$ produced a photoinduced absorption signal in the range of 550–1000 nm (Figure B.4), which matches that observed upon irradiation of $^{NCN}CN_x$ with 4-MBA (Figure 4.3). This spectral feature did not show any evolution over the decay time nor was the shape sensitive to additives, suggesting a single excited state species absorbing over this spectral range. Kinetics were probed at 750 nm with
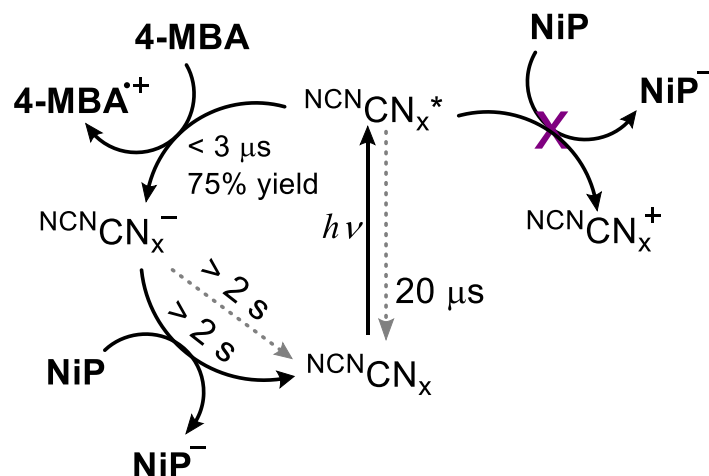
Figure 4.7. Summary of mechanism and kinetic rates from TAS measurements with suspensions prepared with $^{NCN}CN_x$ (1–5 mg mL^{-1}), **NiP** (up to 24 µM) and 4-MBA (10 mM) in an aqueous KP$_i$ solution (0.02 M, pH 4.5, 25 °C). Representative lifetimes, calculated using 3 µs as the initial time, are indicated near reaction arrows. Recombination reactions are indicated by dashed grey arrows.

an aim to reduce the influence of the strong photoluminescence at wavelengths near 550 nm. The intrinsic decay of $^{NCN}CN_x$ (Figure B.5) yielded a representative lifetime ($\tau_{1/2}$) of 21.6 µs, which was the time during which 50% of the initial (at 3 µs) excited state population has decayed by half.

The tens of microsecond timescale of the decay was quite comparable to those found in metal oxide photocatalysts such as hematite[34] and TiO$_2$.[35] Furthermore, the same type of dispersive power law decay dynamics are found in the carbon nitrides studied as for the metal oxides, and has been attributed to bimolecular (i.e. electron-hole) recombination. The exponent of the power law was significantly smaller than unity (~0.35), indicating that charge trapping/detrapping may play a considerable role in excited state dynamics of $^{NCN}CN_x$, as also indicated by slow timescale of this recombination process.

We next performed 4-MBA titration experiments to elucidate the kinetics of 4-MBA oxidation. As the concentration of 4-MBA increased, a long-lived component of the decay became dominant (Figure B.6), which is assigned to long-lived electrons formed after hole scavenging by 4-MBA. For 10 mM 4-MBA, these long-lived electrons

account for about 75% of the initial amplitude (Figure 4.8). Assuming a bimolecular dynamic quenching process, analysis of the concentration-dependent yield and rate of formation of the long-lived electrons (see Appendix for details) provided a reaction rate constant of 1.43×10^7 M^{-1} s^{-1} (Figure B.7 and B.8). The analysis also informed us of a slow background reaction rate k_0 of 8200 s^{-1}, which we tentatively attribute to hole scavenging by small amounts of impurities or H_2O, and explains the non-zero absorption seen in the millisecond regime in the absence of 4-MBA. However, the shape of the decay is more indicative of quenching occurring on timescales faster than the instrument response of 3 µs, perhaps by static quenching. Specifically, the decrease in amplitude seen before 1 ms in the presence of 10 mM 4-MBA showed a $\tau_{1/2}$ of roughly 20 µs, that is, indistinguishable fast phase $\tau_{1/2}$ was observed with or without 4-MBA. The yield of long-lived electrons plateaued for higher concentration of 4-MBA, a possible indication that deeply trapped electrons which decay with microsecond dynamics are unable to participate in the charge transfer reaction.[36] The $^{NCN}CN_x$/4-MBA reaction thus appears to take place faster than the ~20 µs relaxation kinetics of $^{NCN}CN_x$. Comparing to a previously reported photocatalytic system using AA as the sacrificial electron donor, the $^{NCN}CN_x$/4-MBA reaction timescale is faster than reduction of an oxidised Ru(III) dye (**RuP**-TiO$_2$/AA) and maybe comparable to the reduction of the excited state of the Ru dye (**RuP**/AA).[37]

The same TAS spectral feature is seen with and without the addition of 4-MBA while the oxidation of 4-MBA consumes holes, which confirms the assignment of the blue-coloured solution deriving from photogenerated electrons in the $^{NCN}CN_x$ (Figure B.4). The same observation was also made with MeOH as hole scavenger (Figure B.4). An analogous increase of the photogenerated electron lifetime in TiO$_2$ has been observed upon the addition of MeOH as a hole scavenger.[38] Therefore, we may directly monitor the population of electrons in the $^{NCN}CN_x$. This further implies that the formation of separated charge carriers in $^{NCN}CN_x$ occurs within 3 µs.

We attempted to quantify the rate of electron transfer reaction from $^{NCN}CN_x$ to **NiP** but the timescale of this reaction was too long for direct observation by TAS. Both in the absence or presence of 4-MBA, addition of **NiP** did not affect the relaxation kinetics of $^{NCN}CN_x$ (Figures B.2 and B.3). The upper time limit of our measurements was ~2 s due to settling of the heterogeneous $^{NCN}CN_x$ dispersion (see Chapter 5 for details). We thus conclude that the lifetime of long-lived electrons in $^{NCN}CN_x$ is longer
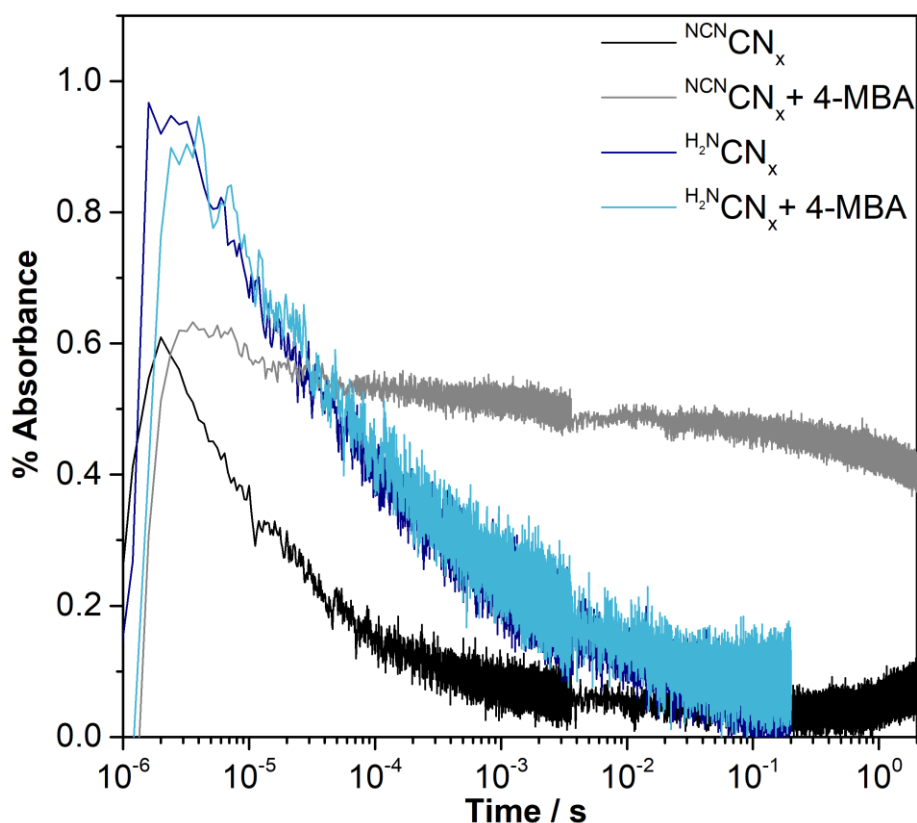
76

Figure 4.8. Transient decays probed at λ = 750 nm of $^{NCN}CN_x$ (1.2 mg mL^{-1}) and $^{H_2N}CN_x$ (1.2 mg mL^{-1}) suspensions in aqueous KP$_i$ solution (0.02 M, pH 4.5, 25 °C) following λ = 355 nm excitation. Traces obtained following the addition of 10 mM 4-MBA are also shown.

than 2 s, which is consistent with the persistent blue colour observed upon irradiation of $^{NCN}CN_x$/4-MBA (see above). Similarly, the reaction lifetime for $^{NCN}CN_x$ electron transfer to **NiP** is also longer than 2 s, in line with disappearance of the blue colour that takes place over 30 min upon **NiP** addition (Figure 4.4). Taking into account the **NiP** concentration, the upper bound of the bimolecular rate constant is thus set to 2 x 10^5 M^{-1} s^{-1}.

The time taken for the electron transfer from $^{NCN}CN_x$ to **NiP** and for $^{NCN}CN_x$ charge recombination is presented as more than 2 s (Figure 4.7), as this is the longest timescale (upper limit) that TAS set-up can record, due to settling nature of the $^{NCN}CN_x$ suspensions. Nevertheless, it should be noted that the electron transfer to **NiP** is more favourable pathway, with faster kinetics, as H$_2$ is detected as the main reduction product in the photocatalytic experiments in longer than 2 s timescale (hours).

We have compared the TAS results of $^{NCN}CN_x$ and the unfunctionalised $^{H_2N}CN_x$ to gain insights in the significant differences in efficiency. Surprisingly, for the studied timescale, we observed slower decay kinetics ($\tau_{\frac{1}{2}}$ = 60.2 μs) for $^{H_2N}CN_x$ dispersions compared to the catalytically more efficient $^{NCN}CN_x$ (Figure 4.8 and B.9). Instead of increasing the lifetime of reactive charges, the increased efficiency of cyanamide-functionalised carbon nitride seems to stem from higher hole transfer reactivity towards oxidation reaction. In particular, we have observed no changes in the decay kinetics of $^{H_2N}CN_x$ upon the addition of 4-MBA, supporting an inefficient alcohol oxidation step, which was also observed in our bulk photocatalytic experiments. It is plausible that oxidation of 4-MBA by $^{NCN}CN_x$ is aided by more favourable hydrogen bonding interactions between the anionic cyanamide moieties on the surface of the material and the benzyl alcohol. This pre-association increases effectiveness of static quenching and/or effectively increases the basicity of the carbon nitride and the driving force for reaction.[39] These observations highlight the necessary consideration of both charge photogeneration and separation as well as complex electron-proton transfer processes in photocatalyst reactivity.

Considering all of the collected experimental evidence, a stepwise mechanism is proposed for the closed redox system of $^{NCN}CN_x$–**NiP**. Initially, irradiation of $^{NCN}CN_x$ results in light absorption and charge separation. The photogenerated holes in the material is first reductively quenched by the 4-MBA for selective alcohol oxidation. The photo-excited electrons accumulated in the $^{NCN}CN_x$ are then transferred to the **NiP**, which carries out reduction of aqueous protons. The rate of photogenerated electron transfer from $^{NCN}CN_x$ to **NiP** is slower than the rate of reductive quenching, giving rise to an intense blue colour.

4.3 Conclusions

The $^{NCN}CN_x$–**NiP** redox system demonstrated to decouple oxidation and reduction reactions in a single pot without a need for any additional mediator. During irradiation $^{NCN}CN_x$ accumulates ultra-long-lived 'trapped electrons', and effectively transfers these charge carriers to the catalyst, **NiP**, in the dark-phase, to generate solar fuel H_2, directly mimicking natural photosynthesis. This approach enables developing systems and devices that are not limited by the diurnal availability of sunlight by temporarily and spatially decoupling light absorption from fuel generation.

Mechanistic investigations on $^{NCN}CN_x-NiP$ revealed that photogenerated electrons are used by **NiP** for proton reduction, with selective use of H^+ from the solution (KP$_i$), while the photogenerated holes are consumed by 4-MBA for oxidation. $^{NCN}CN_x$ behaves as an electron reservoir for long-lived and reductive electrons, whereas the rate of electron extraction from $^{NCN}CN_x$ is the overall rate-limiting step.

TAS results showed that photogenerated holes on $^{NCN}CN_x$ are quenched by 4-MBA in time scales faster than 3 µs whereas electron transfer from $^{NCN}CN_x$ to **NiP** occurs in longer than 2 s. This observation confirms that the rate of electron transfer from $^{NCN}CN_x$ to **NiP** is overall the slowest electron transfer process in the complete redox system. In addition TAS results showed that cyanamide groups on the surface of the material play a vital role in providing enhanced catalytic activity towards selective substrate oxidation, which outperforms possible charge recombination reactions in the presence of 4-MBA. The main reason for the enhanced catalytic activity of $^{NCN}CN_x$ is attributed to better hole transfer ability to 4-MBA, enabling superior oxidation reactivity towards organic substrates, in comparison to the benchmark $^{H_2N}CN_x$.

These results demonstrate that the efficiency of $^{NCN}CN_x-NiP$ redox system is limited by the rate of electron extraction from $^{NCN}CN_x$. Introduction of conductive scaffolds or pre-treatment techniques to speed up this process would overcome this limitation. This work highlights the importance of studying each component individually to develop better understanding on the charge generation and separation kinetics in multi component systems, by bringing photocatalytic experiments together with spectroscopic techniques.

4.4 References

(1)   Nelson, N.; Ben-Shem, A. *Nat. Rev. Mol. Cell Biol.* **2004**, *5*, 971–982.

(2)   Bahnemann, D.; Henglein, A.; Lilie, J.; Spanhel, L. *J. Phys. Chem.* **1984**, *88*, 709–711.

(3)   O'Regan, B.; Grätzel, M.; Fitzmaurice, D. *Chem. Phys. Lett.* **1991**, *183*, 89–93.

(4)   Mohamed, H. H.; Mendive, C. B.; Dillert, R.; Bahnemann, D. W. *J. Phys. Chem. A* **2011**, *115*, 2139–2147.

(5)   Symes, M. D.; Cronin, L. *Nat. Chem.* **2013**, *5*, 403–409.

(6)   Bloor, L. G.; Solarska, R.; Bienkowski, K.; Kulesza, P. J.; Augustynski, J.; Symes, M. D.; Cronin, L. *J. Am. Chem. Soc.* **2016**, *138*, 6707–6710.

(7)   Rausch, B.; Symes, M. D.; Chisholm, G.; Cronin, L. *Science* **2014**, *345*, 1326–1330.

(8)   Kirkaldy, N.; Chisholm, G.; Chen, J. J.; Cronin, L. *Chem. Sci.* **2018**, *9*, 1621–1626.

(9)   You, B.; Liu, X.; Jiang, N.; Sun, Y. *J. Am. Chem. Soc.* **2016**, *138*, 13639–13646.

(10)   Kasap, H.; Caputo, C. A.; Martindale, B. C. M.; Godin, R.; Lau, V. W.-h; Lotsch, B. V.; Durrant, J. R.; Reisner, E. *J. Am. Chem. Soc.* **2016**, *138*, 9183–9192.

(11)   Rosser, T.; Gross, M. A.; Lai, Y.-H.; Reisner, E. *Chem. Sci.* **2016**, *18*, 15464–15475.

(12)   Lau, V. W.-h; Klose, D.; Kasap, H.; Podjaski, F.; Pignié, M.-C.; Reisner, E.; Jeschke, G.; Lotsch, B. V. *Angew. Chem. Int. Ed.* **2017**, *56*, 510–514.

(13)   Wilson, A. D.; Shoemaker, R. K.; Miedaner, A.; Muckerman, J. T.; DuBois, D. L.; DuBois, M. R. *Proc. Natl. Acad. Sci. U.S.A.* **2007**, *104*, 6951–6956.

(14)   Small, Y. A.; DuBois, D. L.; Fujita, E.; Muckerman, J. T. *Energy Environ. Sci.* **2011**, *4*, 3008–3020.

(15)   Kilgore, U. J.; Roberts, J. A. S.; Pool, D. H.; Appel, A. M.; Stewart, M. P.; DuBois, M. R.; Dougherty, W. G.; Kassel, W. S.; Bullock, R. M.; DuBois, D. L. *J. Am. Chem. Soc.* **2011**, *133*, 5861–5872.

(16)   Su, F.; Mathew, S. C.; Möhlmann, L.; Antonietti, M.; Wang, X.; Blechert, S. *Angew. Chem. Int. Ed.* **2011**, *50*, 657–660.

(17)   Long, B.; Ding, Z.; Wang, X. *ChemSusChem* **2013**, *6*, 2074–2078.

(18)   Su, F.; Mathew, S. C.; Lipner, G.; Fu, X.; Antonietti, M.; Blechert, S.; Wang, X. *J. Am. Chem. Soc.* **2010**, *132*, 16299–16301.

(19)   Higashimoto, S.; Suetsugu, N.; Azuma, M.; Ohue, H.; Sakata, Y. *J. Catal.* **2010**, *274*, 76–83.

(20)   Shi, T.; Chang, W.; Zhang, H.; Ji, H.; Ma, W.; Chen, C.; Zhao, J. *Environ. Sci. Technol.* **2015**, *49*, 3024–3031.

(21) Zhao, L.; Zhang, B.; Xiao, X.; Gu, F. L.; Zhang, R.-Q. *J. Mol. Catal. A Chem.* **2016**, *420*, 82–87.

(22) Yuan, B.; Chong, R.; Zhang, B.; Li, J.; Liu, Y.; Li, C. *Chem. Commun.* **2014**, *50*, 15593–15596.

(23) Zhang, B.; Li, J.; Zhang, B.; Chong, R.; Li, R.; Yuan, B.; Lu, S.-M.; Li, C. *J. Catal.* **2015**, *332*, 95–100.

(24) Ahmed, A. Y.; Kandiel, T. A.; Ivanova, I.; Bahnemann, D. *Appl. Surf. Sci.* **2014**, *319*, 44–49.

(25) Wang, F.; Jiang, Y.; Gautam, A.; Li, Y.; Amal, R. *ACS Catal.* **2014**, *4*, 1451–1457.

(26) Zhao, L.-M.; Meng, Q.-Y.; Fan, X.-B.; Ye, C.; Li, X.-B.; Chen, B.; Ramamurthy, V.; Tung, C.-H.; Wu, L.-Z. *Angew. Chem. Int. Ed.* **2017**, *56*, 3020–3024.

(27) Westheimer, F. H. *Chem. Rev.* **1961**, *61*, 265–273.

(28) Roecker, L.; Meyer, T. J. *J. Am. Chem. Soc.* **1987**, *109*, 746–754.

(29) Morimoto, Y.; Park, J.; Suenobu, T.; Lee, Y.-M.; Nam, W.; Fukuzumi, S. *Inorg. Chem.* **2012**, *51*, 10025–10036.

(30) Li, H.; Liu, R.; Lian, S.; Liu, Y.; Huang, H.; Kang, Z. *Nanoscale* **2013**, *5*, 3289–3297.

(31) Zhang, J.; Chen, X.; Takanabe, K.; Maeda, K.; Domen, K.; Epping, J. D.; Fu, X.; Antonietti, M.; Wang, X. *Angew. Chem. Int. Ed.* **2010**, *49*, 441–444.

(32) Megerle, U.; Wenninger, M.; Kutta, R.-J.; Lechner, R.; König, B.; Dick, B.; Riedle, E. *Phys. Chem. Chem. Phys.* **2011**, *13*, 8869–8880.

(33) Kasap, H.; Godin, R.; Jeay-Bizot, C.; Achilleos, D. S.; Fang, X.; Durrant, J. R.; Reisner, E. *ACS Catal.* **2018**, *8*, 6914–6926.

(34) Barroso, M.; Mesa, C. A.; Pendlebury, S. R.; Cowan, A. J.; Hisatomi, T.; Sivula, K.; Gratzel, M.; Klug, D. R.; Durrant, J. R. *Proc. Natl. Acad. Sci. U.S.A.* **2012**, *109*, 15640–15645.

(35) Cowan, A. J.; Tang, J.; Leng, W.; Durrant, J. R.; Klug, D. R. *J. Phys. Chem. C* **2010**, *114*, 4208–4214.

(36) Kuriki, R.; Matsunaga, H.; Nakashima, T.; Wada, K.; Yamakata, A.; Ishitani, O.; Maeda, K. *J. Am. Chem. Soc.* **2016**, *138*, 5159–5170.

(37) Gross, M. A.; Reynal, A.; Durrant, J. R.; Reisner, E. *J. Am. Chem. Soc.* **2014**, *136*, 356–366.

(38) Xiao-e, L.; Green, A. N. M.; Haque, S. A.; Mills, A.; Durrant, J. R. *J. Photochem. Photobiol. A* **2004**, *162*, 253–259.

(39) Waidmann, C. R.; Miller, A. J. M.; Ng, C.-W. A.; Scheuermann, M. L.; Porter, T. R.; Tronic, T. A.; Mayer, J. M. *Energy Environ. Sci.* **2012**, *5*, 7771–7780.

Chapter 5

Interfacial engineering of a carbon nitride−graphene oxide−molecular Ni catalyst hybrid for enhanced photocatalytic activity

The data presented in this chapter was published in a peer-reviewed article: ACS Catal. 2018, 8, 6914–6926. The author of this thesis carried all of the work presented unless specified otherwise. Time resolved spectroscopy measurements were carried out and analysed by Dr. Robert Godin and Chiara Jeay-Bizot. TEM images were recorded by Dr. Heather F. Greer.

5.1 Introduction

Solar-driven water splitting with semiconductor particles is a promising strategy to produce clean and renewable fuels.[1] Traditionally used light harvesters, TiO_2 and ZnO, usually suffer from large band gaps (3.2–3.4 eV),[2,3] requiring dye sensitisation to utilise visible light.[4–6] Semiconductors such as CdSe, CdS and ZnSe have narrower band gaps and can partially absorb visible light, but they are toxic and suffer from photo-corrosion, which limits their practical applications.[7–10] High performance photocatalytic systems based on efficient, economic, and benign photo-absorbers are therefore much needed to accelerate the translation from prototype to products.

Polymeric CN_x has gained increasing popularity as an ideal alternative to traditional photocatalysts. CN_x has a composition based upon "earth-abundant" elements and has suitable band positions straddling the redox potentials of water splitting, and is highly stable under irradiation.[11–14] CN_x materials have been demonstrated to promote solar driven organic substrate oxidation,[15] pollutant degradation,[16,17] H_2 production,[18–20] and water splitting.[14,21,22] Yet its photocatalytic performance is typically limited by the fast recombination of photogenerated hole−electron pairs. To overcome this limitation many strategies have been proposed such as non-metal doping,[23–25] noble metal doping,[26–28] and nanoengineering of CN_x.[29,30] An alternative strategy is to design a system in which photogenerated holes or electrons are consumed faster than charge recombination reactions by accelerating charge transfer to the catalytic sites.

In Chapter 3 and 4, we developed a **$^{NCN}CN_x$−NiP** photocatalytic system to simultaneously produce aldehyde and hydrogen from alcohol oxidation and proton reduction, respectively.[31] This closed photocatalytic redox system showed enhanced photoactivity compared to unfunctionalised (amino-terminated) carbon nitride, **$^{H_2N}CN_x$**, due to the superior hole transfer ability of **$^{NCN}CN_x$** to 4-MBA. However, transient spectroscopy analysis revealed that the rate-limiting step of this photocatalytic systems lies in the electron transfer from the excited **$^{NCN}CN_x$** to **NiP** molecules.[31]

Interfacial engineering of semiconductors with charge separation layers can increase the lifetime of charge carriers and improve photocatalytic activity.[32] Graphene is well known for its high specific surface area (~2,600 $m^2\,g^{-1}$), high electron mobility (~200,000 $cm^2\,V^{-1}\,s^{-1}$), and good chemical and electrochemical stability.[32–36] Graphene oxide (GO) is usually synthesised through a chemical oxidation method using low-cost graphite as the precursor.[37–39] In order to balance the conductivity and hydrophilicity of GO, it is typical to convert it into reduced graphene oxide (RGO).[40,41] Graphene materials have been widely used as mediators to facilitate interfacial electron transfer in various systems including H_2 production,[42–44] CO_2 reduction,[45–48] water splitting,[40,49–52] selective organic transformations,[53–56] and pollutant degradation.[57–60] This behaviour was attributed to the superior electron accepting and transferring capabilities of the GO derivatives, resulting in reduced charge recombination reactions and prolonged lifetimes for the photogenerated charge carriers in the semiconductors.[32,35,61] GO derivatives have also been used as efficient
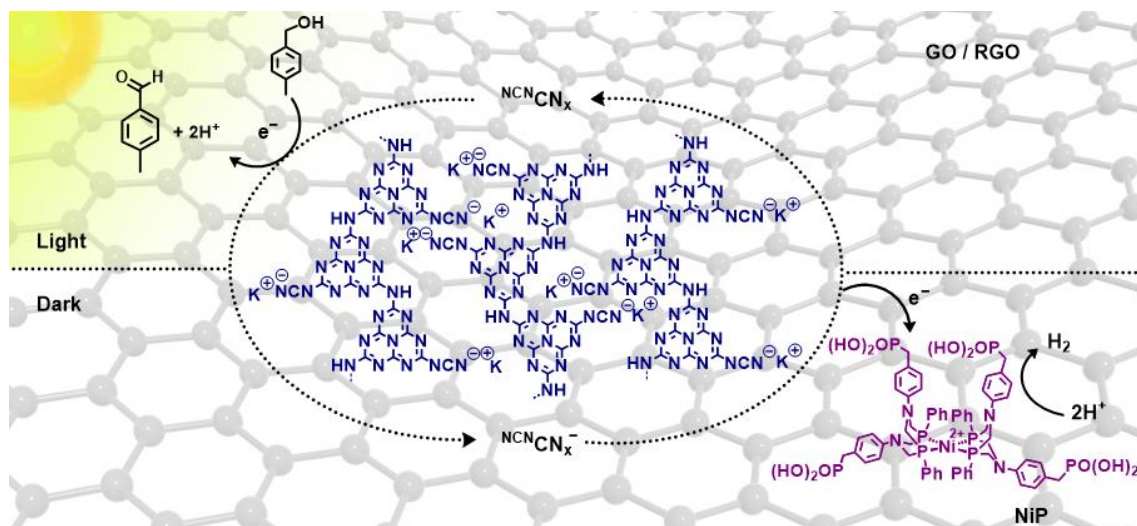
Figure 5.1. Schematic representation of the photocatalytic $^{NCN}CN_x-GO-NiP$ system. Irradiation of $^{NCN}CN_x$ results in the formation of photoexcited state, which is quenched by 4-MBA and results in the formation of trapped electrons in $^{NCN}CN_x$. These 'ultra-long lived' electrons can then be transferred to **NiP** for proton reduction in the dark phase. The electronic communication between $^{NCN}CN_x$ and **NiP** is enhanced by GO/RGO.

hole−extraction layers,[62–65] as well as an electron−extraction layers in heterojunction solar cells, due to their tuneable work function as well as thin film formation ability.[66–68]

In this chapter, we introduce GO and RGO to interface with $^{NCN}CN_x$ and **NiP** to facilitate electron transfer and to enhance the photocatalytic activity.[31] We shed light on the improved performance of the $^{NCN}CN_x-NiP$ photo-redox system in the presence of GO and RGO (Figure 5.1). The charge transfer between $^{NCN}CN_x$, GO/RGO and **NiP** are investigated. The $^{NCN}CN_x-GO-NiP$ and $^{NCN}CN_x-RGO-NiP$ hybrid systems are studied using optical spectroscopy techniques, namely time-resolved photoluminescence (tr-PL), TAS and photoinduced absorption spectroscopy (PIAS), to understand the key kinetics and photophysical properties leading to improved photocatalytic performance.

5.2 Results and discussion

5.2.1 Preparation and characterisation of $^{NCN}CN_x$ hybrids

$^{NCN}CN_x-GO/RGO$ hybrids were prepared by mixing $^{NCN}CN_x$ (5 mg) and GO/RGO in aqueous solution (0.2 mg mL^{-1}) for 16 h prior to experiments. $^{NCN}CN_x-GO_x/RGO_x$ of different compositions were prepared [x denotes the content of GO and RGO in weight percentages loading in reference to $^{NCN}CN_x$; which ranges between 0.063 wt% (3.1 µg) and 50.00 wt% (2.5 mg)]. The samples were allowed to dry under air, prior to characterisation by FT-IR spectroscopy, and the data of the hybrid were compared to bare $^{NCN}CN_x$ and GO (Figure 5.2). The FT-IR spectrum of bare $^{NCN}CN_x$ showed the characteristic heptazine core IR vibration at 803 cm^{-1} and bridging secondary amine –C–N bending vibrations at 1307 and 1211 cm^{-1}, supporting the polymeric nature of the material. The appearance of the (C≡N) stretch at 2181 cm^{-1} confirmed the presence of cyanamide groups on the surface of the material. The spectra recorded in the presence of either GO or RGO showed negligible differences compared to the spectrum of bare $^{NCN}CN_x$ (Figure 5.2a).[20,69]

The XRD pattern of the $^{NCN}CN_x-GO$ hybrid showed the characteristic bands observed for pure $^{NCN}CN_x$, indicating that the crystalline structure of the material is preserved after the physical mixing with GO (Figure 5.2b).[20,69] More specifically, the hybrid showed the characteristic $^{NCN}CN_x$ peak at 28.2º 2θ, which corresponds to an interlayer spacing of 3.16 Å (002). In addition, the hybrid preserved the same (100) in-plane periodicity with pure $^{NCN}CN_x$, as indicated by two bands at 9.83º 2θ (9.00 Å) and 8.04º 2θ (11.00 Å). The characteristic GO band at 10.9º 2θ (8.12 Å), due to (001) interlayer spacing, is less prominent in the XRD pattern of the hybrid due its low content.[20,70]

The UV–vis absorption profile of the $^{NCN}CN_x-GO$ hybrid resembled the characteristic features of bare $^{NCN}CN_x$, $\lambda_{abs} < 450$ nm, (Figure 5.2c). Photoluminescence (PL) studies were carried out to investigate changes in the charge separation efficiency of $^{NCN}CN_x$ in the presence GO and RGO (Figure 5.2d). In contrast to the literature reports,[34,35] we observed that introducing GO/RGO does not quench the emissive states in $^{NCN}CN_x$. This observation indicates that GO/RGO does not affect the rate of charge recombination under visible light irradiation, in timescales less than
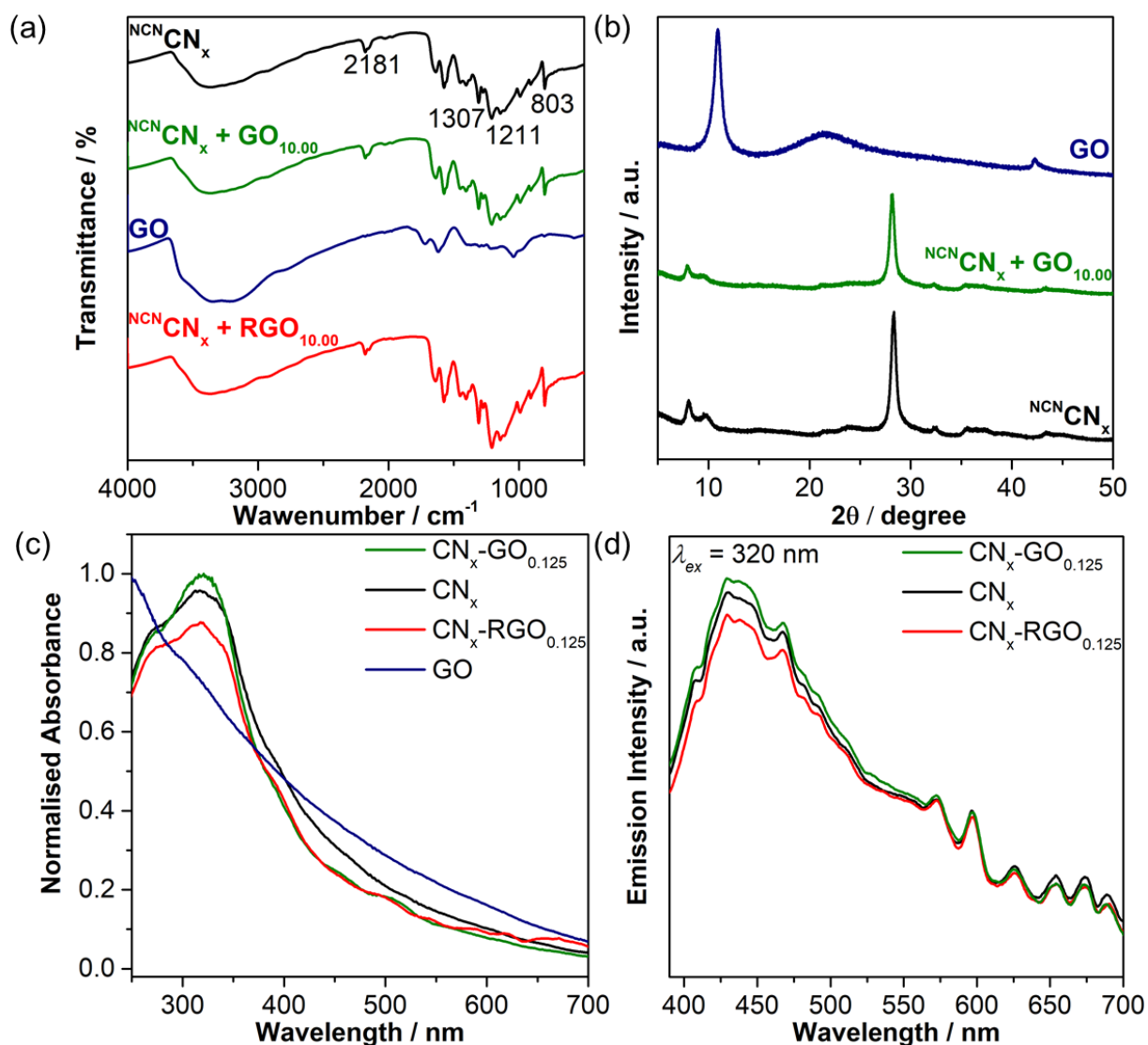
Figure 5.2. (a) ATR-FT-IR spectra, (b) XRD patterns of bare $^{NCN}CN_x$ and GO and that of $^{NCN}CN_x-GO$ and $^{NCN}CN_x-RGO$ hybrids at 10.0 wt% GO/RGO loading. Characterisations were also performed at 0.125 wt%, but this loading was too low to observe any significant differences. Therefore, only data with 10 wt% loading is presented. (c) UV–vis absorption profile of $^{NCN}CN_x$ (0.5 mg), GO, $^{NCN}CN_x-GO$ and $^{NCN}CN_x-RGO$ hybrid in the presence of 0.125 wt% loading in an aqueous KP_i solution (0.1 M, pH 4.5, 3 mL) recorded at 25 °C. (b) Photoluminescence measurements of $^{NCN}CN_x$ (0.5 mg), $^{NCN}CN_x-GO$ and $^{NCN}CN_x-RGO$ hybrids at 0.125 wt% loading, recorded in an aqueous KP_i solution (0.1 M, pH 4.5, 3 mL) with λ_{ex} = 320 nm.

0.1 s (see below for more details).[43,70] Transmission electron microscopy (TEM) images of **NCNCNx−GO** hybrids at different GO loadings showed that GO sheets act as a scaffold to host the approximately 50 nm sized **NCNCNx** particles (Figure C.1).

5.2.2   Photocatalytic assembly and performance

NiP was synthesised and characterised as previously described.[71] **H2NCNx** and **NCNCNx** were prepared by a slight modification to a published procedure, in which **H2NCNx** polymerisation from melamine was carried out at 550 °C for 4 h under air.[19–21] **NCNCNx** (5 mg) was added to an aqueous suspension of GO/RGO (0.2 mg mL^{-1}) in a photoreactor and stirred for 16 h prior to the experiments. This was followed by the addition of an aqueous solution of **NiP** and EDTA or KP_i with 4-MBA (30 µmol). The final suspension contained 3 mL of EDTA (0.1 M, pH 4.5) or KP_i (0.1 M, pH 4.5). The photoreactors were sealed, purged with N_2 (containing 2% CH_4 as internal gas GC standard) and irradiated at 25 °C using a solar light simulator equipped with an AM 1.5G filter, at 1 sun intensity (100 mW cm^{-2}). The headspace H_2 gas was quantified periodically by GC, while oxidation products of 4-MBA were characterised in solution by ^{1}H NMR spectroscopy.

The parameters of the system (solvent, amount of GO, size of GO, amount of **NCNCNx**) were systematically varied and optimised for H_2 production per catalyst, expressed as **NiP** turnover frequency (TOF$_{NiP}$, mol H_2 (mol NiP)$^{-1}$ h^{-1}) and turnover number (TON$_{NiP}$, mol H_2 (mol NiP)$^{-1}$) determined after 1 h and 4 h of irradiation respectively, as well as the conversion yield of alcohol after 4 h (Tables C.1–C.6).

The initial experiments were performed using EDTA (0.1 M) as a sacrificial electron donor (Figure 5.3a). Simulated solar light irradiation resulted in linear H_2 production during the first 4 h and a significant enhancement in photocatalytic activity was detected particularly in the presence of low GO loadings, < 0.50 wt% (25 µg), (Figure C.2a). In the absence of GO, a TOF$_{NiP}$ of 38 ± 1 h^{-1} was achieved, whereas the presence of GO$_{0.125}$ resulted in TOF$_{NiP}$ of 116 ± 3 h^{-1}. After 4 h of irradiation, three times higher H_2 production activity (17 ± 1 µmol, and TON$_{NiP}$, 348 ± 11) was recorded with GO$_{0.125}$ compared to that of bare **NCNCNx**. **NCNCNx−RGO$_{0.125}$** displayed a comparable catalytic activity (TOF$_{NiP}$ of 102 ± 1 h^{-1} and TON$_{NiP}$ of 322 ± 6), potentially indicating *in situ* photoreduction of GO.[40]

It was previously reported that GO can itself act as a p- or n-type semiconductor, depending on the degree of its surface oxidation,[72] as well as a photocatalyst for H_2 production.[73,74] Control experiments in the absence of $^{NCN}CN_x$ with GO/RGO−**NiP** only under simulated solar light and blue filtered (λ > 495 nm) irradiation did not generate H_2, ruling out these possibilities (Table C.1). Increasing GO loadings above 0.50 wt% (25 µg) caused a substantial decrease in the activity (Figure C.2a). This observation may be due to increased light scattering by GO, reducing the amount of light that can be absorbed by $^{NCN}CN_x$.[43]

The enhanced photocatalytic performance of $^{NCN}CN_x$ in the presence of GO/RGO encouraged us to replace excess EDTA by a closed redox system with stoichiometric and selective alcohol oxidation coupled to proton reduction (Figure 5.3b and C.2b). In the presence of 4-MBA (30 µmol) with $^{NCN}CN_x$ and $GO_{0.125}$, a specific activity of 1,159 ± 29 µmol H_2 (g $^{NCN}CN_x)^{-1}$ h^{-1} towards H_2 and aldehyde production, TOF_{NiP} of 116 ± 3 h^{-1} and TON_{NiP} of 367 ± 20 were achieved, whereas bare $^{NCN}CN_x$ showed a lower specific activity of 676 ± 27 µmol H_2 (g $^{NCN}CN_x)^{-1}$ h^{-1}, TOF_{NiP} of 68 ± 3 h^{-1} and TON_{NiP} of 237 ± 20. Consistent with results recorded in EDTA solution, replacing $GO_{0.125}$ by $RGO_{0.125}$ in the presence of 4-MBA yielded similar activity with respect to the photocatalyst at 1,216 ± 55 µmol H_2 (g $^{NCN}CN_x)^{-1}$ h^{-1} and to the catalyst with a TOF_{NiP} of 122 ± 5 h^{-1}.

The reaction rate for alcohol oxidation almost doubled in the presence of GO or RGO, reaching 17 µmol of selective 4-MBAd formation with a conversion yield of 57%. Bare $^{NCN}CN_x$ produced 10 µmol 4-MBAd under the same conditions, corresponding to a 32% conversion. After 4 h of irradiation in the presence of GO/RGO approximately 18 µmol of H_2 and aldehyde were formed, corresponding to a 50% enhancement in photocatalytic activity in comparison to bare $^{NCN}CN_x$.

Control experiments with $^{NCN}CN_x$−**GO**−**NiP** in the absence of $^{NCN}CN_x$ or **NiP** with 4-MBA in KP_i buffer did not generate H_2 (Figure 5.3b). Aldehyde (4-MBAd) was also produced in the latter experiment due to 'solar charging' of the $^{NCN}CN_x$ in the absence of catalyst (Table C.7 and discussion below).[31]
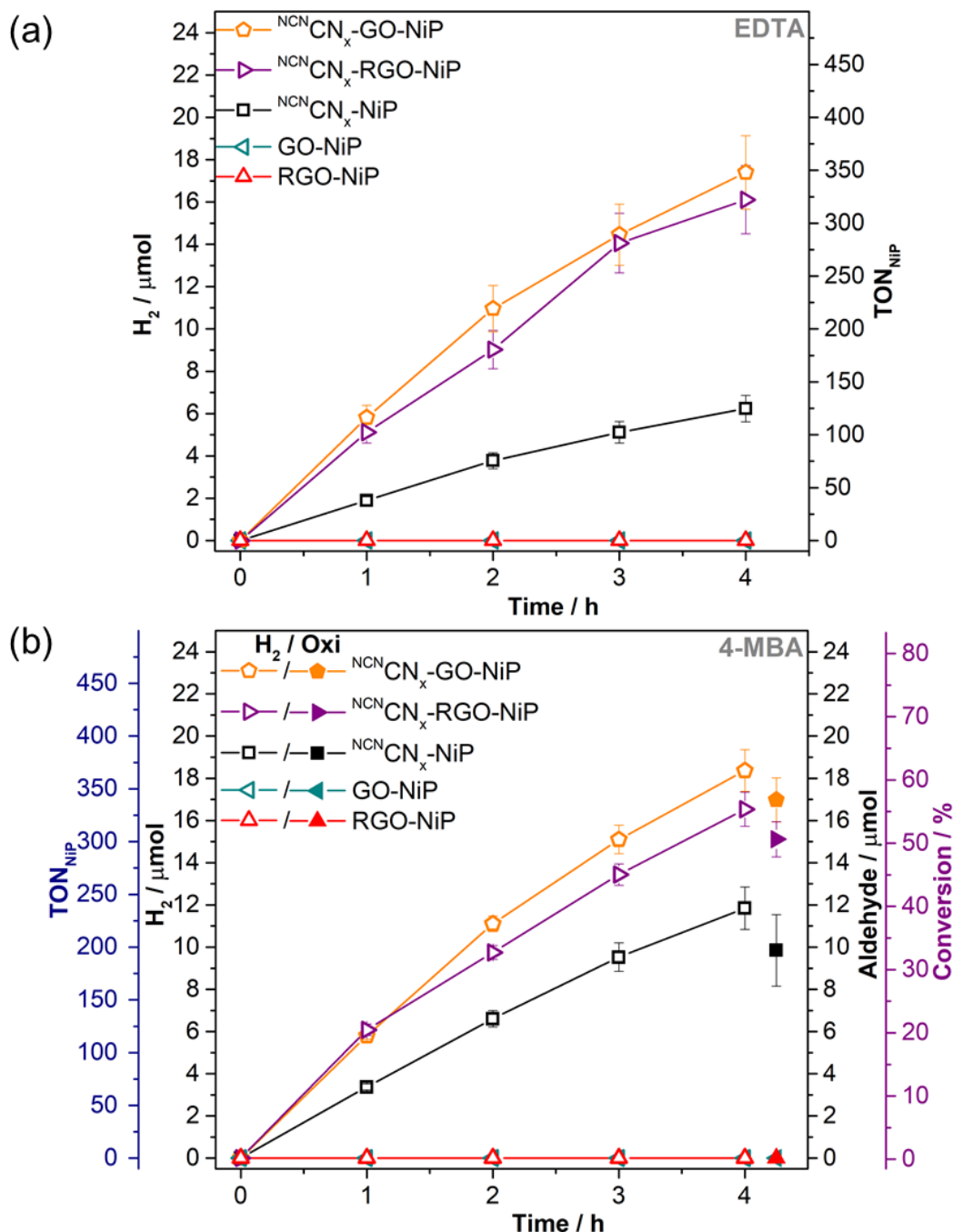
Figure 5.3. Photocatalytic H_2 production under simulated solar light irradiation (100 mW cm^{-2}, AM 1.5G, 25 °C) with 5 mg of $^{NCN}CN_x$, $^{NCN}CN_x-GO$ and $^{NCN}CN_x-RGO$ (0.125 wt% loading of GO or RGO, 6.3 µg) in the presence of **NiP** (50 nmol) in (a) aqueous EDTA solution (0.1 M, pH 4.5, 3 mL), and (b) in aqueous KP$_i$ solution (0.1 M, pH 4.5, 3 mL) containing 4-MBA (30 µmol) under N_2. The pair of hollow and filled symbols of the same shape and colour corresponds to H_2 and aldehyde production, respectively. The amount of aldehyde was quantified after 4 h of irradiation. Control experiments in the absence of $^{NCN}CN_x$ and in the presence of RGO are also presented.

The catalytic turnover rates and numbers of **NiP** are in broad agreement with previously reported H_2 production systems using colloidal light absorbers under sacrificial conditions. Solar light driven H_2 generation with **NiP** was first reported in the presence of phosphonated ruthenium tris(2,2'-bipyridine) (**RuP**) dye sensitised TiO_2 in AA (pH 4.5), which showed a TOF_{NiP} of 72 ± 5 h^{-1}.[71] A hybrid system containing **$^{H_2N}CN_x$** and **NiP** in EDTA (pH 4.5) reported a TOF_{NiP} of 109 ± 11 h^{-1}.[19] Sacrificial photo-H_2 generation was also demonstrated using an amorphous and N-doped carbon-dots as light harvester with **NiP** in EDTA (pH 6), reaching TOF_{NiP} of 41 h^{-1} and TOF_{NiP} of 143 h^{-1} respectively.[75,76]

Tuning the amount of **$^{NCN}CN_x$** at high GO loadings resulted in excellent specific activity (Figure C.3). The highest specific activity of $4,655 \pm 448$ µmol H_2 (g $^{NCN}CN_x)^{-1}$ h^{-1} was achieved with 0.5 mg of **$^{NCN}CN_x$** in the presence of 50 wt% GO loading (0.25 mg) and 50 nmol **NiP**. The H_2 production rate is amongst the highest reported in the literature with respect to the mass of carbon nitride and the highest for selective organic oxidation coupled to fuel generation.[77–81] Previously reported semiconductor-graphene heterojunction systems have been studied with a sacrificial electron donor and noble metal proton reduction catalysts.[82] For CN_x systems, only an eosin Y sensitised CN_x-GO composite with a Pt catalyst in a sacrificial donor TEOA solution shows comparable activity to the system developed in this work (3,820 µmol H_2 (g $CN_x)^{-1}$ h^{-1}).[83] The high activity of our **$^{NCN}CN_x-GO-NiP$** hybrid is even comparable to a toxic CdS/graphene composite with Pt, which reaches up to 6,000 µmol H_2 (g CdS)$^{-1}$ h^{-1}.[84,85] **$^{NCN}CN_x-GO-NiP$** therefore demonstrates benchmark photoactivity for a precious metal free, single photo-absorber system. In addition, the system does not rely on excess sacrificial electron donors and converts organic substrates cleanly into value-added products in high yield.

Different sizes of GO sheets, $< 1-5$ µm, were also studied to improve the understanding of the interaction between **$^{NCN}CN_x$** and GO, but only marginal variations in photocatalytic performance were observed (Table C.4).

The photocatalytic behaviour of amine terminated **$^{H_2N}CN_x$** was also studied in EDTA and KP_i containing 4-MBA (Table C.5 and C.6). As for **$^{NCN}CN_x$**, introduction of GO and RGO enhanced the photocatalytic activity by at least 50%, demonstrating the more general ability of GO and RGO to improve the performance for carbon nitride photocatalysts.

5.2.3   Light and dark cycles of $^{NCN}CN_x$

We have previously established that light exposure of a yellow suspension of $^{NCN}CN_x$ in the presence of an organic substrate results in the formation of blue $^{NCN}CN_x$ (Chapter 4).[31] This blue state is associated with ultra-long lived "trapped electrons" accumulated in $^{NCN}CN_x$ with lifetimes on the order of hours. Addition of a catalyst such as **NiP** can release these low potential electrons in the dark phase to produce H_2. This unique behaviour therefore allows decoupling of oxidative and reductive half-reactions temporarily, making it possible to generate a solar fuel in the dark.[31,86] Thus, the electron storage capacity of $^{NCN}CN_x$−**GO** (5 mg) hybrid suspensions in an aqueous KP_i solution with 4-MBA (30 µmol) without **NiP** was studied. The anaerobic suspensions were irradiated for 30 min, 2 and 4 h and then moved into the dark (Figure 5.4). The H_2 evolution performance was monitored after injecting **NiP** (50 nmol in KP_i solution) to the pre-irradiated, blue suspensions using an airtight syringe (Table C.7).

Independently of the length of charging interval, discharging rates of approximately 0.40 mmol e^- (g $^{NCN}CN_x$)$^{-1}$ h^{-1} were observed, based on 1 µmol of H_2 being produced from 2 µmol of radicals, per 5 mg of $^{NCN}CN_x$ after one hour of **NiP** injection in the dark. Short-term irradiation resulted in a rapid discharge upon injection of **NiP**, whereas 4 h light-exposure required a longer time to consume the larger number of trapped electrons. The total amount of trapped electrons and the corresponding dark H_2 evolution saturated after 4 h irradiation, while irradiating the samples for 12 h did not increase the number of accumulated charges.

The amount of H_2 detected provides an indirect measure on the total number of heptazine based radicals generated during irradiation of the material (Table C.8).[86] After 30 min of irradiation, 0.8 ± 0.1 µmol of H_2 was generated with bare $^{NCN}CN_x$, whereas $^{NCN}CN_x$−**GO** or $^{NCN}CN_x$−**RGO** hybrids produced 1.1 ± 0.1 and 0.9 ± 0.1 µmol, respectively (Figure 5.4a). Assuming that the trapped electrons are quantitatively converted into H_2, we can estimate that 2.1 ± 0.2 and 1.9 ± 0.2 µmol of radicals are accumulated in the $^{NCN}CN_x$−**GO** and $^{NCN}CN_x$−**RGO** hybrids, respectively (1.6 ± 0.1 µmol for bare $^{NCN}CN_x$). This corresponds to approximately a 1:10 ratio of radical to heptazine units in $^{NCN}CN_x$.
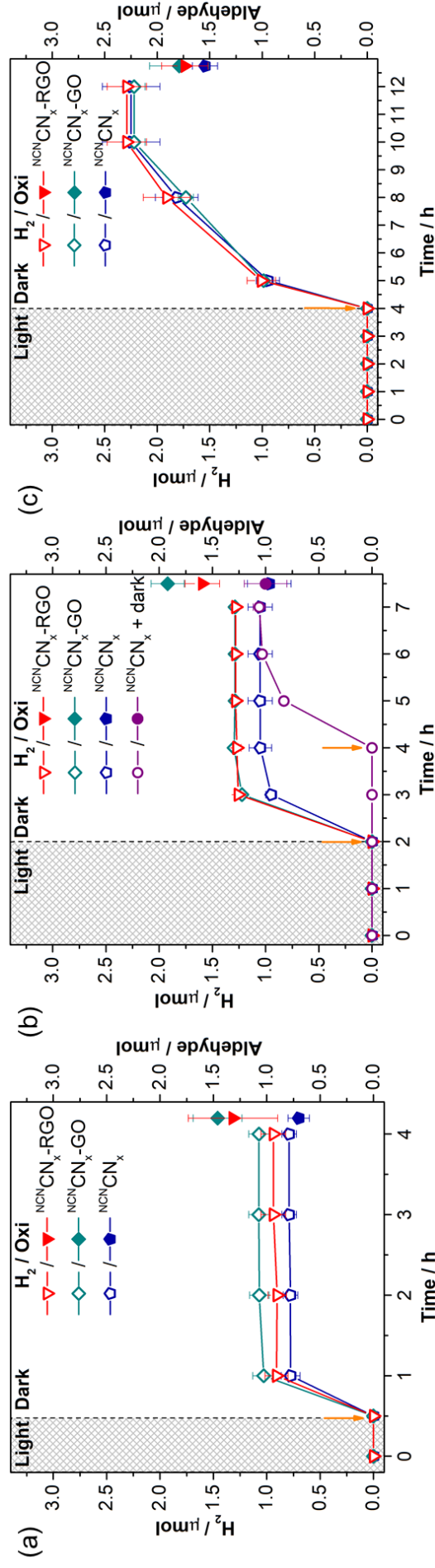
Figure 5.4. Photocatalytic suspensions were prepared with 5 mg of $^{NCN}\text{CN}_x$, $^{NCN}\text{CN}_x$–GO and $^{NCN}\text{CN}_x$–RGO (0.125 wt% loading of GO or RGO, 6.3 μg) in aqueous KP_i solution (0.1 M, pH 4.5, 3 mL) containing 4-MBA (30 μmol) without **NiP** under N_2. The samples were irradiated for (a) 30 min, (b) 2 h and (c) 4 h under 1 sun simulated solar light irradiation (100 mW cm^{-2}, AM 1.5G) at 25 °C. The suspensions were then moved into the dark and an anaerobic **NiP** solution (50 nmol in KP_i solution) was injected. The pair of hollow and filled symbols of the same shape and colour corresponds to H_2 and 4-MBAd production, respectively. The amount of aldehyde formed is detected after 4 h, 7 h and 12 h in (a), (b) and (c), respectively. The orange arrows indicate the point of **NiP** injection; a control experiment with the vial kept in dark for 2 h before injection of **NiP** is shown in (b).

After 4 h of irradiation a saturation concentration of trapped electrons was reached and approximately 2.25 µmol H_2 was detected, which corresponds to 4.50 ± 0.37 µmol of radicals (Figure 5.4c) or roughly a 1:5 ratio of radicals to heptazine units.

5.2.4   Time resolved spectroscopy

Previously reported TAS measurements indicated that 4-MBA quenches the photogenerated holes on $^{NCN}CN_x$ on timescale faster than 3 µs, while the extraction of the photoexcited electrons by **NiP** takes longer than 2 s (Chapter 4).[31] In agreement with the mechanistic studies, the photo-system was determined to be limited by hole transfer to 4-MBA and the accumulation of the low potential electrons in the $^{NCN}CN_x$ on the short timescale (< 3 µs), whereas on the longer timescale (> 1 s) it is limited by the rate of electron extraction from 'electron-saturated' $^{NCN}CN_x$ (Figure 5.1). Acceleration of the rate of electron extraction from $^{NCN}CN_x$ would decrease the steady-state concentration of trapped electrons in $^{NCN}CN_x$ and reduce charge recombination losses. In turn, this will allow an overall higher conversion of 4-MBA and higher yield of electron transfer to **NiP**. We investigate here whether this is the case when the graphene based conductive scaffolds GO and RGO are introduced in the photocatalytic system.[87]

We studied the improved photocatalytic activity of $^{NCN}CN_x$ in the presence of GO and RGO first using tr-PL, namely the time correlated single photon counting (TCSPC) to record the fast PL decay process. For the TCSPC experiments, samples were excited at λ_{ex} = 404 nm and decay of the emissive states were monitored at λ_{em} = 490 nm under Ar atmosphere. Both bare $^{NCN}CN_x$ and $^{NCN}CN_x$−GO/RGO hybrids showed similar decay profiles in the absence and presence of 4-MBA (Figure 5.5 and C.4). These results indicate that the interface between $^{NCN}CN_x$ and GO/RGO does not improve the charge separation of the monitored emissive states on the nanosecond timescale. This is a surprising observation in comparison to previously reported semiconductor-graphene hybrid/composite systems, where quenching of PL is a characteristic behaviour, due to faster charge separation of the emissive excitonic states.[34,35]
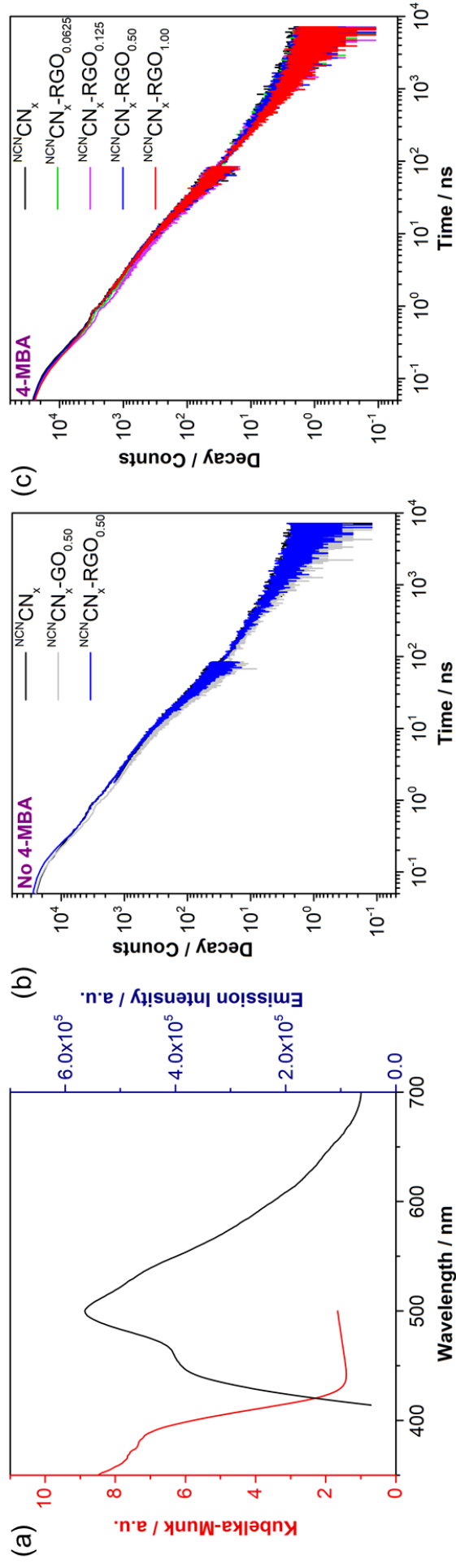
.

Figure 5.5. (a) Absorption spectra (red) and emission spectra (black) of $^{NCN}CN_x$ at the concentration of 1.67 mg mL^{-1} dispersed in KP$_i$ solution (0.1 M, pH 4.5) with λ_{ex} = 404 nm, under Ar atmosphere. (b) tr-PL of $^{NCN}CN_x$ at the concentration of 1.67 mg mL^{-1} dispersed in KP$_i$ solution (0.1 M, pH 4.5) with GO and RGO loadings in the absence and (c) presence of 4-MBA (0.01 M), under Ar atmosphere, with λ_{ex} = 404 nm and λ_{em} = 490 nm at 25 °C.
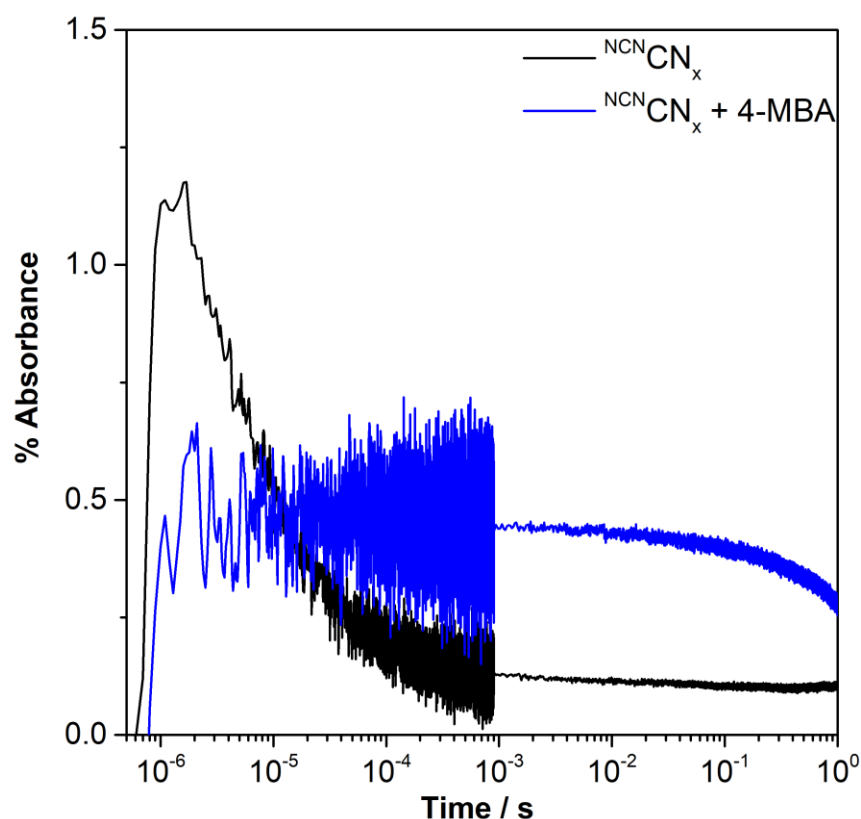
Figure 5.6. Typical µs-TAS decay kinetics of $^{NCN}CN_x$ at the concentration of 1.67 mg mL^{-1} dispersed in KP$_i$ solution (0.1 M, pH 4.5) with and without 4-MBA (0.01 M) under Ar atmosphere monitored at λ = 610 nm under λ = 355 nm pulsed excitation at 25 °C.

TAS were subsequently performed to follow the charge transfer reactions in $^{NCN}CN_x$ and GO/RGO hybrids on microsecond–second timescales. In contrast to tr-PL, TAS measurements monitor both emissive and non-emissive states generated in the material after photoexcitation. Photoexcitation (λ_{ex} = 355 nm) of $^{NCN}CN_x$ produced a broad photoinduced absorption signal in the 470–1000 nm range (Figure C.5a). Similar to behaviour observed in metal oxides, the decay of the signal in $^{NCN}CN_x$ follows a power law and is attributed to bimolecular electron-hole recombination (Figure C.5b). The exponent of the power law is smaller than unity (~0.43), suggesting that a trapping/detrapping process plays a significant role in excited state dynamics of $^{NCN}CN_x$, consistent with relatively slow time scale for the recombination process.[88,89]

Typical µs-TAS decays for $^{NCN}CN_x$ suspension with and without 4-MBA under Ar were also recorded (Figure 5.6) at λ_{ex} = 355 nm pulsed laser excitation with monitoring at 610 nm. In the absence of 4-MBA a decreasing decay is observed in the absorption profile until it remains nearly constant with a low amplitude at 1 ms after

96

the light impulse. In the presence of 4-MBA a constant absorbance is reached from 1 µs with no decay over time (note that data > 100 ms is affected by $^{NCN}CN_x$ settling, see below). In line with previous observations in Chapter 4, this persistent signal is assigned to long-lived trapped electrons in $^{NCN}CN_x$.[31,86]

To gain knowledge on how the interface between $^{NCN}CN_x$ and GO or RGO are affecting the photophysics of $^{NCN}CN_x$ on the microsecond–second timescale, TAS decays were recorded both in the absence and presence of 4-MBA with bare $^{NCN}CN_x$ and hybrid systems containing various GO/RGO loadings (Figure 5.7). The results show that charge recombination took place faster than 1 ms in the absence of 4-MBA, with similar decay profiles with or without GO/RGO (Figure 5.7a). In the presence of 4-MBA (Figure 5.7b), a constant absorbance is reached within the time resolution of the setup and indicated that the photogenerated holes are quenched faster than 1 µs. In all the cases, the transient absorption traces recorded for bare $^{NCN}CN_x$ and GO or RGO hybrid systems showed no significant differences. In addition to the comparable signal amplitudes, we also note that the decay kinetics are unaffected by the presence of GO or RGO, inconsistent with charge separation across the CN_x/GO interface. The results support our interpretation of the PL and tr-PL data, ruling out the possibility of GO and RGO influencing the charge carrier dynamics of $^{NCN}CN_x$ by enhancing the separation of photogenerated charges on shorter than a second timescale.[43,90,91] In line with this observation, TAS experiments conducted for $^{H_2N}CN_x$ also showed no difference between bare $^{H_2N}CN_x$ and GO/RGO hybrids (Figure C.6). The slightly lower signal amplitude for bare $^{H_2N}CN_x$ in the absence of 4-MBA or **NiP** (Figure C.6a) is attributed to experimental fluctuations and is in line with the differences up to 20% observed in repeated measurements. Importantly, no changes in the decay kinetics were observed.

5.2.5 Decay kinetics of charged $^{NCN}CN_x$

We next sought to investigate the electron transfer taking place from $^{NCN}CN_x$ to **NiP**, which is a vital step for H_2 production. This electron transfer has been shown to take place on a timescale longer than few seconds (Chapter 4).[31] During the measurements, $^{NCN}CN_x$ particles were settling in the cuvette, eliminating the possibility to follow any process longer than 0.1 s and preventing an accurate measure of the electron transfer process. To overcome this settling issue of $^{NCN}CN_x$, the powder was
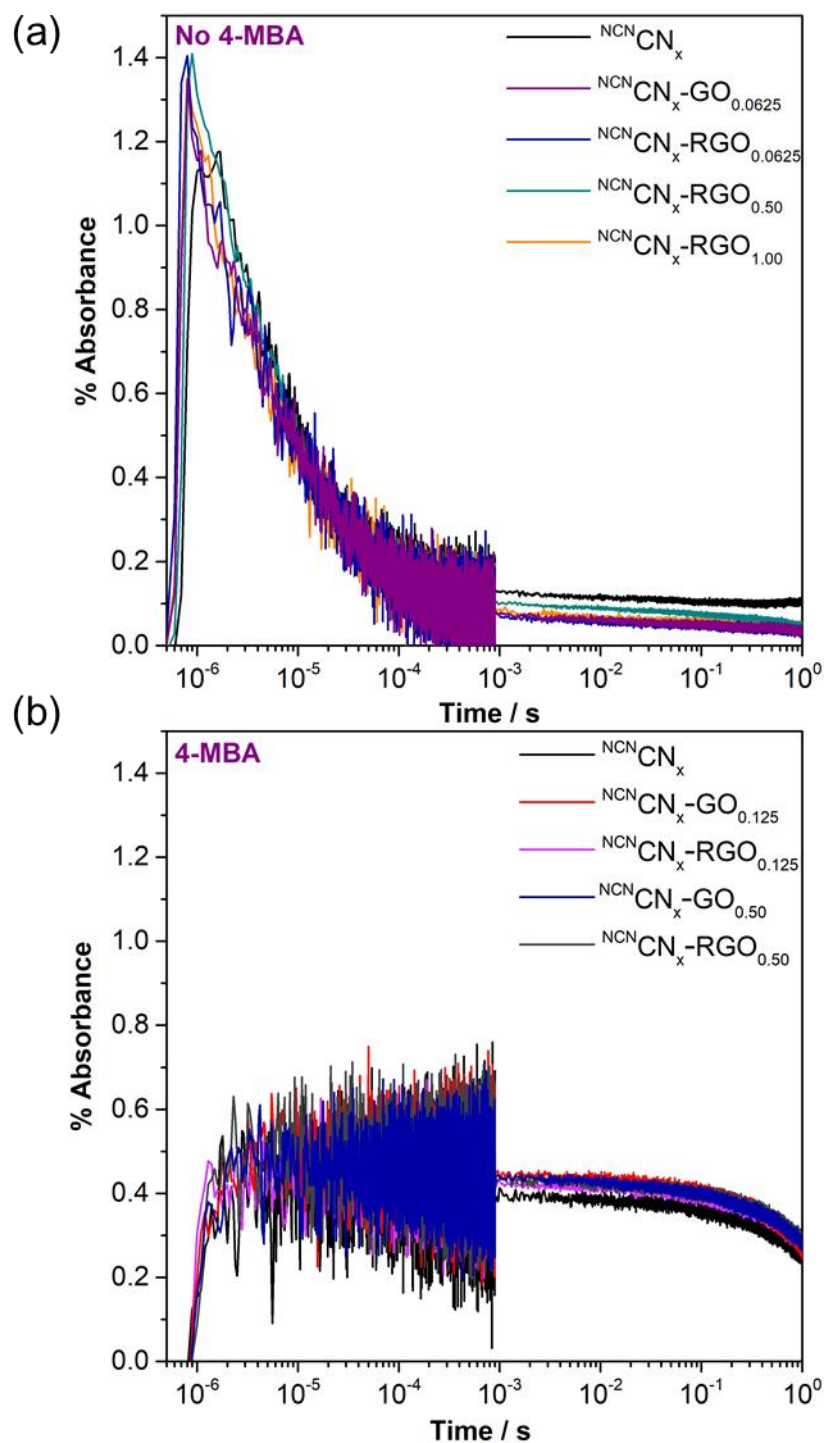
Figure 5.7. μs-TAS decay kinetics of (a) $^{NCN}CN_x$ at the concentration of 1.67 mg mL^{-1} dispersed in KP$_i$ solution (0.1 M, pH 4.5) with various GO and RGO loadings in the absence and (b) presence of 4-MBA (0.01 M), monitoring at λ = 610 nm under λ = 355 nm pulsed excitation.

suspended in a non-intrusive matrix of a sodium deoxycholate (NaDC) hydrogel.[92] This matrix prevented the fast settling of $^{NCN}CN_x$, and the µs-TAS decay kinetics of aqueous $^{NCN}CN_x$ or $^{H2N}CN_x$ suspensions and hydrogels were compared. The initial signal decay on the µs timescale was unchanged by the NaDC matrix (Figures C.7) indicating that the CN_x photophysics were not disrupted. The hydrogel matrix did successfully eliminate the artefacts caused by settling on timescales > 100 ms (Figure C.7), particularly evident in the case of $^{H2N}CN_x$.

PIAS of hydrogel samples were then used to record the long-lived excited states and to monitor the electron transfer kinetics from $^{NCN}CN_x$ on the second to minute timescale. The samples were irradiated with a UV LED (365 nm, 0.5 mW cm^{-2}) pulse for 2 s, as opposed to the nanosecond laser pulse used in TAS experiments. The change in absorbance was monitored at λ = 610 nm during the LED excitation and 58 s following excitation. Similarly as for the TAS experiments, the signal detected is due to absorption from the photogenerated electrons, and the amplitude depends on the quantum yield of photogenerated electron, the recombination lifetime and the intensity of the excitation in steady-state conditions.[93]

PIAS traces were recorded for bare $^{NCN}CN_x$ and hybrid systems with GO or RGO in the presence of different **NiP** concentrations (Figure C.8). Similar traces were recorded for the different samples in the absence of **NiP**, pointing to insignificant changes in the $^{NCN}CN_x$ photophysics when junctions with GO or RGO are introduced. In all cases, as the **NiP** concentration was increased, the absorbance signal was quenched faster, as expected, increasing the concentration of electron accepting molecules increases the rate of electron extraction. Interestingly, much faster absorption decays were observed by increasing the **NiP** concentration both in the presence of GO and RGO, as compared to bare $^{NCN}CN_x$. This trend was observed clearly when the normalised traces of $^{NCN}CN_x$ and GO/RGO hybrids at a single **NiP** concentration are plotted together (Figure 5.8a and Figure C.9). The data set of Figure 5.8a is also shown before normalisation for comparison (Figure C.10). The PIAS amplitude of all three types of samples after switching off the LED pulse for 10 s is also given (Figure 5.8b), again showing the stronger effect of the addition of **NiP** for the GO and RGO hybrids.
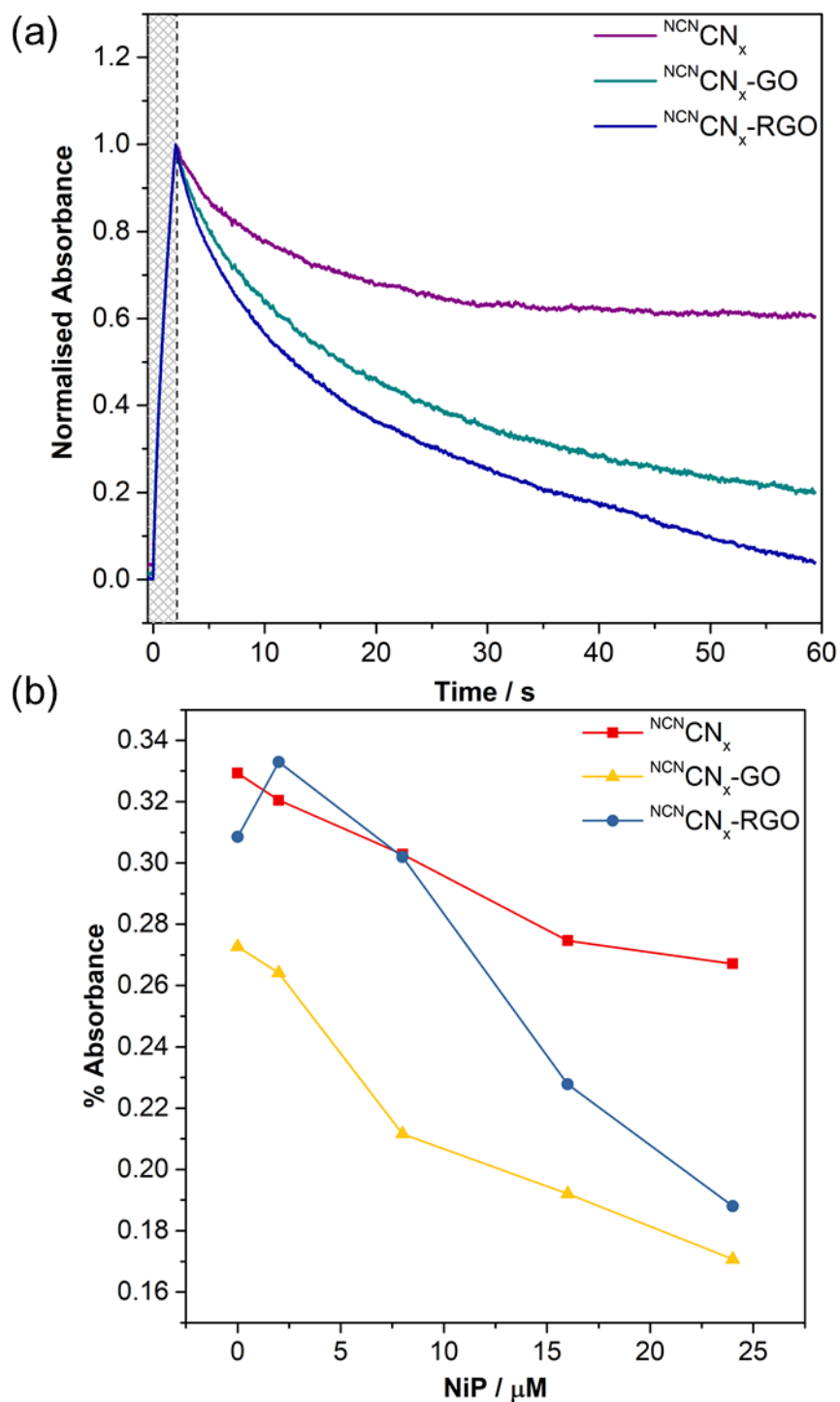
Figure 5.8. Comparison of PIAS of ^{NCN}CN$_x$, ^{NCN}CN$_x$−GO/RGO samples (0.125 wt% loading of GO or RGO, 6.3 µg) in NaDC (13.8 mg mL$^{−1}$) hydrogel monitored at $\lambda = 610$ nm with LED excitation at $\lambda = 365$ nm (0.5 mW cm$^{−2}$), in KP$_i$ solution (0.1 M, pH 4.5) with 4-MBA (0.01 M) under Ar (a) with **NiP** (24 µM) over 60 s and (b) at different **NiP** concentrations (10 seconds after switching off the light).

All of the PIAS data clearly showed that abstraction of the photoexcited electrons from $^{NCN}CN_x$ is faster in the presence of GO and RGO. This qualitatively demonstrated that the interface between $^{NCN}CN_x$ and GO or RGO enhanced the rate of electron extraction and delivery from $^{NCN}CN_x$ to **NiP** on the second timescale. A quantitative description of the kinetics is prevented by the settling nature of the heterogeneous system, which is unfortunately not completely removed when using 13.8 mg mL^{-1} NaDC to form the hydrogel matrix. We also note that addition of **NiP** and release of Ni^{2+} ions may impact the viscoelastic properties of the hydrogels,[94,95] although this does not affect the comparison of the decay kinetics of different samples at the same **NiP** concentration. Stiffer matrices could be prepared at higher NaDC concentrations to completely remove particle settling over the minute timescale, yet complete removal of oxygen from the system was then the issue, which had a strong impact on the observed kinetics due to electron extraction. This led to intractable variations between experiments and was not pursued further.

PIAS for bare $^{H_2N}CN_x$ and hybrids with GO/RGO were also conducted (Figure C.11) and they all showed similar PIAS traces when considering both the amplitude and kinetics, even in the presence of **NiP**. While we expect to monitor only the unreactive trapped charges in the case of amino-terminated, $^{H_2N}CN_x$,[96] the lack of changes in the presence of GO and RGO supports our conclusion that the junction formed generally does not significantly impact the photophysics of CN_x.

Centrifugation experiments were subsequently conducted to better understand the interaction between GO and the **NiP** catalyst (Figure 5.9). First, the UV–visible absorption profile of **NiP** (50 nmol in 3 mL) was recorded alone in aqueous solution. Then, the **NiP** solution was stirred with different amounts of GO, specifically 0.05 mg and 0.5 mg. The resulting suspensions were then centrifuged (10,000 rpm, 10 min) and the UV–vis spectrum of **NiP** remaining in the supernatant was recorded. A significant reduction in the **NiP** absorption peaks was observed as the GO loading was increased, which can be attributed to the H-bonding interactions between the –OH groups of GO or RGO and the phosphonate groups of the **NiP** catalyst.[97] This indicates that GO acts as a scaffold to bring **NiP** in close proximity to $^{NCN}CN_x$ and the greater affinity for the $^{NCN}CN_x$−GO interface enhances the rate of electron transfer from $^{NCN}CN_x$ to **NiP**. It was not possible to fully sediment $^{NCN}CN_x$ and RGO particles in analogous experiments, preventing us to clearly observe the absorption profile of **NiP**.
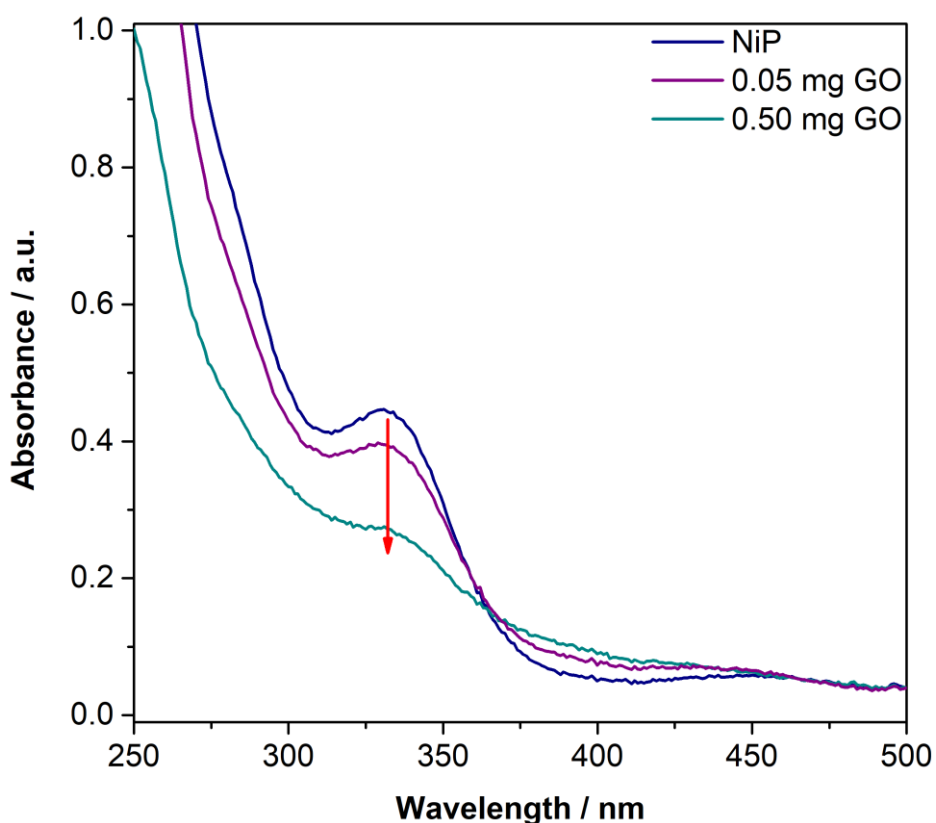
Figure 5.9. UV–visible absorption spectra of **NiP** (40 nmol) in KP$_i$ solution (0.1 M, 3 mL), before and after the addition different amounts of GO (0.05–0.5 mg). GO was separated by centrifugation before recording the electronic absorption spectra of **NiP** in the supernatant. Similar experiments were also attempted with bare $^{NCN}CN_x$ and RGO, but these were hampered by their strong scattering.

Together, these observations highlight once more the importance of brining time resolved spectroscopic techniques and photocatalytic experiments together to develop a better understanding on multi-component hybrid systems.

5.3 Conclusions

The enhanced activity of the closed photo-redox system $^{NCN}CN_x$−**NiP** is investigated upon integration with GO and RGO. Introducing GO/RGO enabled 3-times and 1.5-times enhancement in the presence of EDTA and 4-MBA, respectively. Systematic and precise tuning of the GO loading was found to be essential to reach the best photocatalytic performance due to the highly scattering nature of GO. A maximum specific activity of 4,655 ± 448 µmol H$_2$ (g $^{NCN}CN_x$)$^{-1}$ h^{-1} and a TOF$_{NiP}$ of 116 ± 3 h^{-1} was reached through system optimisation under 1 sun irradiation. To the best of our

knowledge, this is the highest activity reported in CN_x–GO/RGO heterojunction systems and top performance of "closed" CN_x photocatalytic system for selective and stoichiometric alcohol oxidation and proton reduction. The catalytic activity of **NiP** is in line with previously reported colloidal systems. After 4 h of irradiation in the presence of GO, 18 ± 1 µmol of H_2 and 17 ± 1 µmol of 4-MBAd were obtained, corresponding to 57 ± 3% of selective 4-MBA conversion.

The properties of the closed cycle were probed by optical spectroscopic techniques (PL, tr-PL, TAS, PIAS) to gain a better understanding on the charge transfer dynamics between $^{NCN}CN_x$ and GO or RGO and **NiP**. In contrast to previous reports, our results revealed that introducing GO or RGO does not have a significant impact on charge separation or recombination on a timescale shorten than 0.1 s. The charge transfer reactions of the ultra-long lived electrons in $^{NCN}CN_x$ were probed by PIAS on timescales longer than 0.1 s. In the presence of GO and RGO, increasing **NiP** concentration resulted in faster quenching of the signal associated with the trapped electron in $^{NCN}CN_x$ when compared with bare $^{NCN}CN_x$. This effect indicates that GO and RGO improve the rate of electron extraction from $^{NCN}CN_x$. We show that **NiP** can interact with GO, which acts as a conductive binder and improves the affinity between **NiP** and $^{NCN}CN_x$. Therefore, the enhancement in activity upon addition of GO/RGO to $^{NCN}CN_x$ and **NiP** is not a simple electronic effect but GO and RGO act as carbon scaffolds to efficiently bring the components in close proximity, without adversely affecting the charge transport dynamics.

5.4 References

(1)   Ong, W.-J.; Tan, L.-L.; Ng, Y. H.; Yong, S.-T.; Chai, S.-P. *Chem. Rev.* **2016**, *116*, 7159–7329.

(2)   Quintana, M.; Edvinsson, T.; Hagfeldt, A.; Boschloo, G. *J. Phys. Chem. C* **2007**, *111*, 1035–1041.

(3)   Li, P.; Wei, Z.; Wu, T.; Peng, Q.; Li, Y. *J. Am. Chem. Soc.* **2011**, *133*, 5660–5663.

(4)   Chen, X.; Burda, C. *J. Am. Chem. Soc.* **2008**, *130*, 5018–5019.

(5)   Chen, X.; Mao, S. S. *Chem. Rev.* **2007**, *107*, 2891–2959.

(6)   Warnan, J.; Willkomm, J.; Ng, J. N.; Godin, R.; Prantl, S.; Durrant, J. R.; Reisner,

E. *Chem. Sci.* **2017**, *8*, 3070–3079.

(7)   Kudo, A.; Miseki, Y. *Chem. Soc. Rev.* **2009**, *38*, 253–278.

(8)   Wakerley, D. W.; Kuehnel, M. F.; Orchard, K. L.; Ly, K. H.; Rosser, T. E.; Reisner, E. *Nat. Energy* **2017**, *2*, 17021.

(9)   Han, Z.; Qiu, F.; Eisenberg, R.; Holland, P. L.; Krauss, T. D. *Science* **2012**, *338*, 1321–1324.

(10)   Kuehnel, M. F.; Sahm, C. D.; Neri, G.; Lee, J. R.; Orchard, K. L.; Cowan, A. J.; Reisner, E. *Chem. Sci.* **2018**, *9*, 2501–2509.

(11)   Cao, S.; Low, J.; Yu, J.; Jaroniec, M. *Adv. Mater.* **2015**, *27*, 2150–2176.

(12)   Vilela, F.; Zhang, K.; Antonietti, M. *Energy Environ. Sci.* **2012**, *5*, 7819–7832.

(13)   Gong, Y.; Li, M.; Wang, Y. *ChemSusChem* **2015**, *8*, 931–946.

(14)   Wang, X.; Maeda, K.; Thomas, A.; Takanabe, K.; Xin, G.; Carlsson, J. M.; Domen, K.; Antonietti, M. *Nat. Mater.* **2009**, *8*, 76–80.

(15)   Su, F.; Mathew, S. C.; Lipner, G.; Fu, X.; Antonietti, M.; Blechert, S.; Wang, X. *J. Am. Chem. Soc.* **2010**, *132*, 16299–16301.

(16)   Cui, Y.; Ding, Z.; Liu, P.; Antonietti, M.; Fu, X.; Wang, X. *Phys. Chem. Chem. Phys.* **2012**, *14*, 1455–1462.

(17)   Qiu, P.; Chen, H.; Xu, C.; Zhou, N.; Jiang, F.; Wang, X.; Fu, Y. *J. Mater. Chem. A* **2015**, *3*, 24237–24244.

(18)   Maeda, K.; Wang, X.; Nishihara, Y.; Lu, D.; Antonietti, M.; Domen, K. *J. Phys. Chem. C* **2009**, *113*, 4940–4947.

(19)   Caputo, C. A.; Gross, M. A.; Lau, V. W.-h.; Cavazza, C.; Lotsch, B. V.; Reisner, E. *Angew. Chem. Int. Ed.* **2014**, *53*, 11538–11542.

(20)   Lau, V. W.-h; Moudrakovski, I.; Botari, T.; Weinberger, S.; Mesch, M. B.; Duppel, V.; Senker, J.; Blum, V.; Lotsch, B. V. *Nat. Commun.* **2016**, *7*, 12165.

(21)   Liu, J.; Liu, Y.; Liu, N.; Han, Y.; Zhang, X.; Huang, H.; Lifshitz, Y.; Lee, S.-T.; Zhong, J.; Kang, Z. *Science* **2015**, *347*, 970–974.

(22)   Zhu, M.; Kim, S.; Mao, L.; Fujitsuka, M.; Zhang, J.; Wang, X.; Majima, T. *J. Am. Chem. Soc.* **2017**, *139*, 13234–13242.

(23) Zhang, Y.; Mori, T.; Ye, J.; Antonietti, M. *J. Am. Chem. Soc.* **2010**, *132*, 6294–6295.

(24) Wang, Y.; Li, H.; Yao, J.; Wang, X.; Antonietti, M. *Chem. Sci.* **2011**, *2*, 446–450.

(25) Li, J.; Shen, B.; Hong, Z.; Lin, B.; Gao, B.; Chen, Y. *Chem. Commun.* **2012**, *48*, 12017–12019.

(26) Ding, Z.; Chen, X.; Antonietti, M.; Wang, X. *ChemSusChem* **2011**, *4*, 274–281.

(27) Gao, L.-F.; Wen, T.; Xu, J.-Y.; Zhai, X.-P.; Zhao, M.; Hu, G.-W.; Chen, P.; Wang, Q.; Zhang, H.-L. *ACS Appl. Mater. Interfaces* **2016**, *8*, 617–624.

(28) Li, Z.; Kong, C.; Lu, G. *J. Phys. Chem. C* **2016**, *120*, 56–63.

(29) Yang, S.; Gong, Y.; Zhang, J.; Zhan, L.; Ma, L.; Fang, Z.; Vajtai, R.; Wang, X.; Ajayan, P. M. *Adv. Mater.* **2013**, *25*, 2452–2456.

(30) Zhan, Y.; Liu, Z.; Liu, Q.; Huang, D.; Wei, Y.; Hu, Y.; Lian, X.; Hu, C. *New J. Chem.* **2017**, *41*, 3930–3938.

(31) Kasap, H.; Caputo, C. A.; Martindale, B. C. M.; Godin, R.; Lau, V. W.-h; Lotsch, B. V.; Durrant, J. R.; Reisner, E. *J. Am. Chem. Soc.* **2016**, *138*, 9183–9192.

(32) Allen, M. J.; Tung, V. C.; Kaner, R. B. *Chem. Rev.* **2010**, *110*, 132–145.

(33) Geim, A. K.; Novoselov, K. S. *Nat. Mater.* **2007**, *6*, 183–191.

(34) Xiang, Q.; Yu, J.; Jaroniec, M. *Chem. Soc. Rev.* **2012**, *41*, 782–796.

(35) Yang, M.-Q.; Xu, Y.-J. *Phys. Chem. Chem. Phys.* **2013**, *15*, 19102–19118.

(36) Novoselov, K. S.; Geim, A. K.; Morozov, S. V; Jiang, D.; Zhang, Y.; Dubonos, S. V; Grigorieva, I. V; Firsov, A. A. *Science* **2004**, *306*, 666–669.

(37) Luo, J.; Cote, L. J.; Tung, V. C.; Tan, A. T. L.; Goins, P. E.; Wu, J.; Huang, J. *J. Am. Chem. Soc.* **2010**, *132*, 17667–17669.

(38) Luo, J.; Kim, J.; Huang, J. *Acc. Chem. Res.* **2013**, *46*, 2225–2234.

(39) Sun, Y.; Wu, Q.; Shi, G. *Energy Environ. Sci.* **2011**, *4*, 1113–1132.

(40) Ng, Y. H.; Iwase, A.; Kudo, A.; Amal, R. *J. Phys. Chem. Lett.* **2010**, *1*, 2607–2612.

(41) Iwase, A.; Ng, Y. H.; Ishiguro, Y.; Kudo, A.; Amal, R. *J. Am. Chem. Soc.* **2011**,

133, 11054–11057.

(42)   Xiang, Q.; Yu, J.; Jaroniec, M. *Nanoscale* **2011**, *3*, 3670–3678.

(43)   Xiang, Q.; Yu, J.; Jaroniec, M. *J. Phys. Chem. C* **2011**, *115*, 7355–7363.

(44)   Min, S.; Lu, G. *J. Phys. Chem. C* **2011**, *115*, 13938–13945.

(45)   Tu, W.; Zhou, Y.; Liu, Q.; Yan, S.; Bao, S.; Wang, X.; Xiao, M.; Zou, Z. *Adv. Funct. Mater.* **2013**, *23*, 1743–1749.

(46)   Yu, J.; Jin, J.; Cheng, B.; Jaroniec, M. *J. Mater. Chem. A* **2014**, *2*, 3407–3416.

(47)   Shown, I.; Hsu, H.-C.; Chang, Y.-C.; Lin, C.-H.; Roy, P. K.; Ganguly, A.; Wang, C.-H.; Chang, J.-K.; Wu, C.-I.; Chen, L.-C.; Chen, K.-H. *Nano Lett.* **2014**, *14*, 6097–6103.

(48)   Xu, Y.-F.; Yang, M.-Z.; Chen, B.-X.; Wang, X.-D.; Chen, H.-Y.; Kuang, D.-B.; Su, C.-Y. *J. Am. Chem. Soc.* **2017**, *139*, 5660–5663.

(49)   Iwashina, K.; Iwase, A.; Ng, Y. H.; Amal, R.; Kudo, A. *J. Am. Chem. Soc.* **2015**, *137*, 604–607.

(50)   Pan, Z.; Hisatomi, T.; Wang, Q.; Chen, S.; Iwase, A.; Nakabayashi, M.; Shibata, N.; Takata, T.; Katayama, M.; Minegishi, T.; Kudo, A.; Domen, K. *Adv. Funct. Mater.* **2016**, *26*, 7011–7019.

(51)   Mateo, D.; Esteve-Adell, I.; Albero, J.; Royo, J. F. S.; Primo, A.; Garcia, H. *Nat. Commun.* **2016**, *7*, 11819.

(52)   Iwase, A.; Yoshino, S.; Takayama, T.; Ng, Y. H.; Amal, R.; Kudo, A. *J. Am. Chem. Soc.* **2016**, *138*, 10260–10264.

(53)   Zhang, Y.; Tang, Z.-R.; Fu, X.; Xu, Y.-J. *ACS Nano* **2011**, *5*, 7426–7435.

(54)   Zhang, N.; Yang, M.-Q.; Tang, Z.-R.; Xu, Y.-J. *J. Catal.* **2013**, *303*, 60–69.

(55)   Liu, S.; Chen, Z.; Zhang, N.; Tang, Z.-R.; Xu, Y.-J. *J. Phys. Chem. C* **2013**, *117*, 8251–8261.

(56)   Zhang, N.; Zhang, Y.; Pan, X.; Yang, M.-Q.; Xu, Y.-J. *J. Phys. Chem. C* **2012**, *116*, 18023–18031.

(57)   Zhang, H.; Lv, X.; Li, Y.; Wang, Y.; Li, J. *ACS Nano* **2010**, *4*, 380–386.

(58)   Zhang, Y.; Tang, Z.-R.; Fu, X.; Xu, Y.-J. *ACS Nano* **2010**, *4*, 7303–7314.

(59) Xiang, Q.; Lang, D.; Shen, T.; Liu, F. *Appl. Catal. B Environ.* **2015**, *162*, 196–203.

(60) Lou, J.; Liu, Y.; Wang, Z.; Zhao, D.; Song, C.; Wu, J.; Dasgupta, N.; Zhang, W.; Zhang, D.; Tao, P.; Shang, W.; Deng, T. *ACS Appl. Mater. Interfaces* **2016**, *8*, 14628–14636.

(61) Xiang, Q.; Cheng, B.; Yu, J. *Angew. Chem. Int. Ed.* **2015**, *54*, 11350–11366.

(62) Liu, Z.; Liu, Q.; Huang, Y.; Ma, Y.; Yin, S.; Zhang, X.; Sun, W.; Chen, Y. *Adv. Mater.* **2008**, *20*, 3924–3930.

(63) Li, S.-S.; Tu, K.-H.; Lin, C.-C.; Chen, C.-W.; Chhowalla, M. *ACS Nano* **2010**, *4*, 3169–3174.

(64) Liu, J.; Durstock, M.; Dai, L. *Energy Environ. Sci.* **2014**, *7*, 1297–1306.

(65) Lee, D.-Y.; Na, S.-I.; Kim, S.-S. *Nanoscale* **2016**, *8*, 1513–1522.

(66) Liu, Q.; Liu, Z.; Zhang, X.; Yang, L.; Zhang, N.; Pan, G.; Yin, S.; Chen, Y.; Wei, J. *Adv. Funct. Mater.* **2009**, *19*, 894–904.

(67) Yu, D.; Park, K.; Durstock, M.; Dai, L. *J. Phys. Chem. Lett.* **2011**, *2*, 1113–1118.

(68) Wang, D. H.; Kim, J. K.; Seo, J. H.; Park, I.; Hong, B. H.; Park, J. H.; Heeger, A. J. *Angew. Chem. Int. Ed.* **2013**, *52*, 2874–2880.

(69) Horvath-Bordon, E.; Kroke, E.; Svoboda, I.; Fuess, H.; Riedel, R. *New J. Chem.* **2005**, *29*, 693–699.

(70) Liao, G.; Chen, S.; Quan, X.; Yu, H.; Zhao, H. *J. Mater. Chem.* **2012**, *22*, 2721–2726.

(71) Gross, M. A.; Reynal, A.; Durrant, J. R.; Reisner, E. *J. Am. Chem. Soc.* **2014**, *136*, 356–366.

(72) Yeh, T.-F.; Teng, C.-Y.; Chen, S.-J.; Teng, H. *Adv. Mater.* **2014**, *26*, 3297–3303.

(73) Yeh, T.-F.; Syu, J.-M.; Cheng, C.; Chang, T.-H.; Teng, H. *Adv. Funct. Mater.* **2010**, *20*, 2255–2262.

(74) Yeh, T.-F.; Chan, F.-F.; Hsieh, C.-T.; Teng, H. *J. Phys. Chem. C* **2011**, *115*, 22587–22597.

(75) Martindale, B. C. M.; Hutton, G. A. M.; Caputo, C. A.; Reisner, E. *J. Am. Chem.*

Soc. **2015**, *137*, 6018–6025.

(76) Martindale, B. C. M.; Hutton, G. A. M.; Caputo, C. A.; Prantl, S.; Godin, R.; Durrant, J. R.; Reisner, E. *Angew. Chem. Int. Ed.* **2017**, *56*, 6459–6463.

(77) Li, K.; Xie, X.; Zhang, W.-D. *ChemCatChem* **2016**, *8*, 2128–2135.

(78) Wang, H.; Wang, B.; Bian, Y.; Dai, L. *ACS Appl. Mater. Interfaces* **2017**, *9*, 21730–21737.

(79) Qin, J.; Huo, J.; Zhang, P.; Zeng, J.; Wang, T.; Zeng, H. *Nanoscale* **2016**, *8*, 2249–2259.

(80) Song, L.; Li, T.; Zhang, S. *J. Phys. Chem. C* **2017**, *121*, 293–299.

(81) Martin, D. J.; Qiu, K.; Shevlin, S. A.; Handoko, A. D.; Chen, X.; Guo, Z.; Tang, J. *Angew. Chem. Int. Ed.* **2014**, *53*, 9240–9245.

(82) Li, X.; Shen, R.; Ma, S.; Chen, X.; Xie, J. *Appl. Surf. Sci.* **2018**, *430*, 53–107.

(83) Wang, P.; Guan, Z.; Li, Q.; Yang, J. *J. Mater. Sci.* **2018**, *53*, 774–786.

(84) Zeng, P.; Zhang, Q.; Peng, T.; Zhang, X. *Phys. Chem. Chem. Phys.* **2011**, *13*, 21496–21502.

(85) Li, Q.; Guo, B.; Yu, J.; Ran, J.; Zhang, B.; Yan, H.; Gong, J. R. *J. Am. Chem. Soc.* **2011**, *133*, 10878–10884.

(86) Lau, V. W.-h; Klose, D.; Kasap, H.; Podjaski, F.; Pignié, M.-C.; Reisner, E.; Jeschke, G.; Lotsch, B. V. *Angew. Chem. Int. Ed.* **2017**, *56*, 510–514.

(87) Kongkanand, A.; Kamat, P. V. *ACS Nano* **2007**, *1*, 13–21.

(88) Nelson, J. *Phys. Rev. B* **2003**, *67*, 155209.

(89) Barzykin, A. V; Tachiya, M. *J. Phys. Chem. A* **2002**, *106*, 4356–4363.

(90) Lightcap, I. V.; Kamat, P. V. *J. Am. Chem. Soc.* **2012**, *134*, 7109–7116.

(91) Rahman, M. Z.; Zhang, J.; Tang, Y.; Davey, K.; Qiao, S.-Z. *Mater. Chem. Front.* **2017**, *1*, 562–571.

(92) Liang, W.; Guman-Sepulveda, J. R.; He, S.; Dogariu, A.; Fang, J. Y. *J. Mater. Sci. Chem. Eng.* **2015**, *3*, 6–15.

(93) Boschloo, G.; Hagfeldt, A. *Inorganica Chim. Acta* **2008**, *361*, 729–734.

(94)   Chakrabarty, A.; Maitra, U.; Das, A. D. *J. Mater. Chem.* **2012**, *22*, 18268–18278.

(95)   Zhang, J.; Wang, H.; Li, X.; Song, S.; Song, A.; Hao, J. *J. Phys. Chem. B* **2016**, *120*, 6812–6818.

(96)   Godin, R.; Wang, Y.; Zwijnenburg, M. A.; Tang, J.; Durrant, J. R. *J. Am. Chem. Soc.* **2017**, *139*, 5216–5224.

(97)   Ye, S.; Ding, C.; Chen, R.; Fan, F.; Fu, P.; Yin, H.; Wang, X.; Wang, Z.; Du, P.; Li, C. *J. Am. Chem. Soc.* **2018**, *140*, 3250–3256.

Chapter 6

Photoreforming of lignocellulose into H$_2$ using nano-engineered carbon nitride under benign conditions

The data presented in this chapter was published in a peer-reviewed article: J. Am. Chem. Soc., 2018, doi: 10.1021/jacs.8b07853. The author of this thesis carried all of the work presented unless specified otherwise. Dr. Demetra S. Achilleos and the author conceived the research. Ailun Huang shared the photocatalytic experiments with the author and recorded the BET measurements. Dr. Demetra S. Achilleos has helped with characterisation of samples. TEM and SEM images were recorded by Dr. Heather F. Greer.

6.1 Introduction

Direct utilisation of biomass has the potential to provide sustainable and scalable H$_2$ fuel production.[1] Lignocellulose is the most abundant form of biomass and, being an agricultural waste product, its use does not compete with food production. The complex and energy-rich structure of lignocellulose is composed of cellulose, hemicellulose and lignin,[1,2] which have evolved to prevent degradation and are therefore kinetically challenging to utilise under ambient conditions.[3] Gasification at high-temperature (> 750 °C) is the most common method for H$_2$ production from lignocellulose, but is energy-intensive and produces side products such as the fuel-
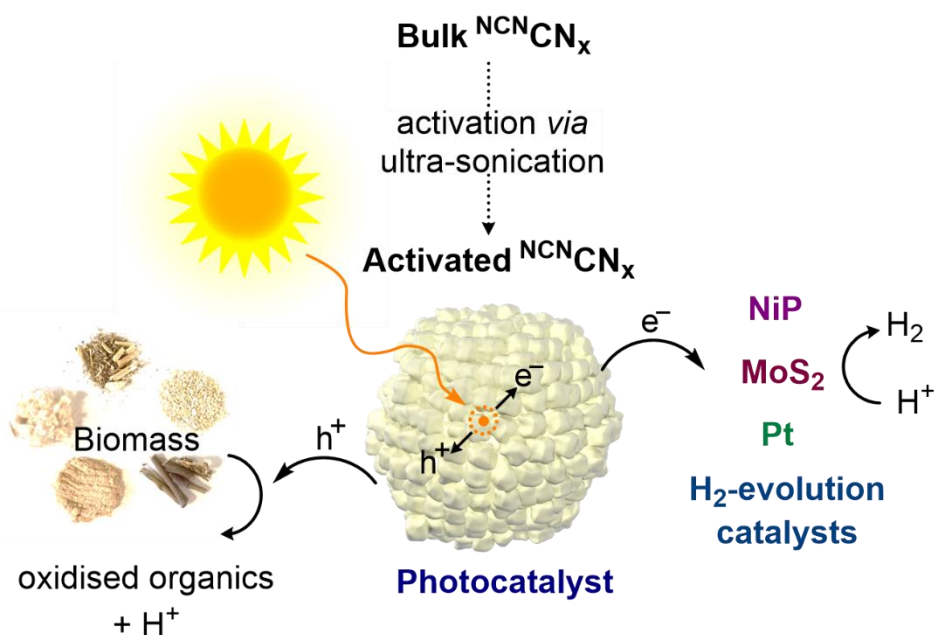
Figure 6.1. Schematic representation of H_2 generation through photoreforming of lignocellulose with $^{NCN}CN_x$ and H_2 production catalysts.

cell inhibitor carbon monoxide.[4] Enzymatic hydrolysis is another process for biomass utilisation, but this multi-step conversion suffers from low overall yields.[3,5] Thus, there is substantial interest in developing novel approaches for the valorisation of lignocellulose.[6–11]

Photoreforming of unprocessed biomass to H_2 has emerged as a more affordable and clean alternative to traditional techniques.[12,13] Photoreforming requires a photocatalyst that generates holes to oxidise the lignocellulose and electrons to drive proton reduction upon photoexcitation.[12] This process is traditionally carried out using UV–light harvesting TiO_2 modified with noble-metal catalysts such as RuO_2 and Pt.[14–16] Visible-light absorbing CdS quantum dots were recently reported for biomass photoreforming, but the system required toxic Cd and strongly alkaline conditions (10 M KOH).[17] There is therefore a great need to identify a photoreforming process that utilises an inexpensive, non-toxic and visible-light absorbing photocatalyst, capable of operating under benign aqueous conditions.

Polymeric CN_x is a metal-free and inexpensive carbonaceous photocatalyst.[18–20] The well-positioned band edges of CN_x give enough driving force for many photocatalytic reactions including proton reduction,[20–22] CO_2 reduction,[23,24] organic transformations,[25,26] redox catalysis[25,27] and water splitting.[28,29] Herein, we report a

straightforward approach to enhance the photocatalytic activity of bulk cyanamide-functionalised carbon nitride ($^{NCN}CN_x$) by ultra-sonication. The activated $^{NCN}CN_x$ is subsequently used to photoreform lignocellulosic biomass and generate H_2, in the presence of a molecular Ni-bis(diphosphine) catalyst, **NiP**, and heterogeneous Pt or MoS_2 in aqueous media over a range of pH values (2–15), (Figure 6.1).

6.2 Results and discussion

6.2.1 Characterisation of $^{NCN}CN_x$

Bulk $^{NCN}CN_x$ was prepared and characterised as previously reported (see Chapter 5).[22,30] Activated $^{NCN}CN_x$ was obtained by ultra-sonicating an aqueous suspension of bulk $^{NCN}CN_x$ (5 mg mL^{-1}) in KP$_i$ solution using a sonication probe (Fisher, Sonic Dismembrator) for 10 min at 40 ºC (Figure 6.2). UV–vis spectroscopy of the bulk and ultra-sonicated $^{NCN}CN_x$ revealed strong UV absorption, which tails into the visible region (λ_{abs} < 450 nm). A significant increase in absorbance was observed upon ultra-sonication of $^{NCN}CN_x$, which may be due to disruption of aggregated $^{NCN}CN_x$ and subsequently reduced light scattering and enhanced light absorption.[31] Photoluminescence studies (λ_{ex} = 360 nm) also revealed an increased emission intensity for the ultra-sonicated $^{NCN}CN_x$, possibly suggesting a higher density of photoexcited states.

Brunauer-Emmett-Teller (BET) measurements indicated a 60% increase in the surface area after ultra-sonication (97.4 ± 0.6 m^2 g^{-1}),[32] while a smaller aggregate size following ultra-sonication was confirmed by TEM and scanning electron microscopy (SEM). The digital photography of $^{NCN}CN_x$ samples before and after ultra-sonication also showed significant increase in the volume of the dried sample after ultra-sonication, supporting increased surface area and possibly easier access to catalytically active sites of activated $^{NCN}CN_x$. Nearly identical XRD patterns and FT-IR spectra were observed, indicating that the characteristic functional group features of bulk $^{NCN}CN_x$, cyanamide surface functionality and the polymeric nature of the material, were preserved after ultra-sonication (Figure 6.2).[22,33]

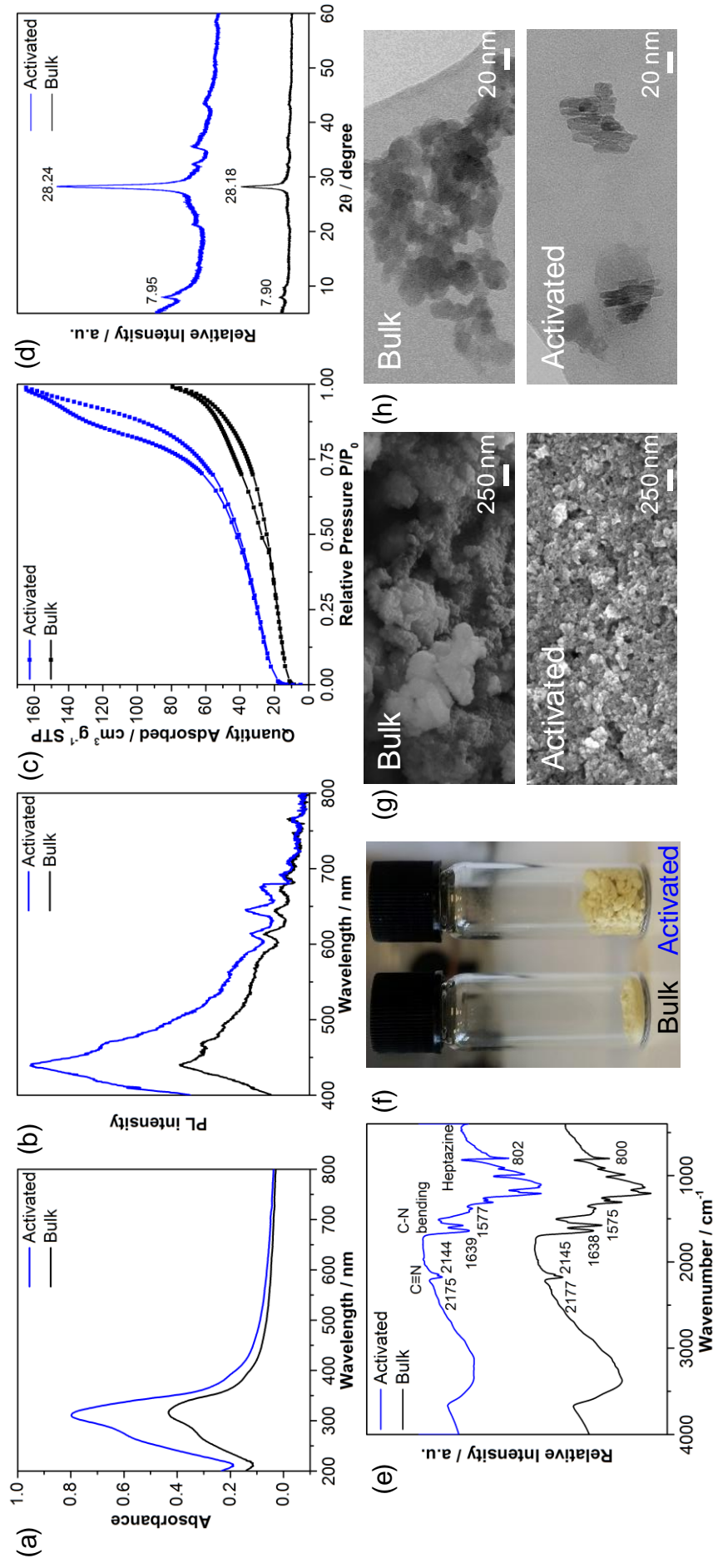Figure 6.2. Characterisation of bulk and activated $^{NCN}\textbf{CN}_x$. (a) UV–vis recorded in KP$_i$ buffer at 8.3 µg mL^{-1} concentration. (b) Photoluminescence spectra with λ_{ex} = 360 nm. (c) BET surface area measurement, activated (97.4 ± 0.6 m^2 g^{-1}) and bulk (59.5 ± 0.5 m^2 g^{-1}). (d) XRD with inter-layer (28° 2θ) and intra-layer (7.9° 2θ) periodicities. (e) ATR-FT-IR with -C≡N (2175 and 2144 cm^{-1}) and heptazine core (802 cm^{-1}) vibrations. (f) Photograph comparing the volume of 20 mg bulk and activated $^{NCN}\textbf{CN}_x$. (g) SEM and (h) TEM images.

6.2.2 Photocatalytic assembly and performance

A photocatalytic screening assay was carried out by dispersing $^{NCN}CN_x$ in KP_i (pH 4.5) solution containing a DuBois-type Ni-proton reduction catalyst, **NiP**,[34] with 4-MBA (30 µmol).[25] 4-MBA was selected as the electron donor as it may be considered as an easily oxidised model cellulose substrate. The samples were irradiated under a N_2 atmosphere with simulated solar light (100 mW cm^{-2}, AM 1.5G, 25 °C). The reaction conditions were optimised systematically with respect to $^{NCN}CN_x$-based H_2 production activity (specific activity; µmol H_2 (g $^{NCN}CN_x$)$^{-1}$ h^{-1}), **NiP**-based activity represented by Ni-based turnover frequency (TOF$_{NiP}$; mol H_2 (mol NiP)$^{-1}$ h^{-1}) and turnover number (TON$_{NiP}$; mol H_2 (mol NiP)$^{-1}$), and overall proton reduction and alcohol oxidation rates (Tables D.1-D.7).

Initially the conditions for ultra-sonication were optimised for the highest H_2 production rate by systematically varying the parameters including time, temperature, solvent and the concentration of $^{NCN}CN_x$ (Figure 6.3). Photocatalytic activity increased approximately by 5-times after 10 mins of ultra-sonication in KP_i (Figure 6.3a). During 10 mins of sonication, temperature of the solvent went up to 40 °C. Control experiments showed that highest H_2 production rate was reached at 40 °C, while standard sonication bath found to be inefficient in enhancing the activity (Figure 6.3b).

A range of solvents have been reported to ultra-sonicate carbon nitride,[35,36] while the photocatalytic performance of $^{NCN}CN_x$ after sonicating in different solvents including KP_i, isopropanol (^{i}PrOH), methanol (MeOH) and water, showed negligible difference (Figure 6.3c). Photocatalytic experiments carried out by dispersing different concentration of $^{NCN}CN_x$ in KP_i showed almost identical H_2 production rates (Figure 6.3d). Therefore, the optimised conditions were to ultra-sonicate bulk $^{NCN}CN_x$ (5 mg mL^{-1}) for 10 min in KP_i (0.1 M, pH 4.5) at 40 °C, to activate prior to experiments.

The results of photoreforming 4-MBA using 0.5 mg bulk and activated $^{NCN}CN_x$ with 300 nmol of **NiP** are shown in Figure 6.4. After 1 h of irradiation, activated $^{NCN}CN_x$ displayed more than three times the photocatalytic activity of bulk $^{NCN}CN_x$, reaching 17.2 ± 0.6 µmol H_2 h^{-1}, TOF$_{NiP}$ of 57.5 ± 2.1 h^{-1} and a specific activity of 34,480 ± 1240 µmol H_2 (g $^{NCN}CN_x$)$^{-1}$ h^{-1}. Quantitative and selective oxidation of 4-MBA into 4-MBAd was observed in less than 6 h of simulated solar light irradiation.
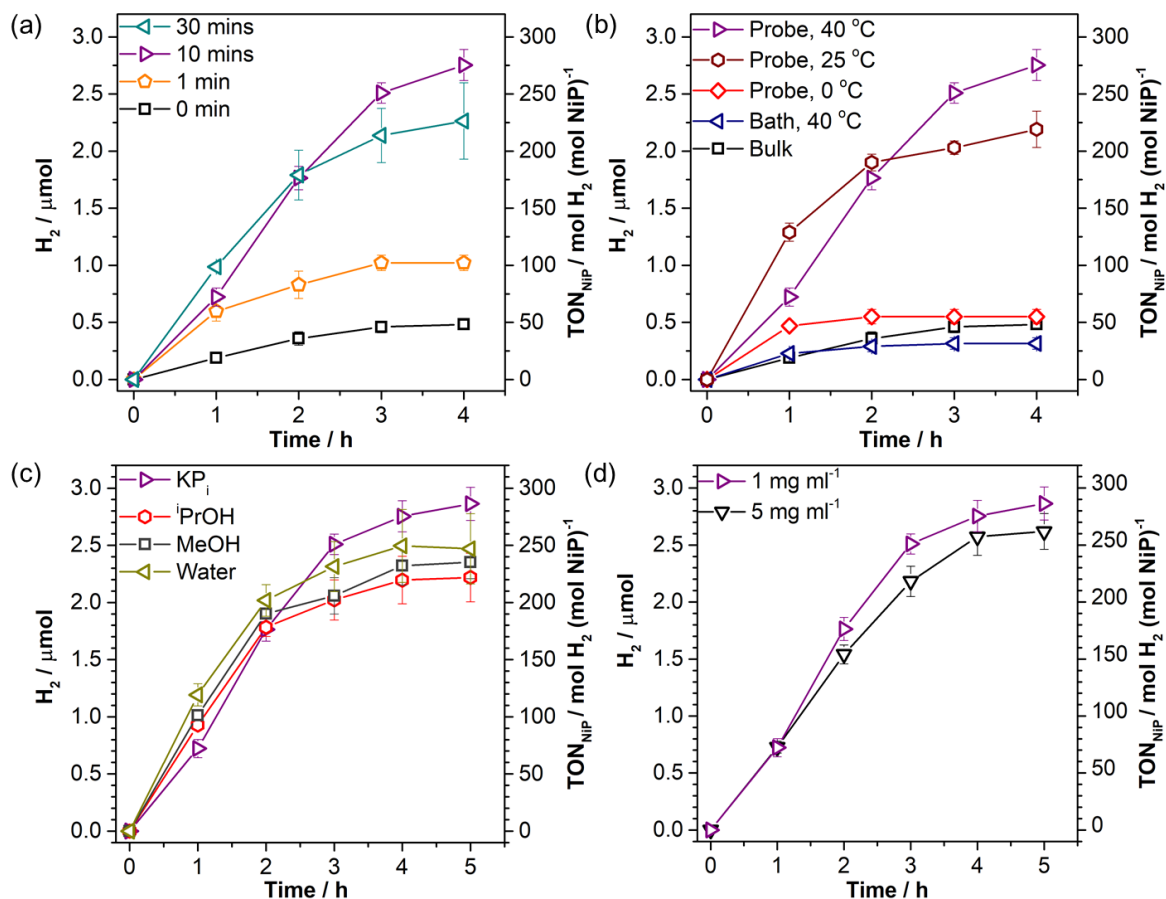
Figure 6.3. Photocatalytic H_2 production with $^{NCN}CN_x$ (0.5 mg), **NiP** (10 nmol) and 4-MBA (30 µmol) under 1 sun irradiation (AM 1.5G) at 25 °C. (a) $^{NCN}CN_x$ dispersed in KP_i and sonicated for different times. (b) Comparing photocatalytic activity by ultra-sonicating bulk $^{NCN}CN_x$ in KP_i using ultra-sonication probe or standard sonication bath at different temperature. (c) Comparing the activity by sonicating $^{NCN}CN_x$ in different solvents. (d) Photocatalytic performance using different concentrations of $^{NCN}CN_x$ for sonication in KP_i.
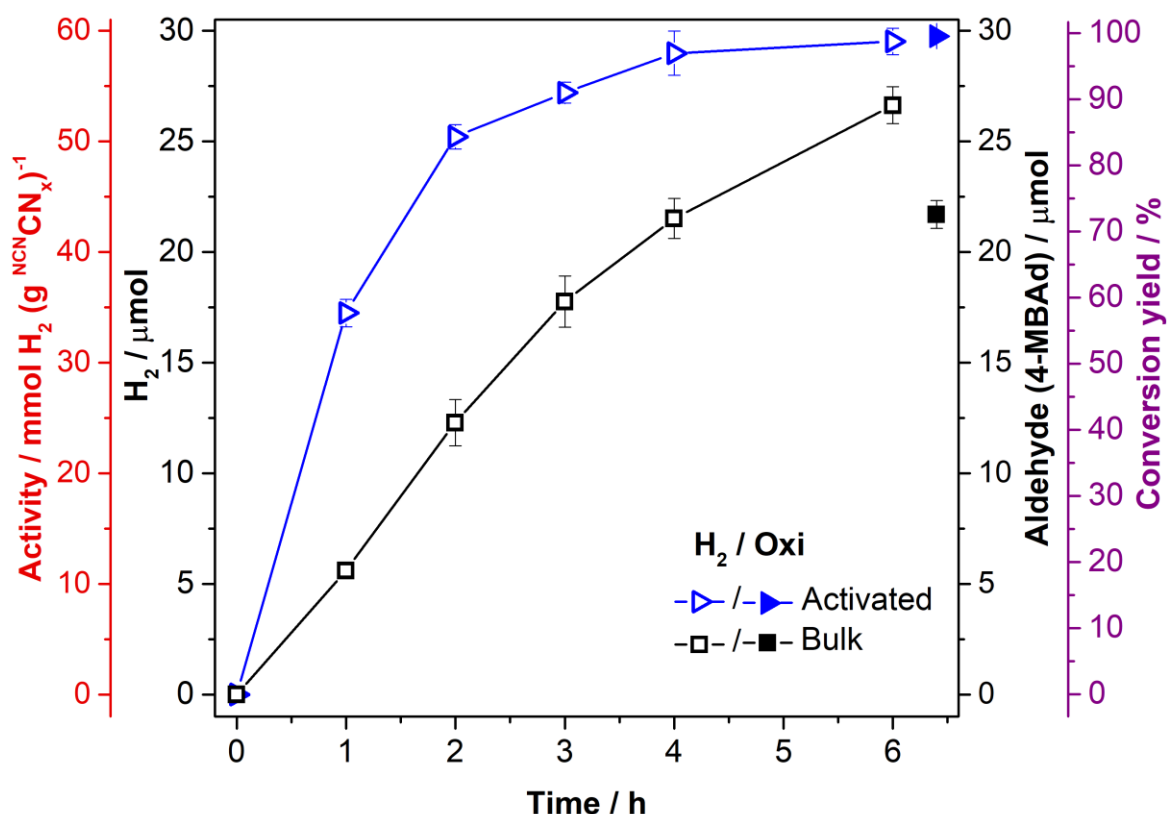
Figure 6.4. Photocatalytic H_2 and 4-MBAd formation using activated and bulk $^{NCN}CN_x$ (0.5 mg) with **NiP** (300 nmol) in KP_i solution (0.1 M, pH 4.5, 3 mL) containing 4-MBA (30 µmol) under simulated solar irradiation (100 mW cm^{-2}, AM 1.5G, 25 °C). The pair of hollow and filled symbols of the same shape and colour correspond to H_2 and aldehyde production, respectively.

The linear H_2 production starts to plateau after 3 h of irradiation as the conversion yield around 80% is reached, reducing the 4-MBA concentration, and the system becomes limited by the availability of the substrate (Figure 6.4). Control experiments in the absence of $^{NCN}CN_x$, **NiP**, 4-MBA or light did not produce H_2 for the activated $^{NCN}CN_x$ and **NiP** system (Table D.6). A specific activity of 39,310 ± 1970 µmol H_2 (g $^{NCN}CN_x$)$^{-1}$ h^{-1} was reached with 0.5 mg activated $^{NCN}CN_x$ and 400 nmol of **NiP** (Figure D.1). This is to the best of our knowledge a benchmark H_2 evolution rate for a CN_x photocatalyst.[37,38] To date, the highest H_2-evolution rate reported was with urea-derived $^{H2N}CN_x$ in the presence of Pt co-catalyst in TEOA as the sacrificial electron donor, reaching up to 20,000 µmol H_2 g^{-1} h^{-1}.[37] Very recently defect engineered $^{H2N}CN_x$, with nitrogen vacancies and enhanced light absorption, reported to have H_2 production rate of 37,680 µmol H_2 g^{-1} h^{-1} in TEOA with Pt.[38]
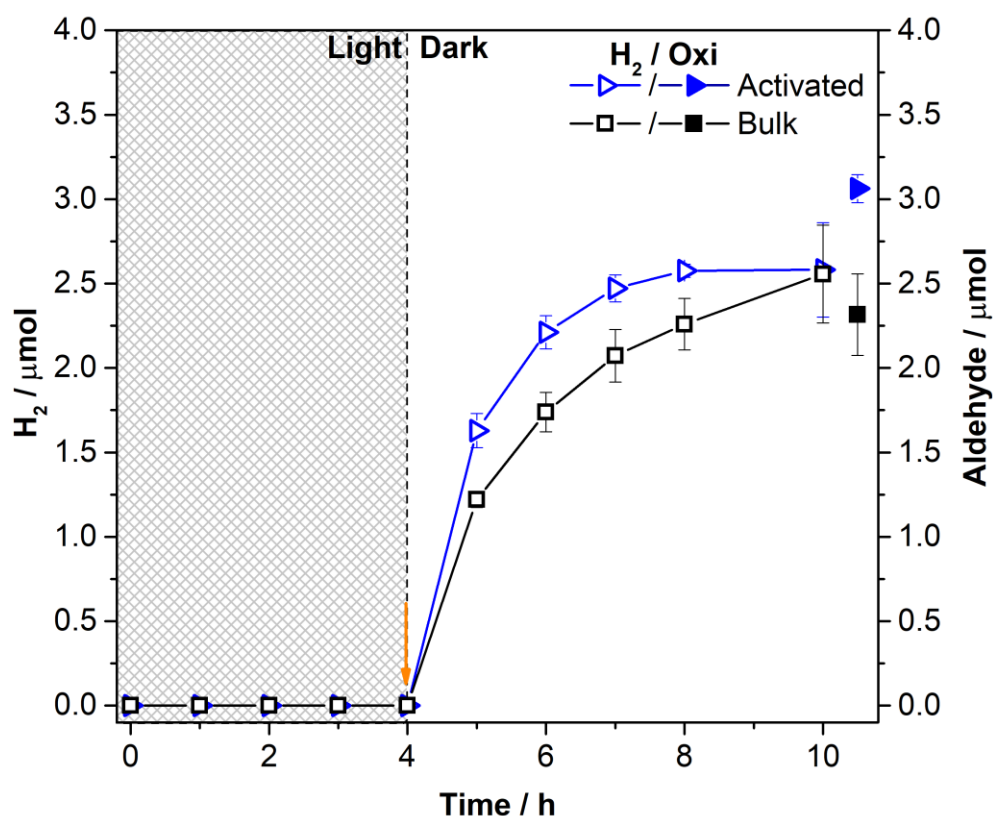
Figure 6.5. Photoreactors were prepared using bulk and activated $^{NCN}CN_x$ (5 mg) in the presence of 4-MBA (30 µmol) in an aqueous KP_i solution (0.1 M, pH 4.5, 3 mL) without **NiP** and irradiated for 4h under simulated solar light irradiation (100 mW cm^{-2}, AM 1.5G, 25 °C). The suspensions were then moved into dark and **NiP** (100 nmol) was injected. The H_2 production in dark phase was monitored for the next 6 h. The pair of hollow and filled symbols of the same shape and colour corresponds to H_2 and aldehyde production, respectively, under the specified reaction conditions.

We have previously showed that $^{NCN}CN_x$ can photo-charge and accumulate ultra-long-lived trapped electrons in the presence of 4-MBA under N_2 atmosphere.[25,39] The density of accumulated charges remained approximately the same for bulk and activated $^{NCN}CN_x$, but activated $^{NCN}CN_x$ showed a faster discharging behaviour (Figure 6.5 and Table D.7). This observation suggests that ultra-sonication enables the co-catalyst to more easily access catalytically active sites, due to the higher surface area of the material as confirmed by the characterisation data, and thus improves the charge transfer dynamics between 4-MBA, $^{NCN}CN_x$ and **NiP** in the designed system.

The EQE of the $^{NCN}CN_x-$**NiP** photosystems was determined using simulated solar light at a single wavelength (λ = 360 ± 10 nm, I = 4.05 mW cm^{-2}). The EQE of

the activated and bulk systems were determined to be 22 ± 1% and 13 ± 1%, respectively. This suggests a 60% improvement in the photocatalytic performance of the $^{NCN}CN_x$ after ultra-sonication, which matches with the increase in the surface area of the material as determined by BET (see characterisation). These results are suggesting that more charge carriers are generated and utilised efficiently with the activated $^{NCN}CN_x$. The EQE determined is significantly higher than previously reported unfunctionalised benchmark amino-terminated $^{H_2N}CN_x$ and **NiP** with an EQE of 0.37 ± 0.02%.[21]

6.2.3 Lignocellulosic substrates

The model substrate 4-MBA was subsequently replaced with purified lignocellulose components. α-Cellulose was initially selected as the most abundant form of wood-derived biomass while being the most unreactive form of cellulose.[40] The photoreactors were prepared as described above, with α-cellulose replacing 4-MBA as the electron donor. The reaction conditions were optimised for the overall amount of H_2 being produced by varying the amount of α-cellulose, activated $^{NCN}CN_x$ and **NiP** loadings (Table D.8).

The system containing 0.5 mg $^{NCN}CN_x$ and 50 nmol **NiP** gave a specific activity of 1,690 ± 100 µmol H_2 (g $^{NCN}CN_x$)$^{-1}$ h^{-1} and TOF$_{NiP}$ of 17.0 ± 1.1 h^{-1}. The highest overall H_2 production yield of 2.62 ± 0.09 µmol H_2 was observed with 5 mg activated $^{NCN}CN_x$ and 50 nmol **NiP** in purely aqueous KP$_i$ (pH 4.5) after 4 h of irradiation under 1 sun (Figure 6.6), while bulk $^{NCN}CN_x$ produced only 1.91 ± 0.07 µmol H_2. Under UV-filtered simulated solar light irradiation ($\lambda > 400$ nm), activated $^{NCN}CN_x$ produced 1.10 ± 0.03 µmol of H_2, indicating efficient utilisation of visible light (Table D.8).

The importance of surface-functionalisation for α-cellulose photoreforming was highlighted by the insignificant photocatalytic activity of benchmark, amine-terminated bulk $^{H_2N}CN_x$ (only 0.13 ± 0.04 µmol H_2), while ultra-sonication had a negligible effect on the activity of this material (Figure 6.6).[25] This significant difference in the activity of $^{NCN}CN_x$ has been previously attributed to the superior oxidising ability, due to more positively positioned valence band position (+2.2 V *vs.* NHE at pH 6; band gap of 2.7 eV),[41] as well as the improved hole transfer to the electron donor *via* the cyanamide moieties on the surface of the material through the built-in potential differences, across the polymer chains.[25,30,42]
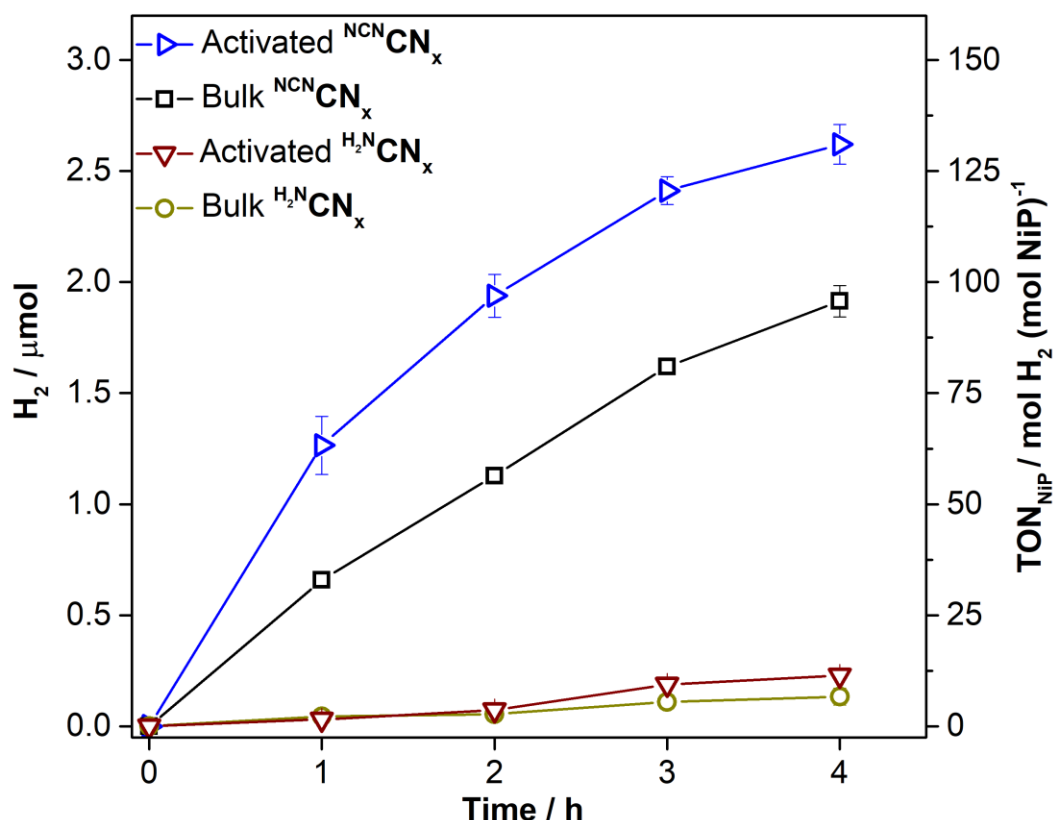
Figure 6.6. Photocatalytic H_2 production in the presence of bulk and activated $^{H_2N}CN_x$, bulk and activated $^{NCN}CN_x$ (5 mg), **NiP** (50 nmol) with α-cellulose (100 mg) in KP_i (0.1 M, pH 4.5, 3 mL) under 1 sun irradiation (100 mW cm^{-2}, AM 1.5G, 25 °C).

Photocatalytic biomass reformation into H_2 was then expanded to the other components of lignocellulose, xylan and lignin as well as the most common units found in their structures (Figure 6.7, Table D.9). As the substrate size is reduced, solubility improves in pH 4.5 KP_i, resulting in significantly enhanced photoactivity. After 24 h of irradiation, up to 32.1 ± 4.8 µmol of H_2 was produced from glucose, corresponding to specific activity of 1,120 ± 80 µmol H_2 (g $^{NCN}CN_x$)$^{-1}$ h^{-1} and TOF_{NiP} of 112 ± 8 h^{-1}. In the presence of xylose and galactose monosaccharides, 19.9 ± 2.3 and 28.0 ± 2.5 µmol of H_2 were produced respectively after 24 h of irradiation. Photoreforming of polymeric xylan generated 4.92 ± 0.17 µmol of H_2. Despite the strong light absorbing nature and robustness of lignin, 0.20 ± 0.03 µmol H_2 production was achieved, with TOF_{NiP} of 4.0 ± 0.7 h^{-1} and a specific activity of 40.8 ± 6.8 µmol H_2 (g $^{NCN}CN_x$)$^{-1}$ h^{-1}. The results demonstrate that the system is capable of photoreforming biomass under mildly acidic aqueous conditions but is still limited by substrate availability to quench the photogenerated holes in $^{NCN}CN_x$.
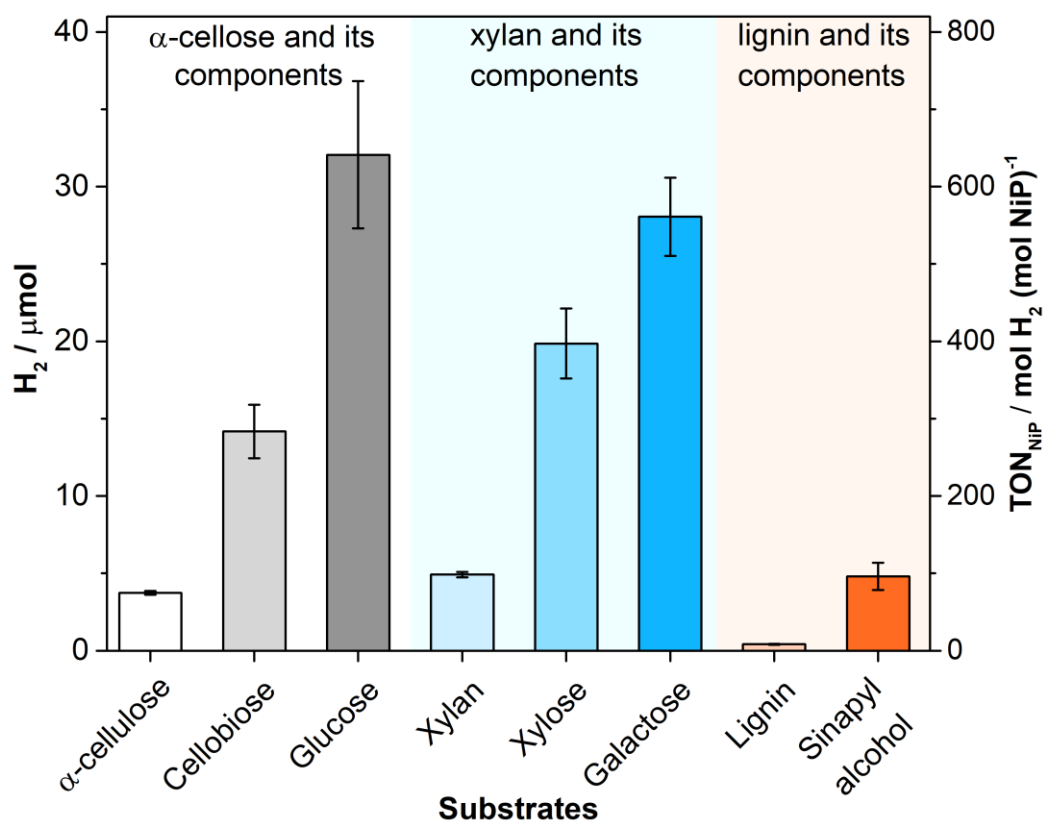
Figure 6.7. Photocatalytic H_2 production using activated $^{NCN}CN_x$ (5 mg) and **NiP** (50 nmol) with purified lignocellulose components (100 mg) in KP_i solution (0.1 M, pH 4.5, 3 mL) under 1 sun irradiation for 24 h (100 mW cm^{-2}, AM 1.5G, 25 °C). For lignin and sinapyl alcohol experiments 0.5 mg and 10 mg of substrates were used respectively.

These promising results encouraged us to replace the purified lignocellulosic components with raw and unprocessed 'real-world' biomass samples (Figure D.2, Table D.10). Photo-reformed H_2 was detected for a range of samples (including paper and cardboard despite difficulties with stirring) and sawdust produced 3.89 ± 0.34 µmol of H_2 with TOF_{NiP} of 20.2 ± 0.4 h^{-1} and a specific activity of 202.0 ± 3.8 µmol H_2 (g $^{NCN}CN_x)^{-1}$ h^{-1}, in the presence of $^{NCN}CN_x$ in aqueous KP_i solution.

The long-term performance of the designed system was investigated by comparing the activity of **NiP** with benchmark proton reduction co-catalysts, Pt and MoS$_2$ (Figure 6.8, Table D.11) in the presence of α-cellulose.[22,43] **NiP** showed a superior initial rate, but the fragile molecular framework degrades after 24 h,[44] whereupon 3.7 ± 0.1 µmol of H_2 have been produced with $^{NCN}CN_x$−**NiP**. Substituting molecular catalyst **NiP** with heterogenous Pt and MoS$_2$ catalysts *via in situ* photodeposition of metallic precursors, H$_2$PtCl$_6$[24] or H$_8$N$_2$MoS$_4$[61] respectively, showed
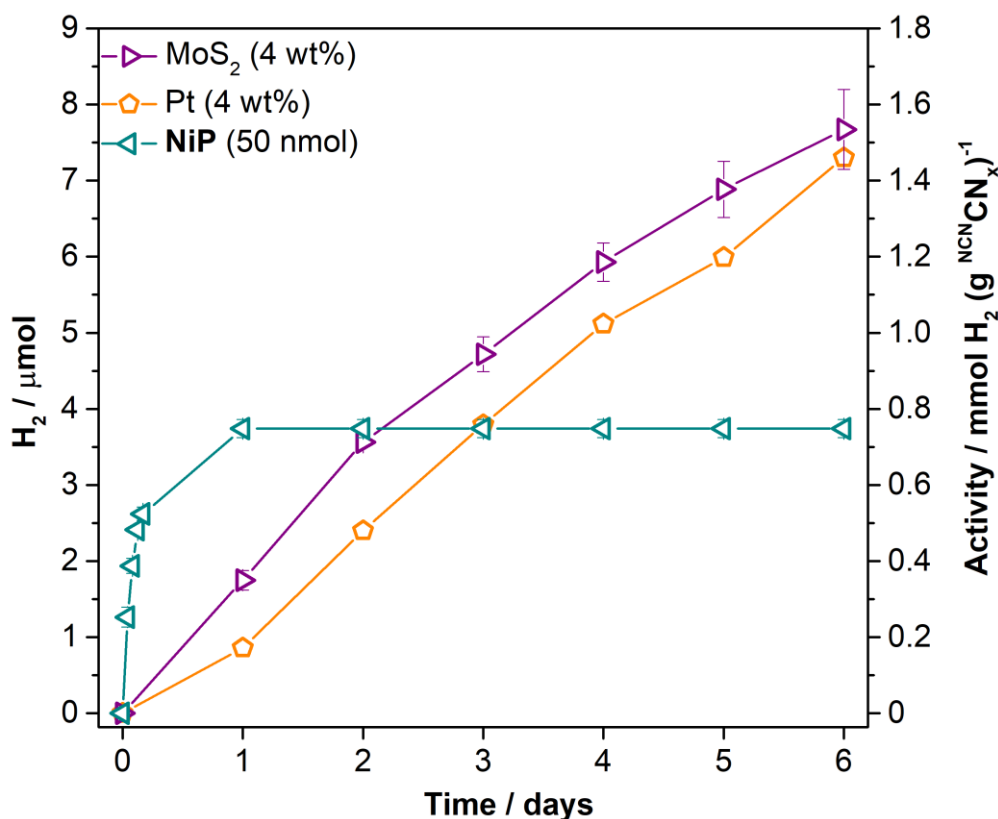
Figure 6.8. Photocatalytic H_2 production with activated $^{NCN}CN_x$ (5 mg), α-cellulose (100 mg) in KP_i (0.1 M, pH 4.5, 3 mL) under 1 sun irradiation (AM 1.5G) in the presence of different catalysts; **NiP** (50 nmol), H_2PtCl_6 (4 wt%) or $H_8N_2MoS_4$ (4 wt%).

relatively slow initial H_2-evolution kinetics. Yet, both the $^{NCN}CN_x-MoS_2$ and the $^{NCN}CN_x-Pt$ photosystems displayed enhanced stability and outperformed the $^{NCN}CN_x-NiP$ system over long term due to their robustness, while photocatalytic systems with Pt were still active after twelve days.

Mass spectrometry of the photocatalytic samples prepared in H_2O and D_2O, showed selective growth of H_2 and D_2 peaks respectively, confirming that H_2 production originates from the protons in the KP_i solution (Figure D.3, Table D.12). The oxidation products of α-cellulose after photocatalysis were characterised using ^{13}C-NMR spectroscopy with uniformly ^{13}C-labelled cellulose. Photoreforming of ^{13}C-labelled cellulose was carried out over activated $^{NCN}CN_x$ (5 mg) and Pt (4 wt%) in pH 4.5 KP_i solution prepared in D_2O over six days of irradiation. The suspension was then filtered to remove insoluble parts of cellulose and the reaction solution was analysed.
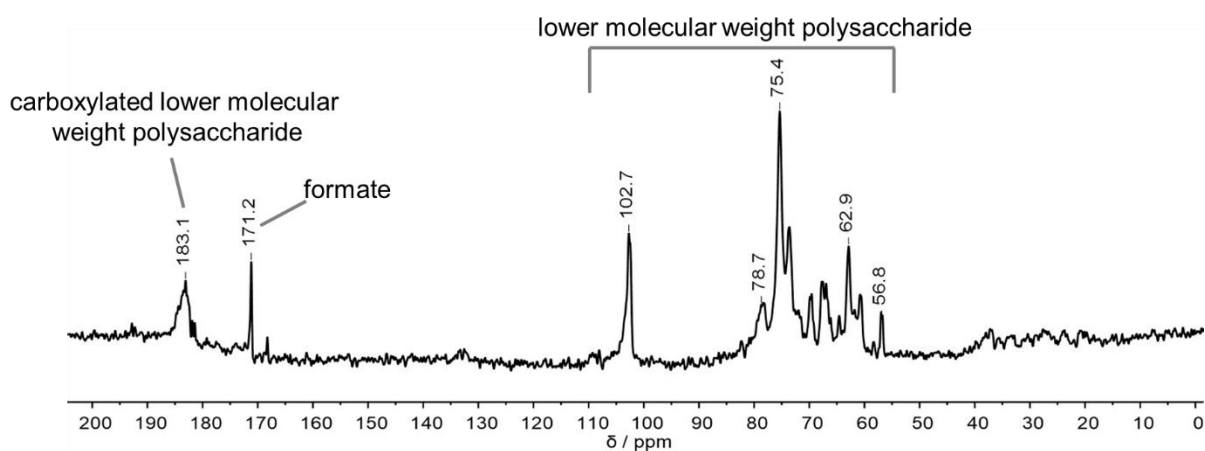
Figure 6.9. ^{13}C NMR of spectroscopy of uniformly labelled ^{13}C-α-cellulose (10 mg) after 6 days of irradiation in KP_i (pH 4.5) prepared in D_2O with $^{NCN}CN_x$ (5 mg) and H_2PtCl_6 (4 wt%).[17,45]
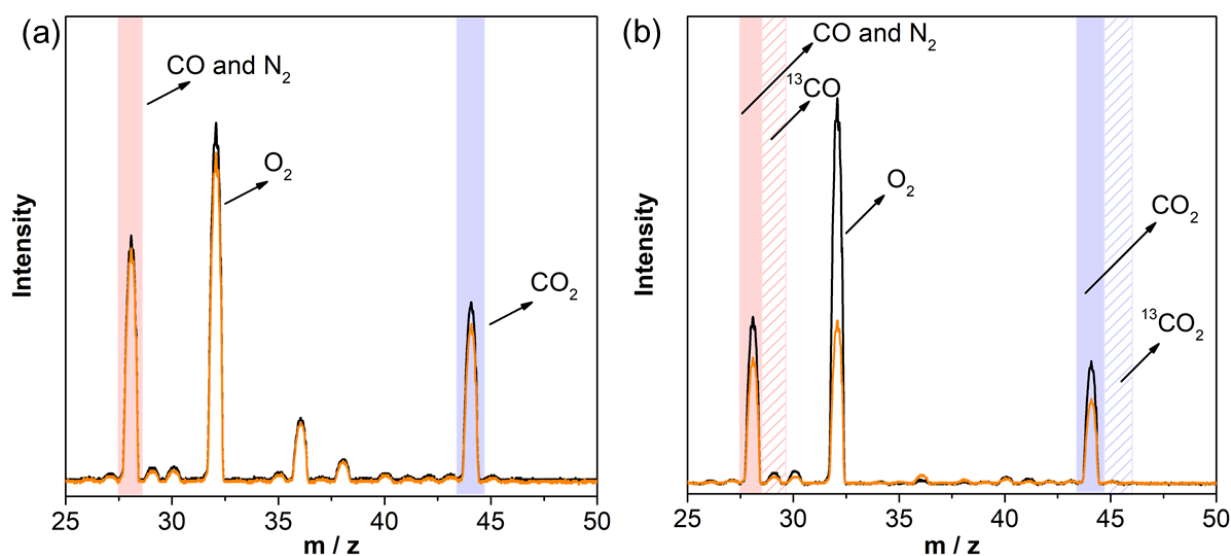

Figure 6.10. Mass spectra of headspace gas recorded after 6 days of solar light irradiation of activated $^{NCN}CN_x$ (5 mg) and H_2PtCl_6 (4 wt%) in the presence of (a) α-cellulose (100 mg) and (b) ^{13}C-labelled α-cellulose (100 mg) in KP_i (pH 4.5). Black and orange traces indicate the background and the headspace gases measured respectively.

^{13}C-NMR of the resulting solution showed the formation of formate (δ = 171 ppm) and carboxylate end groups (δ = 183 ppm) of lower molecular weight polysaccharides (δ = 50–110 ppm), as the products of the photoreforming process (Figure 6.9).[17,45] Other gaseous oxidation products in the headspace were monitored by GC and mass spectrometry after 6 days of irradiation (Figure 6.10, Table D.13).

Negligible amounts of CO and CO_2 were measured (Figure 6.10), which is in agreement with the insignificant quantities of carbonate detected by ^{13}C-NMR. Lignocellulose oxidation traditionally occurs *via* the formation of hydroxyl radicals (HO[·]), but photogenerated holes in [NCN]CN_x are not oxidising enough to produce HO[·] (Chapter 4).[25,30] Therefore the oxidation is likely to occur directly *via* hole transfer due to strong interaction between the lignocellulosic substrates and [NCN]CN_x.[17,25,30]

The versatility of photoreforming system under various conditions was investigated by suspending α-cellulose in 1, 5, 10 M KOH (~pH 14–15), KP_i solution (pH 4.5, pH 7) or H_2SO_4 (pH 2) and stirring for 24 h at 25 °C prior to the addition of H_2PtCl_6 (4 wt%) and activated [NCN]CN_x (Figure 6.11, Table D.14). After six days of irradiation under 10 M KOH conditions, 39.5 ± 1.1 µmol of H_2 was produced, which is twice the H_2 production yield observed in 5 M KOH. 1 M KOH, H_2SO_4 and pH 7 KP_i solution all resulted in H_2 production activities comparable to that of a pH 4.5 KP_i solution. These results are consistent with the fact that cellulose is easier to solubilise under alkaline conditions, as it is hydrolysed towards lower molecular weight polysaccharides with higher solubilities.[46,47] This was further supported by the higher H_2 evolution rates of pure biomass components in 10 M KOH, which showed activity up to 12 days in the presence of [NCN]CN_x and Pt (Figure D.4, Table D.15).

The conversion yield was then determined with different α-cellulose loadings in the presence of [NCN]CN_x and Pt under simulated solar light irradiation. Conversion yield of 22% is reached after six days of irradiation in 10 M KOH solution (Table D.16).[48] This calculation is based on the assumption that maximum 12 equivalent of H_2 can be produced per anhydroglucose unit in α-cellulose structure.[48] The conversion yield reached is more than twice the yield reported previously with CdS/CdO$_x$ quantum dots under similar conditions (9.7%).[17]
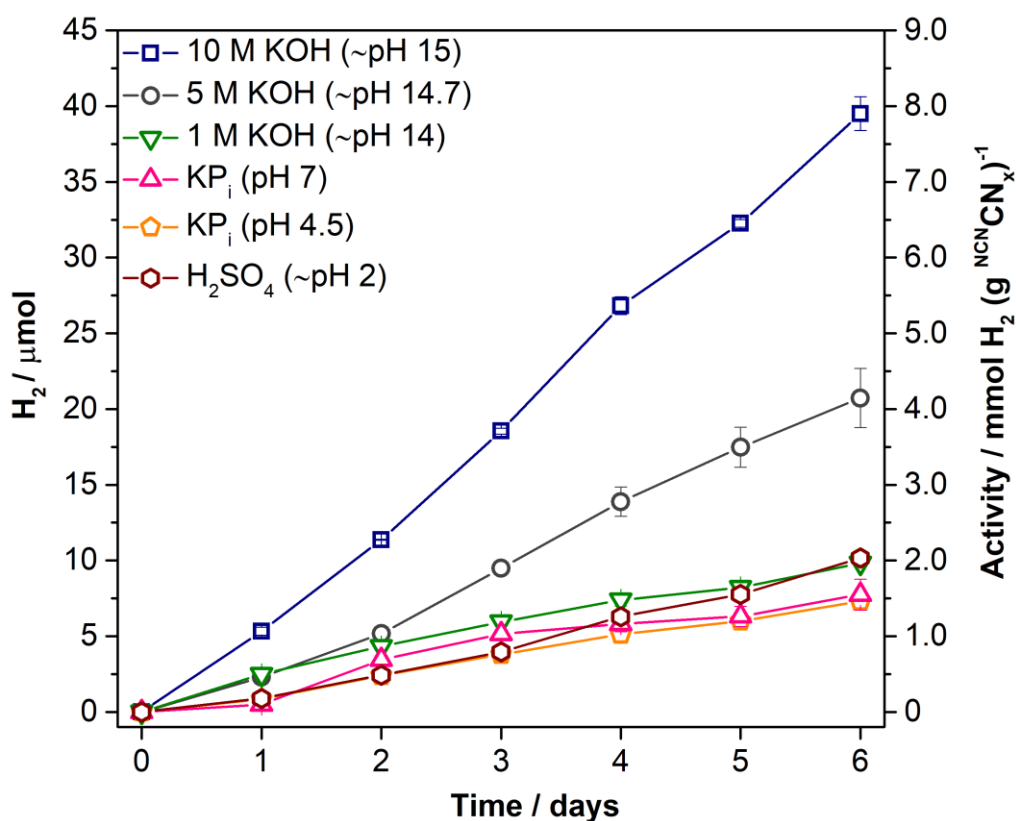
Figure 6.11. Photocatalytic H_2 production using activated $^{NCN}CN_x$ (5 mg) with H_2PtCl_6 (4 wt%) and α-cellulose (100 mg) in different media; 1, 5, 10 M KOH (pH 14-15), H_2SO_4 (pH 2) or KP_i (pH 4.5 and pH 7) under 1 sun irradiation (100 mW cm^{-2}, AM 1.5G, 25 °C).

6.3 Conclusions

In summary, we report a straightforward ultra-sonication approach to break down the aggregates of $^{NCN}CN_x$, which results in enhanced photocatalytic performance. The activated $^{NCN}CN_x$ reaches a benchmark specific activity of 39,310 ± 1970 µmol H_2 (g $^{NCN}CN_x$)$^{-1}$ h^{-1} for the photoreforming of 4-MBA. Both purified lignocellulosic components and raw biomass substrates are photoreformed to H_2 in the presence of activated $^{NCN}CN_x$ and **NiP** in KP_i (pH 4.5) at 25 °C. This is the first example of a precious metal-free, Cd-free and visible light-promoted photocatalytic system for photoreforming of biomass under benign conditions.

Activated $^{NCN}CN_x$ is also demonstrated to be highly versatile, as it operates with molecular and heterogeneous co-catalysts as well as under different reaction media. MoS_2 functions at the same rate as Pt under slightly acidic conditions for a least 6

days. Systems in the presence of Pt, over a wide range of pH values (2–15), show activity beyond twelve days. Alkaline conditions exhibit the best photocatalytic performance and a conversion yield of α-cellulose to H_2 beyond 22%. The utilisation of a carbon-based photocatalyst for photoreforming of biomass therefore offers a new perspective for clean solar fuel H_2 production from abundant waste sources.

6.4 References

(1)   Isikgor, F. H.; Becer, C. R. *Polym. Chem.* **2015**, *6*, 4497–4559.

(2)   Hendriks, A. T. W. M.; Zeeman, G. *Bioresour. Technol.* **2009**, *100*, 10–18.

(3)   Himmel, M. E.; Ding, S.-Y.; Johnson, D. K.; Adney, W. S.; Nimlos, M. R.; Brady, J. W.; Foust, T. D. *Science* **2007**, *315*, 804–807.

(4)   Sikarwar, V. S.; Zhao, M.; Clough, P.; Yao, J.; Zhong, X.; Memon, M. Z.; Shah, N.; Anthony, E. J.; Fennell, P. S. *Energy Environ. Sci.* **2016**, *9*, 2939–2977.

(5)   Himeshima, N.; Amao, Y. *Green Chem.* **2005**, *7*, 742–746.

(6)   Reichert, J.; Brunner, B.; Jess, A.; Wasserscheid, P.; Albert, J. *Energy Environ. Sci.* **2015**, *8*, 2985–2990.

(7)   Albert, J.; Jess, A.; Kern, C.; Pöhlmann, F.; Glowienka, K.; Wasserscheid, P. *ACS Sustain. Chem. Eng.* **2016**, *4*, 5078–5086.

(8)   Zhang, P.; Guo, Y.-J.; Chen, J.; Zhao, Y.-R.; Chang, J.; Junge, H.; Beller, M.; Li, Y. *Nat. Catal.* **2018**, *1*, 332–338.

(9)   Grande, P. M.; Viell, J.; Theyssen, N.; Marquardt, W.; Domínguez de María, P.; Leitner, W. *Green Chem.* **2015**, *17*, 3533–3539.

(10)   Zinoviev, S.; Müller-Langer, F.; Das, P.; Bertero, N.; Fornasiero, P.; Kaltschmitt, M.; Centi, G.; Miertus, S. *ChemSusChem* **2010**, *3*, 1106–1133.

(11)   Albert, J.; Wölfel, R.; Bösmann, A.; Wasserscheid, P. *Energy Environ. Sci.* **2012**, *5*, 7956–7962.

(12)   Puga, A. V. *Coord. Chem. Rev.* **2016**, *315*, 1–66.

(13)   Kuehnel, M. F.; Reisner, E. *Angew. Chem. Int. Ed.* **2018**, *57*, 3290–3296.

(14)   Kawai, T.; Sakata, T. *Nature* **1980**, *286*, 474–476.

(15) Speltini, A.; Sturini, M.; Dondi, D.; Annovazzi, E.; Maraschi, F.; Caratto, V.; Profumo, A.; Buttafava, A. *Photochem. Photobiol. Sci.* **2014**, *13*, 1410–1419.

(16) Caravaca, A.; Jones, W.; Hardacre, C.; Bowker, M. *Proc. R. Soc. A* **2016**, *472*, 20160054.

(17) Wakerley, D. W.; Kuehnel, M. F.; Orchard, K. L.; Ly, K. H.; Rosser, T. E.; Reisner, E. *Nat. Energy* **2017**, *2*, 17021.

(18) Cao, S.; Low, J.; Yu, J.; Jaroniec, M. *Adv. Mater.* **2015**, *27*, 2150–2176.

(19) Antonietti, M.; Oschatz, M. *Adv. Mater.* **2018**, *30*, 1706836.

(20) Wang, X.; Maeda, K.; Thomas, A.; Takanabe, K.; Xin, G.; Carlsson, J. M.; Domen, K.; Antonietti, M. *Nat. Mater.* **2009**, *8*, 76–80.

(21) Caputo, C. A.; Gross, M. A.; Lau, V. W.-h; Cavazza, C.; Lotsch, B. V.; Reisner, E. *Angew. Chem. Int. Ed.* **2014**, *53*, 11538–11542.

(22) Lau, V. W.-h; Moudrakovski, I.; Botari, T.; Weinberger, S.; Mesch, M. B.; Duppel, V.; Senker, J.; Blum, V.; Lotsch, B. V. *Nat. Commun.* **2016**, *7*, 12165.

(23) Kuriki, R.; Yamamoto, M.; Higuchi, K.; Yamamoto, Y.; Akatsuka, M.; Lu, D.; Yagi, S.; Yoshida, T.; Ishitani, O.; Maeda, K. *Angew. Chem. Int. Ed.* **2017**, *56*, 4867–4871.

(24) Cometto, C.; Kuriki, R.; Chen, L.; Maeda, K.; Lau, T.-C.; Ishitani, O.; Robert, M. *J. Am. Chem. Soc.* **2018**, *140*, 7437–7440.

(25) Kasap, H.; Caputo, C. A.; Martindale, B. C. M.; Godin, R.; Lau, V. W.-h; Lotsch, B. V.; Durrant, J. R.; Reisner, E. *J. Am. Chem. Soc.* **2016**, *138*, 9183–9192.

(26) Zhao, Y.; Shalom, M.; Antonietti, M. *Appl. Catal. B Environ.* **2017**, *207*, 311–315.

(27) Yang, P.; Wang, R.; Zhou, M.; Wang, X. *Angew. Chem. Int. Ed.* **2018**, *57*, 8674–8677.

(28) Liu, J.; Liu, Y.; Liu, N.; Han, Y.; Zhang, X.; Huang, H.; Lifshitz, Y.; Lee, S.-T.; Zhong, J.; Kang, Z. *Science* **2015**, *347*, 970–974.

(29) Zhang, G.; Lan, Z.-A.; Lin, L.; Lin, S.; Wang, X. *Chem. Sci.* **2016**, *7*, 3062–3066.

(30) Kasap, H.; Godin, R.; Jeay-Bizot, C.; Achilleos, D. S.; Fang, X.; Durrant, J. R.; Reisner, E. *ACS Catal.* **2018**, *8*, 6914–6926.

(31) Wu, M.; Yan, J.-M.; Zhang, X.-W.; Zhao, M.; Jiang, Q. *J. Mater. Chem. A* **2015**, *3*, 15710–15714.

(32) Lau, V. W.-h; Yu, V. W.-z; Ehrat, F.; Botari, T.; Moudrakovski, I.; Simon, T.; Duppel, V.; Medina, E.; Stolarczyk, J. K.; Feldmann, J.; Blum, V.; Lotsch, B. V. *Adv. Energy Mater.* **2017**, *7*, 1602251.

(33) Horvath-Bordon, E.; Kroke, E.; Svoboda, I.; Fuess, H.; Riedel, R. *New J. Chem.* **2005**, *29*, 693–699.

(34) Gross, M. A.; Reynal, A.; Durrant, J. R.; Reisner, E. *J. Am. Chem. Soc.* **2014**, *136*, 356–366.

(35) Yang, S.; Gong, Y.; Zhang, J.; Zhan, L.; Ma, L.; Fang, Z.; Vajtai, R.; Wang, X.; Ajayan, P. M. *Adv. Mater.* **2013**, *25*, 2452–2456.

(36) Hong, J.; Yin, S.; Pan, Y.; Han, J.; Zhou, T.; Xu, R. *Nanoscale* **2014**, *6*, 14984–14990.

(37) Martin, D. J.; Qiu, K.; Shevlin, S. A.; Handoko, A. D.; Chen, X.; Guo, Z.; Tang, J. *Angew. Chem. Int. Ed.* **2014**, *53*, 9240–9245.

(38) Han, Q.; Cheng, Z.; Wang, B.; Zhang, H.; Qu, L. *ACS Nano* **2018**, *12*, 5221–5227.

(39) Lau, V. W.-h; Klose, D.; Kasap, H.; Podjaski, F.; Pignié, M.-C.; Reisner, E.; Jeschke, G.; Lotsch, B. V. *Angew. Chem. Int. Ed.* **2017**, *56*, 510–514.

(40) Sun, Y.; Cheng, J. *Bioresour. Technol.* **2002**, *83*, 1–11.

(41) Meyer, A. U.; Lau, V. W.-h; König, B.; Lotsch, B. V. *European J. Org. Chem.* **2017**, 2179–2185.

(42) Ou, H.; Chen, X.; Lin, L.; Fang, Y.; Wang, X. *Angew. Chem. Int. Ed.* **2018**, *57*, 8729–8733.

(43) Gu, Q.; Sun, H.; Xie, Z.; Gao, Z.; Xue, C. *Appl. Surf. Sci.* **2017**, *396*, 1808–1815.

(44) Martindale, B. C. M.; Joliat, E.; Bachmann, C.; Alberto, R.; Reisner, E. *Angew. Chem. Int. Ed.* **2016**, *55*, 9402–9406.

(45) Ramos, M. L.; Caldeira, M. M.; Gil, V. M. S. *Carbohydr. Res.* **1997**, *304*, 97–109.

(46) Budtova, T.; Navard, P. *Cellulose* **2016**, *23*, 5–55.

(47)   Medronho, B.; Romano, A.; Miguel, M. G.; Stigsson, L.; Lindman, B. *Cellulose* **2012**, *19*, 581–587.

(48)   Zhang, G.; Ni, C.; Huang, X.; Welgamage, A.; Lawton, L. A.; Robertson, P. K. J.; Irvine, J. T. S. *Chem. Commun.* **2016**, *52*, 1673–1676.

Chapter 7

Conclusions

7.1 Summary

The main goal of this thesis was to use carbon nitride as a photocatalyst to develop straight-forward-to-assemble hybrid systems for solar light driven H_2 evolution while eliminating the need for expensive and non-innocent sacrificial reagents.

First, a full redox system was prepared with the use of $^{NCN}CN_x$, in which controlled 4-MBA oxidation and H_2 evolution was achieved in the presence of Ni-based molecular catalyst, **NiP**. The system demonstrated 1:1 stoichiometric amount solar fuel (H_2) and solar chemical (4-MBAd) formation over 24 h of simulated solar light irradiation, under purely aqueous conditions. The designed system eliminated the need for complex product isolation stage, due to *in situ* separation of H_2 and 4-MBAd in the gas and solution phases, respectively. The $^{NCN}CN_x-$**NiP** system showed an activity of 763 μmol (g $^{NCN}CN_x)^{-1}$ h^{-1} toward H_2 and 4-MBAd production and a **NiP**-based TOF of 76 h^{-1}. After 24 h of irradiation, a 4-MBA conversion yield of 83% towards quantitative and selective 4-MBAd formation was reached. This was the first colloidal system which coupled solar H_2 generation with value-added organic substrate oxidation in a single pot.

Further spectroscopic studies demonstrated that photoexcited $^{NCN}CN_x$ in the presence of an organic substrate could accumulate ultralong-lived "trapped electrons", with lifespan extending from hours to days. This charged state of $^{NCN}CN_x$ allowed

spatially and temporarily decoupling light and dark cycles of the full redox system, which replicates natural photosynthesis in an artificial set-up and makes it possible to produce H_2 in the dark, independent of the light. Mechanistic studies on this full photoredox system revealed that direct hole transfer from $^{NCN}CN_x$ to 4-MBA is the first step followed by electron transfer from $^{NCN}CN_x$ to **NiP**, for H_2 evolution, while selectively reducing the aqueous protons originated from the buffer solution. TAS studies showed that photogenerated holes in $^{NCN}CN_x$ are quenched by 4-MBA in shorter than 3 µs, while the extraction of photoexcited electrons from $^{NCN}CN_x$ takes longer than 2 s. Thus, the delivery of electrons from $^{NCN}CN_x$ to **NiP** demonstrated to have the slowest kinetics amongst all the electron transfer reactions in the full redox system; being the overall rate limiting step.

Having established a better understanding of the mechanism behind this full redox system, the focus shifted towards tackling this limitation. Enhanced photocatalytic activity for simultaneous alcohol oxidation and proton reduction was observed when GO or RGO were employed as an interlayer between $^{NCN}CN_x$ and **NiP**. Introduction of these conductive scaffolds (GO or RGO) enhanced the photocatalytic activity by three times, reaching a specific activity of 4,655 µmol H_2 (g $^{NCN}CN_x$)$^{-1}$ h^{-1} for H_2 and 4-MBAd formation with a **NiP**-based TOF of 116 h^{-1}. The presence of GO and RGO did not alter the number of "trapped electrons" generated or stored in $^{NCN}CN_x$. Time resolved spectroscopy revealed that GO and RGO did not have a significant effect on the charge recombination and separation kinetics of $^{NCN}CN_x$−**NiP** hybrid system in nano−microsecond timescale. However, PIAS demonstrated that on timescales longer than 0.1 s, "trapped electrons" in $^{NCN}CN_x$ were quenched faster in the presence of GO/RGO, showing accelerated electron transfer between $^{NCN}CN_x$ and **NiP**. The absorption profile of **NiP** in the presence of different GO loadings revealed that GO acts as a conductive interfacial "binder" between **NiP** and $^{NCN}CN_x$. Therefore, overall the enhancement in activity did not primarily arise from changes in the photophysics of the $^{NCN}CN_x$, but rather from GO/RGO enabling better electronic communication between $^{NCN}CN_x$ and **NiP**.

All the systems demonstrated to this point showed a full redox system employing 4-MBA for controlled oxidation while carrying out H_2 production. Yet, the ultimate goal was always to minimise the number of "shop bought" chemicals when designing a sustainable system with large-scale application. For this purpose, a

straight forward ultrasonication approach was introduced to enhance the activity of bulk $^{NCN}CN_x$. The activated $^{NCN}CN_x$ showed significantly improved photocatalytic activity than the bulk $^{NCN}CN_x$, reaching a benchmark specific activity of a 39,310 μmol H_2 (g $^{NCN}CN_x$)$^{-1}$ h^{-1} in the presence of **NiP**, toward H_2 and 4-MBAd formation. The system demonstrated quantitative and selective oxidation of 4-MBA into 4-MBAd in less than 6 h of irradiation. The improved activity was attributed to better utilisation of light by the activated $^{NCN}CN_x$ due to increased surface area, making active sites of $^{NCN}CN_x$ more accessible. The activated $^{NCN}CN_x$ was subsequently used to photoreform purified and raw lignocellulose biomass samples to generate H_2, with various co-catalysts including **NiP**, Pt and MoS_2. The system operated in aqueous media over a broad range of pH values (2–15) at room-temperature. The best performances were achieved under alkaline conditions with conversion yields reaching up to 22%. This was the first biomass photoreforming system reported using a carbon-based photocatalyst, which operates in aqueous solution without the need for any precious metal or toxic components.

7.2 Future work

The systems reported in this thesis show great potential to extend the use of carbon nitride as a photocatalyst in a wide range of applications. With the approaches introduced during the course of this work, very high specific activities were reached with respect to $^{NCN}CN_x$ towards H_2 generation and organic substrate oxidation. The direction forward from this point would be to use low cost $^{NCN}CN_x$ as a photocatalyst to drive a variety of organic transformations (including oxidation, reduction and more complex new bond formation reactions) and to replace the traditionally used expensive and short-lived Ru and Ir-based catalysts in the field of light-driven catalysis.

The other approach would be to use highly active and heterogenous $^{NCN}CN_x$ in a reactor and design a flow device. The aim of such a device would be to use it as a rapid screening tool for solar chemicals and solar fuels production. We are in the progress of designing such devices based on information from computational models, which could serve as prototypes. This work is currently in progress and preliminary results have been obtained with Mark Bajada (Figure 7.1).
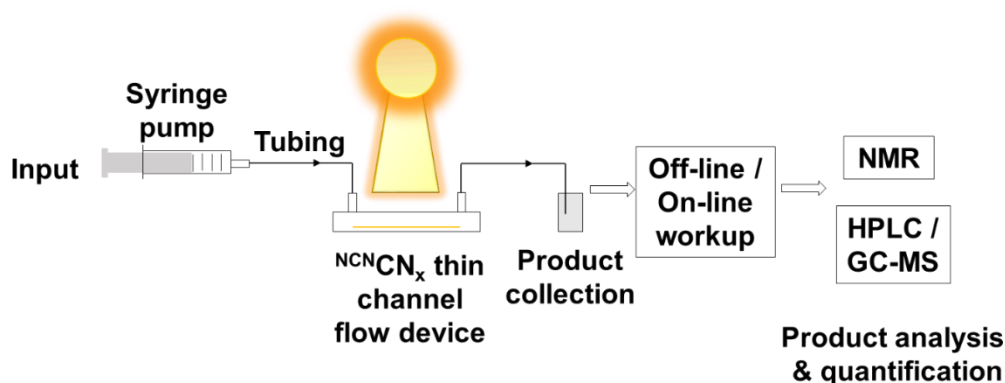
Figure 7.1. Representation of a flow device using $^{NCN}CN_x$ as the photocatalyst.

As determined by the kinetic studies, the slowest step in the $^{NCN}CN_x$ hybrid systems is the rate of electron transfer from $^{NCN}CN_x$ to **NiP**. In addition, **NiP** has a fragile structure which limits the lifetime of the reported systems. Therefore, finding alternative catalysts with better stability and faster electron collection ability will speed up this process while minimising the losses due to inefficient charge separation. The main goal would still be to replace **NiP** with metal salts or waste metals and eliminate the need for purchasing precursors and/or long synthetic procedures to prepare catalysts, in order to develop economically sustainable and practically appealing systems.

The possibility of expanding the photoreforming into plastics and other types of wastes is also of great interest. Plastic photoreformation under alkaline (pH~15) conditions has been very recently demonstrated using CdS dots. Initial screening experiments showed that food waste as well as plastics including polyethylene terephthalate, polyurethane and polystyrene can be photoreformed under aqueous condition in the presence of $^{NCN}CN_x$. Currently we are working on screening a wide range of abundant waste sources to develop a library of chemicals which can be utilised in a similar way. In the meantime, the aim is to develop a bench-scale reactor to demonstrate H_2 generation in larger scale with Taylor Uekert, to show the potential of our systems for real-world applications.

It has been shown that ultra-sonication that breaks the aggregates of bulk $^{NCN}CN_x$ enhances the photocatalytic activity significantly. Therefore, one direction we are working towards is to synthesise carbon nitride dots, with particle sizes less than

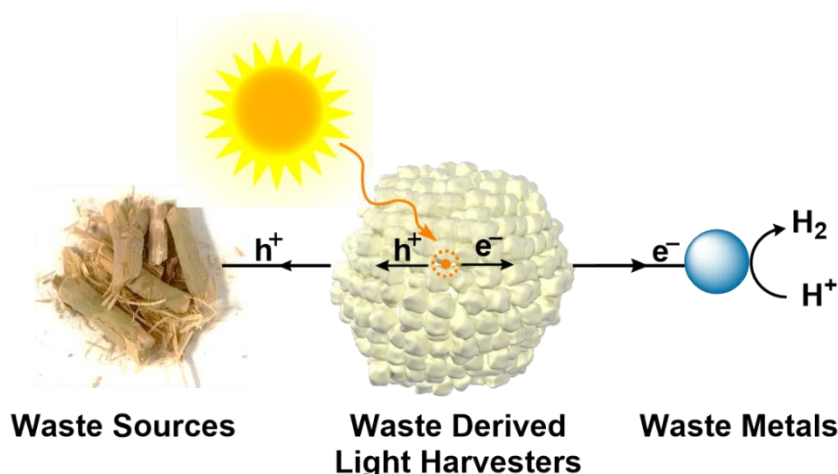**Waste Sources**   **Waste Derived Light Harvesters**   **Waste Metals**

Figure 7.2. Schematic representation of a photocatalytic system using waste for a sustainable design.

10 nm. This will bring together high photocatalytic activity and charging/discharging ability of $^{NCN}CN_x$ with good water dispersibility and enhanced photoluminescence and photoconductivity of the carbon dots. Two different approaches will be taken for the preparation of carbon nitride dots. For the bottom-up approach, dots will be prepared from carbon and nitrogen containing precursors followed by a post treatment for surface functionalisation. For the top-down approach bulk $^{NCN}CN_x$ will be synthesised followed by its chemical/thermal treatment to convert it into dots.

Ideally, any system designed from this point onward should aim to replace "synthetic" laboratory prepared components, which are heavily used in the field of photocatalysis, with waste and available abundant sources. This includes using abundant waste sources as precursors for synthesising light harvesters and as economical sacrificial electron donors, whereas metal waste can serve as co-catalysts for fuel production (Figure 7.2). Above all, any future work should be planned around the fundamental principles of large-scale applicability and sustainability.

Appendix

A. Appendix to chapter 3

A.1 Supplementary figures
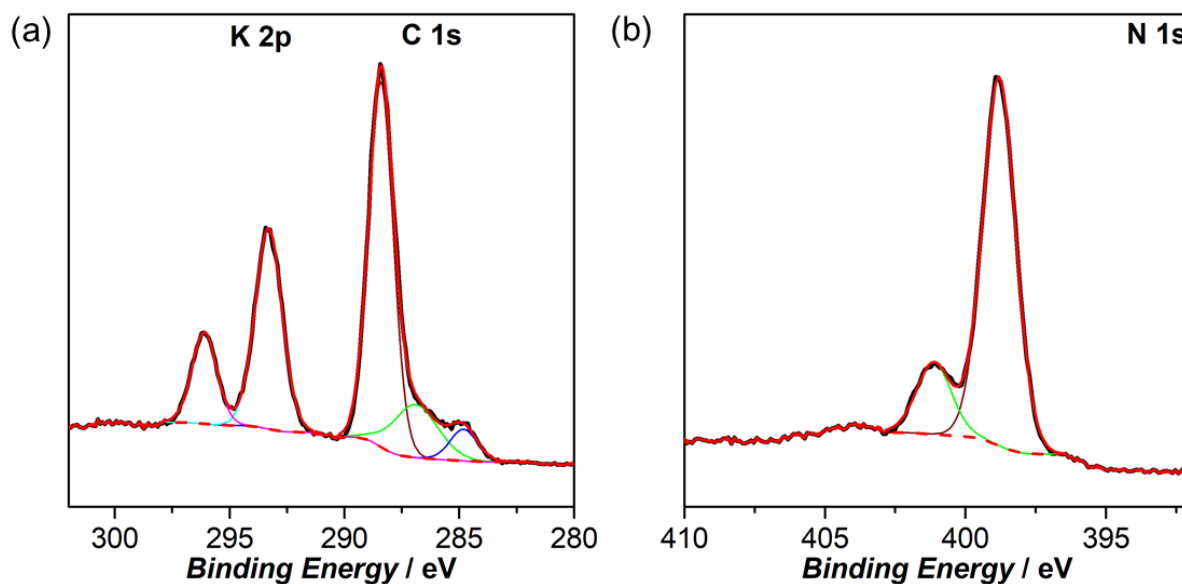
Figure A.1. XPS of $^{NCN}CN_x$ in the regions of (a) K_{2p} and C_{1s} and (b) N_{1s}. The heptazine core was identified by the presence of sp^2 carbon, 288.4 eV, and nitrogen, 398.8 eV, signals. The polymeric nature of the material was confirmed by the appearance of the signal at 401.1 eV, corresponding for the bridging secondary amine groups.
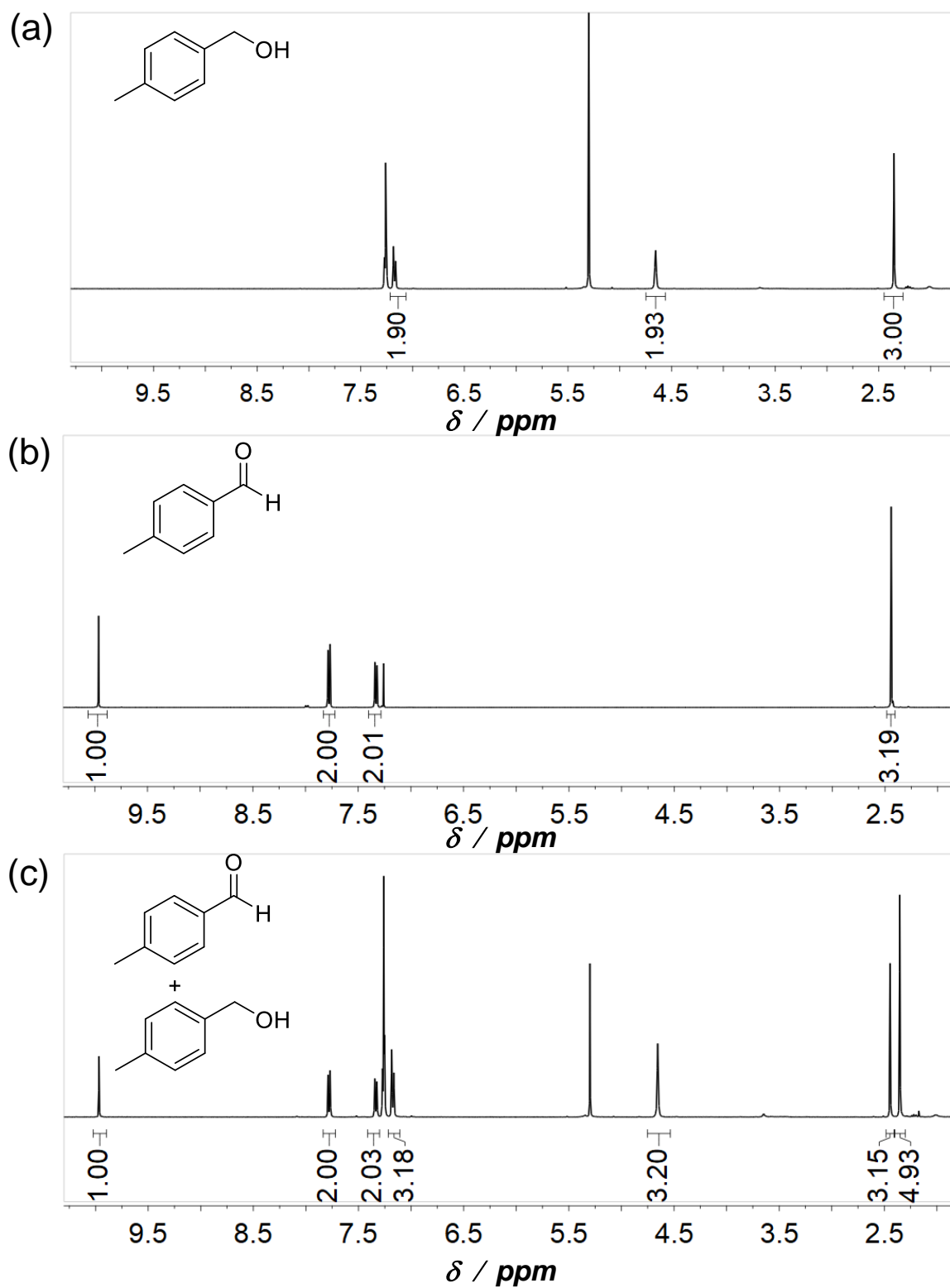
Figure A.2. ^{1}H NMR spectra of (a) 4-MBA, (b) 4-MBAd, (c) a representative residue extracted after 24 h of irradiation in CDCl$_3$.
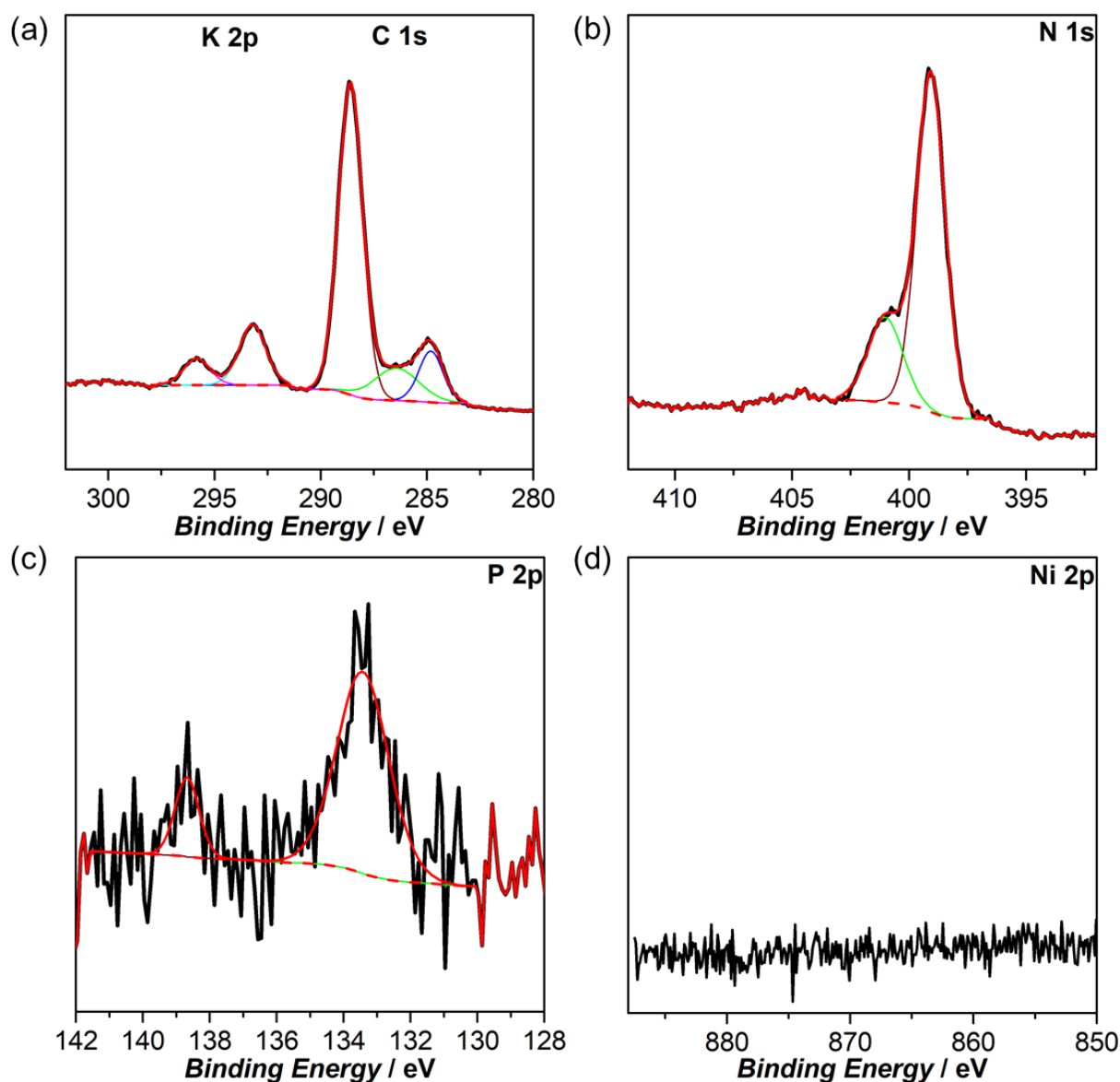
Figure A.3. Characterisation of $^{NCN}CN_x$ after 24 h of irradiation, in the presence of $^{NCN}CN_x$ (5 mg), 4-MBA (30 μmol) and **NiP** (50 nmol) in KP_i (0.02 M, pH 4.5, 3 mL) solution (1 sun irradiation, AM 1.5G, 25°C), with XPS in the regions of (a) K_{2p} and C_{1s}, (b) N_{1s}, (c) P_{2p} and (d) Ni_{2p}. The K_{2p} and C_{1s} as well as N_{1s} spectrum are in good correlation with XPS results obtained from $^{NCN}CN_x$ prior to photocatalysis. In the Ni_{2p} spectrum, there is no signal, indicating that most probably there is not any **NiP** catalyst physically adsorbed on the material surface after 24 h of irradiation. The peaks in P_{2p} spectrum are likely to be due to KP_i used during photocatalysis.
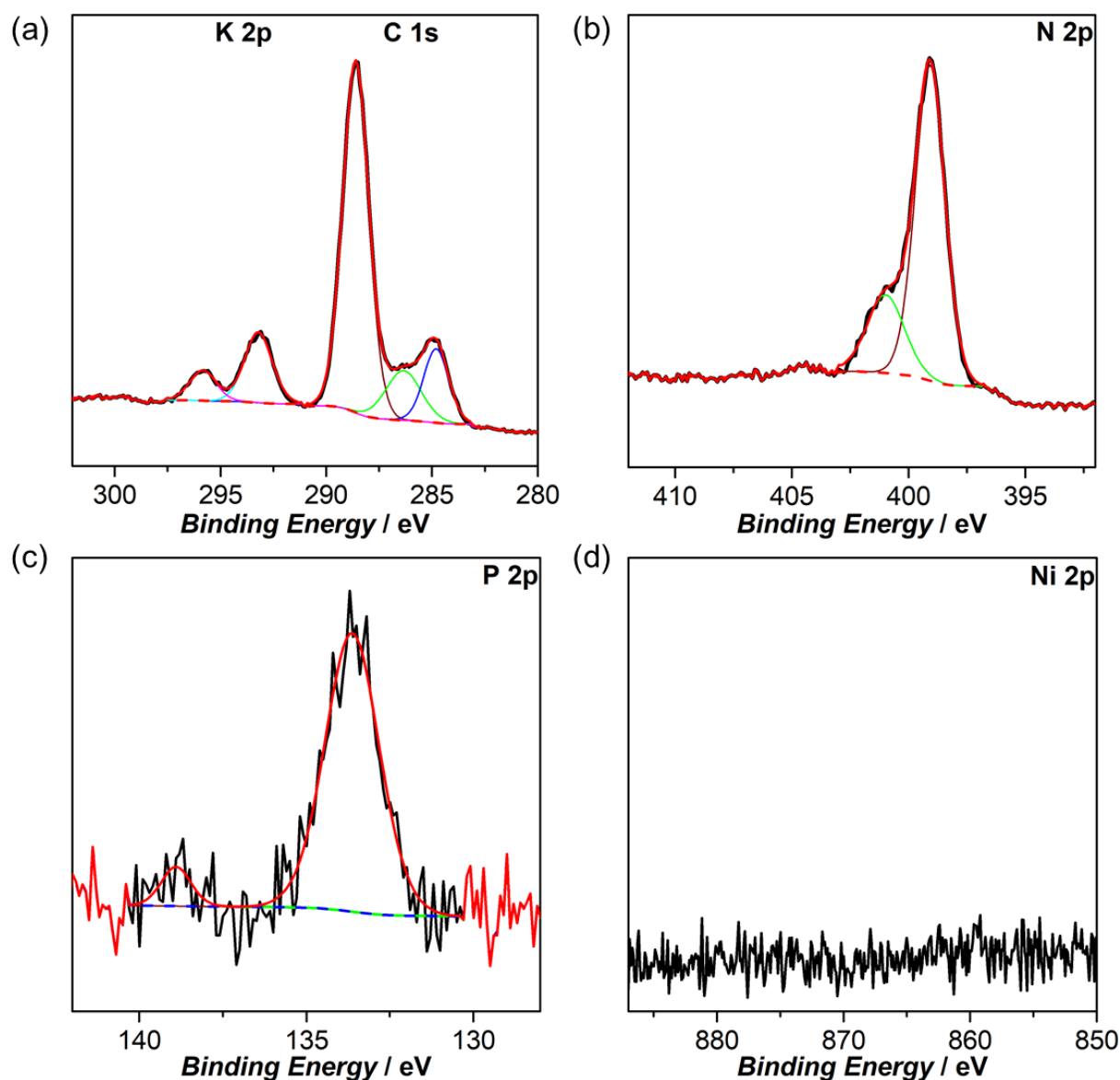
Figure A.4. Characterisation of $^{NCN}CN_x$ 24 h of irradiation, in the presence of $^{NCN}CN_x$ (5 mg) and 4-MBA (30 μmol) in KP_i (0.02 M, pH 4.5, 3 mL) solution (1 sun irradiation, AM 1.5G, 25°C), with XPS in the regions of a) K_{2p} and C_{1s}, b) N_{1s}, c) P_{2p} and d) Ni_{2p}. The K_{2p} and C_{1s} as well as N_{1s} spectrum are in good correlation with XPS results obtained from the pure $^{NCN}CN_x$ prior to photocatalysis. The peaks in P_{2p} spectrum are likely to be due to KP_i used during photocatalysis. As predicted, no peak in Ni_{2p} spectrum was detected as the photocatalysis was performed in the absence of **NiP**.
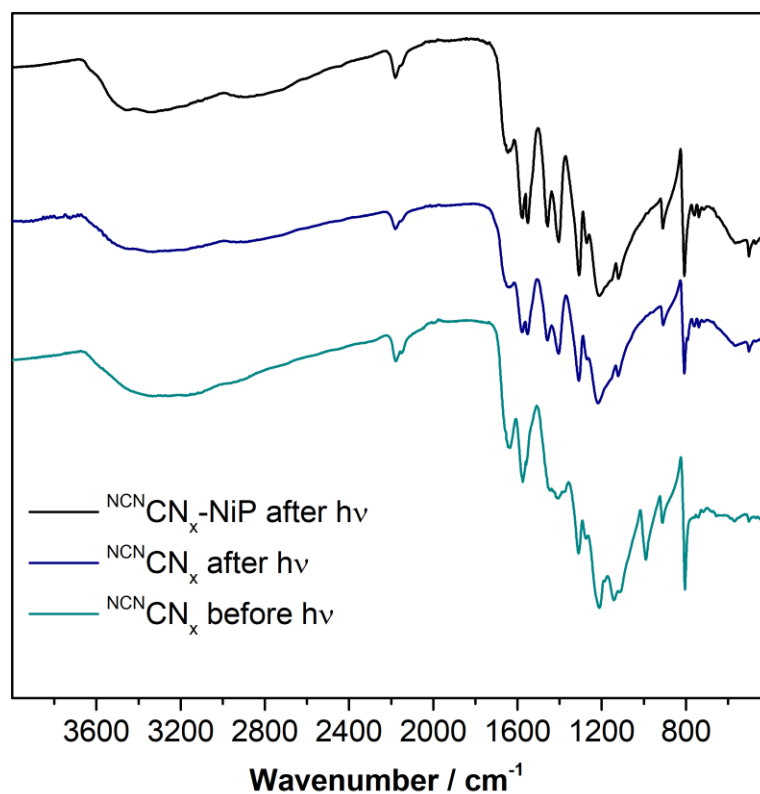
Figure A.5. Comparing FT-IR spectrum of $^{NCN}CN_x$ (5 mg) before and after irradiation (1 sun, AM 1.5G, 25°C) for 24 h in the presence of 4-MBA (30 μmol) in KP_i (0.02 M, pH 4.5, 3mL) with and without **NiP** (50 nmol).

A.2 Supplementary tables

Table A.1. Solar light driven simultaneous H_2 and aldehyde production with **NiP** and **$^{NCN}CN_x$**. Experiments were performed using **$^{NCN}CN_x$** (5 mg) in KP_i at pH 4.5 (0.02 M) containing 4-MBA and **NiP** as a hydrogen evolution catalyst under simulated solar light irradiation (100 mW cm^{-2}, AM 1.5G, 25 °C). All the experiments showed 100% selectivity towards aldehyde formation and no carboxylic acid was detected.

Entry	NiP / nmol	Alcohol / µmol	pH	Aldehyde ± σ / µmol (after 24 h)	Alcohol Conversion ± σ / (%)	H₂ ± σ / µmol (after 24 h)	TON (24 h) ± σ / mol H₂ NiP⁻¹	Activity/ µmol H₂ (g CNₓ)⁻¹h⁻¹ (after 1h)	TOF ± σ / h⁻¹ (after 1h)
pH dependence									
1	50	30	3	14.63 ± 2.35	48.77 ± 7.83	13.13 ± 1.31	262.63 ± 26.26	293.36 ± 29.34	29.34 ± 2.93
2	50	30	4.5	19.80 ± 19.8	66.0 ± 6.60	21.27 ± 2.13	425.38 ± 42.54	311.18 ± 31.12	31.12 ± 3.11
3	50	30	6	16.25 ± 1.62	54.16 ± 5.42	14.80 ± 1.48	296.02 ± 29.60	232.70 ± 23.27	23.27 ± 2.33
[Alcohol] dependence									
4	50	15	4.5	11.93 ± 1.19	79.51 ± 7.95	13.46 ± 1.35	269.17 ± 26.92	266.89 ± 26.69	26.69 ± 2.67
5	50	30	4.5	19.80 ± 1.98	66.0 ± 6.60	21.27 ± 2.13	425.38 ± 42.54	311.18 ± 31.12	31.12 ± 3.11
6	50	60	4.5	16.54 ± 1.71	27.57 ± 2.86	15.46 ± 1.55	309.13 ± 30.91	240.59 ± 24.06	24.06 ± 2.41
[NiP] dependence									
7	10	30	4.5	8.60 ± 0.86	28.67 ± 2.87	2.48 ± 0.46	247.72 ± 46.10	86.83 ± 9.70	43.42 ± 4.85
8	25	30	4.5	11.10 ± 2.46	37.00 ± 8.19	5.22 ± 1.21	208.95 ± 48.37	158.51 ± 15.85	31.70 ± 3.17
9	50	30	4.5	19.80 ± 1.98	66.0 ± 6.60	21.27 ± 2.13	425.38 ± 42.54	311.18 ± 31.12	31.12 ± 3.11
10	100	30	4.5	24.60 ± 2.95	82.00 ± 9.85	24.97 ± 2.50	249.72 ± 24.97	409.80 ± 40.98	20.49 ± 2.05

Table A.2. Time dependent solar light driven H_2 and aldehyde production in the presence of $^{NCN}CN_x$ (5 mg), 4-MBA (30 µmol) and **NiP** (50 nmol) in KP_i (0.02 M, pH 4.5, 3 mL) with 1 sun irradiation (AM 1.5G) in water-jacketed rack at 25 °C. All the experiments showed 100% selectivity towards aldehyde formation and no carboxylic acid was detected.

Entry	Time / h	Aldehyde ± σ / µmol	Alcohol Conversion ± σ / (%)	H_2 ± σ / µmol	TON ± σ / mol H_2 NiP^{-1}
11	1	2.37 ± 0.47	7.90 ± 1.56	1.64 ± 0.16	32.88 ± 3.23
12	2	3.55 ± 0.84	11.84 ± 2.79	3.74 ± 0.37	74.83 ± 7.48
13	3	5.33 ± 0.53	17.78 ± 1.78	5.23 ± 0.52	104.59 ± 10.46
14	4	6.55 ± 0.66	21.84 ± 2.18	5.92 ± 0.59	118.30 ± 11.83
15	5	6.65 ± 0.66	22.16 ± 2.22	8.04 ± 0.80	160.72 ± 16.07
16	6	8.27 ± 1.39	27.57 ± 4.64	10.28 ± 1.03	205.66 ± 20.57
17	12	11.47 ± 1.51	38.57 ± 4.64	12.37 ± 1.24	247.40 ± 24.74
18	24	19.80 ± 1.98	66.0 ± 6.60	21.27 ± 2.13	425.38 ± 42.54

Table A.3. Photocatalytic H_2 and aldehyde production in the presence of $^{NCN}CN_x$ (5 mg), 4-MBA (30 µmol) and **NiP** (50 nmol) in KP$_i$ (0.02 M, pH 4.5, 3 mL) under visible-light-only ($\lambda > 400$ nm) irradiation. Control experiments were also performed in the absence of $^{NCN}CN_x$, **NiP**, 4-MBA and in dark. Different para substituted benzyl alcohol (BA) derivatives (30 µmol) were tested in the presence $^{NCN}CN_x$ (5 mg) and **NiP** (50 nmol) in KP$_i$ (0.02 M, pH 4.5, 3 mL) under 1 sun irradiation (AM 1.5G). All the experiments showed 100% selectivity towards aldehyde formation and no carboxylic acid was detected unless specified otherwise.

Entry	NiP / nmol	Alcohol	Alcohol / µmol	Aldehyde ± σ / µmol (after 24 h)	Alcohol Conversion (%)	H_2 ± σ / µmol (after 24 h)	TON (24 h) ± σ / mol H_2 NiP^{-1}	Activity/ µmol H_2 (g CN$_x$)$^{-1}$h^{-1} (after 1h)	TOF ± σ / h^{-1} (after 1h)
Visible Light only Irradiation ($\lambda > 400$ nm)									
19	50	4-MBA	30	10.02 ± 2.08	33.67 ± 6.50	10.31 ± 1.20	206.25 ± 24.07	122.93 ± 12.29	12.29 ± 1.23
Control Experiments									
20	0	4-MBA	30	7.30 ± 0.73	24.33 ± 2.43	0.33 ± 0.03	–	3.37 ± 3.37	–
21	50	0	–	–	–	0.11 ± 0.02	2.10 ± 0.30	16.04 ± 3.05	1.60 ± 0.31
22	50, No $^{NCN}CN_x$	4-MBA	30	0	0	0	0	–	–
23	50, dark	4-MBA	30	0	0	0	0	0	0
Alcohol Dependence									
24	50	BA	30	13.70 ± 2.70	45.67 ± 9.02	21.47 ± 2.15	429.55 ± 42.96	289.62 ± 39.48	28.96 ± 3.95
25	50	4-OMeBA	30	13.73 ± 1.37	45.78 ± 4.58	9.84 ± 0.98	196.70 ± 19.67	233.33 ± 23.33	23.33 ± 2.33
26	50	4-ClBA	30	13.4 ± 2.11	44.67 ± 7.02	14.06 ± 2.98	281.23 ± 59.60	254.09 ± 25.41	25.41 ± 2.51
27	50	4-CF$_3$BA	30	1.83 ± 0.61	6.09 ± 2.03	5.15 ± 0.55	103.09 ± 11.04	99.60 ± 9.96	9.96 ± 1.00
28	50	4-^{t}BuBA	30	7.84 ± 1.41	40.83 ± 9.00*	9.90 ± 0.99	198.07 ± 19.80	823.24 ± 82.32	82.32 ± 8.23
29	50	MeOH	30	0	0	0	0	0	0

*These experiments resulted in 41% alcohol oxidation with 64% selectivity towards 4-*tert*-Butylbenzaldehyde and 36% to 4-*tert* butylbenzoic acid formation.

Table A.4. Solar light driven H_2 and aldehyde production in the presence of $^{NCN}CN_x$ (5 mg), 4-MBA (30 μmol) and **NiP** (50 nmol) in aqueous sodium acetate buffer, and KP_i (pH 4.5, 3 mL) at different concentrations under 1 sun irradiation (AM 1.5G). Sacrificial conditions were also tested in EDTA (0.1 M, pH 4.5, 3 mL) without 4-MBA and in KP_i (0.02 M, pH 4.5, 3 mL) under air without **NiP**. All the experiments showed 100% selectivity towards aldehyde formation and no carboxylic acid was detected unless specified otherwise.

Entry	NiP / nmol	Solution	[Solution]	Aldehyde ± σ / μmol (after 24 h)	Alcohol Conversion ± σ / (%)	H_2 ± σ / μmol (after 24 h)	TON (24 h) ± σ / mol H_2 NiP^{-1}	Activity / μmol H_2 $(g CN_x)^{-1}$ h^{-1} (after 1h)	TOF ± σ / h^{-1} (after 1h)
Solution dependence									
30	50	CH_3COONa	0.1 M	12.03 ± 1.20	40.11 ± 4.01	9.69 ± 0.97	193.74 ± 19.37	360.02 ± 36.00	36.00 ± 3.60
31	50	KP_i	0.1 M	24.90 ± 2.49	83.0 ± 8.30	20.44 ± 2.04	408.76 ± 40.88	762.70 ± 76.27	76.27 ± 7.63
32	50	KP_i	0.5 M	18.13 ± 1.81	60.44 ± 6.04	18.62 ± 1.86	372.39 ± 37.24	1114.21 ± 111.42	111.42 ± 11.14
33	50	KP_i + KCl	0.02 M + 0.08 M	20.27 ± 3.77	67.56 ± 12.58	23.34 ± 2.33	466.78 ± 46.68	539.28 ± 59.12	53.93 ± 5.91
34	50	KP_i + K_2SO_4	0.02 M + 0.08 M	20.00 ± 2.00	66.67 ± 6.67	20.97 ± 2.10	419.45 ± 41.95	492.04 ± 49.20	49.20 ± 4.92
Sacrificial Conditions									
35	50	EDTA	0.1 M	-	-	21.21 ± 2.12	424.18 ± 42.42	532.32 ± 53.22	52.23 ± 5.23
36	0	KP_i, under air	-	6.04 ± 2.09	100†	-	-	-	-
37	0, dark	KP_i, under air	-	0	0	-	-	-	-

†These experiments resulted in 100% alcohol conversion with 70% selectivity towards 4-methyl benzoic acid, 20% 4-methyl benzaldehyde and 10% to further oxidation products (benzene-1, 4-dicarbaldehyde and 4-formylbenzoic acid) formation.

Table A.5. Photocatalytic H$_2$ and aldehyde production with ^{H_2N}**CN$_x$** (5 mg), 4-MBA (30 μmol) and **NiP** (50 nmol) in KP$_i$ (0.02 M, pH 4.5, 3 mL) were conducted under 1 sun irradiation (AM 1.5G, 25 °C). Photocatalytic experiments in the presence of ^{NCN}**CN$_x$** (5 mg) or ^{H_2N}**CN$_x$** (5 mg), 4-MBA (30 μmol) and H$_2$PtCl$_6$ (10 μL, 8 wt%) in KP$_i$ (0.02 M, pH 4.5, 3 mL) were also carried out. A control experiment in EDTA (0.1 M, pH 4.5, 3 mL) solution with 4-MBAd, ^{NCN}**CN$_x$** (5 mg) and H$_2$PtCl$_6$ was also tested. All the experiments showed 100% selectivity towards aldehyde formation and no carboxylic acid was detected unless specified otherwise.

Entry	Catalyst	CN$_x$	Substrate	Solution	Aldehyde ± σ / μmol (after 24 h)	Substrate Conversion ± σ / (%)	H$_2$ ± σ / μmol (after 24 h)	TON (24 h) ± σ / mol H$_2$ NiP^{-1}	Activity/ μmol H$_2$ (g CN$_x$)$^{-1}$ h^{-1} (after 1h)	TOF ± σ / h^{-1} (after 1h)
Irradiate for 4 h										
38	NiP	^{H_2N}CN$_x$	4-MBA	KP$_i$	1.44 ± 0.71	4.80 ± 2.36	2.02 ± 0.20	40.31 ± 4.03	125.05 ± 12.50	12.50 ± 1.25
39	Pt#	^{H_2N}CN$_x$	4-MBA	KP$_i$	1.28 ± 0.55	4.26 ± 1.85	0	0	0	0
40	Pt#	^{NCN}CN$_x$	4-MBA	KP$_i$	1.79 ± 1.21	5.98 ± 4.05	1.56 ± 0.16	0.80 ± 0.08	170.68 ± 18.97	0.44 ± 0.05
Irradiate for 24 h										
41	NiP	^{H_2N}CN$_x$	4-MBA	KP$_i$	1.44 ± 0.71	4.80 ± 2.36	2.49 ± 0.71	49.79 ± 14.18	117.30 ± 11.73	11.73 ± 1.17
42	Pt#	^{NCN}CN$_x$	4-MBA	KP$_i$	11.99 ± 2.29	41.1 ± 7.85‡	14.22 ± 1.42	7.29 ± 0.73	138.43 ± 13.08	0.35 ± 0.03
43	Pt#	^{NCN}CN$_x$	4-MBAd	EDTA	5.42 ± 0.54	18.07 ± 1.81**	3.50 ± 0.44	1.79 ± 0.23	9.46 ± 4.88	0.02 ± 0.01

#These experiments were conducted in the presence of 10 μL of 8 wt% aqueous solution of H$_2$PtCl$_6$ corresponding for 8 wt% Pt loading.

‡These experiments resulted in 41% alcohol oxidation with 97:3% selectivity towards 4-MBAd and 4-methylbenzoic acid formation respectively.

**These experiments resulted in 18% 4-methylbenzoic acid formation.

Table A.6. Photocatalytic H_2 and aldehyde production in the presence of $^{NCN}\textbf{CN}_\textbf{x}$ (5 mg), 4-MBA (30 µmol) and **NiP** (50 nmol) in KP_i (0.02 M, pH 4.5, 3 mL) with the addition of neutral density filters (50% and 80% absorbance of the incident light) were conducted. All the experiments showed 100% selectivity towards aldehyde formation and no carboxylic acid was detected.

Entry	Aldehyde ± σ / µmol (after 1 h)	Alcohol Conversion ± σ / (%)	Selectivity ± σ / (%)	H_2 ± σ / µmol (after 1 h)	Activity/ µmol H_2 (g CN_x)$^{-1}$ h^{-1} (after 1h)	TOF ± σ / h^{-1} (after 1h)
No neutral density filter						
44	2.29 ± 0.23	7.64 ± 0.76	100	1.49 ± 0.15	297.73 ± 18.29	29.77 ± 1.83
50% neutral density filter						
45	1.37 ± 0.16	4.27 ± 0.43	100	0.95 ± 0.10	190.01 ± 12.35	19.00 ± 1.90
80% neutral density filter						
46	0.88 ± 0.09	2.94 ± 0.29	100	0.54 ± 0.05	108.30 ± 1.87	10.83 ± 1.08

Table A.7. Long-term photocatalytic H_2 and Aldehyde production in the presence of ^{NCN}**CN$_x$** (5 mg), 4-MBA (30 µmol) and **NiP** (50 nmol) in KP$_i$ (0.02 M, pH 4.5, 3 mL) under 1 sun irradiation (AM 1.5G, 25 °C). After 25 h of irradiation, fresh **NiP** (50 nmol), fresh 4-MBA (30 µmol), and both **NiP** (50 nmol) and 4-MBA (30 µmol) were added to photoreactors to test the system re-activation, and placed back into solar light simulator for monitoring over 25 more h (Total irradiation time of 50 h). All the experiments showed 100% selectivity towards aldehyde formation and no carboxylic acid was detected.

Entry	NiP / nmol	Alcohol/ µmol	Aldehyde ± σ / µmol	Alcohol Conversion ± σ / (%)	H_2 ± σ / µmol	Activity / µmol H_2 (g CN_x)$^{-1}$ h^{-1} (after 1h)	TOF ± σ / h^{-1} (after 1h)
Re-activation by NiP addition							
47	50+50	30	25.04 ± 2.90	83.47 ± 9.66	26.96 ± 2.70	244.59 ± 24.46	24.46 ± 2.45
Re-activation by 4-MBA addition							
48	50	30+30	13.47 ± 2.40	22.44 ± 3.99	16.97 ± 1.70	230.21 ± 12.92	23.02 ± 2.30
Re-activation by NiP and 4-MBA addition							
49	50+50	30+30	21.13 ± 2.21	35.21 ± 3.68	28.29 ± 2.83	227.86 ± 6.45	22.79 ± 2.28

B. Appendix to chapter 4

B.1 Supplementary text

Analysis of transient absorption spectroscopy data

Decays could be fit to a power law of the form $y = y_0 + |t - t_0|^{-b}$ (Figure B.5). t_0 represents the time offset between the trigger signal and the arrival of the excitation pulse to the sample, while y_0 is the absorbance offset at infinite times. The parameter b was about 0.35 and t_0 was typically 1 x 10^{-7} s. No trends with respect to the concentration of 4-MBA or **NiP** were observed.

In order to quantify the concentration of long-lived species, we used the amplitude at 3 µs to estimate the initial population of excited species, and the amplitude at 100 ms for the population of long-lived species. The yield of the long-lived species was then calculated as:

$$\Phi_{long-lived} = \frac{A_{t=100ms}}{A_{t=3\mu s}}$$

(B.1)

The calculated yields are shown in Figure B.7. As mentioned in Chapter 4, the amplitude at 3 µs will underestimate the excited state species concentration immediately after the excitation pulse. As a result, the yields calculated from equation B.1 are overestimated. Without data spanning femtoseconds to nanoseconds under similar excitation conditions, we are not able to quantify the total photogenerated excited species population. Despite the issues identified, the data clearly indicated

that 4-MBA affect the transient absorption signal in the microsecond timescale, while reaction with **NiP** occurs on timescales longer than 2 s.

Assuming dynamic quenching, we can estimate the bimolecular rate constant of hole transfer from $^{NCN}CN_x^*$ to 4-MBA (k_{rxn}) by first writing the expression for the yield for competitive kinetics:

$$\Phi_{long-lived} = \frac{k_{form}}{k_{1/2} + k_{form}} \quad \text{(B.2)}$$

$$where \ k_{form} = k_0 + k_{rxn}[4 - MBA]$$

$k_{1/2}$ is the inverse of the characteristic lifetime ($\tau_{1/2}$) of the decay of $^{NCN}CN_x$ without scavengers. We then rearrange equation B.2 to calculate the rate of formation (k_{form}):

$$k_{form} = -\frac{\Phi_{long-lived}k_{1/2}}{\Phi_{long-lived} - 1} \quad \text{(B.3)}$$

Finally, a linear fit of the plot k_{form} vs. [4-MBA] yields k_{rxn} as the slope.

B.2 Supplementary figures
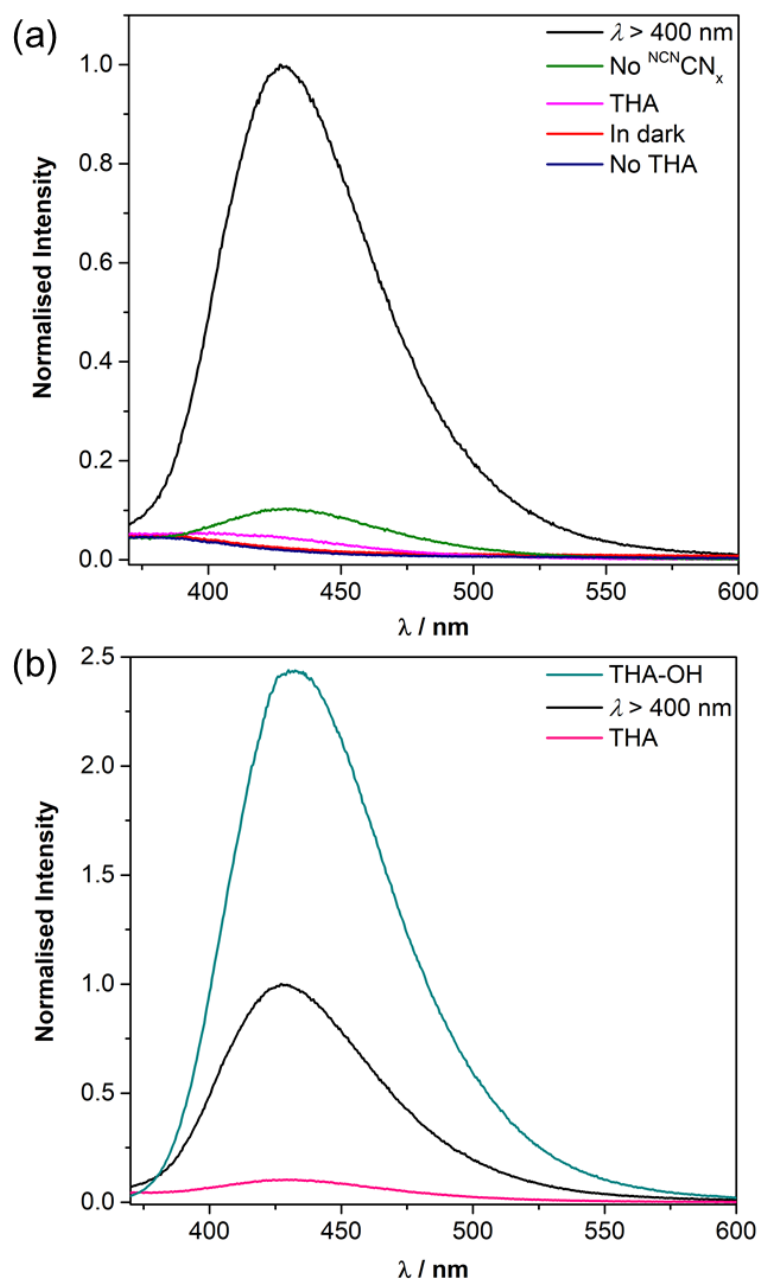
Figure B.1. (a) PL spectra recorded with spectrofluorometer equipped with an integrating sphere for $^{NCN}CN_x$ (5 mg) and terephthalic acid, THA (30 μmol) in KP$_i$ solution (0.1 M, pH 4.5, 3 mL) after 1 h of irradiation ($\lambda > 400$ nm). The sample was centrifuged, and the emission spectrum was recorded for the supernatant with λ_{ex} = 315 nm and λ_{em} = 360–600 nm. Control experiments in the absence of THA, light, $^{NCN}CN_x$ and only THA are also shown. (b) PL spectra recorded for THA and 2-hydroxyterephthalic acid, THA-OH (0.05 μmol), as reference are also shown. Black trace in both plots corresponds to same conditions. Formation of < 0.02 μmol of THA-OH was detected.
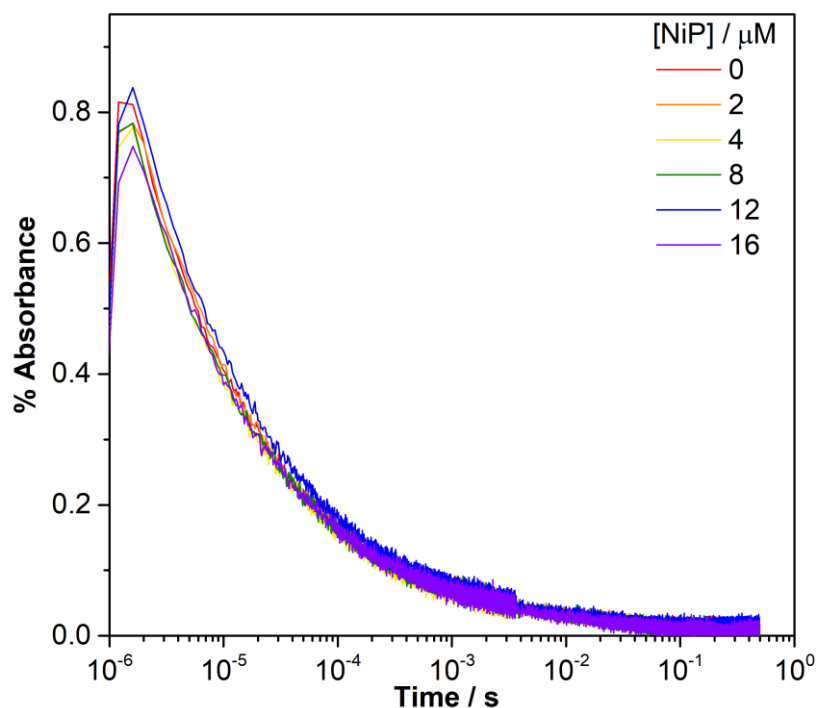
Figure B.2. Transient decays probed at λ = 750 nm of $^{NCN}CN_x$ (5 mg mL^{-1}) suspension in aqueous KP$_i$ solution (0.02 M, pH 4.5, 25 °C) with varying concentrations of **NiP** following λ = 355 nm excitation.
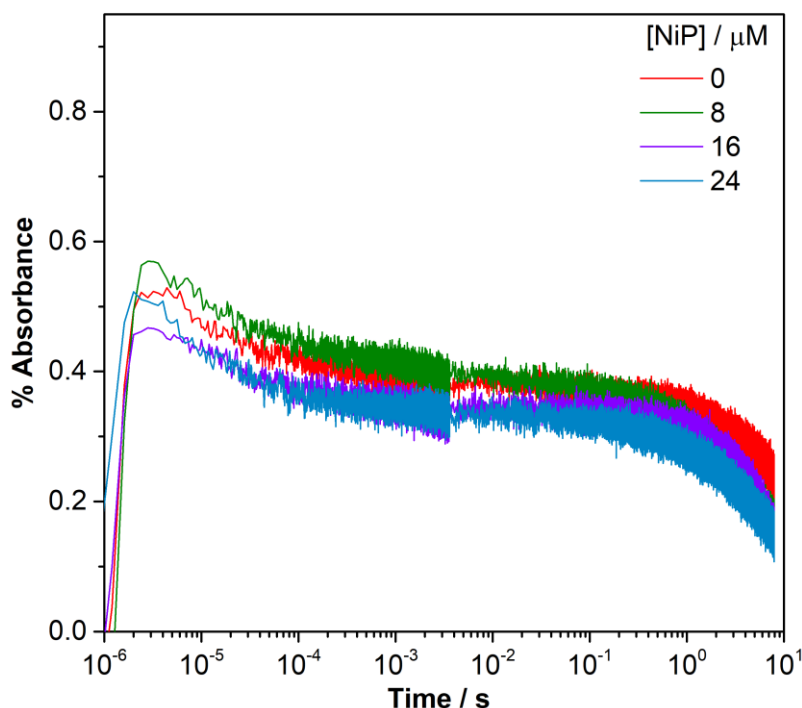
Figure B.3. Transient decays probed at λ = 750 nm of $^{NCN}CN_x$ (1.2 mg mL^{-1}) suspension in aqueous KP$_i$ solution (0.02 M, pH 4.5, 25 °C) in the presence 4-MBA (10 mM) with varying concentrations of **NiP** following λ = 355 nm excitation. Note that changes in the absorbance past ~2 s are caused by settling of the heterogeneous dispersion.
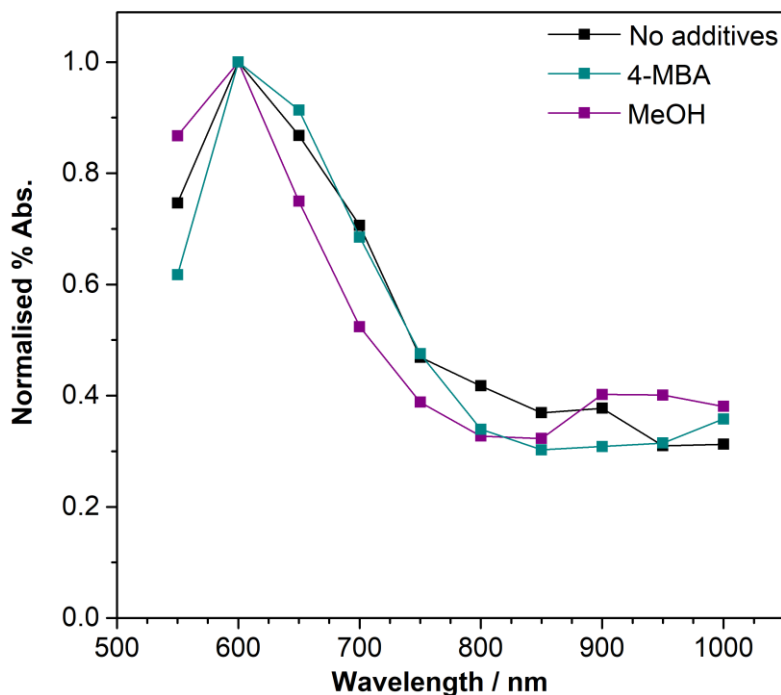
Figure B.4. Normalised transient absorption spectra of $^{NCN}CN_x$ (1.2 or 5 mg mL^{-1}) suspension in aqueous KP$_i$ solution (0.02 M, pH 4.5, 25 °C, black line), spectra in the presence of 4-MBA (10 mM) and in a MeOH solution (20% by volume) following λ = 355 nm excitation are also shown. Spectra were taken at 100 µs delay time.
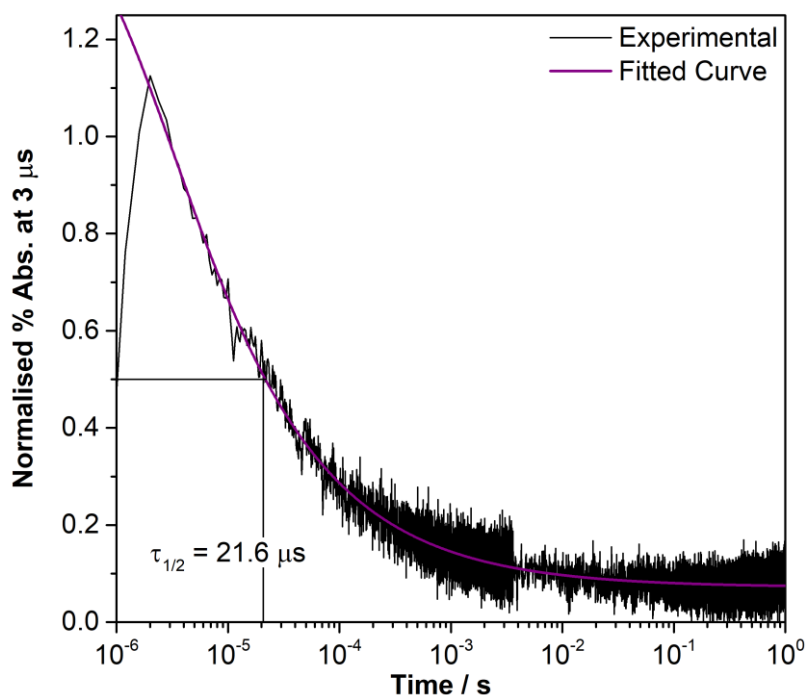
Figure B.5. Normalised transient decay of $^{NCN}CN_x$ (1.2 mg mL^{-1}) suspension in aqueous KP$_i$ solution (0.02 M, pH 4.5, 25 °C) probed at λ = 750 nm following λ = 355 nm excitation. A power law fit (purple line) is overlaid to the experimental data (black line).
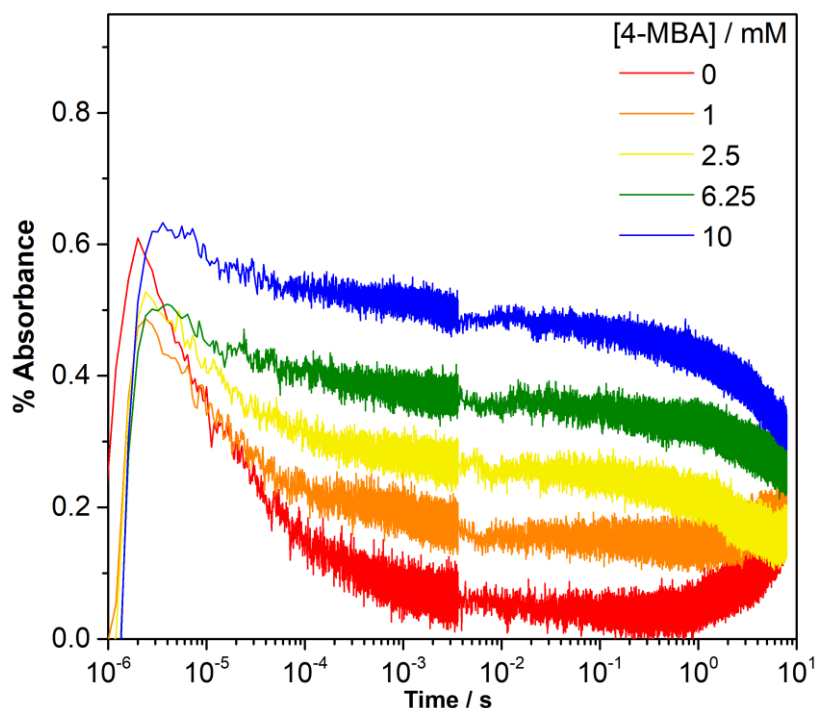
Figure B.6. Transient decays probed at λ = 750 nm of $^{NCN}CN_x$ (1.2 mg mL^{-1}) suspension in aqueous KP$_i$ solution (0.02 M, pH 4.5, 25 °C) in the presence of varying concentrations of 4-MBA following λ = 355 nm excitation. Note that changes in absorbance past ~2 s are caused by settling of the heterogeneous dispersion.
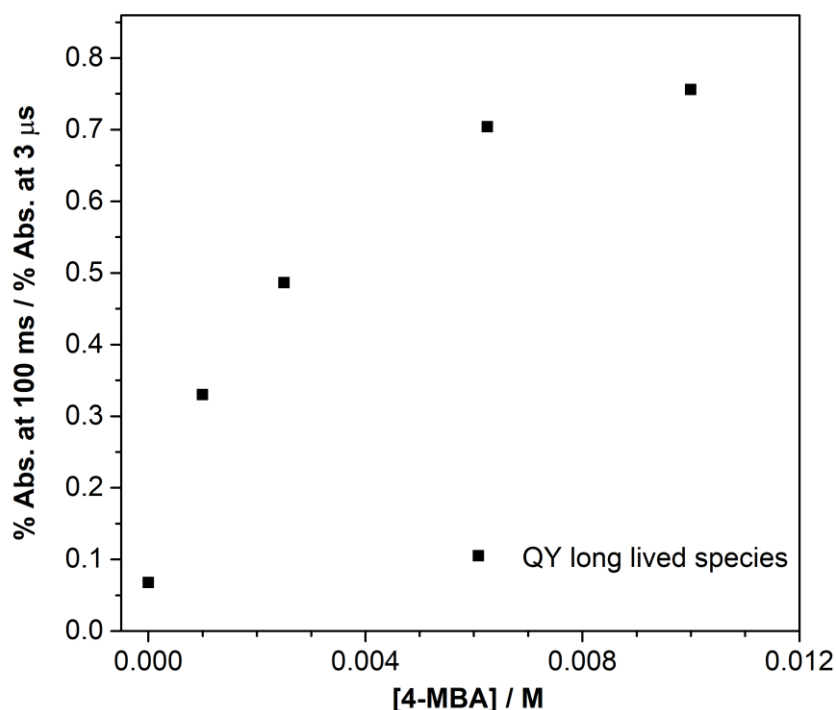
Figure B.7. Yield of formation of the long-lived electron species versus 4-MBA concentration.

151
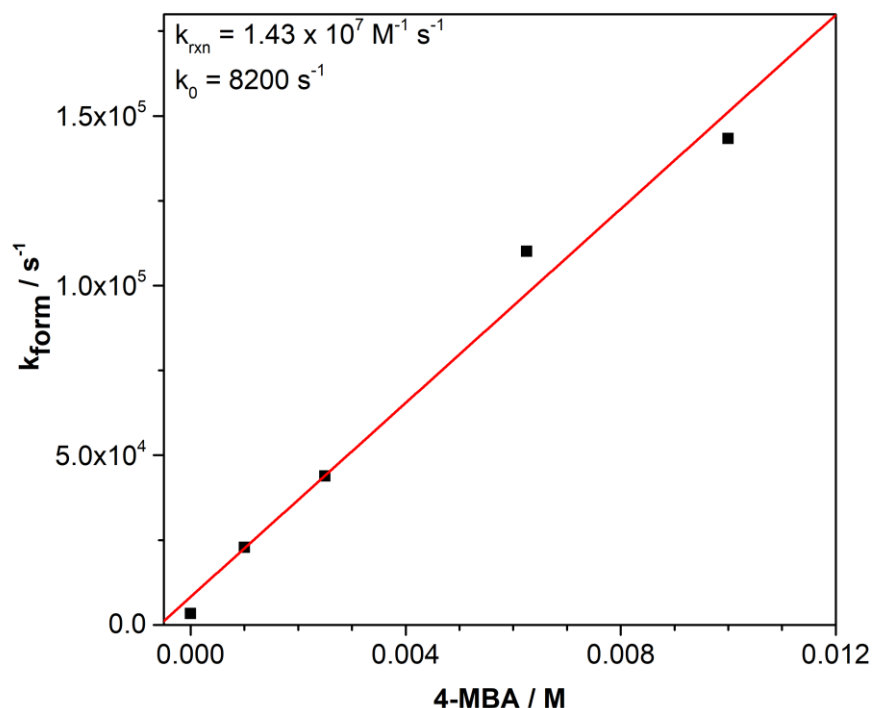
Figure B.8. Rate of formation of the long-lived electron species versus 4-MBA concentration. The rate constant of the reaction between $^{NCN}CN_x$ and 4-MBA is obtained from the slope of the linear fit, whereas the background rate is taken from the intercept.
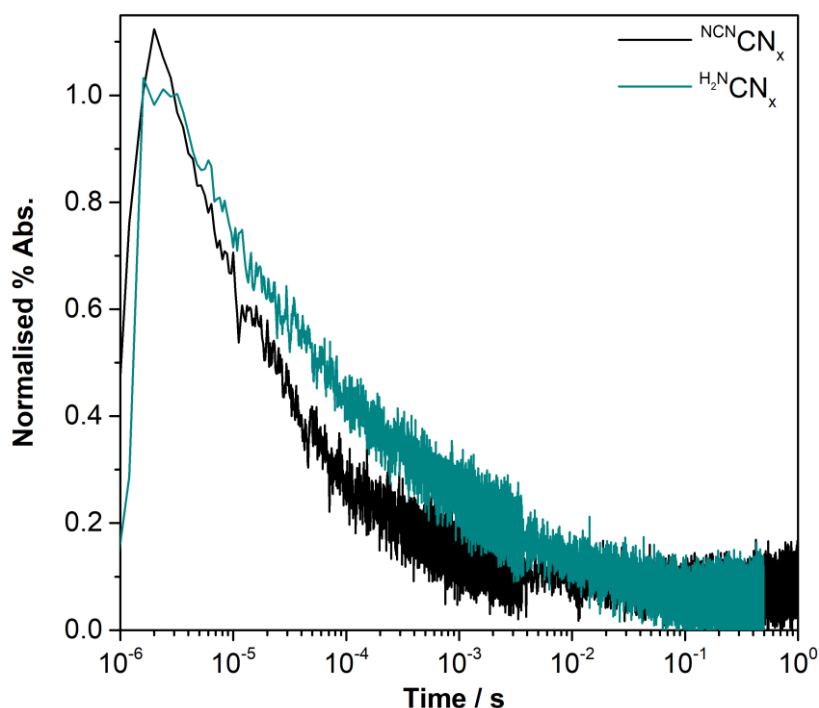
Figure B.9. Normalised (at 3 µs) transient decays probed at λ = 750 nm of $^{NCN}CN_x$ (1.2 mg mL^{-1}) and $^{H_2N}CN_x$ (1.2 mg mL^{-1}) suspensions in aqueous KP$_i$ solution (0.02 M, pH 4.5, 25 °C) following λ = 355 nm excitation.

B.3 Supplementary tables

Table B.1. Two photoreactors were prepared with $^{NCN}CN_x$ (5 mg) and 4-MBA (30 µmol) in the absence of **NiP** in an aqueous KP_i solution (0.02 M, pH 4.5, 3 mL) and irradiated for 4 h under 1 sun (AM 1.5G, 25°C). The vials were then taken into the dark, **NiP** (50 nmol) was added to one of them and the H_2 production was monitored for both of the vials over the next 20 h.

Entry	NiP / nmol	Aldehyde ± σ / µmol	Alcohol Conversion ± σ / (%)	H_2 ± σ / µmol	TON (24 h) ± σ / mol H_2 NiP^{-1}	Activity/ µmol H_2 (g CN_x)$^{-1}$ h^{-1} (after 1h)	TOF ± σ / h^{-1} (after 1h)
Irradiate for 4h and move to dark							
1	0	1.56 ± 0.40	5.18 ± 1.34	0.26 ± 0.03	–	9.34 ± 0.09	–
Irradiate for 4h, move to dark and add NiP							
2	50	1.97 ± 0.65	6.50 ± 2.17	1.46 ± 0.15	24.89 ± 2.49	11.71 ± 1.17	1.17 ± 0.12

153

Table B.2. Solar light driven alcohol oxidation and proton reduction in the presence of $^{NCN}CN_x$ and **NiP** for mechanistic interpretation. Experiments were performed using $^{NCN}CN_x$ (5 mg) in aqueous KP_i solution (0.1 M, pH 4.5) containing 4-MBA (30 μmol), or benzyl alcohol, BA (30 μmol) and **NiP** (50 nmol). The samples were irradiated under 1 sun (AM 1.5G, 100 mW cm^{-2}, 25 °C). Total solvent volume was 3 mL with a headspace volume of 4.74 mL.

Entry	Conditions	Gas detected	Aldehyde ± σ / μmol (after 4 h)	Alcohol Conversion ± σ / (%)	H_2/D_2 ± σ / μmol (after 4 h)	TON (4 h) ± σ / mol H_2 NiP^{-1}	Activity/ μmol H_2 (g CN$_x$)$^{-1}$h^{-1} (after 1h)	TOF ± σ / h^{-1} (after 1h)
Solvent Screening								
3	H_2O, 4-MBA	H_2	9.85 ± 1.69	32.83 ± 5.64	11.85 ± 1.00	236.92 ± 20.09	675.92 ± 27.10	67.59 ± 2.71
4	D_2O, 4-MBA	D_2	8.18 ± 1.21	27.27 ± 4.03	10.80 ± 0.03	215.92 ± 0.56	489.78 ± 23.17	48.98 ± 2.32
Substrate Screening								
5	BA	H_2	6.63 ± 0.51	22.11 ± 1.71	7.19 ± 0.37	143.83 ± 7.46	445.71 ± 9.70	44.57 ± 0.97
6	D_2-BA	H_2	6.33 ± 0.25	21.11 ± 0.84	6.26 ± 0.26	125.21 ± 5.25	366.38 ± 19.70	36.64 ± 1.97
Electron Acceptors								
7	N_2, NiP	H_2	9.85 ± 1.69	32.83 ± 5.64	11.85 ± 1.00	236.92 ± 20.09	675.92 ± 27.10	67.59 ± 2.71
8	N_2, No NiP	H_2	1.89 ± 1.04	6.29 ± 3.46	0	0	0	0
9	Air, No NiP	H_2	13.78 ± 1.15	45.94 ± 3.84	0	0	0	0

*All the experiments showed 100% selectivity towards aldehyde formation and no carboxylic acid was detected.

154
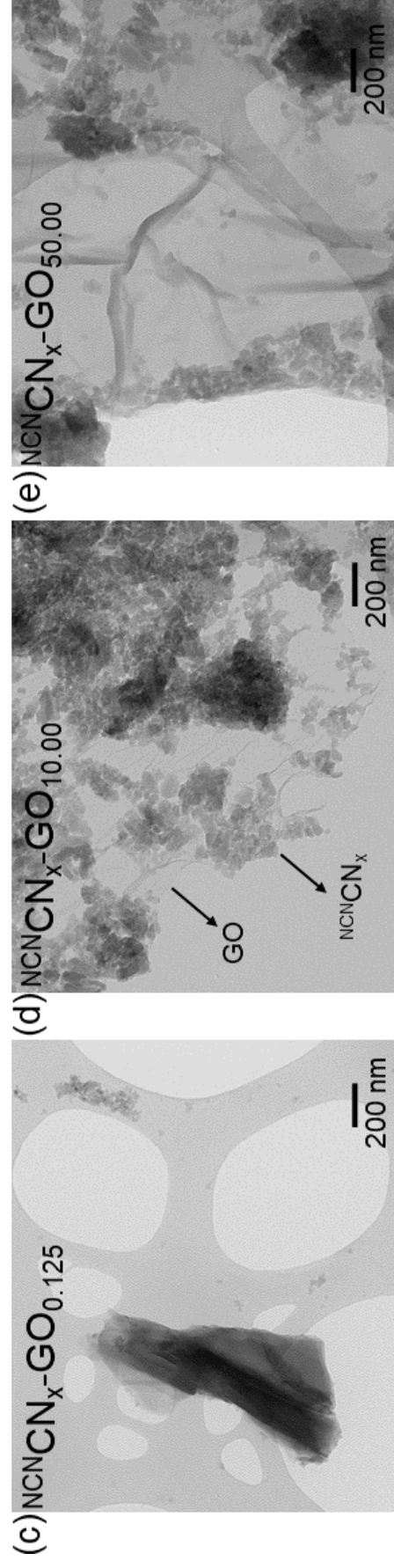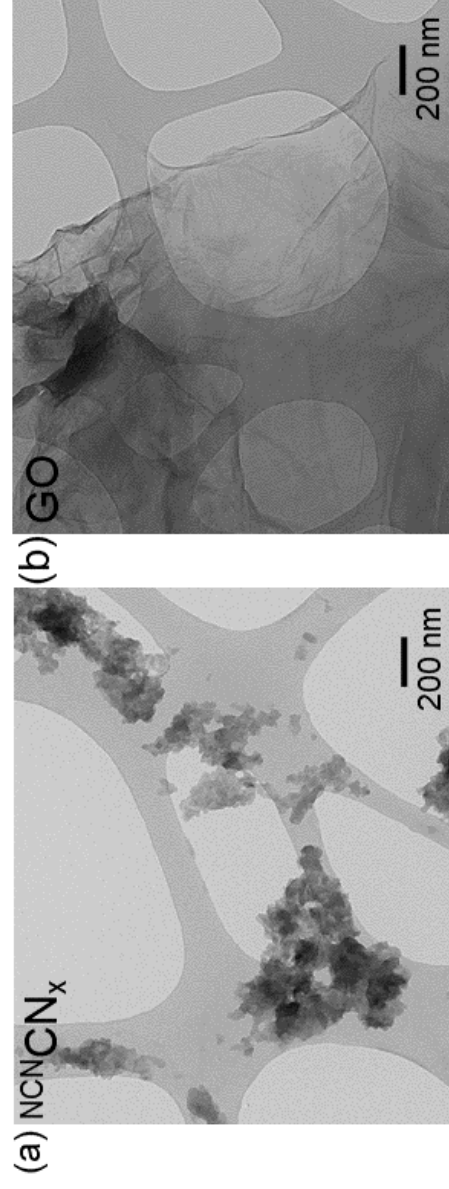
C. Appendix to chapter 5

C.1 Supplementary figures

Figure C.1. TEM images of (a) bare $^{NCN}CN_x$, (b) bare GO and $^{NCN}CN_x$–GO hybrids with (c) 0.125, (d) 10.00 and (e) 50.00 wt% GO loading.
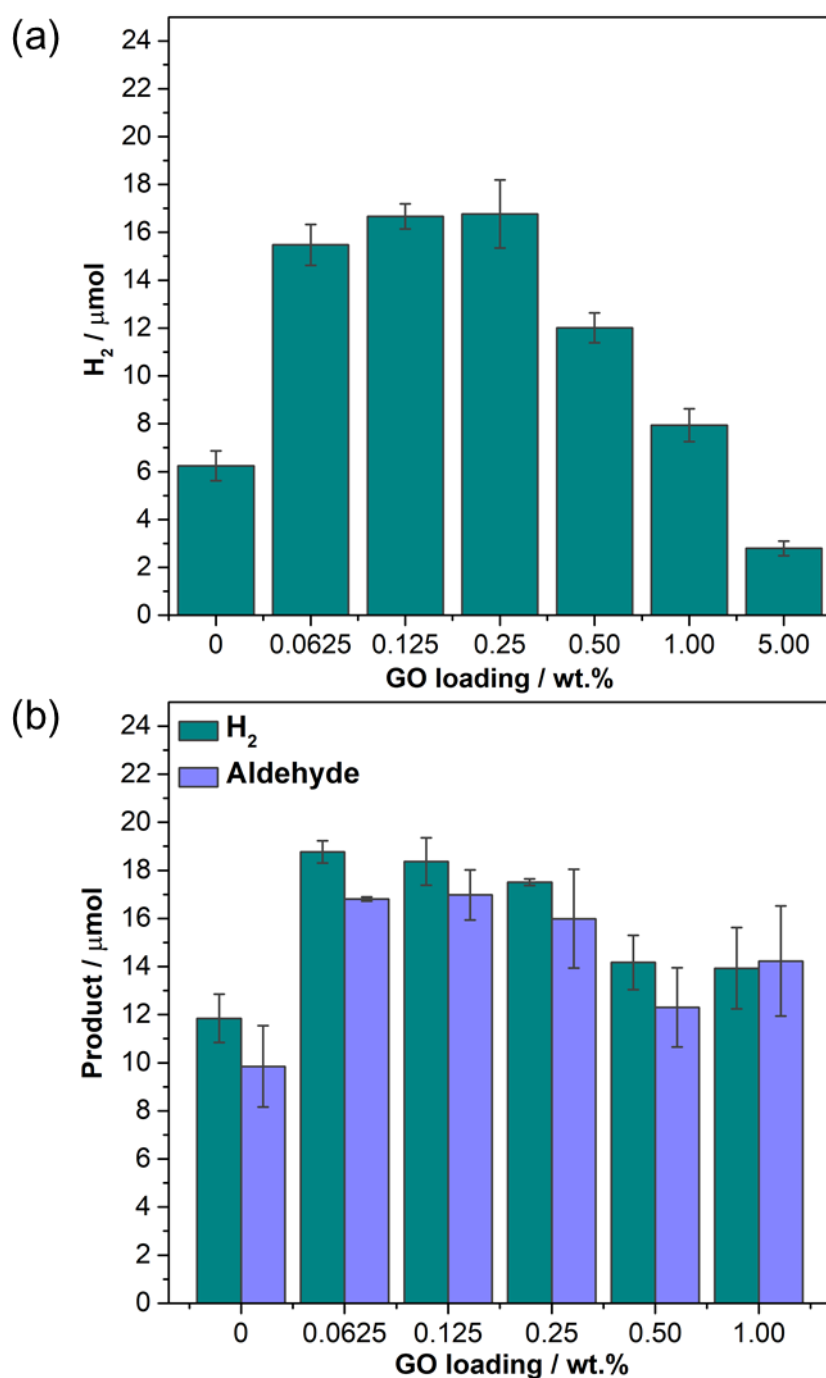
156

Figure C.2. Photocatalytic H_2 production in the presence of $^{NCN}CN_x$ (5 mg) with different GO loadings and **NiP** (50 nmol) in (a) aqueous EDTA solution (0.1 M, pH 4.5, 3 mL), and in (b) KP$_i$ solution (0.1 M, pH 4.5, 3 mL) containing 4-MBA (30 μmol), under 1 sun irradiation (100 mW cm^{-2}, AM 1.5G, 25 °C) for 4 h.
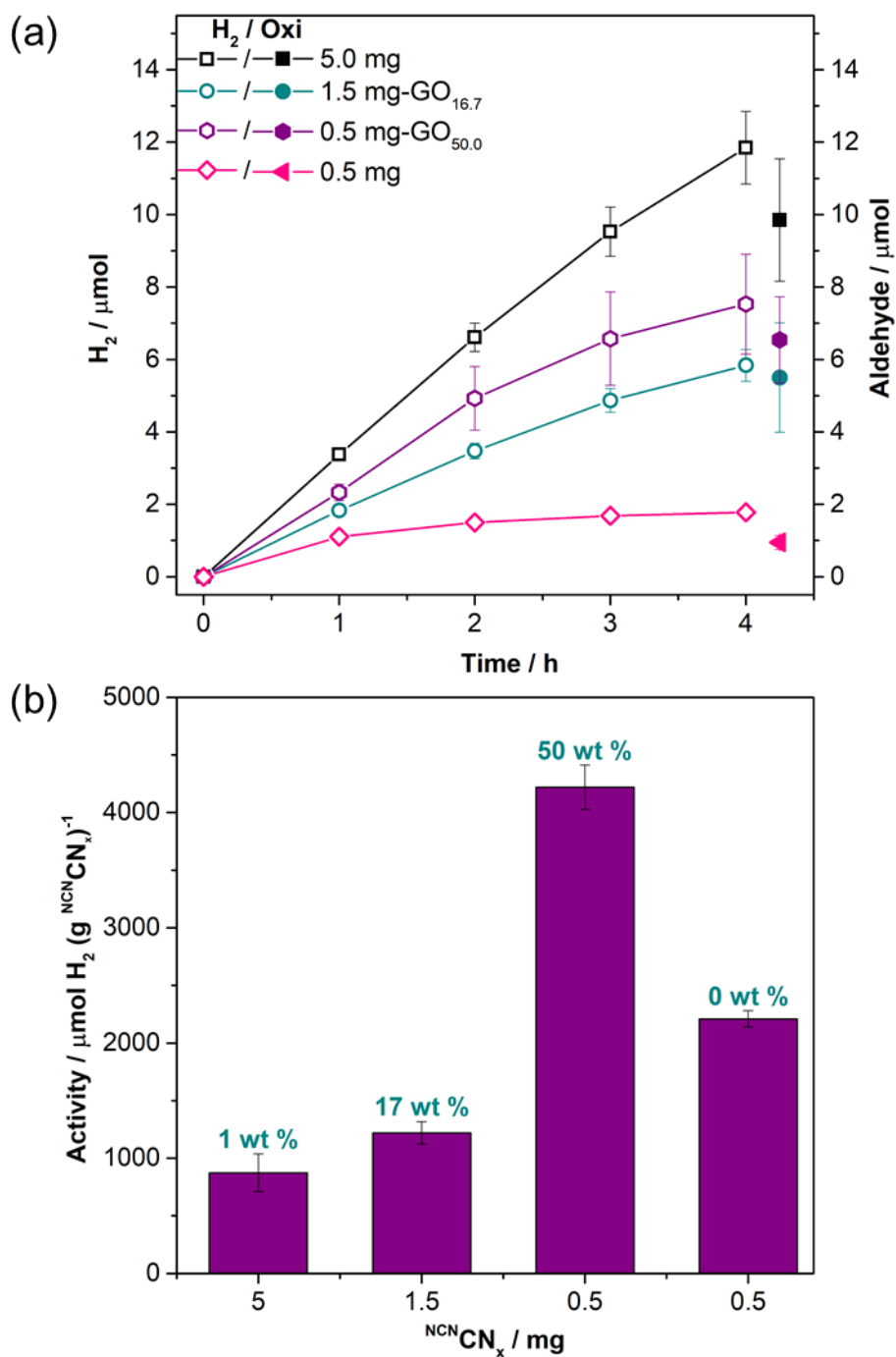
Figure C.3. (a) Photocatalytic H_2 production and 4-MBA oxidation in the presence of different amounts of $^{NCN}CN_x$ and GO loadings, 4-MBA (30 μmol) and **NiP** (50 nmol) in an aqueous KP_i solution (0.1 M, pH 4.5, 3 mL) under 1 sun irradiation (100 mW cm^{-2}, AM 1.5G, 25 °C). The pair of hollow and filled symbols of the same shape and colour corresponds to H_2 and aldehyde production, respectively. Amount of aldehyde formed is detected after 4 h of irradiation. (b) Bar chart comparing specific activity of $^{NCN}CN_x$ after 1 h of irradiation.
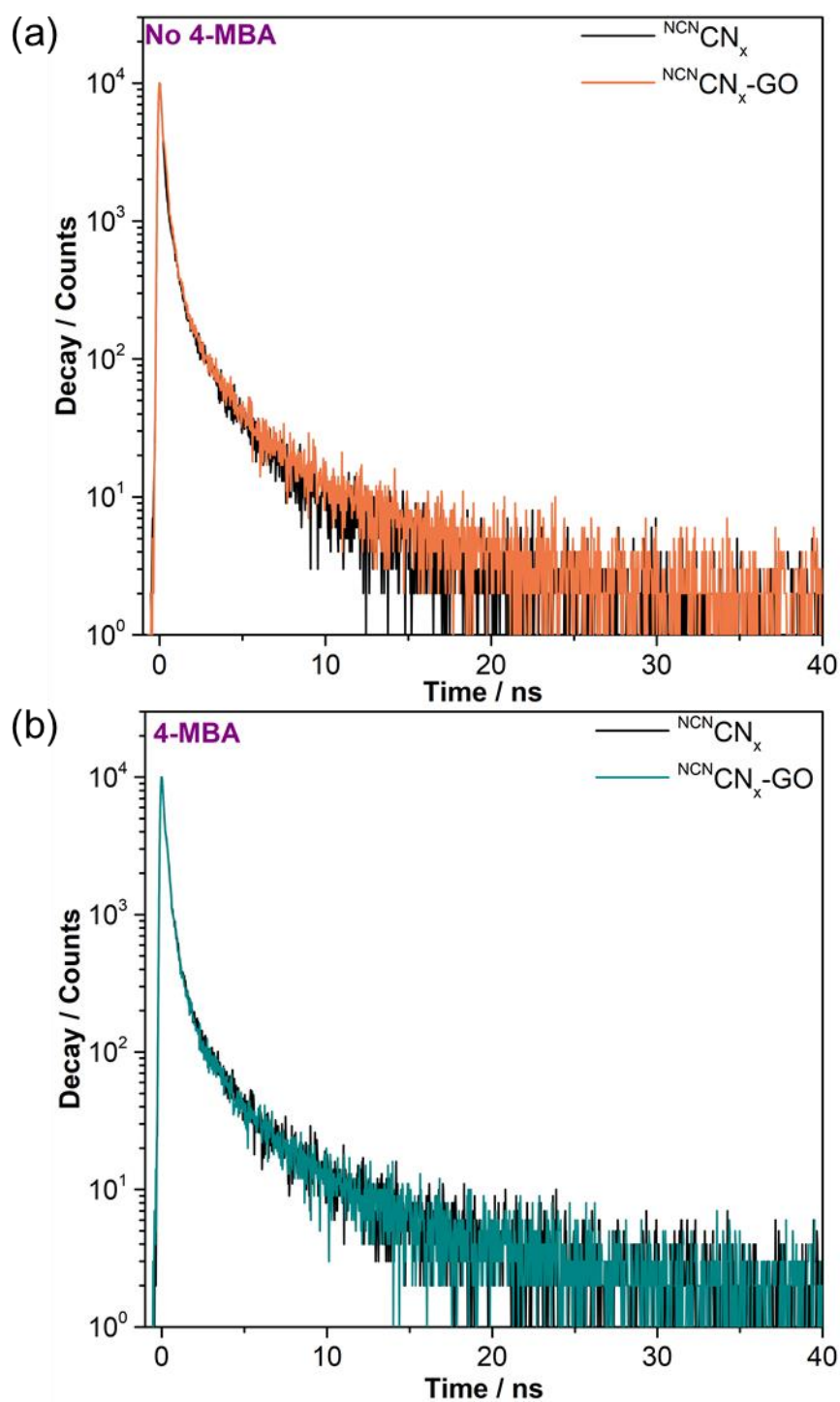
Figure C.4. tr-PL of $^{NCN}CN_x$ at the concentration of 1.67 mg mL^{-1} dispersed in KP$_i$ solution (0.1 M, pH 4.5) with 50 wt% GO loading in the (a) absence and (b) presence of 4-MBA (0.01 M), under Ar atmosphere, with λ_{ex} = 404 nm and λ_{em} = 490 nm at 25 °C.
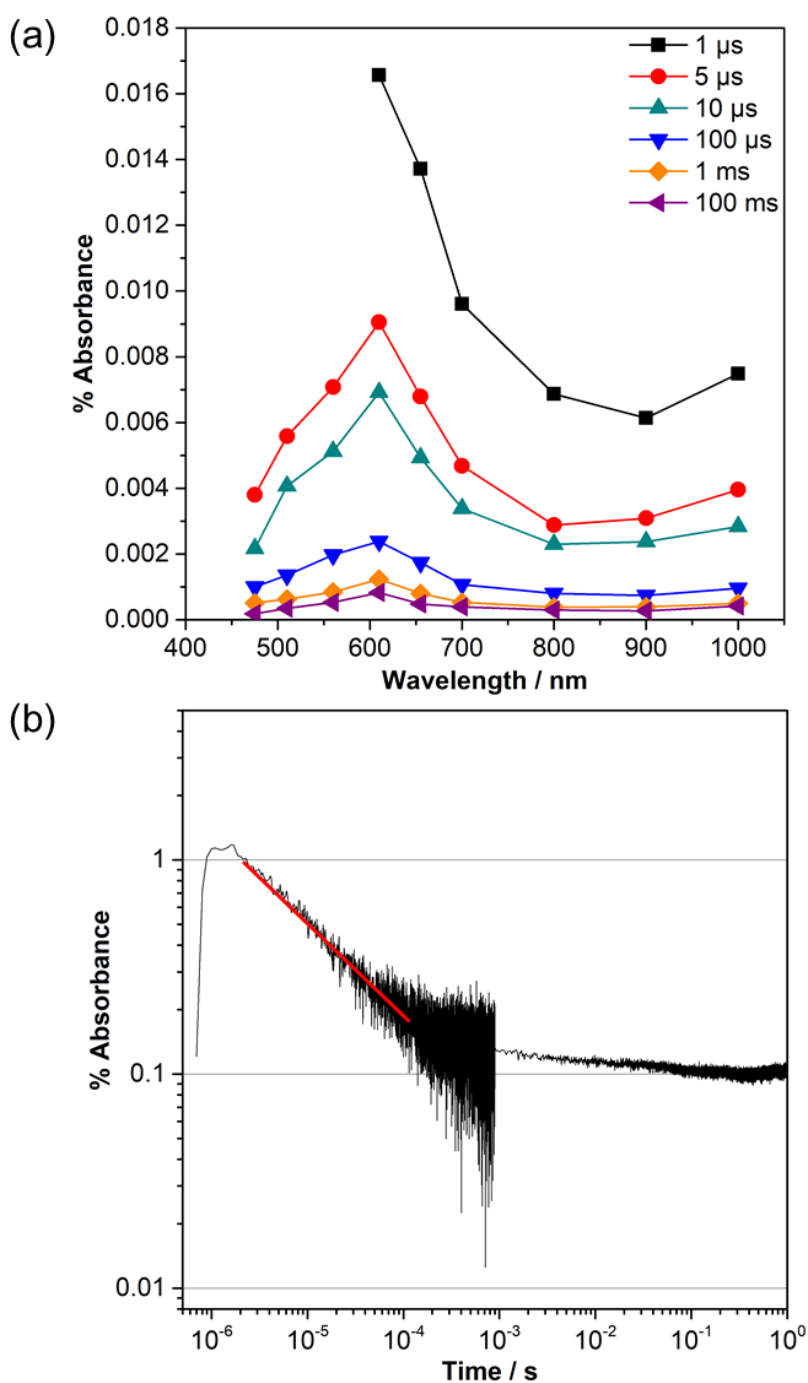
Figure C.5. (a) µs-TAS spectra from 470 nm to 1000 nm at several time delays after photoexcitation of $^{NCN}CN_x$ at the concentration of 1.67 mg mL^{-1} dispersed in KP$_i$ solution (0.1 M, pH 4.5). (b) Typical µs-TAS decay of 1.67 mg mL^{-1} $^{NCN}CN_x$ dispersed KP$_i$ solution (0.1 M, pH 4.5) monitored at λ = 610 nm under λ = 355 nm pulsed excitation at 25 °C. The power law fitting is overlaid in red and is of the form $y = y_0 + |t - t_0|^{-b}$. t_0 represents the time offset between the trigger signal and the arrival of the excitation pulse to the sample, typically $t_0 = 1 \times 10^{-7}$ s. y_0 is the absorbance offset at infinite times and the b value is 0.43.
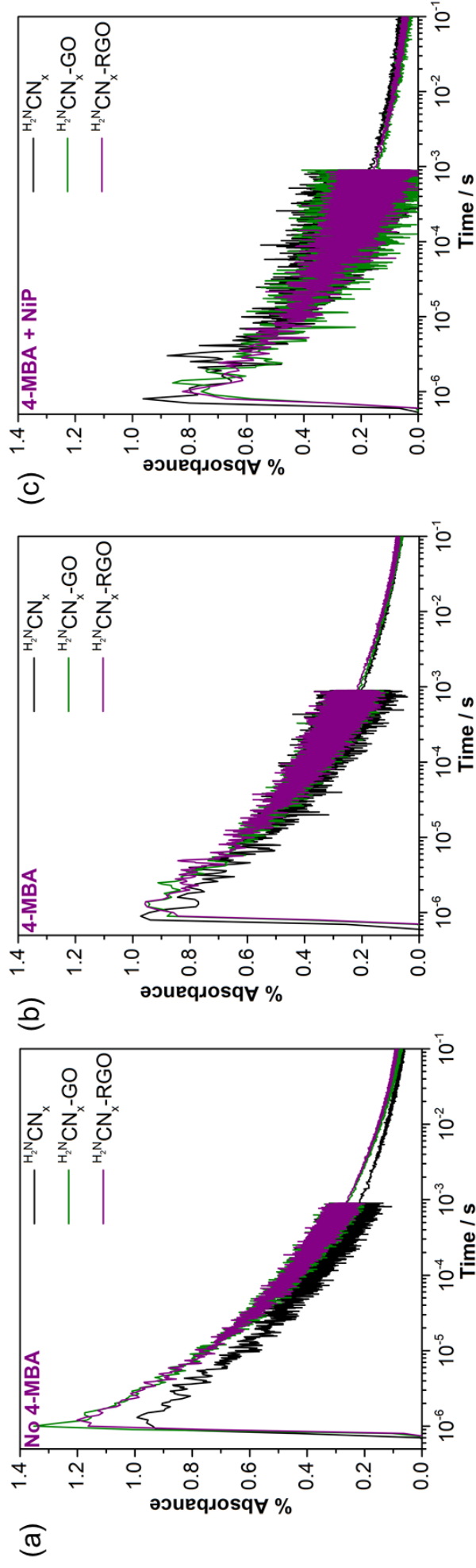
160

Figure C.6. μs-TAS decay kinetics of (a) H₂NCNₓ, H₂NCNₓ and GO/RGO samples with 0.125 wt% loading (6.3 μg) at the concentration of 1.67 mg mL⁻¹ dispersed in KPᵢ solution (0.1 M, pH 4.5) monitored at λ = 800 nm under λ = 355 nm pulsed excitation, (a) without 4-MBA, (b) with 4-MBA (0.01 M) and (c) with 4-MBA (0.01 M) and NiP (50 nmol) in KPᵢ solution at 25 °C.

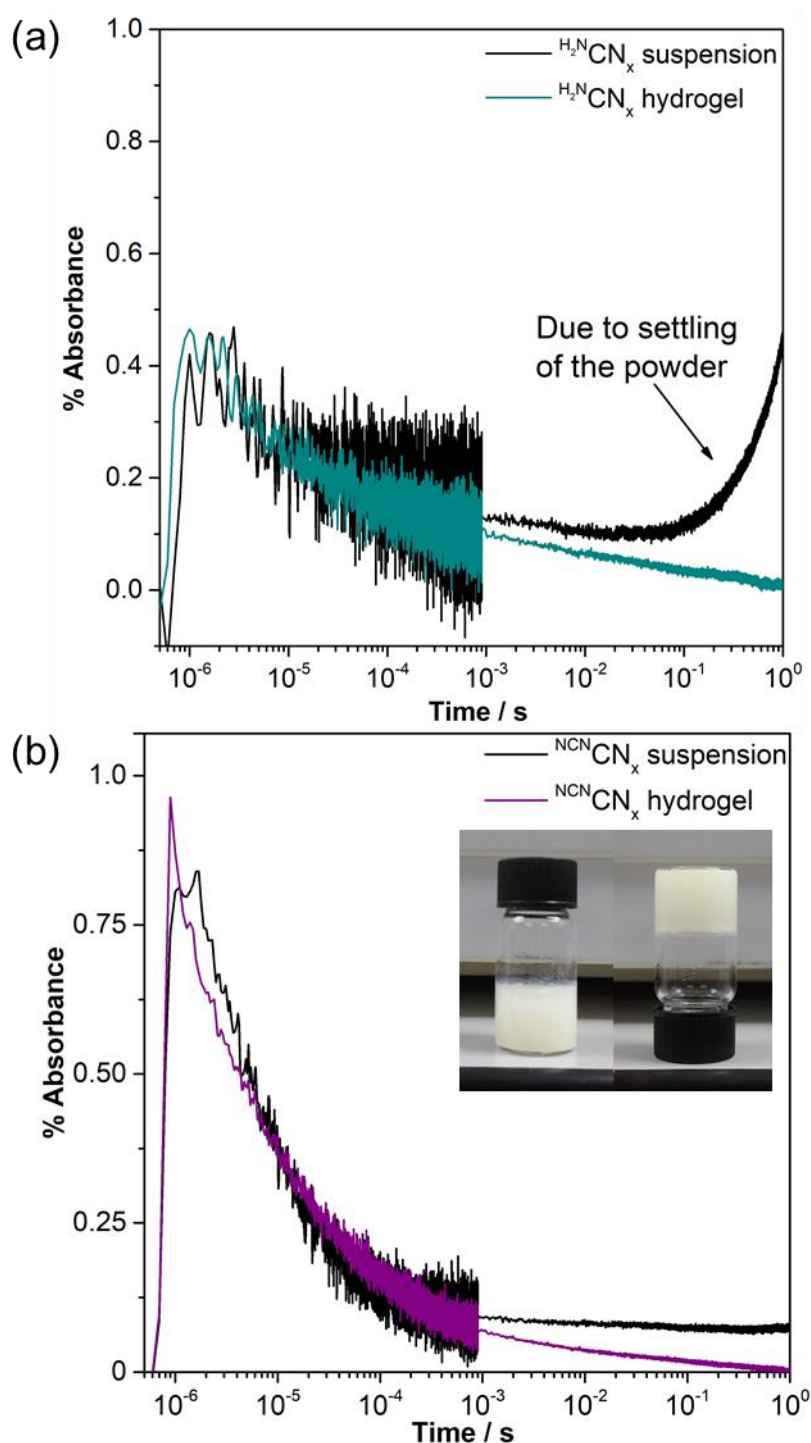Figure C.7. μs-TAS decay kinetics monitored at the concentration of 1.67 mg mL^{-1} for a) ^{H_2N}**CN$_x$** and b) ^{NCN}**CN$_x$** suspensions, and in NaDC (13.8 mg mL^{-1}) hydrogel, in KP$_i$ solution (0.1 M, pH 4.5) under Ar, monitored at λ = 1000 nm (^{H_2N}**CN$_x$**) or 610 nm (^{NCN}**CN$_x$**) with laser pulse excitation at λ = 355 nm at 25 °C. (b) Inset: Photograph of hydrogel (50 mg mL^{-1}) prepared from NaDC and ^{NCN}**CN$_x$** powder.
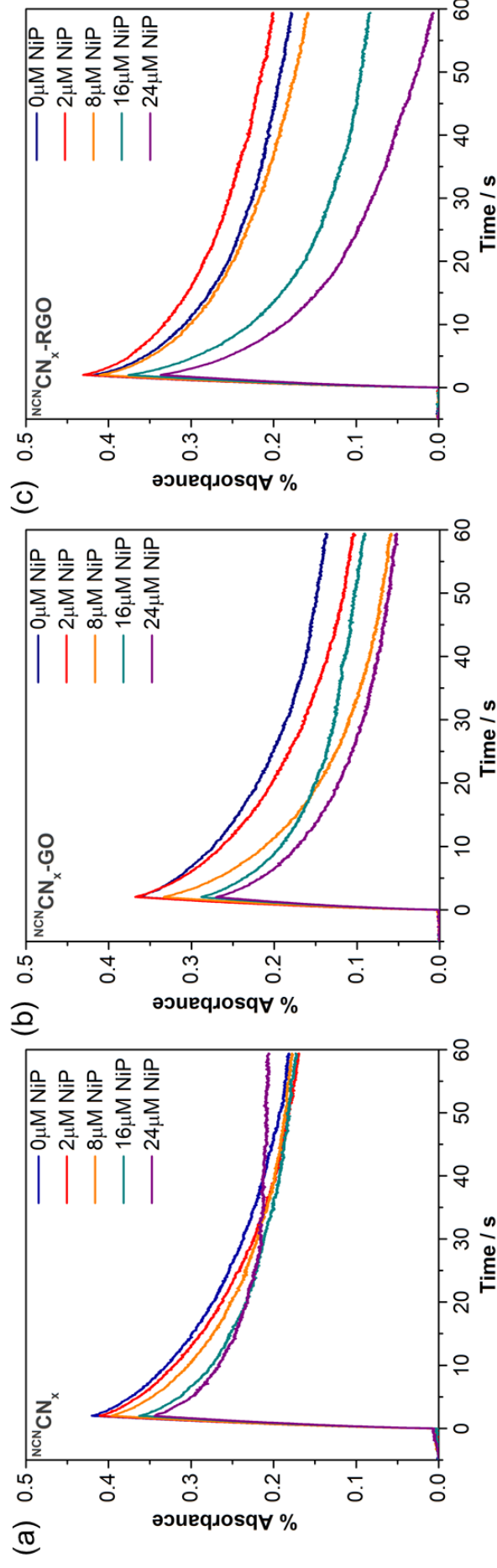
Figure C.8. PIAS of (a) ^{NCN}**CN$_x$**, (b) ^{NCN}**CN$_x$–GO**, (c) ^{NCN}**CN$_x$–RGO** samples with 0.125 wt% GO and RGO loading (6.3 µg) in NaDC (13.8 mg mL^{-1}) hydrogel monitored at 610 nm with LED excitation at λ= 365 nm (0.5 mW cm^{-2}), in KP$_i$ solution (0.1 M, pH 4.5) with 4-MBA (0.01 M) and different concentrations of **NiP**, under Ar at 25 °C. The samples were only irradiated for 2 s and the absorbance was monitored during irradiation and for the next 58 s.
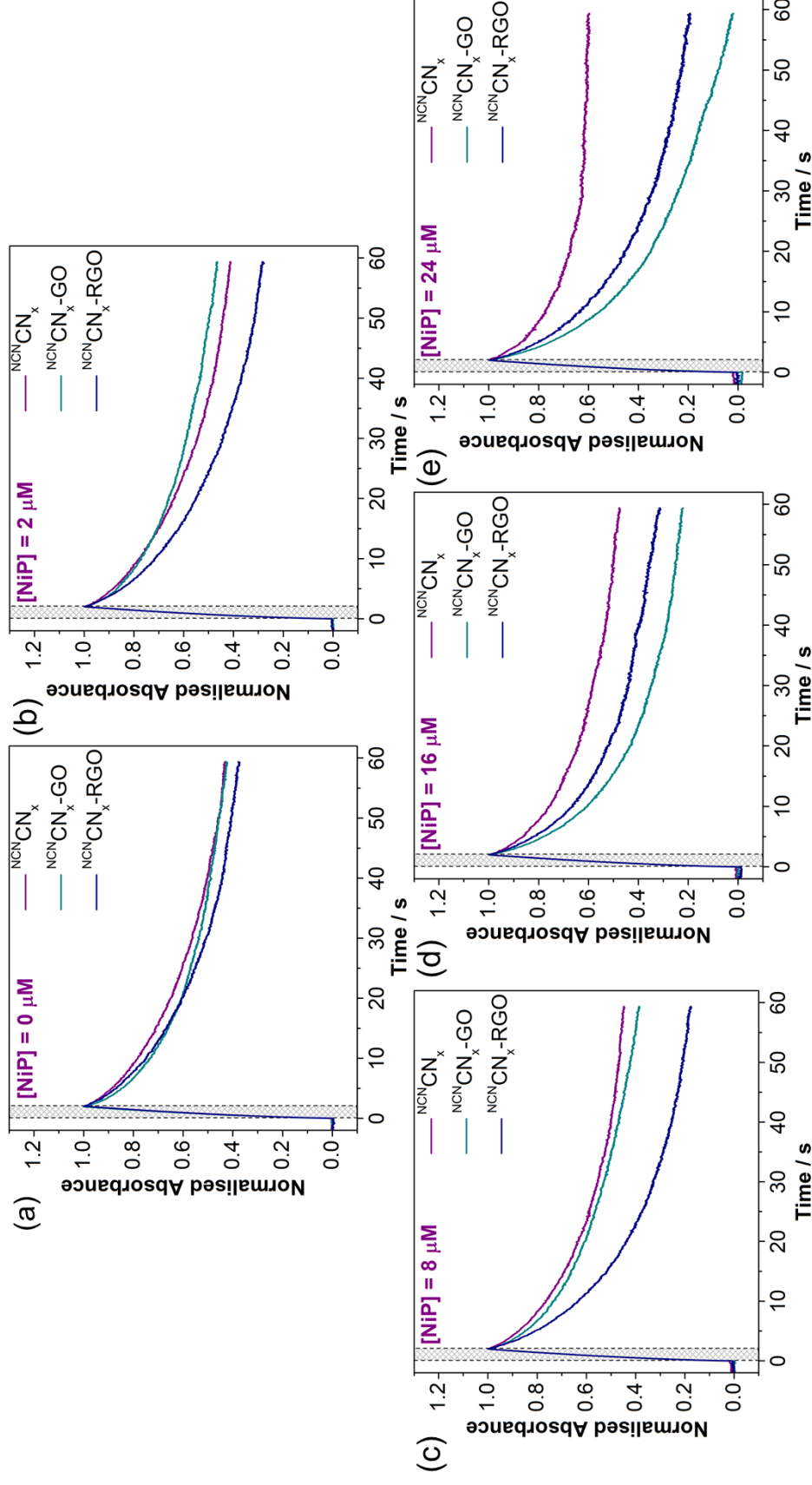
Figure C.9. Normalised PIAS traces for $^{NCN}CN_x$, $^{NCN}CN_x$–GO/RGO samples (0.125 wt% loading of GO or RGO) in NaDC (13.8 mg mL^{-1}) hydrogel monitored at $\lambda = 610$ nm with LED excitation at $\lambda = 365$ nm (0.5 mW cm^{-2}), in KP$_i$ solution (0.1 M, pH 4.5) with 4-MBA (0.01 M) under Ar. The concentration of **NiP** was varied as indicated. The samples were irradiated for 2 s and the light was switched off.

164
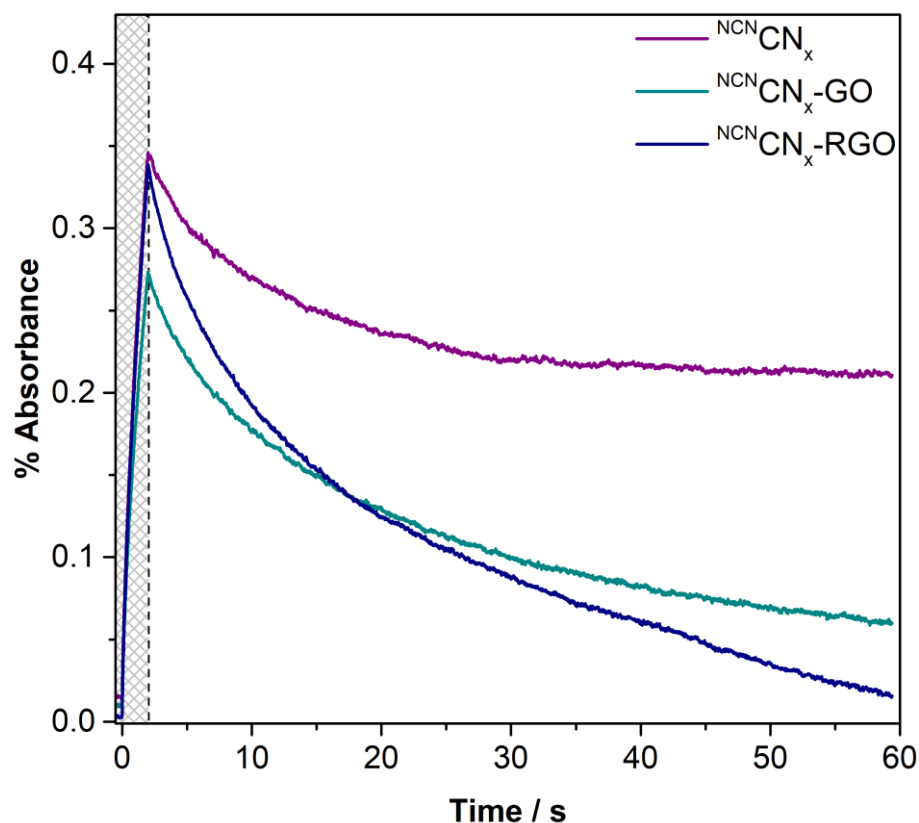
Figure C.10. PIAS of ^{NCN}**CN$_x$**, ^{NCN}**CN$_x$−GO** and ^{NCN}**CN$_x$−RGO** samples with 0.125 wt% loading (6.3 µg) in NaDC (13.8 mg mL^{-1}) hydrogel monitored at 610 nm with LED excitation at λ = 365 nm (0.5 mW cm^{-2}), in KP$_i$ solution (0.1 M, pH 4.5) with 4-MBA (0.01 M) and **NiP** (24 µM), under Ar at 25 °C. The samples were only irradiated for 2 s and the absorbance was monitored during irradiation and for the next 58 s.

Figure C.11. PIAS of H₂ᴺCNₓ and GO/RGO hybrid samples with 0.125 wt% loading (6.3 μg) recorded in KPᵢ solution (a) without 4-MBA (b) with 4-MBA and (c) with 4-MBA (0.01 M) and **NiP** (50 nmol) monitored at 800 nm at LED excitation of λ = 365 nm (0.5 mW cm⁻²), under Ar at 25 °C. The samples were only irradiated for 2 s and the absorbance was monitored during irradiation and for the next 5 s.
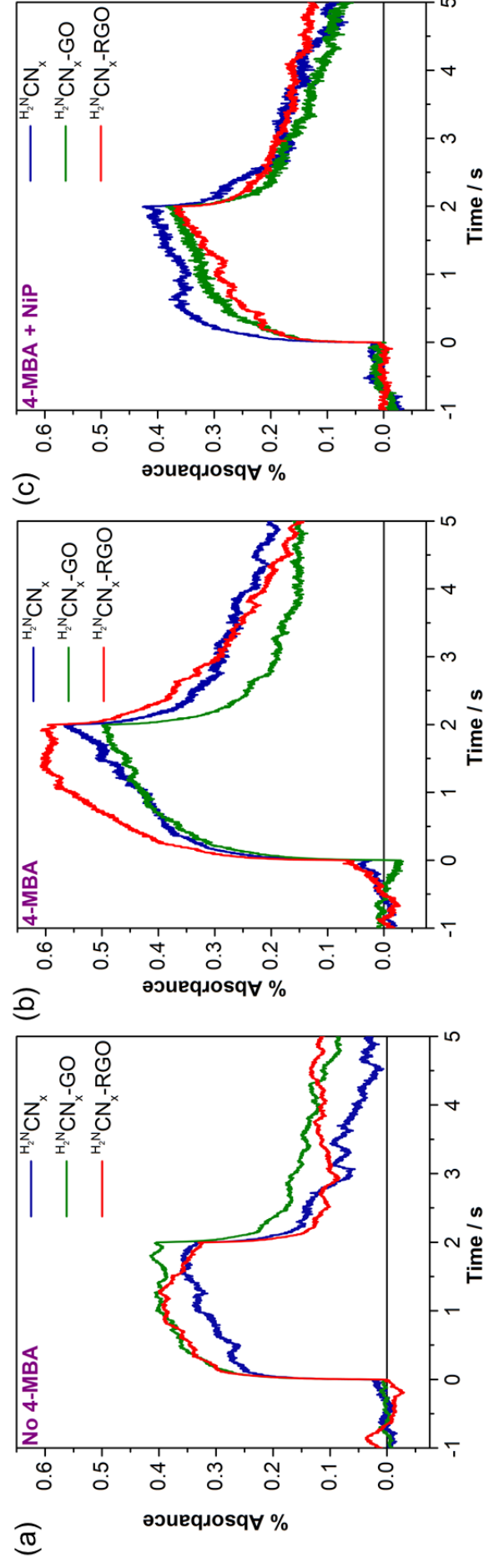
C.2 Supplementary tables

Table C.1. Solar light driven (AM 1.5G, 100 mW cm^{-2}, 25 °C) H$_2$ production in the presence of ^{NCN}CN$_x$ (5 mg) and NiP (50 nmol) in EDTA (0.1 M, pH 4.5) solution with different GO loadings. Control experiments in the absence of GO, ^{NCN}CN$_x$ and in the presence of reduced RGO were also conducted. Total solvent volume was 3 mL with a headspace volume of 4.74 mL.

Entry	GO loading / wt%	H$_2$ ± σ / μmol (after 4 h)	TON (4 h) ± σ / mol H$_2$ NiP^{-1}	Activity / μmol H$_2$ (g CN$_x$)$^{-1}$ h^{-1} (after 1 h)	TOF ± σ / h^{-1} (after 1 h)
GO loading					
1	0	6.24 ± 0.62	124.86 ± 0.28	378.17 ± 8.22	37.82 ± 0.82
2	0.0625	16.16 ± 0.90	323.24 ± 17.90	1032.29 ± 81.50	103.23 ± 8.15
3	0.125	17.40 ± 0.55	348.00 ± 10.96	1162.54 ± 29.06	116.25 ± 2.91
4	0.25	17.51 ± 1.49	350.27 ± 29.71	1056.02 ± 142.38	105.60 ± 14.24
5	0.50	12.54 ± 0.65	250.81 ± 13.07	776.97 ± 69.38	77.70 ± 6.94
6	1.00	8.30 ± 0.71	165.93 ± 14.30	549.24 ± 35.60	54.92 ± 3.56
7	5.00	2.92 ± 0.32	58.4 ± 6.35	251.05 ± 27.14	25.10 ± 2.71
Control Experiments					
8	GO, 0.125 λ > 495 nm	0	0	0	0
9	GO, 0.125 (No ^{NCN}CN$_x$)	0	0	0	0
10	RGO, 0.125[a]	16.11 ± 0.28	322.20 ± 5.66	1023.97 ± 11.37	102.40 ± 1.14
11	RGO, 0.125 (No ^{NCN}CN$_x$)	0	0	0	0

[a] GO replaced by RGO.

Table C.2. Solar light driven (AM 1.5G, 100 mW cm^{-2}, 25 °C) H_2 and aldehyde production in the presence of $^{NCN}CN_x$ (5 mg) and **NiP** (50 nmol) in KP$_i$ solution (0.1 M, pH 4.5) containing 4-MBA (30 μmol) with different GO loadings. Control experiments in the absence of GO, $^{NCN}CN_x$ and in the presence of RGO were also conducted. Total solvent volume was 3 mL with a headspace volume of 4.74 mL.

Entry	GO loading / wt%	Aldehyde ± σ / μmol (after 4 h)	Alcohol Conversion ± σ / (%)	H_2 ± σ / μmol (after 4 h)	TON (4 h) ± σ / mol H_2 NiP^{-1}	Activity / μmol H_2 (g CN$_x$)$^{-1}$h^{-1} (after 1h)	TOF ± σ / h^{-1} (after 1h)
GO screening							
12	0	9.85 ± 1.69	32.83 ± 5.64	11.85 ± 1.00	236.92 ± 20.09	675.92 ± 27.10	67.59 ± 2.71
13	0.0625	16.81 ± 0.09	56.04 ± 0.29	18.77 ± 0.46	375.31 ± 9.27	1191.80 ± 30.60	119.18 ± 3.06
14	0.125	16.98 ± 1.05	56.60 ± 3.48	18.37 ± 0.99	367.40 ± 19.74	1158.82 ± 29.21	115.88 ± 2.92
15	0.25	15.99 ± 2.05	53.29 ± 6.84	17.51 ± 0.14	350.21 ± 2.71	1073.18 ± 14.43	107.32 ± 1.44
16	0.50	12.30 ± 1.64	41.01 ± 5.47	14.17 ± 1.13	283.43 ± 22.54	895.77 ± 54.16	89.58 ± 5.42
17	1.00	14.23 ± 2.29	47.43 ± 7.64	13.93 ± 1.69	278.63 ± 33.81	874.14 ± 162.81	87.41 ± 16.28
18	5.00	4.83 ± 0.07	16.1 ± 0.24	3.33 ± 0.73	66.70 ± 14.64	294.57 ± 45.30	29.46 ± 4.53
Control Experiments							
19	GO, 0.125 λ > 495 nm	0	0	0	0	0	0
20	GO, 0.125 (No $^{NCN}CN_x$)	0	0	0	0	0	0
21	RGO, 0.125[a]	15.11 ± 0.84	50.38 ± 2.79	16.53 ± 0.81	330.69 ± 16.17	1216.13 ± 54.60	121.61 ± 5.46
22	RGO, 0.125 (No $^{NCN}CN_x$)	0	0	0	0	0	0

[a] GO replaced by RGO.

Table C.3. Solar light driven (AM 1.5G, 100 mW cm^{-2}, 25 °C) H$_2$ and aldehyde production in the presence of different amount of ^{NCN}**CN$_x$** loadings and **NiP** (50 nmol) in KP$_i$ (0.1 M, pH 4.5) containing 4-MBA (30 μmol) with different GO loadings. Total solvent volume was 3 mL with a headspace volume of 4.74 mL.

Entry	CN$_x$ loading / mg	GO loading / wt%	Aldehyde ± σ / μmol (after 4 h)	Alcohol Conversion ± σ / (%)	H$_2$ ± σ / μmol (after 4 h)	TON (4 h) ± σ / mol H$_2$ NiP^{-1}	Activity / μmol H$_2$ (g CN$_x$)$^{-1}$h^{-1} (after 1h)	TOF ± σ / h^{-1} (after 1h)
CN$_x$ loading								
23	0.5	0	0.95 ± 0.19	3.17 ± 0.64	1.78 ± 0.14	35.65 ± 2.84	2208.72 ± 71.24	22.09 ± 0.71
24	0.5	50.00	6.54 ± 1.19	21.80 ± 3.96	7.53 ± 1.38	150.53 ± 27.51	4654.93 ± 448.37	46.55 ± 4.48
25	1.5	16.70	5.50 ± 1.51	18.33 ± 5.03	5.84 ± 0.44	116.76 ± 8.81	1219.96 ± 97.99	36.60 ± 2.94

Table C.4. Solar light driven (AM 1.5G, 100 mW cm^{-2}, 25 °C) H$_2$ and aldehyde production in the presence of ^{NCN}**CN$_x$** (5 mg) loadings and **NiP** (50 nmol) in KP$_i$ (0.1 M, pH 4.5) containing 4-MBA (30 μmol) in the presence of 0.125 wt% GO loading (6.3 μg) with different sizes of GO. Total solvent volume was 3 mL with a headspace volume of 4.74 mL.

Entry	GO size / μm	Aldehyde ± σ / μmol (after 4 h)	Alcohol Conversion ± σ / (%)	H$_2$ ± σ / μmol (after 4 h)	TON (4 h) ± σ / mol H$_2$ NiP^{-1}	Activity / μmol H$_2$ (g CN$_x$)$^{-1}$h^{-1} (after 1h)	TOF ± σ / h^{-1} (after 1h)
GO size screening							
26	<1	15.92 ± 1.04	53.06 ± 3.47	19.94 ± 1.06	398.79 ± 21.17	1238.23 ± 70.27	123.82 ± 7.03
27	<2	14.73 ± 0.75	49.10 ± 2.51	20.11 ± 0.91	402.21 ± 18.21	1770.20 ± 18.79	177.02 ± 1.88
28	2-5	16.98 ± 1.05	56.60 ± 3.48	18.37 ± 0.99	367.40 ± 19.74	1158.82 ± 29.21	115.88 ± 2.92

Table C.5. Solar light driven (AM 1.5G, 100 mW cm^{-2}, 25 °C) H$_2$ production in the presence of ^{H2N}CN$_x$ (5 mg) and **NiP** (50 nmol) in EDTA (0.1 M, pH 4.5) with different GO loadings. Control experiments in the absence of GO, ^{H2N}CN$_x$ and in the presence of RGO were also conducted. Total solvent volume was 3 mL with a headspace volume of 4.74 mL.

Entry	GO loading / wt%	H$_2$ ± σ / μmol (after 4 h)	TON (4 h) ± σ / mol H$_2$ NiP^{-1}	Activity / μmol H$_2$ (g CN$_x$)$^{-1}$h^{-1} (after 1h)	TOF ± σ / h^{-1} (after 1h)
GO loading					
29	0	2.05 ± 0.09	40.92 ± 1.75	82.34 ± 14.21	8.23 ± 1.42
30	0.125	2.58 ± 0.22	51.68 ± 4.37	135.16 ± 29.38	13.52 ± 2.94
31	1.00	3.03 ± 0.44	60.68 ± 8.87	210.07 ± 34.43	21.01 ± 3.44
32	5.00	2.46 ± 0.21	49.21 ± 4.12	111.51 ± 3.02	11.15 ± 0.30
Control Experiments					
33	GO, 1.00 (No ^{NCN}CN$_x$)	0	0	0	0
34	RGO, 1.00[a]	5.22 ± 0.71	104.36 ± 14.24	373.65 ± 61.41	37.36 ± 6.14
35	RGO, 1.00 (No ^{NCN}CN$_x$)	0	0	0	0

[a] GO replaced by RGO.

Table C.6. Solar light driven (AM 1.5G, 100 mW cm^{-2}, 25 °C) H$_2$ and aldehyde production in the presence of ^{H_2N}CN$_x$ (5 mg) and **NiP** (50 nmol) in KP$_i$ (0.1 M, pH 4.5) containing 4-MBA (30 μmol) with different GO loadings. Control experiments in the absence of GO, ^{H_2N}CN$_x$ and in the presence of RGO were also conducted. Total solvent volume was 3 mL with a headspace volume of 4.74 mL.

Entry	GO loading / wt%	Aldehyde ± σ / μmol (after 4 h)	Alcohol Conversion ± σ / (%)	H$_2$ ± σ / μmol (after 4 h)	TON (4 h) ± σ / mol H$_2$ NiP^{-1}	Activity / μmol H$_2$ (g CN$_x$)$^{-1}$h^{-1} (after 1h)	TOF ± σ / h^{-1} (after 1h)
GO screening							
36	0	1.17 ± 0.32	3.89 ± 1.06	1.43 ± 0.10	28.53 ± 2.07	116.90 ± 3.81	11.69 ± 0.38
37	0.125	2.55 ± 0.41	8.50 ± 1.38	3.08 ± 0.39	61.50 ± 7.82	282.52 ± 23.97	28.25 ± 2.40
38	0.50	1.72 ± 0.20	5.74 ± 0.66	2.22 ± 0.27	44.43 ± 5.39	282.57 ± 21.00	28.26 ± 2.10
39	1.00	1.29 ± 0.29	4.29 ± 0.97	1.09 ± 0.05	21.57 ± 1.02	96.25 ± 10.88	9.62 ± 1.09
Control Experiments							
40	GO, 1.00 (No ^{NCN}CN$_x$)	0	0	0	0	0	0
41	RGO, 1.00[a]	2.04 ± 1.10	6.80 ± 3.68	2.76 ± 0.68	55.18 ± 13.50	305.62 ± 64.29	30.56 ± 6.43
42	RGO, 1.00 (No ^{NCN}CN$_x$)	0	0	0	0	0	0

[a] GO replaced by RGO.

171

Table C.7. Charging and discharging experiments were executed with a photoreactor containing $^{NCN}CN_x$ (5 mg) and $^{NCN}CN_x$ (5 mg) - GO/RGO (0.125 wt%; 6.3 µg) hybrids in the presence of 4-MBA (30 µmol) in an aqueous KP$_i$ solution (0.1 M, pH 4.5) without NiP. Total solvent volume was 3 mL with a headspace volume of 4.74 mL. The samples were irradiated under 1 sun (AM 1.5G, 100 mW cm^{-2}, 25 °C) for 30 min, 2 h and 4 h. The vials were then moved into dark, NiP (50 nmol in KP$_i$ solution) was injected and the amount of H$_2$ and aldehyde production was monitored.

Entry	GO loading / wt%	Aldehyde ± σ / µmol (after 4 h)	Alcohol Conversion ± σ / (%)	H$_2$ ± σ / µmol (after 4 h)	TON (4 h) ± σ / mol H$_2$ NiP^{-1}	Activity / µmol H$_2$ (g CN$_x$)$^{-1}$ h^{-1} (after 1h)	TOF ± σ / h^{-1} (after 1h)
30 mins irradiation							
43	0	0.70 ± 0.10	2.34 ± 0.35	0.79 ± 0.07	15.79 ± 1.37	155.28 ± 17.56	15.53 ± 1.76
44	0.125	1.46 ± 0.23	4.87 ± 0.76	1.07 ± 0.09	21.48 ± 1.88	205.65 ± 20.64	20.56 ± 2.06
45	RGO, 0.125[a]	1.32 ± 0.42	4.39 ± 1.40	0.94 ± 0.12	18.76 ± 2.32	181.60 ± 21.65	18.16 ± 2.16
2 h irradiation							
46	0	0.97 ± 0.21	3.22 ± 0.68	1.05 ± 0.11	21.03 ± 2.27	189.50 ± 10.35	18.95 ± 1.03
47	0, 2h in dark	1.00 ± 0.20	3.33 ± 0.67	1.06 ± 0.06	21.17 ± 1.16	165.50 ± 3.70	16.55 ± 0.37
48	0.125	1.92 ± 0.16	6.40 ± 0.52	1.29 ± 0.03	25.74 ± 0.52	244.57 ± 4.21	24.46 ± 0.42
49	RGO, 0.125[a]	1.60 ± 0.16	5.32 ± 0.54	1.28 ± 0.03	25.63 ± 0.64	251.44 ± 4.04	25.14 ± 0.40
4 h irradiation							
50	0	1.55 ± 0.12	5.15 ± 0.40	2.25 ± 0.27	44.97 ± 5.48	189.15 ± 22.18	18.91 ± 2.22
51	0.125	1.79 ± 0.28	5.97 ± 0.94	2.22 ± 0.10	44.39 ± 2.07	197.51 ± 3.88	19.75 ± 0.39
52	RGO, 0.125[a]	1.74 ± 0.22	5.79 ± 0.73	2.29 ± 0.19	45.78 ± 3.73	201.74 ± 27.08	20.17 ± 2.71
12 h irradiation							
53	0	1.89 ± 0.24	5.93 ± 0.66	2.19 ± 0.19	43.75 ± 3.94	229.02 ± 24.00	20.17 ± 2.71

[a] GO replaced by RGO.

Table C.8. Calculation of the number of radicals per heptazine unit generated during charging and discharging experiments of $^{NCN}CN_x$ and $^{NCN}CN_x$–GO/RGO (same order as in Table S7). The calculations were based on the assumptions that 2 trapped radicals are used to produce one molecule of H_2 and no other decay pathway is available for the radicals.[18] Each vial contained 5 mg of $^{NCN}CN_x$ with a repeating heptazine unit of 249 g mol^{-1}, which corresponded to 20 μmol of NCN-heptazine units.

Entry	GO loading / wt%	$H_2 \pm \sigma$ / μmol (after 4 h)	Calculated radicals / μmol[b]	Charge accumulated per heptazine unit / %
30 mins irradiation				
54	0	0.79 ± 0.07	1.58 ± 0.14	7.9
55	0.125	1.07 ± 0.10	2.14 ± 0.20	10.7
56	RGO, 0.125[a]	0.94 ± 0.12	1.88 ± 0.24	9.4
2 h irradiation				
57	0	1.05 ± 0.11	2.10 ± 0.22	10.5
58	0, 2 h in dark	1.06 ± 0.06	2.12 ± 0.12	10.6
59	0.125	1.29 ± 0.03	2.58 ± 0.06	12.9
60	RGO, 0.125[a]	1.28 ± 0.03	2.56 ± 0.06	12.8
4 h irradiation				
61	0	2.25 ± 0.27	4.50 ± 0.54	22.5
62	0.125	2.22 ± 0.10	4.44 ± 0.20	22.2
63	RGO, 0.125[a]	2.29 ± 0.19	4.58 ± 0.38	22.9

[a] GO replaced by RGO. [b] Radicals calculated from generated H_2 in dark phase.

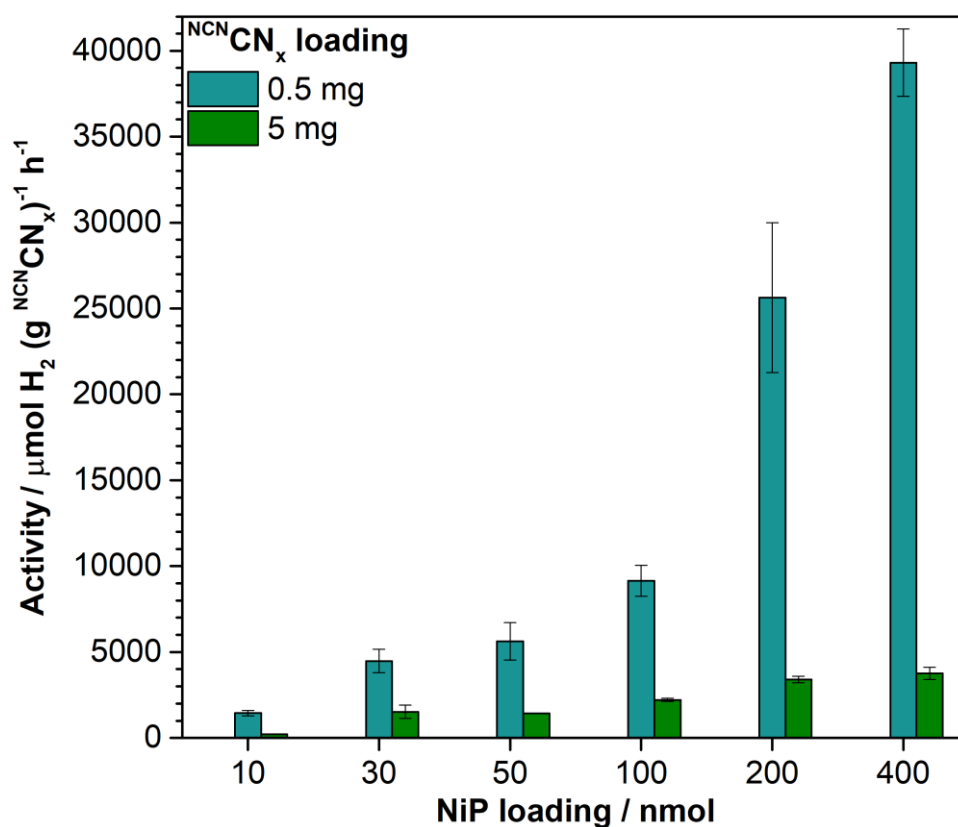# D. Appendix to chapter 6

D.1 Supporting figures

Figure D.1. Monitoring the specific H_2 production activities with activated $^{NCN}CN_x$ (0.5 or 5 mg) at different **NiP** loadings in KP_i solution (0.1 M, pH 4.5, 3 mL) containing 4-MBA (30 µmol) under simulated solar light irradiation (100 mW cm^{-2}, AM 1.5G, 25 °C).
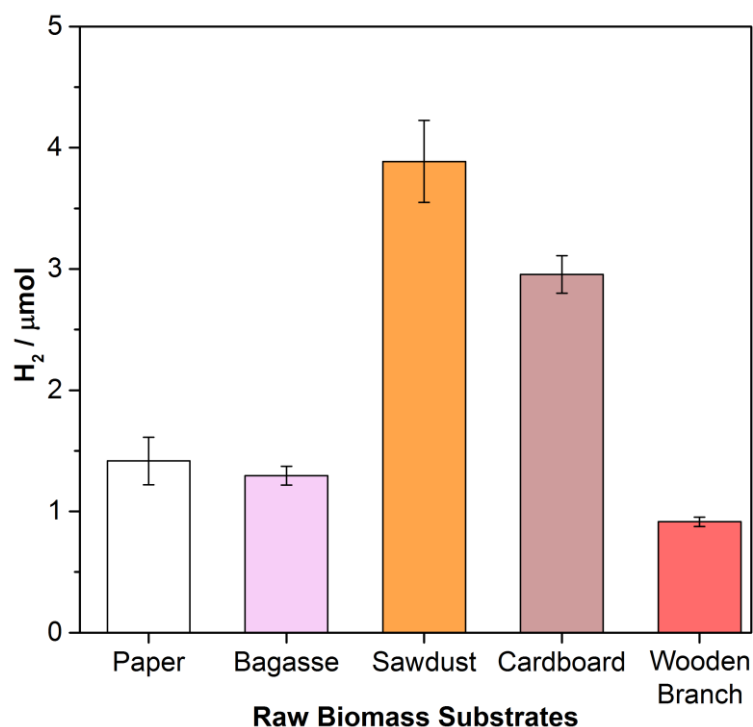
Figure D.2. Photocatalytic H_2 production using activated $^{NCN}CN_x$ (5 mg) and **NiP** (50 nmol) with raw biomass substrates (100 mg) in KP_i solution (0.1 M, pH 4.5, 3 mL) under simulated solar light irradiation for 24 h (100 mW cm^{-2}, AM 1.5G, 25 °C).
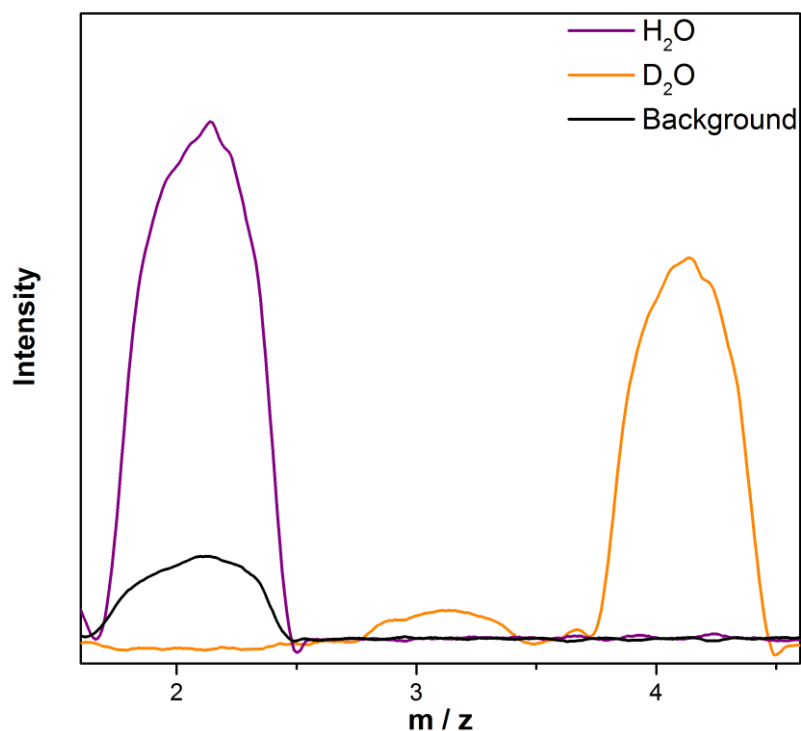

Figure D.3. Mass spectra of headspace gas recorded after 24 h of simulated solar light irradiation (AM 1.5G, 100 mW cm^{-2}, 25 °C) with activated $^{NCN}CN_x$ (5 mg) and H_2PtCl_6 (4 wt%) in the presence of α-cellulose (100 mg) in KP_i (0.1 M, pH 4.5, 3 mL) solution prepared in H_2O or D_2O.
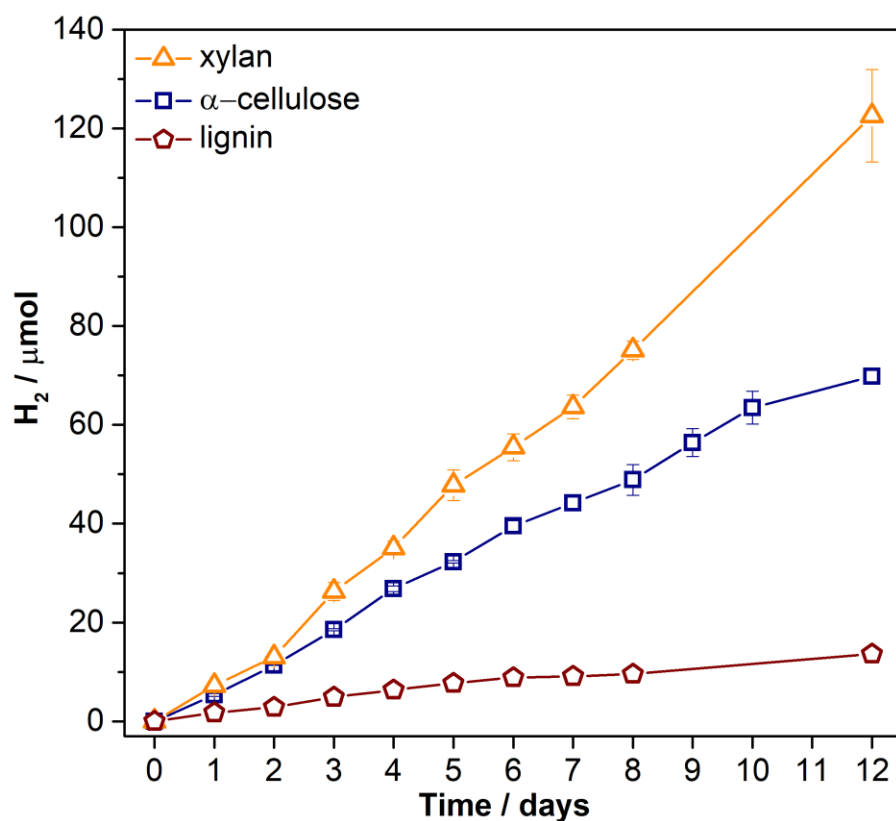
Figure D.4. Photocatalytic H_2 production using activated $^{NCN}CN_x$ (5 mg) with H_2PtCl_6 (4 wt%) and lignocellulose components (cellulose, xylan, lignin with 100, 50, 0.5 mg loading respectively) in KOH solution (10 M, pH 15, 3 mL) under simulated solar light irradiation (100 mW cm^{-2}, AM 1.5G, 25 °C) for 12 days. Cellulose, xylan and lignin samples were suspended in 10 M KOH and stirred for 24 h at 25 °C prior to injection of $^{NCN}CN_x$ and H_2PtCl_6.

D.2 Supporting tables

Table D.1. Simulated solar light driven (AM 1.5G, 100 mW cm^{-2}, 25 °C) H$_2$ production with bulk and 1, 10 and 30 min ultra-sonicated ^{NCN}**CN$_x$** (0.5 mg) and **NiP** (10 nmol) in KP$_i$ (0.1 M, pH 4.5, 3 mL) containing 4-MBA (30 μmol). The suspension was assembled in a photoreactor with a total volume of 7.74 mL.

Entry	Sonication time / min	TON cat / mol H$_2$ (mol cat)$^{-1}$ (4 h)	± σ / mol H$_2$ (mol cat)$^{-1}$	H$_2$ / μmol (4 h)	± σ / μmol	TOF / h^{-1}	± σ / h^{-1}	Activity / μmol H$_2$ (g CNx)$^{-1}$ h^{-1}	± σ / μmol H$_2$ (g CNx)$^{-1}$ h^{-1}
1	0	48.3	3.5	0.48	0.04	18.9	4.0	379	79
2	1	102	7	1.02	0.07	59.7	8.6	1190	170
3	×10	275	14	2.75	0.14	91.1	13.4	1820	270
4	30	74.8	7.4	0.75	0.07	42.6	7.1	852	142

×10 min ultra-sonication was chosen as the optimised condition to prepare the activated ^{NCN}**CN$_x$**.

Table D.2. Solar light driven (AM 1.5G, 100 mW cm^{-2}, 25 °C) H$_2$ production using activated ^{NCN}**CN$_x$** (0.5 mg), prepared in different sonication solvents (KP$_i$, isopropanol, methanol or water) at 1 mg mL^{-1} of ^{NCN}**CN$_x$** concentration, in the presence of **NiP** (10 nmol) in KP$_i$ (0.1 M, pH 4.5, 3 mL) containing 4-MBA (30 μmol).

Entry	Sonication Solvent	TON cat / mol H$_2$ (mol cat)$^{-1}$ (6 h)	± σ / mol H$_2$ (mol cat)$^{-1}$	H$_2$ / μmol (6 h)	± σ / μmol	TOF / h^{-1}	± σ / h^{-1}	Activity / μmol H$_2$ (g CNx)$^{-1}$ h^{-1}	± σ / μmol H$_2$ (g CNx)$^{-1}$ h^{-1}
5	iPrOH	222	21	2.22	0.21	92.7	2.6	1850	50
6	MeOH	235	14	2.35	0.14	101	4	2030	70
7	H$_2$O	247	31	2.47	0.31	119	10	2380	190
8	KP$_i$	286	14	2.86	0.14	91.1	13.4	1820	270
9	*KP$_i$	262	16	2.62	0.16	72.7	5.2	1450	100

*Sonication concentration of 5 mg mL^{-1}. KP$_i$ and 5 mg mL^{-1} concentration were chosen as the optimised condition.

Table D.3. Solar light driven (AM 1.5G, 100 mW cm^{-2}, 25 °C) H$_2$ production with activated ^{NCN}**CN$_x$** (0.5 mg) at 0 °C, 25 °C, 40 °C and **NiP** (10 nmol) in KP$_i$ (0.1 M, pH 4.5, 3 mL) containing 4-MBA (30 μmol). Control experiment for 10 min sonication of ^{NCN}**CN$_x$** using standard sonication bath at 40 °C is also shown.

Entry	Sonication temperature /°C	TON cat / mol H$_2$ (mol cat)$^{-1}$ (4 h)	± σ / mol H$_2$ (mol cat)$^{-1}$	H$_2$ / μmol (4 h)	± σ / μmol	TOF / h^{-1}	± σ / h^{-1}	Activity / μmol H$_2$ (g CN$_x$)$^{-1}$ h^{-1}	± σ / μmol H$_2$ (g CN$_x$)$^{-1}$ h^{-1}
10	0	55.0	6.3	0.55	0.06	46.9	2.4	938	48
11	25	219	16	2.19	0.16	129	8	2580	160
12	40	275	14	2.75	0.14	91.1	13.4	1820	270
13	*40	31.5	5.0	0.31	0.05	22.8	2.5	455	49

*Standard sonication bath.

Table D.4. Solar light driven (AM 1.5G, 100 mW cm^{-2}, 25 °C) H$_2$ production with bulk and activated ^{NCN}**CN$_x$** (0.5 mg) and **NiP** (10 nmol) in KP$_i$ (0.1 M, pH 4.5, 3 mL) containing 4-MBA (30 μmol) or in EDTA (0.1 M, pH 4.5, 3 mL) solution.

Entry	Solvent	^{NCN}CN$_x$	TON cat / mol H$_2$ (mol cat)$^{-1}$ (4 h)	± σ / mol H$_2$ (mol cat)$^{-1}$	H$_2$ / μmol (4 h)	± σ / μmol	TOF / h^{-1}	± σ / h^{-1}	Activity / μmol H$_2$ (g CN$_x$)$^{-1}$ h^{-1}	± σ / μmol H$_2$ (g CN$_x$)$^{-1}$ h^{-1}
14	KP$_i$	Bulk	48.3	3.5	0.48	0.04	18.9	4.0	379	79
15	KP$_i$	Activated	275	14	2.75	0.14	91.1	13.4	1820	270
16	EDTA	Bulk	56.4	10.8	0.56	0.11	22.8	2.2	456	43
17	EDTA	Activated	173	0	1.73	0.02	70.2	4.2	1400	80

Table D.5. Solar light driven (AM 1.5G, 100 mW cm⁻², 25 °C) H₂ production with activated ^{NCN}**CN**$_x$ and **NiP** at various loadings in KP$_i$ (0.1 M, pH 4.5, 3 mL) containing 4-MBA (30 µmol).

Entry	NiP / nmol	CNₓ / mg	TON cat / mol H₂ (mol cat)⁻¹ (6 h)	± σ / mol H₂ (mol cat)⁻¹	H₂ / µmol (6 h)	± σ / µmol	TOF / h⁻¹	± σ / h⁻¹	Activity / µmol H₂ (g CNₓ)⁻¹ h⁻¹	± σ / µmol H₂ (g CNₓ)⁻¹ h⁻¹
18	100	0.1	20.3	0.2	2.03	0.02	3.20	0.17	3960	100
19	10	0.1	236	24	2.36	0.24	41.4	0.4	4140	410
20	10	0.5	286	14	2.86	0.14	72.2	8.0	1440	160
21	30	0.5	206	31	5.62	0.89	72.7	10.3	4360	620
22	50	0.5	193	45	9.23	1.90	56.2	10.9	5620	1090
23	100	0.5	195	17	19.5	1.7	45.7	4.5	9140	900
24	200	0.5	140	13	28.1	2.7	64.1	10.9	25630	4370

Table D.6. Solar light driven (AM 1.5G, 100 mW cm^{-2}, 25 °C) simultaneous H$_2$ and 4-MBA oxidation to 4-MBAd with activated ^{NCN}**CN$_x$** and **NiP** at various loadings in KP$_i$ (0.1 M, pH 4.5, 3 mL) containing 4-MBA (30 µmol). Control experiments were also performed without **NiP**, ^{NCN}**CN$_x$** and in dark.

Entry	NiP / nmol	CN$_x$ / mg	TON cat / mol H$_2$ (mol cat)$^{-1}$ (6 h)	± σ / mol H$_2$ (mol cat)$^{-1}$	H$_2$ / µmol (6 h)	± σ / µmol	TOF / h^{-1}	± σ / h^{-1}	Activity / µmol H$_2$ (g CN$_x$)$^{-1}$ h^{-1}	± σ / µmol H$_2$ (g CN$_x$)$^{-1}$ h^{-1}	4-MBAd / µmol (6 h)	± σ / µmol	4-MBA Conversion / % (6 h)	± σ / %
25	300	0.5	98.4	2.0	29.5	0.6	57.5	2.1	34480	1240	29.8	0.2	99.2	0.6
26	400	0.5	79.2	0.3	31.7	0.1	49.1	0.3	39310	1970	29.9	0.1	99.5	0.2
27	10	5	209	19	2.09	0.19	106	12	211	25	5.5	0.5	18.3	1.6
28	20	5	625	62	12.5	1.2	149	17	595	67	9.7	1.0	32.5	3.5
29	30	5	701	20	21.0	0.6	254	19	1520	380	17.0	1.4	56.8	4.7
30	50	5	512	18	25.6	0.9	142	2	1420	20	24.2	1.1	80.8	3.7
31	100	5	300	20	30.0	2.0	111	5	2220	100	29.1	0.9	97.1	3.1
32	200	5	158	6	31.7	1.1	85.2	4.8	3410	190	29.8	0.1	99.5	0.2
33	0	0.5	0.00	0.00	0.00	0.00	0.92	0.10	3.08	0.33	0.00	0.00	0.00	0.00
34	FeCl$_3$	0.5	0.00	0.00	0.00	0.00	0.72	0.05	2.39	0.16	0.00	0.00	0.00	0.00
35	NiCl$_2$	0.5	1.15	0.24	383	81	1.18	0.07	3.93	0.23	1.15	0.24	383	81
36	50	0	0.00	0.00	0.00	0.00	0.00	0.00	-	-	0.00	0.00	0.00	0.00
37	50, No 4-MBA	5	0.00	0.00	0.00	0.00	0.00	0.00	0.00	0.00	-	-	-	-
38	50, dark	5	0.00	0.00	0.00	0.00	0.00	0.00	0.00	0.00	0.00	0.00	0.00	0.00

Table D.7. Solar light driven (AM 1.5G, 100 mW cm⁻², 25 °C) dark H_2 production with bulk and activated $^{NCN}CN_x$ (5 mg) in KP_i solution (0.1 M, pH 4.5, 3 mL) containing 4-MBA (30 µmol) in the absence of **NiP**. The samples were irradiated under 1 sun (100 mW cm⁻², AM 1.5G, 25 °C) for 30 min, 2 h or 4 h then moved to the dark and **NiP** (in KP_i solution) was injected under anaerobic conditions.

Entry	$^{NCN}CN_x$	TON cat / mol H_2 (mol cat)⁻¹	± σ / mol H_2 (mol cat)⁻¹	H_2 / µmol	± σ / µmol	TOF / h⁻¹	± σ / h⁻¹	Activity / µmol H_2 (g CN_x)⁻¹ h⁻¹	± σ / µmol H_2 (g CN_x)⁻¹ h⁻¹	4-MBAd / µmol	± σ / µmol	4-MBA Conversion / %	± σ / %
0.5 h irradiation, move to dark and inject 50 nmol NiP													
39	Activated	24.1	1.4	1.20	0.07	22.5	1.3	225	13	0.86	0.24	2.87	0.81
40	Bulk	16.3	0.6	0.81	0.03	15.6	0.6	156	6	0.70	0.03	2.32	0.10
2 h irradiation, move to dark and inject 50 nmol NiP													
41	Activated	36.8	5.1	1.84	0.25	24.3	1.7	243	17	1.97	0.22	6.56	0.73
42	Bulk	34.2	0.7	1.71	0.03	19.5	1.2	195	12	1.60	0.16	5.33	0.53
4 h irradiation, move to dark and inject 50 nmol NiP													
43	Activated	54.0	4.1	2.70	0.20	26.9	0.9	269	9	3.24	0.71	10.81	2.37
44	Bulk	48.2	5.1	2.41	0.26	20.0	1.2	200	12	2.14	0.41	7.13	1.36
4 h irradiation, move to dark and inject 100 nmol NiP													
45	Activated	25.8	2.8	2.58	0.28	16.3	1.0	326	20	3.06	0.08	10.21	0.28
46	Bulk	25.6	2.9	2.56	0.29	12.2	0.5	244	10	2.32	0.24	7.72	0.80

Table D.8. Solar light driven (AM 1.5G, 100 mW cm^{-2}, 25 °C) H$_2$ production with bulk ^{H_2N}**CN$_x$**, bulk and activated ^{NCN}**CN$_x$** and **NiP** at different concentrations in KP$_i$ (0.1 M, pH 4.5, 3 mL) containing α-cellulose. A control experiment in the presence of visible light only irradiation (λ > 400 nm) was also performed.

Entry	Substrate loading / mg	CN$_x$ type	CN$_x$ loading / mg	NiP / nmol	H$_2$ / μmol (4 h)	± σ / μmol	Activity / μmol H$_2$ (g CN$_x$)$^{-1}$ h^{-1}	± σ / μmol H$_2$ (g CN$_x$)$^{-1}$ h^{-1}
AM 1.5G filter								
47	50	^{NCN}CN$_x$	5	20	0.67	0.00	58.4	2.2
48	100	^{NCN}CN$_x$	5	20	0.77	0.02	54.5	2.6
49	150	^{NCN}CN$_x$	5	20	0.58	0.04	41.3	7.3
50	100	^{NCN}CN$_x$	5	50	2.62	0.09	253	26
51	100	^{NCN}CN$_x$	0.5	50	1.43	0.02	1690	100
52	100	Bulk ^{NCN}CN$_x$	5	50	1.91	0.07	132	4
53	100	Bulk ^{H_2N}CN$_x$	5	50	0.13	0.04	8.81	3.89
Visible light only irradiation (λ > 400 nm)								
54	100	^{NCN}CN$_x$	5	50	1.10	0.03	48.6	4.3

182

Table D.9. Solar light driven (AM 1.5G, 100 mW cm^{-2}, 25 °C) H$_2$ production using activated ^{NCN}**CN$_x$** (5 mg) and **NiP** (50 nmol) in the presence of lignocellulosic substrates (100 mg) in KP$_i$ (0.1 M, pH 4.5, 3 mL).

Entry	Substrate type	H$_2$ / μmol (4 h)	± σ / μmol	Activity / μmol H$_2$ (g CN$_x$)$^{-1}$ h^{-1}	± σ / μmol H$_2$ (g CN$_x$)$^{-1}$ h^{-1}	H$_2$ / μmol (24 h)	± σ / μmol
55	no substrate	0	0	0	0	0	0
56	α-cellulose	2.62	0.09	253	26	3.74	0.12
57	xylan	3.89	0.23	137	6	4.92	0.17
58	lignin	0	0	0	0	0	0
59	*lignin	0.20	0.03	40.8	6.8	0.42	0.03
60	cellobiose	8.03	0.68	511	54	14.2	1.7
61	glucose	13.9	0.3	1120	80	32.1	4.8
62	xylose	8.30	0.81	553	54	19.9	2.3
63	galactose	13.2	0.7	762	11	28.0	2.5
64	conifeyl alcohol	0	0	0	0	0	0
65	sinapyl alcohol	0	0	0	0	0	0
66	‡sinapyl alcohol	3.29	0.42	157	10	4.81	0.89

*0.5 mg lignin was used.

‡10 mg of sinapyl alcohol was used.

Table D.10. Solar light driven (AM 1.5G, 100 mW cm^{-2}, 25 °C) H$_2$ production using activated ^{NCN}CN$_x$ (5 mg) and **NiP** (50 nmol) in the presence of raw biomass substrates (100 mg) in KP$_i$ (0.1 M, pH 4.5, 3 mL).

Entry	Substrate type	H$_2$/μmol (4 h)	± σ / μmol	Activity / μmol H$_2$ (g CN$_x$)$^{-1}$ h^{-1}	± σ / μmol H$_2$ (g CN$_x$)$^{-1}$h^{-1}	H$_2$/ μmol (24 h)	± σ / μmol
67	sawdust	2.36	0.43	202	3.8	3.89	0.34
68	paper	0.85	0.04	42.7	2.0	1.42	0.20
69	cardboard	0.94	0.05	46.9	2.5	2.95	0.16
70	bagasse	0.70	0.08	34.8	3.8	1.30	0.08
71	wooden branch	0.71	0.01	35.7	0.3	0.91	0.04

Table D.11. Solar light driven (AM 1.5G, 100 mW cm^{-2}, 25 °C) H$_2$ production with activated ^{NCN}CN$_x$ (5 mg) and **NiP** (50 nmol), H$_2$PtCl$_6$ (4 wt%) or H$_8$N$_2$MoS$_4$ (4 wt%) in the presence of α-cellulose (100 mg) in KP$_i$ (0.1 M, pH 4.5, 3 mL).

Entry	Catalyst	Activity / μmol H$_2$ (g CN$_x$)$^{-1}$ day^{-1}	± σ / μmol H$_2$ (g CN$_x$)$^{-1}$ day^{-1}	Time / day	H$_2$ / μmol (24 h)	± σ / μmol
72	**NiP**	748	24	1	3.74	0.12
				2	3.74	0.12
				3	3.74	0.12
				4	3.74	0.12
				5	3.74	0.12
				6	3.74	0.12
73	Pt	172	23	1	0.86	0.11
				2	2.40	0.12
				3	3.79	0.23
				4	5.12	0.12
				5	5.99	0.05
				6	7.30	0.15
				7	11.7	2.3
				8	12.8	2.4
				9	14.0	2.6
				10	15.7	3.3
				12	16.7	3.7
74	MoS$_2$	356	6	1	1.75	0.13
				2	3.56	0.06
				3	4.72	0.23
				4	5.93	0.25
				5	6.88	0.37
				6	7.67	0.52

Table D.12. Solar light driven (AM 1.5G, 100 mW cm^{-2}, 25 °C) H$_2$ production with activated ^{NCN}CN$_x$ (5 mg) and H$_2$PtCl$_6$ (4 wt%) in the presence of α-cellulose (100 mg) in KP$_i$ (0.1 M, pH 4.5, 3 mL) solution prepared in H$_2$O or D$_2$O.

Entry	Solvent	H$_2$ or D$_2$ / μmol (24 h)	± σ / μmol	k_H / k_D	k_H / k_D error
75	H$_2$O	0.86	0.11	1.48	0.22
76	D$_2$O	0.58	0.05		

Table D.13. Monitoring the CO production after solar light driven (AM 1.5G, 100 mW cm^{-2}, 25 °C) H$_2$ production using activated ^{NCN}CN$_x$ (5 mg) with H$_2$PtCl$_6$ (4 wt%) and α-cellulose (100 mg) in 10 M KOH, pH 2 H$_2$SO$_4$, pH 4.5 and pH 7 KP$_i$ solution (0.1 M, pH 4.5, 3 mL). All the samples were suspended in specified solutions and stirred for 24 h at 25 °C prior to injection of ^{NCN}CN$_x$ and H$_2$PtCl$_6$.

Entry	Conditions	Time / day	CO / μmol	± σ / μmol
77	H$_2$SO$_4$, pH 2	1	0.00	0.00
		6	0.0120	0.0072
78	KP$_i$, pH 4.5	1	0.00	0.00
		6	0.0123	0.0049
79	KP$_i$, pH 7	1	0.00	0.00
		6	0.0280	0.0072
80	10 M KOH, pH 15	1	0.00	0.00
		6	0.00	0.00

Table D.14. Solar light driven (AM 1.5G, 100 mW cm^{-2}, 25 °C) H$_2$ production using activated ^{NCN}CN$_x$ (5 mg) with H$_2$PtCl$_6$ (4 wt%) and α-cellulose (100 mg) in 1, 5, 10 M KOH, pH 2 H$_2$SO$_4$, pH 4.5 and pH 7 KP$_i$ solution (0.1 M, pH 4.5, 3 mL). All the samples were suspended in specified solution and stirred for 24 h at 25 °C prior to injection of ^{NCN}CN$_x$ and H$_2$PtCl$_6$.

Entry	Solvent and pH	Activity / µmol H$_2$ (g CN$_x$)$^{-1}$ day^{-1}	± σ / µmol H$_2$ (g CN$_x$)$^{-1}$ day^{-1}	Time /day	H$_2$ / µmol	± σ / µmol
81	H$_2$SO$_4$, 2	178	5	1	0.89	0.03
				2	2.44	0.03
				3	3.97	0.06
				4	6.29	0.09
				5	7.76	0.35
				6	10.2	0.4
82	KP$_i$, 4.5	172	23	1	0.86	0.11
				2	2.40	0.12
				3	3.79	0.23
				4	5.12	0.12
				5	5.99	0.05
				6	7.30	0.15
83	KP$_i$, 7	98.5	2.7	1	0.49	0.01
				2	3.45	0.28
				3	5.16	0.19
				4	5.82	0.51
				5	6.31	0.67
				6	7.75	1.02
84	1 M KOH	497	32	1	2.49	0.16
				2	4.33	0.05
				3	5.94	0.09
				4	7.40	0.40
				5	8.22	0.47
				6	9.82	0.23
85	5 M KOH	458	24	1	2.29	0.12
				2	5.17	0.30
				3	9.48	0.41
				4	13.9	1.0
				5	17.5	1.3
				6	20.7	2.0
86	10 M KOH	1070	50	1	5.33	0.26
				2	11.4	0.03
				3	18.5	0.2
				4	26.8	0.6
				5	32.3	0.3
				6	39.5	1.1

Table D.15. Solar light driven (AM 1.5G, 100 mW cm^{-2}, 25 °C) H$_2$ production using activated $^{NCN}CN_x$ (5 mg) with H$_2$PtCl$_6$ (4 wt%) and cellulose (100 mg), xylan (50 mg) or lignin (0.5 mg) in 10 M KOH. All the samples were suspended in 10 M KOH and stirred for 24 h at 25 °C prior to injection of $^{NCN}CN_x$ and H$_2$PtCl$_6$.

Entry	Substrate	Activity / μmol H$_2$ (g CN$_x$)$^{-1}$ day^{-1}	± σ / μmol H$_2$ (g CN$_x$)$^{-1}$ day^{-1}	Time /day	H$_2$ / μmol	± σ / μmol
87	α-cellulose	1070	50	1	5.33	0.26
				2	11.4	0.0
				3	18.5	0.2
				4	26.8	0.6
				5	32.3	0.3
				6	39.5	1.1
				7	40.6	1.3
				8	48.9	3.1
				9	56.4	2.8
				10	63.5	3.3
				12	69.8	1.4
88	xylan	1450	30	1	7.24	0.17
				2	13.0	0.3
				3	26.3	1.8
				4	35.1	1.4
				5	47.8	3.1
				6	55.5	2.7
				7	63.6	2.4
				8	75.1	1.8
				12	123	9
89	lignin	350	11	1	1.75	0.06
				2	2.86	0.20
				3	4.87	0.37
				4	6.36	0.43
				5	7.70	0.63
				6	8.85	0.74
				7	9.11	0.76
				8	9.56	0.98
				12	13.6	1.3

Table D.16. Photoreactors were prepared using activated $^{NCN}CN_x$ (5 mg) with H_2PtCl_6 (4 wt%) and α-cellulose (1.65, 1,18 or 0.81 mg) in 10 M KOH. All the samples were suspended in 10 M KOH and stirred for 24 h at 25 °C prior to injection of $^{NCN}CN_x$ and H_2PtCl_6. Percentage conversion yields were calculated after irradiating (AM 1.5G, 100 mW cm^{-2}, 25 °C) the samples for 6 days.

Entry	α-Cellulose / mg	Anhydroglucose monomers[a] / μmol	Theoretical maximum H_2[b] / μmol	H_2 / μmol	Conversion / %
90	1.65	10.2	122.2	14.4	11.8
91	1.18	7.28	87.3	11.3	13.0
92	0.81	5	60	13.2	22.0

[a] Moles of anhydroglucose monomer units were calculated by dividing the total amount of α-cellulose used with the molecular mass of an anhydroglucose repeating unit (162.14 g mol^{-1}). [b] The theoretical maximum H_2 was calculated based on the assumption that maximum 12 equivalent of H_2 can be produced per anhydroglucose unit in α-cellulose structure.[5]

E. Reprinting permissions

Title: Interfacial Engineering of a Carbon Nitride–Graphene Oxide–Molecular Ni Catalyst Hybrid for Enhanced Photocatalytic Activity

Author: Hatice Kasap, Robert Godin, Chiara Jeay-Bizot, et al

Publication: ACS Catalysis

Publisher: American Chemical Society

Date: Aug 1, 2018

Copyright © 2018, American Chemical Society

PERMISSION/LICENSE IS GRANTED FOR YOUR ORDER AT NO CHARGE

This type of permission/license, instead of the standard Terms & Conditions, is sent to you because no fee is being charged for your order. Please note the following:

- Permission is granted for your request in both print and electronic formats, and translations.
- If figures and/or tables were requested, they may be adapted or used in part.
- Please print this page for your records and send a copy of it to your publisher/graduate school.
- Appropriate credit for the requested material should be given as follows: "Reprinted (adapted) with permission from (COMPLETE REFERENCE CITATION). Copyright (YEAR) American Chemical Society." Insert appropriate information in place of the capitalized words.
- One-time permission is granted only for the use specified in your request. No additional uses are granted (such as derivative works or other editions). For any other uses, please submit a new request.

ACS Publications
Most Trusted. Most Cited. Most Read.

Title: Photoreforming of Lignocellulose into H2 Using Nanoengineered Carbon Nitride under Benign Conditions

Author: Hatice Kasap, Demetra S. Achilleos, Ailun Huang, et al

Publication: Journal of the American Chemical Society

Publisher: American Chemical Society

Date: Sep 1, 2018

Copyright © 2018, American Chemical Society

ACS Publications
Most Trusted. Most Cited. Most Read.

Title:	Theoretical Analysis of the Sequential Proton-Coupled Electron Transfer Mechanisms for H2 Oxidation and Production Pathways Catalyzed by Nickel Molecular Electrocatalysts
Author:	Laura E. Fernandez, Samantha Horvath, Sharon Hammes-Schiffer
Publication:	The Journal of Physical Chemistry C
Publisher:	American Chemical Society
Date:	Feb 1, 2012
	Copyright © 2012, American Chemical Society

PERMISSION/LICENSE IS GRANTED FOR YOUR ORDER AT NO CHARGE

BACK   CLOSE WINDOW